ALMA MATER STUDIORUM - UNIVERSITÀ DI BOLOGNA

DOTTORATO DI RICERCA IN
ASTROFISICA

Ciclo XXXIII

MAGNETIC FIELDS IN RADIO RELICS AND IN THE OUTSKIRTS OF GALAXY CLUSTERS

Presentata da: **Chiara Stuardi**

Coordinatore di Dottorato:
Prof. Francesco Rosario Ferraro

Supervisore:
Prof.ssa Annalisa Bonafede

Esame finale anno 2021

Settore Concorsuale: 02/C1 – Astronomia, Astrofisica, Fisica della Terra e dei Pianeti
Settore Scientifico Disciplinare: FIS/05 – Astronomia e Astrofisica

Abstract

The observation of diffuse synchrotron radio emission in galaxy clusters reveals the existence of relativistic electrons and large-scale magnetic fields permeating the intra-cluster volume. Shocks developed during mergers of galaxy clusters are thought to originate the elongated, arc-shaped, and polarized sources found in cluster outskirts known as radio relics. The properties of the magnetic fields in radio relics, the possible magnetic field amplification caused by the shock passage, and its connection to the relics formation mechanism, as well as the value of large-scale magnetic fields in cluster outskirts, are the main topics addressed in this Thesis.

Using polarimetric radio observations performed with the *Jansky Very Large Array* (JVLA) and with the *Low Frequency Array* (LOFAR), I have investigated the properties of magnetic fields in galaxy clusters outskirts via both statistical Faraday rotation measures and diffuse source polarimetry. The comparison of measured quantities with advanced numerical simulations of, both, radio relic emission and intra-cluster magnetic fields has proved to be a fundamental tool to constrain magnetic field physical parameters.

Among the results, the Faraday rotation studies of two double relic galaxy clusters presented in this Thesis show that magnetic-fields are not significantly amplified in the shock region. Despite this, low Mach numbers shocks can stretch and align magnetic field lines, which appear well ordered on the emission scales of radio relics from polarimetric observations. The magnetic field structure inside radio relics is complex and likely filamentary. These results will be corroborated by an ongoing systematic study of clusters with double radio relics.

The results achieved in this Thesis proved the extraordinary potential of low-frequency polarization observations for the study of large-scale magnetic fields in the outskirts of galaxy clusters and beyond.

Contents

List of Acronyms

AGN Active Galactic Nucleus/Nuclei

APERITIF APERture Tile In Focus

ASKAP Australian Square Kilometre Array Pathfinder

BCG Brightest Cluster Galaxy

CDM Cold Dark Matter

CMB Cosmic Microwave Background

CR Cosmic Ray

DSA Diffusive Shock Acceleration

FDF Faraday Dispersion Function

FRI Fanaroff-Riley type I

FRII Fanaroff-Riley type II

FT Fourier Transform

FWHM Full Width Half Maximum

GMRT Giant Metrewave Radio Telescope

GRG Giant Radio Galaxy

HBA High Band Antenna

HETDEX Hobby-Eberly Telescope Dark Energy eXperiment

IC Inverse Compton

ICM Intra-Cluster Medium

IGM Inter-Galactic Medium

KS Kolmogorov-Smirnov

JVLA Jansky Very Large Array

LLS Largest Linear Size

LOFAR LOw Frequency ARray

LoTSS LOFAR Two-meter Sky Survey

LoTSS DR1 LoTSS first Data Release

LoTSS DR2 LoTSS second Data Release

MHD Magneto-HydroDynamical

MWA Murchison Widefield Array

NAT Narrow Angle Tail

NRAO National Radio Astronomy Observatory

NVSS NRAO VLA Sky Survey

POSSUM POlarization Sky Survey of the Universe's Magnetism

RM Rotation Measure

rms root mean square

RMSF Rotation Measure Sampling Function

ROSAT ROentgen SATellite

SKA Square Kilometre Array

SZ Sunyaev-Zel'dovich

uGMRT upgraded GMRT

VLASS VLA Sky Survey

VLA Very Large Array

WAT Wide Angle Tail

WHIM Warm-Hot Inter-galactic Medium

WSRT Westerbork Synthesis Radio Telescope

Thesis outline

Galaxy clusters are unique laboratories for the study of a plethora of physical phenomena: large scale structure formation processes driven by the dark matter assembly, acceleration and propagation of cosmic rays, high-β plasma physics, and turbulence, to name a few. Clusters form through a hierarchical accretion in which mergers of sub-clusters and virialization processes follow one another. Dark matter constitutes about the 80% of clusters mass. A hot ($T \sim 10^7 - 10^8$ keV) and diluted ($n \sim 10^{-3} - 10^{-4}$ cm^{-3}) plasma, named the intra-cluster medium (ICM), accounts for another $\sim 15\%$ and emits in the X-ray via thermal bremsstrahlung. Galaxies constitutes only $\sim 5\%$ of galaxy clusters mass.

In the last decades, astrophysicists have realized that non-thermal components are also present in the ICM. While negligible in the total mass and energy budgets of galaxy clusters, these non-thermal components, in the form of cosmic rays and magnetic fields, are key ingredients to understand the (micro-)physics of the ICM. The smoking gun that reveals the presence of relativistic electrons ($E \sim$ GeV) and large-scale magnetic fields ($B \sim \mu$G) in the ICM is the observation of diffuse synchrotron radio emission on Mpc scales in some galaxy clusters. In particular, a fraction of galaxy clusters showing the signs of a recent merger has been found to host two types of diffuse radio emission: radio halos and radio relics. While radio halos are centrally located in galaxy clusters, radio relics are observed in the outskirts, at ~ 1 Mpc distance from the cluster center.

Most of the discovered radio relics are associated with low Mach number ($M \sim 1.5 - 3$) shock waves detected in the X-rays. Shock waves generated during cluster mergers are thought to propagate outwards into the ICM and, once they reach the cluster outskirts, the Mach number increases, and they could (re)accelerate particles and amplify cluster magnetic fields, leading to the observed synchrotron emission. This interpretation is supported by the observation of double radio relics. These are pairs of quasi-symmetric radio relics that are thought to originate from the same merger event. Numerical simulations showed that double radio relics are best observed when the merger axis is almost perpendicular to the line-of-sight. Hence, it is reasonable to assume that projection effects are minimized for these systems and, for this reason, they are good targets for any study that needs to take into

account the three-dimensional structure of the cluster.

This Thesis is focused on radio relics and on the study of magnetic fields in the extreme peripheries of galaxy clusters. Although the general properties of radio relics are interpreted within the described framework, low Mach number shocks require an unrealistically high particle acceleration efficiency to explain the radio power of some relics. In the last years, theoretical studies have focused on the role of magnetic fields, whose properties could have a key role in understanding the radio relic emission. Current estimates established intra-cluster magnetic fields with a strength of 0.1-10 μG, peaking at the cluster center and decreasing radially together with the thermal electron density profile. Present estimates of magnetic fields in radio relics are mainly based on the equipartition assumption and the possible amplification of the magnetic field at the shock is poorly explored.

The investigation of the magnetic fields in cluster outskirts and beyond has also emerged as a new frontier for understanding large-scale magnetic fields origin. The outcomes of different magnetogenesis scenarios differ in cluster outskirts, filaments, and voids so that finding new methods to probe these unexplored territories is crucial. The last-generation radio interferometers, such as the *Low Frequency Array* (LOFAR), the *APERture Tile In Focus* (APERITIF) mounted on the *Westerbork Synthesis Radio Telescope* (WSRT) and the *Australian Kilometre Array Pathfinder* (ASKAP), have a fundamental role in this research, because, due to the large observational bandwidth and the unprecedented spectral resolution, they allow to apply sophisticated techniques for the study of magnetic fields through polarimetric observations. In particular, low-frequency observations are sensitive to the extremely weak magnetic fields which are expected in the most rarefied regions of the Universe.

During my PhD, I have analyzed the radio emission of two double relic galaxy clusters. These works allowed me to investigate different aspects concerning the open questions about the origin of radio relics and their magnetic fields. The two galaxy clusters belong to a larger sample of double relic galaxy clusters which will be used to give strong constraints to the magnetic field amplification in low Mach number shocks. At the same time, I had the chance of exploiting low-frequency polarization observations performed with LOFAR to study the weak magnetic fields outside galaxy clusters. This PhD project allowed me to explore magnetic fields from the center of merging galaxy clusters up to their extreme peripheries. In particular, in this Thesis I address the following questions:

- What are the properties of magnetic fields in radio relics? Are they consistent with current particle acceleration models?
- What are the properties of magnetic fields in merging galaxy clusters with double radio relics?
- How strong is the magnetic field at the cluster outskirts that can eventually

be amplified by shock waves?

This Thesis is structured as follow:

- In Chapter 1, I provide an overview of the physics of merging galaxy clusters, with a particular focus on magnetic fields and diffuse radio emission.

- In Chapter 2, I give an introduction to the techniques used in this Thesis to obtain magnetic field estimates starting from radio polarimetric observations.

- In Chapter 3, I present the study carried out on the double relic galaxy cluster RXC J1314.4-2515, aimed at the detailed investigation of the magnetic field structure internal to the relics. The study was performed using *Jansky Very Large Array* (JVLA) observations in the frequency range 1-4 GHz. This cluster was chosen because new radio observations revealed regions of emission that were not detected before, and this allowed us to step forward in the comprehension of the origin of radio relic emission. Furthermore, current particle acceleration models were tested by combining total intensity and polarization observations. This work has been published in "Particle re-acceleration and Faraday-complex structures in the RXC J1314.4-2515 galaxy cluster" (Stuardi et al., 2019).

- In Chapter 4, I report on the results of the study performed on the double relic galaxy cluster Abell 2345. Five polarized sources, in addition to the relics, were detected in this cluster with our 1-2 GHz JVLA observations. The sources span a projected distance of $\sim$ 1 Mpc from the X-ray center. This opened up the opportunity of studying the magnetic field profile and structure in this complex merging system, from the center up to the region where a relic is observed. This work has been published in "The intracluster magnetic field in the double relic galaxy cluster Abell 2345" (Stuardi et al., 2021).

- In Chapter 5, I show the preliminary results of a JVLA 1-2 GHz study of the magnetic field amplification in clusters with double radio relics addressing, both, prospects and current limitations (Stuardi et al. in prep.). Some of these results have been published in Zhang et al. (2020).

- In Chapter 6, I focus on the peculiarities of radio polarization observations performed with LOFAR in the 120-160 MHz frequency range for the study of magnetic fields in the peripheries of galaxy clusters. In particular, I report on the search for polarized emission from the radio relic in the Coma cluster (Bonafede et al. in prep.) and the study of the magnetization of the cosmic web (O'Sullivan et al., 2020), both performed at frequencies below 1 GHz.

- In Chapter 7, I present the work published in "The LOFAR view of intergalactic magnetic fields with giant radio galaxies" (Stuardi et al., 2020). This study exploited the superb LOFAR capabilities of unveiling the effects of weak magnetic fields in a low-density plasma. To this end, a polarization analysis at 120-168 MHz was carried out on a sample of giant radio galaxies that have a total projected size of $\sim$ 1 Mpc

and are thought to be located in very rarefied environments.

- In the Thesis conclusions, I summarize the results achieved in this Thesis and I provide an outlook about future work.

Chapter 1

The physics of merging galaxy clusters

1.1 Galaxy clusters

The large-scale structure of the Universe formed through the gravitational amplification of small density fluctuations already present in the early epoch (e.g., Kravtsov & Borgani, 2012). Cosmological simulations show that the matter has concentrated over time, generating a network constituted by filaments and sheets (e.g., Springel et al., 2005; Vogelsberger et al., 2014). In the local Universe, galaxy clusters represent the deepest gravitational well at the nodes of this cosmic web (see Fig. 1.1).

Clusters of galaxies were first identified as over-densities of galaxies on spatial scales of R $\sim$ 1 Mpc and they were cataloged on the basis of their richness, ranging from tens to hundreds of members (Abell, 1958). Spectroscopic observations showed that cluster members have a typical velocity dispersion $\sigma_v \sim 10^3$ km s^{-1} (e.g., Ruel et al., 2014). The typical crossing time, t_c, of a cluster over a distance R is thus:

$$t_c = \frac{\mathrm{R}}{\sigma_v} \approx \left(\frac{\mathrm{R}}{1\ \mathrm{Mpc}}\right)\left(\frac{\sigma_v}{10^3\ \mathrm{km\ s^{-1}}}\right)^{-1} \mathrm{Gyr}\ . \tag{1.1}$$

Hence, in one Hubble time ($\sim$ 14 Gyr), the central region of the system reaches the dynamical equilibrium while, in the outskirts, the in-fall and virialization of matter from the cosmic filaments continues (see e.g., Rosati, Borgani & Norman, 2002; Walker et al., 2019).

Assuming dynamical equilibrium, the virial theorem allows us to obtain an estimate of the mass, $M_{\rm vir}$, of the system:

$$M_{\rm vir} \approx \frac{\sigma_v^2 R_{\rm vir}}{G} \approx \left(\frac{\mathrm{R_{vir}}}{1\ \mathrm{Mpc}}\right)\left(\frac{\sigma_v}{10^3\ \mathrm{km\ s^{-1}}}\right)^{2} \times 10^{15}\ \mathrm{M_\odot}\ , \tag{1.2}$$

where G is the gravitational constant. This relation also defines the virial radius,

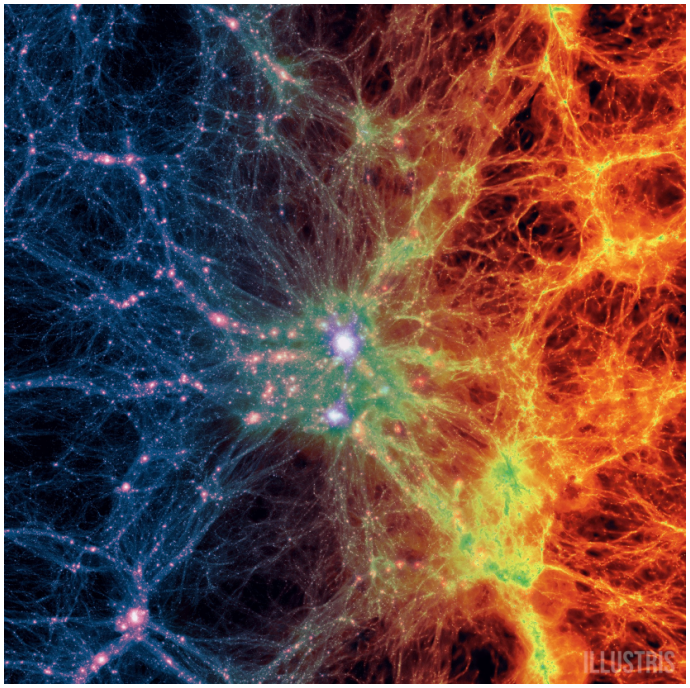

Figure 1.1: Large scale projection through the Illustris cosmological simulation volume at z=0, centered on the most massive galaxy cluster. The dark matter density (left) transits to the gas density (right). Clusters form at the nodes of this cosmic web. Credits: Illustris Collaboration, Vogelsberger et al. (2014).

R_{vir}, which is the radius within which the virial theorem holds and, for typical cluster masses ($\sim 10^{14} - 10^{15}$ $M_{\odot}$), it is $\sim$ 1 - 1.5 Mpc. Other significant scales for galaxy clusters are R_{500} and R_{200}, defined as the radius within which the mean gas density is 500 and 200 times the critical density of the Universe, respectively. Their relation is approximately $R_{500} \approx 0.65\ R_{200}$ (Reiprich et al., 2013). For historical reasons, R_{200} is also often referred to as the virial radius, although $R_{vir} \approx R_{200}$ holds only for an Einstein-de Sitter cosmological model, while for a Λ Cold Dark Matter (ΛCDM) model (i.e., $\Omega_M = 0.3$, $\Omega_\Lambda = 0.7$) $R_{vir} \approx R_{100}$.

The observed optical luminosity of a galaxy cluster is another indicator of the approximate amount of matter contained in the system. This technique requires a good knowledge of the mass-to-light relation in galaxy clusters (e.g., Proctor et al., 2015; Shan, McDonald & Courteau, 2015). The discrepancy between the virial mass of clusters, computed through their gravitational potential, and the mass derived from optical components is a strong evidence of the presence of the dark matter (Zwicky, 1937). In fact, only the $\sim$ 5% of the total mass of galaxy clusters is in the form of galaxies, while the $\sim$ 80% is in the form of dark matter. The remaining $\sim$ 15% of the mass is instead constituted by a hot gas which fills the cluster volume: the intra-cluster medium (ICM). The ICM is hot ($T \sim 10^7 - 10^8$ keV), has a low particle number density ($n \sim 10^{-3} - 10^{-4}$ cm^{-3}) and emits in the X-ray through

optically thin bremsstrahlung emission (see Sec. 1.1.1).

Clusters are classified on the basis of their X-ray morphology in a sequence ranging from relaxed to disturbed clusters. Relaxed clusters have a regular and spherical gas distribution peaked at the center, while disturbed clusters have an irregular morphology, often showing elongation along one axis and a number of sub-structures. The X-ray morphology of a galaxy cluster is highly indicative of its dynamical state since it depends on the stage of structure formation processes currently ongoing in the cluster (e.g., Rossetti et al., 2016; Lovisari et al., 2017; Yuan & Han, 2020). Furthermore, spectroscopic and photometric observations of galaxy clusters members allow for estimation of the dynamical properties of individual sub-clusters (e.g., Boschin, Barrena & Girardi, 2010; Dawson et al., 2015; Golovich et al., 2019b).

A fraction of clusters show diffuse radio synchrotron emission which reveals the presence of relativistic electrons and magnetic fields over scales comparable to the ones of the hot gas (e.g., Feretti et al., 2012; van Weeren et al., 2019). The importance of these non-thermal components has been recognized during the last decades, yet the origin of cluster radio diffuse emission is still under debate (see Sec. 1.1.2 and Sec. 1.4). The lack of knowledge concerns, both, the particle acceleration processes acting in galaxy clusters and the large-scale magnetic fields. Although the main properties of intra-cluster magnetic fields are established, the effective strength, structure and connection to the dynamical state of the clusters have yet to be fully understood (Johnston-Hollitt et al., 2015). In particular, which is the strength of the magnetic field in the outskirts of galaxy clusters and beyond, if and how much the magnetic field is amplified by shocks injected in the ICM during structure formation processes, are the outstanding questions that motivate this Thesis.

The number density of relativistic particles in the ICM is $\sim 10^{-10}$ cm^{-3} and the global energy density of the relativistic plasma is $\sim 1\%$ of the thermal gas (Feretti et al., 2012). Nevertheless, non-thermal components are important for a comprehensive physical description of the ICM. The dynamical evolution of the ICM is affected by radiative cooling and non-gravitational heating from active galactic nuclei (AGN) whose activity may affect turbulent velocities and magnetic fields in clusters (Gitti, Brighenti & McNamara, 2012; Ehlert et al., 2021). In turn, magnetic fields have effect on heat conduction and gas dynamic (e.g., Ruszkowski & Oh, 2010), as well as in the propagation of cosmic rays (CRs, Enßlin et al., 2011). Relativistic particles are sources of non-thermal pressure in the ICM (e.g., Miniati et al., 2001) and their aging and acceleration processes are strictly connected to gas dynamic. It is in fact established that ICM shocks waves and turbulence, are able to accelerate particles to relativistic energies (e.g., Brunetti & Jones, 2014). Magnetic fields can also play an important role in the acceleration of CRs (e.g., Caprioli & Spitkovsky, 2014; Guo, Sironi & Narayan, 2014a). Thus, comprehensive cosmological simulations

must include also non-thermal components, since they are necessary to properly constrain the large-scale structure formation scenario (e.g., Marinacci et al., 2015; Vazza et al., 2018). Clearly, a deeper knowledge of the the non-thermal components of galaxy clusters will have an important impact in the study of cluster astrophysics and cosmology at large.

1.1.1 Thermal component

The ICM permeates the potential well of galaxy clusters. The speed of sound in the gas ($c_s = \sqrt{\gamma kT/\mu m_p}$, where γ is the adiabatic index, k is the Boltzmann constant, T is the gas temperature, μ is the mean molecular weight and m_p is the proton mass) is approximately equal to the velocity dispersion of member galaxies. The temperature of the ICM is thus:

$$kT \approx \frac{\mu m_p \sigma_v^2}{\gamma} \approx 6 \left(\frac{\sigma_v}{10^3 \text{ km s}^{-1}} \right)^2 \text{ keV} \ . \tag{1.3}$$

At these temperatures ($T \sim 10^7 - 10^8$ K) the gas is completely ionized. Felten et al. (1966) first proposed that the X-ray emission from clusters was due to the hot ionized gas with a particle number density $n \sim 10^{-3}$ cm^{-3}. The emissivity of the bremsstrahlung process, $\epsilon_{\nu,X}$, at frequency ν is given by:

$$\epsilon_{\nu,X} = a Z^2 n_e n_i T^{-0.5} g_{ff} e^{-\frac{h\nu}{kT}} \ , \tag{1.4}$$

where Z is the charge of ions, n_e and n_i the number density of electrons and ions, respectively, and g_{ff} the Gaunt factor, slowly varying with frequency and temperature (Sarazin, 1986). The constant a is equal to $5.4{\times}10^{-39}$ erg s^{-1}Hz^{-1}cm^{-3} when the temperature is given in K. The exponential dependence on frequency causes the maximum of the emission to be in the soft X-ray band (i.e., 0.1-2 keV). Hence, from the spectral analysis of the X-ray emission, it is possible to obtain the temperature and the density of the gas. Integrated over volume and frequency, the typical X-ray luminosity of galaxy clusters is $L_X \sim 10^{43} - 10^{45}$ erg s^{-1}.

The total gravitational mass of the cluster can be determined from the temperature and density (ρ) distribution of the X-ray emitting gas. Assuming a spherically symmetric distribution of gas in hydrostatic equilibrium, the gas pressure ($P = \rho kT/\mu m_p$) is related to the gravitational mass within the radius r by:

$$\frac{dP(r)}{dr} = -\frac{GM(\leq r)\rho(r)}{r^2} \ , \tag{1.5}$$

and thus,

$$M(\leq r) = -\frac{kTr}{\mu m_p G} \left(\frac{d\ln(\rho(r))}{d\ln(r)} + \frac{d\ln(T(r))}{d\ln(r)} \right) \ . \tag{1.6}$$

The gas density profile of galaxy clusters is often well represented by the so called β-model (Cavaliere & Fusco-Femiano, 1976):

$$n(r) = n_0 \left[1 + \left(\frac{r}{r_c}\right)^2\right]^{-3\beta/2} , \tag{1.7}$$

where n_0 is the central number density and r_c is the core radius of the cluster. The β parameter is the ratio between the kinetic energy of galaxies and the thermal gas energy ($\mu m_p \sigma_v^2 / kT$). This profile describes an isothermal gas in hydrostatic equilibrium within the potential well associated with a King profile (King, 1972). The projection of this profile on the plane of the sky gives origin to the X-ray surface brightness (S_X) distribution which, for a spherical symmetric cluster is:

$$S_X(r) = S_{X0} \left[1 + \left(\frac{r}{r_c}\right)^2\right]^{-3\beta+0.5} , \tag{1.8}$$

where S_{X0} is the X-ray surface brightness at the center of the cluster.

A bimodality in the gas distribution of galaxy clusters has been observed bringing to the distinction of cool-core clusters and non cool-core clusters (Molendi & Pizzolato, 2001; Sanderson, O'Sullivan & Ponman, 2009). Cool-core clusters are relaxed and show a prominent X-ray surface brightness peak within the inner 100 kpc, together with a significant drop in temperature. This is caused by an increase in gas density towards the cluster center which implies a cooling time much shorter than the Hubble time ($\ll$ 1 Gyr). To balance the radiative losses and the consequent inward gas flow, a source of heating is necessary. To date, the AGN feedback represents the most promising scenario to explain the low cooling flow rates observed in cool-core clusters (Peterson & Fabian, 2006; McNamara & Nulsen, 2007). Conversely, non cool-core clusters are typically found in disturbed systems, which have a shallower X-ray emissivity (Leccardi, Rossetti & Molendi, 2010). Hence, mergers can either disrupt galaxy cluster's core or lead to its mixing with the surrounding hot gas through sloshing (e.g., ZuHone, Markevitch & Johnson, 2010; Wang, Markevitch & Giacintucci, 2016).

Thanks to current X-ray facilities such as *Chandra* and *XMM-Newton*, the X-ray surface brightness can be mapped at high resolution and over large scales. The original β-model was found to be inadequate to describe the central cusp of cool-core clusters or more complex systems. A double β-model was then introduced to overcome such problems (e.g., Xue & Wu, 2000; Lovisari, Reiprich & Schellenberger, 2015). As observations became more and more sensitive to the details of cluster thermal properties, other methods have been proposed to characterize the radial properties up to the cluster periphery (e.g., Ghirardini et al., 2019b).

X-ray spectroscopy is an important tool to study the ICM properties. The *Suzaku* satellite has provided the first X-ray spectroscopic constraints on the gas temperature and density up to the virial radius of galaxy clusters (Walker et al., 2013; Simionescu et al., 2017). These studies revealed that also dynamically relaxed clusters can deviate from spherical symmetry due to large-scale gas sloshing (Simionescu et al., 2012). X-ray spectral analysis can also measure the level of turbulence in the ICM either via the broadening of the emission lines due to gas motions or with the study of resonant scattering (e.g., Inogamov & Sunyaev, 2003). This was one of the aims of the instruments mounted on board of *Hitomi*, which was lunched in 2016 and lost after few weeks of operation. The main result of this mission was to detect for the first time the turbulent motions of the ICM of the Perseus galaxy cluster (Hitomi Collaboration et al., 2016). This demonstrated that turbulent pressure support would correspond to a 2-6% of the thermodynamic pressure in the case of isotropic turbulent motions, or to a 11-13%, in the case of large-scale sloshing (Hitomi Collaboration et al., 2018). The knowledge of the exact contribution given by non-thermal pressure support is necessary to correctly estimate clusters masses on the basis of the hydrostatic equilibrium (Ettori et al., 2019).

Sunyaev-Zeldovich effect

Another observable of the hot plasma contained within clusters is the distortion that it produces on the emission from the Cosmic Microwave Background (CMB, Penzias & Wilson, 1965). This phenomenon is known as the Sunyaev-Zeldovich effect (SZ, Sunyaev & Zeldovich, 1972) and it is due to the inverse Compton (IC) scattering of the CMB photons with free electrons in the ICM.

The temperature variation of the CMB is proportional to the density and temperature of the gas integrated along the line of sight. Hence, this effect can be used to detect the presence of galaxy clusters and to measure their mass, provided that the temperature is known. Since the SZ effect is a scattering process, it is redshift independent, and it can be used to build large samples of galaxy clusters (e.g., the Planck SZ catalog, Planck Collaboration et al., 2016b) and to study their dynamical evolution with cosmic time (e.g., Lovisari et al., 2020).

When the gas density profile of a cluster is reconstructed with X-ray observations and the pressure profile is measured from the SZ effect, the two quantities can be combined in order to study the temperature and entropy profiles (Eckert et al., 2013b,a). The entropy, defined as $K = kTn_e^{-2/3}$, is derived from the density and temperature profiles. This technique can be extended beyond the virial radius of clusters, allowing to study the ICM thermodynamical properties in the cluster outskirts (Ghirardini et al., 2019a).

Galaxy cluster outskirts

In recent years, the interest in the thermal properties of the outskirts of galaxy clusters has grown considerably. The common reference radius for cluster outskirts studies is R_{200}. This is a new territory for the study of clusters physics, since, beyond R_{200}, some of the effects typical of non-virialazed regions are already observable. Some of these effects are: inhomogeneous gas density distributions, internal bulk and turbulent gas motions, deviation from hydrostatic equilibrium and from thermal equilibrium between electrons and ions (see Walker et al., 2019, for a recent review). Recent progresses in this field have been made with the XMM Cluster Outskirt project (Eckert et al., 2017) which obtained temperature, entropy and mass profiles for the 13 clusters with the highest signal-to-noise in the Planck SZ survey.

An enhanced inhomogeneity of the gas density distribution, i.e. clumpiness, in the outskirts of galaxy clusters is predicted by simulations (e.g., Roncarelli et al., 2013). This is a source of systematic bias in X-ray measurements of density and temperature profiles, in particular at $r > R_{200}$, and can lead to underestimate the observed entropy profile. The clumpiness level can be estimated by different methods: using thermodynamical profiles (Walker et al., 2013), comparing the mean and median X-ray surface brightness profiles (Eckert et al., 2015) and with direct highly resolved X-ray imaging (Morandi & Cui, 2014). These three methods give consistent results and also agree with numerical simulations.

An additional bias in the gas fraction estimates can be caused by an excess of non-thermal pressure in the outskirts of galaxy clusters. Hydrodynamical simulations predict that the non-thermal pressure support can increase up to the $15-30\%$ at the virial radius (Vazza et al., 2009; Angelinelli et al., 2020). The non-thermal pressure support can be evaluated comparing measurements of the total mass obtained through the hydrostatic equilibrium and via independent techniques such as gravitational lensing (e.g., Sereno et al., 2018). Using this method, Eckert et al. (2019) found that the median non-thermal pressure fraction ranges from $\sim 6\%$ to $\sim 10\%$ at R_{500} and R_{200}, respectively. These studies open up a deeper understanding of cluster mass content in the outskirts of galaxy clusters.

1.1.2 Non-thermal components

In addition to the optical and X-ray emission, galaxy clusters also show detectable emission in the radio band. The radio emission can be directly connected to individual radio galaxies or quasars, or can be diffused throughout the ICM.

Individual radio sources have now been detected in a variety of morphologies and flavors. The common model to explain their radio emission invokes the central AGN where the gas feeds the super-massive back hole (Urry & Padovani, 1995). Generally, the radio emission consists of an unresolved radio core, coincident with

the optical host galaxy, and a pairs of jets extending from tens to hundreds of kpc. The jets contain a relativistic and magnetized plasma which emits radio synchrotron emission and, interacting with the surrounding thermal gas, may originate different features: lobes, hotspots and plumes (Blandford & Rees, 1974). Fanaroff & Riley (1974) first classified radio galaxies on the basis of their morphology: Fanaroff-Riley type I sources (FR I) are edge-darkened radio sources with the core dominating their emission, Fanaroff-Riley type II sources (FR II) are instead edge-brightened sources with the lobes terminating in bright hotspots (see Fig. 1.2). These two classes of sources were found to have different total luminosity, with FR II being the most powerful. It is also generally assumed, but still debated, that the FR I-FR II dichotomy is related to the large scale environment of the sources (e.g., Massaro et al., 2019).

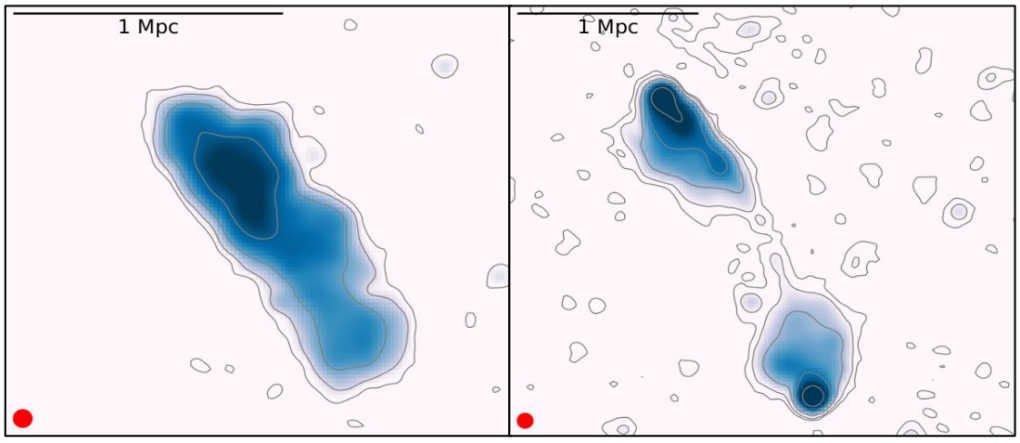

Figure 1.2: Example of a FR I (left panel) and a FR II (right panel) radio galaxy, detected by LOFAR at 144 MHz and 20″ resolution (red filled circle). The surface brightness of the FR I radio galaxy decreases at the edges, while the FR II show two bright hotspots. The two sources are also giant radio galaxies. Adapted from Stuardi et al. (2020).

Nowadays, the unprecedented detail reached by low-frequency radio observations, mainly performed with the *Low Frequency Array* (LOFAR, van Haarlem et al., 2013), demonstrated that the original scheme used for the classification and interpretation of radio galaxies should be regarded with caution (Mingo et al., 2019). Furthermore, a large variety of distorted and peculiar morphologies are populating the radio galaxy zoo, indicating a strong interplay between jets and the external medium (e.g., Hardcastle et al., 2019). Bent radio galaxies constitute a class of radio sources which clearly show a signature of environmental interactions. They are classified as head-tail, if the two jets are non distinguishable (so that the source can appear one-sided, e.g., Terni de Gregory et al., 2017), or narrow angle tail (NAT, e.g., Miley, 1980), and wide angle tail (WAT) if the lobes show two warm-spots after which the deviation occurs (e.g., Missaglia et al., 2019). These sources are mainly

FR I and are commonly found at the center of merging galaxy clusters, where the dynamic pressure resulting from their motion through the surrounding ICM can swept back their jets (Sakelliou & Merrifield, 2000).

Giant radio galaxies (GRGs) are another class of radio galaxies. GRGs are mainly FR II type sources, with almost symmetric lobes, extending up to scales of ∼1 Mpc (e.g., Willis, Strom & Wilson, 1974; Dabhade et al., 2020). Two GRGs are shown in Fig. 1.2. The origin of their large size is still debated. It can be caused by the high kinetic jet power (Wiita et al., 1989). This would be supported by the correlation found between the size of a radio source and its radio luminosity and jet power (Parma et al., 1999; Shabala & Godfrey, 2013). Another explanation could be related to the low density environment in which they evolve (e.g. Malarecki et al., 2015; O'Sullivan et al., 2019) although this interpretation is still debated and challenged by recent observations (Seymour et al., 2020; Tang et al., 2020).

Multi-frequency radio observations are providing increasing evidences of recurrent activity in radio galaxies (e.g., Orrù et al., 2015; Brienza et al., 2020; Morganti et al., 2020). These periods are thought to be caused by the AGN cycling through phases of activity and quiescence. The impact of their energy release on the host galaxy and the environment is an important ingredient in the galaxy cluster formation (e.g., Gaspari & Sądowski, 2017). Low-frequency observations are crucial to recover the duty cycle of restarted sources because they can unveil the oldest electron population ejected in the former phase (Brienza et al., 2017; Quici et al., 2021). The remnant lobes of these radio galaxies are candidate sources of seed relativistic particles re-accelerated in cluster merger events (see Sec. 1.2.3).

Radio galaxies can be used to study magnetic fields, both, in the ICM and in the inter-galactic medium (IGM) outside galaxy clusters (see Vernstrom et al., 2019; O'Sullivan et al., 2020, and see also the results in Chapter. 7 and published in Stuardi et al. 2020). The method used to investigate the existence and the properties of large-scale magnetic fields exploits the Faraday rotation effect that will be further discussed in Chapter 2.

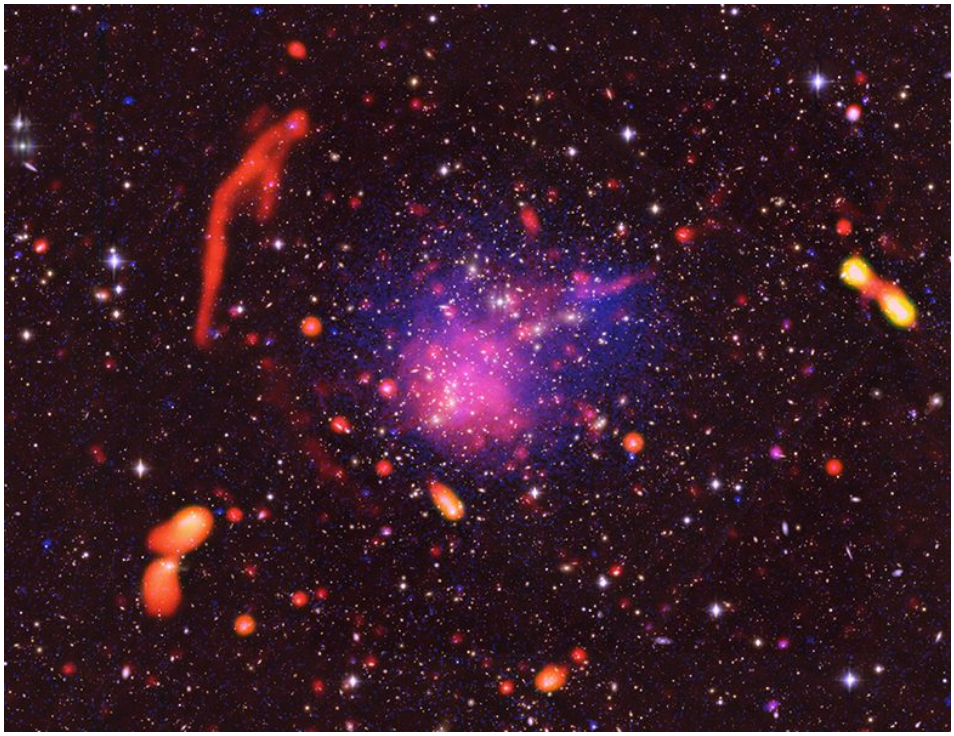

Figure 1.3: The galaxy cluster Abell 2744. The radio emission in red is overlaid over the optical image: both, the emission from individual radio sources and cluster diffuse emission, in the form of a halo and a relic, are visible. At the center, purple indicates the X-ray emission from the thermal gas. Credits: Pearce et al. (2017); Bill Saxton, NRAO/AUI/NSF; *Chandra*, *Subaru*; ESO.

Diffuse radio emission on Mpc scales has been first discovered in the Coma cluster by Large, Mathewson & Haslam (1959). Later, Willson (1970) suggested that the observed radio halo was unrelated to the single point-like sources embedded within it, and that it could be a common feature in rich clusters. Since then, a large number of these objects has been observed and these sources were historically cataloged in three main classes based on their morphology and location: halos, mini-halos, and relics (Feretti & Giovannini, 1996). An example of a cluster with diffuse radio emission is Abell 2744, shown in Fig. 1.3. Radio halos and relics will be further discussed in Sec. 1.4.

Diffuse cluster sources emit in radio via synchrotron radiation, probing the existence of relativistic electrons (with GeV energies and Lorentz factors of $\gamma > 10^3$) and μG magnetic fields in the galaxy clusters volume. The synchrotron power, P_S, emitted by a single electron and averaged over the solid angle is

$$< P_S >= \frac{4}{3\pi}\sigma_T u_B \gamma^2 \beta^2 c \ , \tag{1.9}$$

where $u_B = B^2/8\pi$ is the magnetic energy density, σ_T is the Thomson scattering cross section and β is the ratio of the particle speed and the light speed, which can be approximated with $\beta \approx 1$ if $\gamma >> 1$. Therefore the synchrotron power only depends on the magnetic field energy density, particle number density and Lorentz factor.

The same electrons emitting in the radio band are also responsible for the IC scattering of photons from the CMB to X-ray energies. The emitted IC power can be written with the same expression of Eq. 1.9 substituting to u_B the equivalent energy density of the CMB, $u_{CMB} = B^2_{CMB}/8\pi$, where $B_{CMB} = 3.25(1+z)^2$ μG is the magnetic field equivalent to the CMB at the cluster's redshift, z (e.g., Murgia et al., 1999). Considering together synchrotron and IC energy losses, the characteristic radiative age, t_{age}, of relativistic electrons can be expressed as:

$$t_{age} \approx 3.2 \frac{B^{0.5}}{B^2 + B^2_{CMB}} [(1+z)\nu]^{-0.5} \times 10^{10} \text{ yr} , \tag{1.10}$$

where the magnetic field B is in μG and ν is the observing frequency expressed in MHz (e.g., van Weeren et al., 2019).

The origin of Mpc-size radio sources cannot be simply explained advocating diffusion of relativistic particles. For typical magnetic field strengths of 1-10 μG, t_{age} is lower than 10^8 yr for electrons emitting at radio frequencies. Considering a plasma diffusion and/or bulk velocities of $\sim 10^5$ m s^{-1} (e.g., Bagchi et al., 2002) these high-energy electrons have totally lost they radiative power at GHz frequencies after distances of few tens kpc. This is often referred to as the "diffusion problem". The observation of radio diffuse emission on scales of ~ 1 Mpc shows that relativistic electrons have to be (re)accelerated or produced *in-situ* in the ICM (Jaffe, 1977). The acceleration mechanism of non-thermal particles in the ICM is one of current research topics in the study of this class of sources (e.g., Brunetti & Jones, 2015; Kang, Ryu & Ha, 2019; Bykov et al., 2019).

Assuming that the CR energy distribution is described by a power-law of index δ between Lorentz factors γ_1 and γ_2, $N(\gamma) = K\gamma^{-\delta}$ (see Sec. 1.2.3), the synchrotron emissivity, $\epsilon_{\nu,S}$, of an electron population is:

$$\epsilon_{\nu,S} = \frac{1}{4\pi} \int_{\gamma_1}^{\gamma_2} N(\gamma) P_S(\gamma) d\gamma \propto K B^{(\delta+1)/2} \nu^{-(\delta-1)/2} . \tag{1.11}$$

Thus, the spectral index of the radiation, α, is related to the power-law electron distribution by

$$\alpha = \frac{\delta - 1}{2} \tag{1.12}$$

and the monochromatic synchrotron flux density is a power law with frequency: $S_\nu \propto \nu^{-\alpha}$. The spectrum of the radio emission changes with time, depending on the

energy gain and losses, that in turn depend on the particle acceleration processes in the ICM.

The synchrotron emission is linearly polarized, with the polarization vector perpendicular to the projection of the magnetic field on the plane of the sky. The intrinsic degree of polarization, p, again depends the particle energy distribution (Le Roux, 1961):

$$p = \frac{3\delta + 3}{3\delta + 7} \, . \tag{1.13}$$

For δ=2 (typical of a population of electrons accelerated via Fermi I process, see Sec. 1.2.3) the fractional polarization should be $p \sim 70\%$. The degree of polarization can be enhanced if the magnetic field is not uniform but preferentially ordered along one direction. The degree of polarization can be also reduced by several depolarization effects, both observational and physical, as discussed in Chapter 2.

Cluster radio sources demonstrate that CRs are mixed with the thermal gas and that some re-acceleration or continuous injection process is taking place in the ICM. Relativistic particles are also involved in two emission processes at higher frequencies. The IC scattering of the radio emitting electrons should be responsible for a hard X-ray emission from galaxy clusters (Rephaeli, 1979). Although few conclusive detections of such radiation were obtained up to date, even a non-detection, together with radio observations, can be used to set lower limits on the magnetic fields strength in the cluster (see Sec. 1.3.1). Finally, if also protons get accelerated together with electrons, they can interact with the thermal gas to produce γ-rays in hadronic interactions (Blasi, Gabici & Brunetti, 2007). The upper limits to the γ-ray emission of galaxy clusters obtained by the *Fermi* satellite (Ackermann et al., 2014, 2016) are important to test particle acceleration models actually proposed to explain the origin of cluster radio sources (e.g., Vazza & Brüggen, 2014; Wittor, Vazza & Brüggen, 2017; Brunetti, Zimmer & Zandanel, 2017).

1.2 Mergers of galaxy clusters

Galaxy clusters form through hierarchical structure formation processes. Mergers of galaxy clusters are the most energetic phenomena in the Universe, with $10^{63} - 10^{64}$ erg of kinetic energy dissipated in a crossing time scale ($\sim$ 1 Gyr).

Assuming that the properties of the ICM are entirely determined by gravitational processes, such as adiabatic compression and heating, simple relations can be derived between cluster properties at different redshifts (Kaiser, 1986). In this self-similar spherical collapsing model, clusters of different masses are just a scaled version of each other. However, X-ray observations only partially agree with these predictions and the discrepancies are related to non-gravitational processes. In fact, the contribution of non-gravitational sources (such as AGN, galactic winds, super-

novae, turbulence) to the ICM energy budget depends on the mass of the cluster while the merging history introduces an intrinsic scatter in the relations (e.g., Diaferio, Schindler & Dolag, 2008). The complex interplay between gravitational and non-gravitational processes during cluster mergers was tackled in the past years with, both, semi-analytical approaches and numerical simulations, which can include shocks, magnetic fields, CR particles and turbulence (e.g., Dolag, Bykov & Diaferio, 2008; Arieli, Rephaeli & Norman, 2010; Martin-Alvarez, Planelles & Quilis, 2017; Chisari et al., 2019).

1.2.1 Shocks

During cluster mergers, shock waves are generated in the ICM (see e.g., Ha, Ryu & Kang, 2018). In an idealized binary merger, after the dark matter core passage, two shock waves are injected into the opposite directions along the merger axis (see Fig. 1.4). Merger shocks are strictly connected to the formation of double radio relics (see Sec. 1.4.1). Additionally, simulations show that external shocks originate from the first infall of matter into accreting structures and are continuously generated at several Mpc from clusters center, in cold non-virialized regions (e.g., Vazza, Brunetti & Gheller, 2009a).

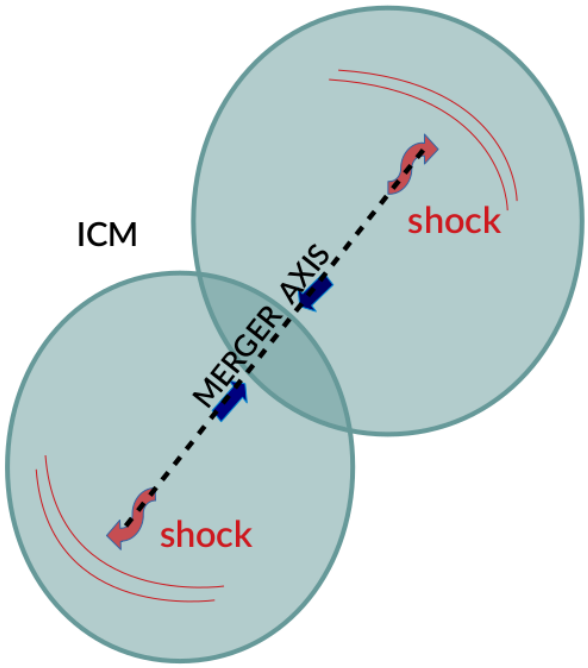

Figure 1.4: Schematic view of a a binary merger between two gas halos and the propagation of shocks.

The shock strength is characterized by its Mach number, M, which is defined as:

$$M = \frac{v_{sh}}{c_s} \ , \tag{1.14}$$

where v_{sh} is the shock velocity and c_s is the sound speed in the pre-shock medium. As discussed in Sec. 1.1.1, the sound speed in the ICM is close to the in-falling velocity of a virialized system (i.e., the shock velocity) so that merger shocks are weak, with $M \sim 2-5$. They dissipate a substantial fraction of their energy in gas heating and the Mach number, together with the amount of dissipated energy, increases with distance from the cluster center (e.g., Schindler & Muller, 1993; Ryu et al., 2003; Vazza et al., 2012). External accretion shocks are instead stronger ($M \gg 10$) but the amount of dissipated energy is lower since they develop in low density environments (e.g., Ryu et al., 2003; Vazza, Brunetti & Gheller, 2009a).

The Rankine-Hugoniot jump conditions relate the thermal properties of the gas in the pre- (upstream) and post- (downstream) shock regions. In particular, the ratio of the downstream (n_d) and upstream (n_u) gas number density, also known as compression ratio C, is related to the Mach number by the simple relation:

$$C = \frac{n_d}{n_u} = \frac{4M^2}{M^2+3} \ . \tag{1.15}$$

Similar relations hold for temperature and pressure jumps across the shock. Using the dependence of the bremsstrahlung emission on density and temperature (Eq. 1.4), X-ray observations have been primarily used to search for and characterize shocks in galaxy clusters (e.g., Markevitch & Vikhlinin, 2007; Finoguenov et al., 2010; Akamatsu & Kawahara, 2013). The temperature jump can be determined by spectral analysis in the upstream and downstream regions, while the density jump can be inferred from the surface brightness analysis across the discontinuity. In the latter case, spherical symmetry is assumed and the underlying density profile is modeled with a broken power-law in the form:

$$n(r) = \begin{cases} n_d(r) = C n_0 (\frac{r}{r_j})^{a_d} & , \text{ if } r \leq r_j \\ n_u(r) = n_0 (\frac{r}{r_j})^{a_u} & , \text{ if } r > r_j \end{cases} \tag{1.16}$$

where n_0 is a normalization factor, a_d and a_u are power-law indexes, and r_j is the radius at the position of the shock front. Once C is determined, the shock Mach number can be derived inverting Eq. 1.15.

Surface brightness jumps are maximized when the merger occurs almost in the plane of the sky since the front is seen edge-on. Projection effects can smooth the discontinuities mixing different structures along the line of sight. Hence, the search for shocks is not trivial due to geometrical assumptions and low count statistics, in

particular in cluster outskirts (e.g., Botteon, Gastaldello & Brunetti, 2018).

1.2.2 Turbulence

Mergers between clusters and accretion of sub-structures are expected to inject turbulence in the ICM (e.g., Vazza, Roediger & Brüggen, 2012). The Reynolds number, R_e, is the ratio of inertial forces to viscous forces within a fluid and it is defined as

$$R_e = \frac{v\rho L}{\mu} \ , \tag{1.17}$$

where v is the flow speed, ρ is the fluid density, L is the characteristic linear dimension of the fluid motions, and μ is the dynamic viscosity of the fluid. A fluid becomes turbulent when $R_e \gg 1$. During mergers, plasma motions are injected on scales comparable to cluster core scales, $\sim 100 - 400$ kpc, with typical velocities of $\sim 300 - 700$ km s^{-1} (e.g., Subramanian, Shukurov & Haugen, 2006). The ICM is weakly collisional because the mean free path of particles due to Coulomb interaction is much larger than the Larmor gyroradius. In these conditions, plasma instabilities and kinetic effects become important and might further reduce the particle mean free path (Lazarian & Beresnyak, 2006). This increases the effective Reynolds number of the ICM to $R_e \gg 10^3$, typical of a highly turbulent medium.

Large scale turbulent motions are subsonic (with Mach numbers 0.2-0.5) but super-Alfvénic, i.e. their velocity is higher than the Alfvén speed, V_A:

$$V_A = B/\sqrt{\mu_0 \rho} \ , \tag{1.18}$$

where B is the magnetic field strength, μ_0 is the permeability of the vacuum and ρ is total mass density of the charged plasma particles. These conditions imply that, in a process resembling a cascade, the turbulence injected in the ICM by large-scale motions is transferred from large to small scales, i.e. below the Alfvén scale, where the velocity of turbulent eddies equals V_A. The transition between hydro and magneto-hydrodynamical (MHD) turbulence happens approximately at the Alfvén scale. Plasma instabilities can also generate self-excited turbulent waves on small scales (e.g., Yan & Lazarian, 2011). Small scale turbulence is expected to have a strong impact on the micro-physics of the ICM (e.g., Brunetti & Jones, 2014) and on the particle acceleration processes that lead to the formation of radio halos (see Sec. 1.4.2).

Observational probes for the presence of turbulence in the ICM require very high spatial and spectral resolution. Indeed, the turbulence can be measured both via X-ray surface brightness fluctuations, which correspond to velocity fluctuations, or with the spectroscopic measurements of the emission line broadening due to gas motion (e.g., Inogamov & Sunyaev, 2003; Gaspari & Churazov, 2013). As discussed

in Sec. 1.1.1, the first spectroscopic detection of turbulent motions in the ICM was obtained by Hitomi Collaboration et al. (2016) studying the central region of the Perseus galaxy cluster. In this system, they found line-of-sight velocity dispersion of ~ 200 km s^{-1} in a region of 30-60 kpc from the core (Hitomi Collaboration et al., 2018). New-generations high-resolution X-ray instrumentation on board of *XRISM* and *Athena* are expected to extend these studies to a larger number of galaxy clusters (Simionescu et al., 2019).

1.2.3 Particle acceleration mechanisms

Turbulence and shocks injected by the merger process into the ICM are able to accelerate particles via several physical mechanisms.

Adiabatic compression. A shock wave can adiabatically compress a bubble of fossil relativistic plasma confined in the ICM (Enßlin & Gopal-Krishna, 2001). Fossil electrons may be supplied by former AGN activity and should be observable only at very low-frequencies (tens of MHz). Since the sound speed in the bubble is high, the mildly relativistic plasma gets adiabatically compressed and not shocked. Due to the compression, the CR electrons are re-energized but they maintain the original spectral slope which should be steep and curved, due to the experienced energy losses. The compression also changes the energy density of the magnetic field within the bubble, resulting in an amplification of the magnetic field of a factor ~ 2 for $M = 2 - 3$ (Iapichino & Brüggen, 2012). If the magnetic field inside the bubble is not too strong (of the order of few μG), the compression of the shock wave can transform the spherical bubble into a torus with filaments of small diameter (Enßlin & Brüggen, 2002).

Diffusive shock acceleration (DSA). Particle acceleration at shocks is described by the DSA theory which can be applied to several astrophysical environments (e.g., Krymskii, 1977; Jones & Ellison, 1991). This is essentially a Fermi I acceleration mechanism, where thermal particles are scattered back and forward across the shock front by magnetic inhomogeneities (Fermi, 1949). At each reversal, particles gain additional energy and their spectrum assumes a power-law distribution with the injection index, δ_{inj}, defined by the shock Mach number (Blandford & Eichler, 1987)

$$\delta_{inj} = 2\frac{M^2 + 1}{M^2 - 1} \ . \tag{1.19}$$

The resulting synchrotron spectral index, α_{inj}, is referred to as the injection spectral index and it is obtained from δ_{inj} with Eq. 1.12

In the downstream region, the maximum particle energy is reduced by radiative losses (see Eq. 1.10). The volume integrated electron spectrum is thus steeper than

the injection spectrum and described by a power-law index

$$\delta = \delta_{inj} + 1 \ , \tag{1.20}$$

if the equilibrium between acceleration end energy losses is reached and provided that other mechanisms do not play a role behind the shock (Kardashev, 1962; Ensslin et al., 1998). Using the relation between the electron power-law and the radio spectral index (Eq. 1.12), it is possible to derive the relation between the observed spectral index and the shock Mach number:

$$\alpha = \alpha_{inj} + \frac{1}{2} = \frac{M^2 + 1}{M^2 - 1} \ . \tag{1.21}$$

As a consequence, DSA predicts that for strong shocks ($M \to \infty$), $\delta_{inj} \to 2$ and $\alpha \to 1$, while for weak shocks (i.e., $M < 5$), $\delta_{inj} > 2$ and $\alpha > 1$ (e.g., Brunetti & Jones, 2014).

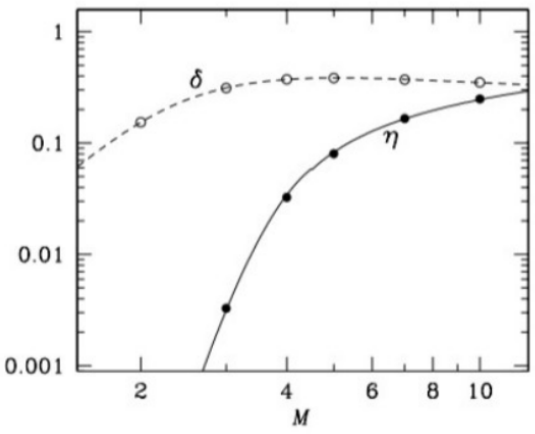

.

Figure 1.5: Gas thermalization efficiency, δ, and CR acceleration efficiency, η, as function of the shock Mach number estimated from numerical simulations. Credits: Brüggen et al. (2012)

The DSA theory was originally developed in the framework of supernova remnants, where strong shocks with $M \sim 10^3$ are able to transfer $\sim 10\%$ of their energy into relativistic protons (e.g., Bell, 2013, for a review). However, several simulations showed that the acceleration efficiency decreases with the shock Mach number (see Fig. 1.5). The fraction of kinetic energy injected by merger shocks into proton acceleration, η, is still uncertain and the electrons acceleration efficiency, ϵ_e, should be a small fraction of η since the Fermi I acceleration process is less efficient for small Larmor gyroradii (see Bykov et al., 2019, for a recent review). Overall, the energy fraction made available by weak shocks to power radio emission is likely $\ll 1\%$ of

their kinetic energy (Vazza, Brunetti & Gheller, 2009a; Brüggen et al., 2012; Kang & Ryu, 2013; Ryu, Kang & Ha, 2019).

In the classic DSA theory, particles are injected into the acceleration process directly from the thermal pool. An additional scenario is the one in which the population of seed electrons is already supra-thermal. This pre-existing population of mildly relativistic electrons may be supplied by previous AGN activity or merger events (Pinzke, Oh & Pfrommer, 2013; Kang & Ryu, 2015, 2016). In this case, the resulting synchrotron spectral index is the one predicted by the DSA only if this is flatter (i.e. closer to zero) than the one of the fossil electrons. If the spectral index of the pre-existing population is instead flatter than the one that could be produced by the shock, the spectrum is boosted but retains the spectral index of the pre-existing population (Gabici & Blasi, 2003; Kang & Ryu, 2011).

Another mechanism which is able to pre-accelerate electrons at the shock front and inject them into the DSA cycle, is the shock drift acceleration (SDA, Guo, Sironi & Narayan, 2014a,b). In SDA, electrons gain energy by drifting along magnetic field lines down the shock front (Kang, Ryu & Ha, 2019). This process is particularly efficient for electrons when the shock normal is quasi-perpendicular to the magnetic field lines in the pre-shock region. In this case, the final synchrotron spectrum is the one produced by the DSA.

Turbulent acceleration. Small scale magnetic field inhomogeneities, such as the ones produced by turbulence in the ICM, are responsible for the Fermi II acceleration process (Brunetti et al., 2001; Petrosian, 2001). This process is a stochastic scattering where particles gain energy only in head-on collisions. Since the probability for a head-on collision is slightly higher than for inverse collisions, the overall electron population gain energy, but the process is poorly efficient. In particular, the direct acceleration of electrons from the thermal pool is very inefficient and a population of pre-accelerated electrons is often invoked to explain diffuse radio emission on Mpc scales (Brunetti & Jones, 2014; Brunetti & Vazza, 2020).

Large-scale turbulent motions are driven from large towards small scales generating a broad turbulent spectrum. Particle re-acceleration can be triggered by, both, compressive and incompressive turbulence on small scales. The compressive turbulence of magnetosonic waves seems to be the most effective in the physical conditions of the ICM. A few to $\sim 10\%$ of the total turbulent energy of these modes is expected to be converted in CR re-acceleration via the Transit Time Damping resonance (Brunetti & Lazarian, 2011). If the energy budget of compressive magnetosonic waves on scales of tens kpc is larger than $\sim 3-5\%$ of the thermal energy, CR electrons can be re-accelerated up to GeV energies by these modes. The acceleration processes can be even more efficient if incompressive Alfvénic modes are also active via gyro-resonance (Brunetti et al., 2004). The resonant interaction of CRs with low-frequency Alfvénic (incompressive) waves and magnetosonic (compressive)

waves transfers an increasing amount of energy from the waves to the CRs. As a consequence, waves are damped and the initial turbulent spectrum is modified. The acceleration gets saturated by the combination of radiative losses and the damping of the waves.

1.3 Magnetic fields in galaxy clusters

Magnetic fields are known to be pervasive throughout the Universe on all scales, from the fields surrounding planets up to diffuse fields in the intra-cluster and inter-galactic media. In recent years, the role of magnetic fields in both galactic and extra-galactic regimes has gained increased attention across many astrophysical disciplines. Magnetic fields with strengths of few μG are found in the lobes of radio galaxies (e.g., Croston et al., 2005) while similar or weaker fields are detected in the ICM of galaxy clusters (e.g., Johnston-Hollitt, Dehghan & Pratley, 2015). The study of the magnetic field on the scales of galaxy clusters and beyond is recognized to be relevant for the understanding of the physical conditions of the ICM and for the implications on structure formation processes (e.g., Ryu et al., 2008; Subramanian, 2016).

Despite the numerous progresses made in the last decades, the study of magnetic fields still poses several observational and numerical challenges. On one hand, the magnetic field is not directly measurable and all the observational methods to constrain it are based on several assumptions and often make use of tailored simulations (e.g., Govoni & Feretti, 2004; Ferrari et al., 2008). On the other hand, the origin of large scale magnetic fields is largely uncertain, and the subsequent amplification processes, which are strongly connected to structure formation history and the micro-physics of the ICM, constitutes a serious challenge for cosmological simulations (e.g., Grasso & Rubinstein, 2001; Donnert et al., 2018). Questions as which is the magnetic fields strength and structure on the largest scales of the Universe, how uniform they are across different cluster populations, what the seeding and amplification mechanisms are, and what their contribution is to the energy density of the IGM, remain topics of present research. These questions will be one of the main science cases faced by the next generation radio telescopes such as the *Square Kilometre Array* (SKA, e.g., Johnston-Hollitt et al., 2015).

1.3.1 Observational constraints on cluster magnetic fields

There are three main methods used to constrain cluster magnetic fields: the equipartition estimate from the synchrotron emission of cluster diffuse sources, the measure of hard X-ray emission from clusters where also diffuse radio sources are present, and the Faraday rotation of sources both embedded and behind clusters.

Equipartition. The measure of the synchrotron power emitted by diffuse radio sources in clusters does not allows us to disentangle the energy content of particles and magnetic fields. The equipartition estimate relies on the assumption that the energy is distributed between the two in order to reach the minimum total energy. This condition is satisfied when the energy of the particles is almost equal to the magnetic field energy. The magnetic energy contained in a source of volume V can be expressed as $U_B = u_B \phi V$, where ϕ is the filling factor, or the fraction of the source volume occupied by the magnetic field. The equipartition is reached when:

$$U_B = \frac{3}{4}(1+k)U_e \ , \tag{1.22}$$

where U_e is the electron total energy and k is the ratio of the energy contained in protons and electrons, U_p/U_e. The value of k is largely uncertain but it is generally assumed to be in the range 1-10^2, where the upper limit is inferred for the measurements performed in the Milky Way (Schlickeiser et al., 2002). Following this assumption, the equipartition magnetic field is

$$B_{eq} = \left[\frac{24\pi}{7}\epsilon(\alpha,\nu_1,\nu_2)\right]^{1/2}(1+k)^{2/7}\nu^{2\alpha/7}I_\nu^{2/7}(1+z)^{(6+2\alpha)/7}d^{-2/7} \ , \tag{1.23}$$

where $\epsilon(\alpha,\nu_1,\nu_2)$ is a constant depending on the spectral index and on the frequency range of the emission, I_ν is the surface brightness observed at frequency ν, z is the redshift of the source and d is the source depth along the line of sight (Govoni & Feretti, 2004).

This method leads to magnetic field estimates in the range 0.1-10 μG within clusters of galaxies showing diffuse radio emission (e.g., Giovannini et al., 1993; Feretti et al., 2012). Instead of using the constant value of $\epsilon(\alpha,\nu_1,\nu_2)$, it has been suggested to derive the equipartition magnetic field by integrating the electron luminosity over an energy range between given $\gamma_{\rm min}$ and $\gamma_{\rm max}$ (Brunetti, Setti & Comastri, 1997; Beck & Krause, 2005). This approach gives magnetic field values 2-5 times larger than the original method. Anyway, these estimates should be used with caution because they are based on several simplified and working assumptions.

Hard X-ray emission. Since the same electron population is at the origin of, both, the radio synchrotron and the hard X-ray IC emission (see Sec. 1.1.2), it is possible to derive a volume averaged estimate of the magnetic field in clusters where both emissions are observed. The equations for the synchrotron flux density F_S at the frequency ν_S and the IC flux F_{IC} at the frequency ν_{IC} share the same power-law index δ, therefore following Blumenthal & Gould (1970):

$$B \propto \left(\frac{F_S}{F_{IC}}\right)^{\frac{2}{\delta+1}}\left(\frac{\nu_S}{\nu_{IC}}\right)^{\frac{\delta-1}{\delta+1}} \ . \tag{1.24}$$

Even if this method has the great advantage of using only measured quantities, the difficulties are related to present observations in the hard X-ray domain and to the problem of distinguishing the IC emission from thermal emission and instrumental and astronomical backgrounds. Up to date, no conclusive claim was made on the detection of hard X-ray emission from the ICM. However, also using upper limits on the IC emission together with radio flux density measurements, lower limits can be computed. They are generally consistent with the values derived from equipartition, ranging from 0.1 to 0.5 μG for radio halos (e.g., Rossetti & Molendi, 2004; Eckert et al., 2008; Wik et al., 2009, 2014). The lower limits obtained for radio relics are in general more stringent than the one obtained for radio halos with values between 0.4 and 3 μG (e.g., Itahana et al., 2015; Locatelli et al., 2020).

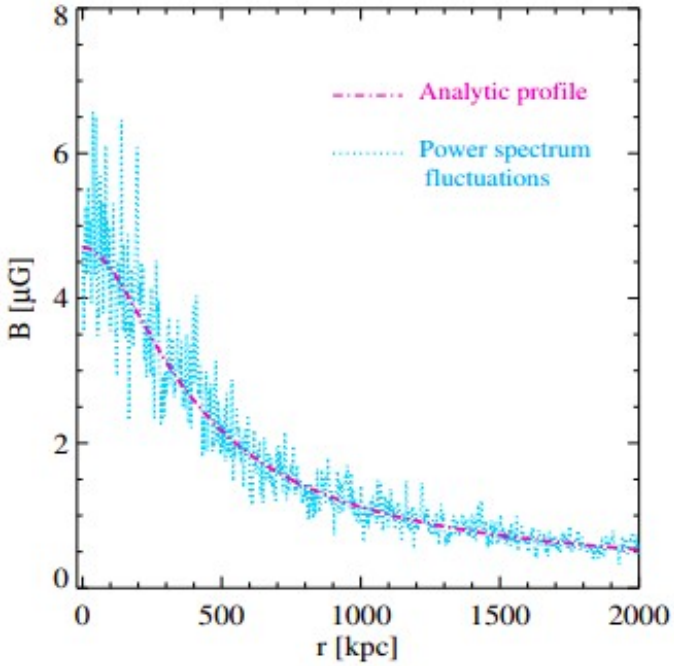

Figure 1.6: The magnetic field profile derived from Faraday rotation measurements in the Coma galaxy cluster. The plot show, both, the radial decrease of the magnetic field magnitude and the fluctuations on different scales. Credits: Bonafede et al. (2010).

Faraday rotation. The Faraday rotation effect occurs when a linearly polarized radiation passes through a ionized medium filled with magnetic field and thermal electrons. The right-handed and left-handed circularly polarized waves, in which the linearly polarized wave can be decomposed, propagate with different phase velocities within the medium and the polarization plane gets rotated. This might affect

the rotation of the intrinsic polarization angle of the emission and its fractional polarization and both effects are frequency-dependent. The Rotation Measure (RM) and depolarization depend on the magnetic field of the intervening medium which can thus be indirectly measured with frequency-resolved observations of polarized sources both behind and embedded in galaxy clusters. This method will be used through all this Thesis and will be described in more detail in Chapter 2.

The Faraday rotation method relies on the reconstruction of the thermal gas distribution and on the assumed 3D model of magnetic field (Johnson et al., 2020). Furthermore, the contribution to the Faraday rotation due to the local source environment and the Milky way foreground are still not completely understood (e.g., Vernstrom et al., 2019). However, the power of this method is that in principle it enables to measure both the strength and the structure of magnetic fields in clusters.

The results achieved in the last decades are numerous. Statistical studies demonstrated that the Faraday rotation of sources seen in projection within cluster is larger than for sources outside them (Clarke, Kronberg & Böhringer, 2001; Johnston-Hollitt & Ekers, 2004; Böhringer, Chon & Kronberg, 2016). This is consistent with ubiquitous cluster magnetic fields with few μG strength and coherence length on $\sim$ 10 kpc scales. Single cluster studies were performed both on merging and relaxed clusters (e.g. Guidetti et al., 2008; Bonafede et al., 2010, 2013; Govoni et al., 2017). Relaxed clusters seem to have larger central magnetic field strengths, of the order of a few 10 μG (Vacca et al., 2012), but lower RM dispersion, with respect to disturbed clusters, which suggest turbulence on smaller scales (Stasyszyn & de los Rios, 2019). In general, magnetic fields have been found to be turbulent and tangled on spatial scales between 5 and 500 kpc (e.g., van Weeren et al., 2019). The magnetic field profile scales with the gas density but different scaling factors were found for different clusters (Dolag et al., 2001; Bonafede et al., 2010; Govoni et al., 2017). This result in a decreasing radial profile of the magnetic field strength from the center to the outskirts of the cluster, as was found for the Coma cluster by Bonafede et al. (2010) (Fig. 1.6). This is also confirmed by Faraday depolarization studies (Bonafede et al., 2011). Using a small cluster sample, Govoni et al. (2017) found a hint of a correlation between the central electron densities and magnetic field strengths, therefore supporting dependence of the magnetic field strength on the cluster mass, but the number of clusters studied with this method is still low.

Although for some specific cluster discrepancies may exist between the magnetic field strengths obtained with the three main methods, overall the estimates are in good agreement, also considering the different assumptions required. Furthermore, while the estimates provided by the equipartition and the hard X-ray methods are volume averaged, the information provided by the Faraday rotation method give an average of the field along the line of sight, weighted by the thermal gas distribution.

A recently developed method to study magnetic field morphology in the ICM is

the gradient technique (Lazarian et al., 2018; Lazarian & Yuen, 2018). This method relies on the fact that the density and velocity gradients in a turbulent plasma are perpendicular to the magnetic field lines. Hence, the magnetic field structure can be inferred from the density gradient of either synchrotron or X-ray radiation, since both of them reflect the turbulent structure of the medium (e.g., Hu et al., 2020). Although promising, this method is still at its dawn.

1.3.2 Evolution of large scale magnetic fields

Despite the reasonable certainty that large-scale magnetic fields are ubiquitous in galaxy clusters, numerous questions remain about their origin and evolution during cosmic time (Brüggen et al., 2012; Ryu et al., 2012). Competing models for the origin of cosmic magnetism are the one of a primordial, pre-recombination, origin (e.g., Grasso & Rubinstein, 2001; Kulsrud & Zweibel, 2008) and the astrophysical one, which predicts the injection of magnetic fields in later times through AGN and/or galactic outflows (e.g., Zweibel & Heiles, 1997; Furlanetto & Loeb, 2001; Beck et al., 2013).

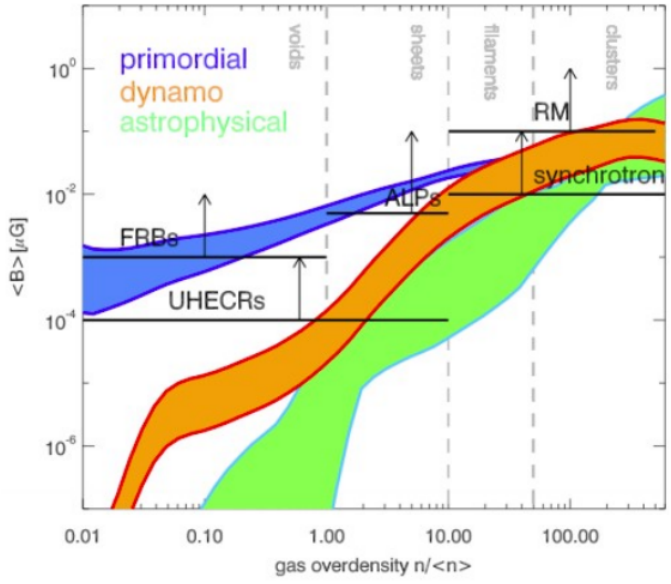

.

Figure 1.7: Distribution of extra-galactic magnetic fields resulting from cosmological simulations following different magnetogenesis scenarios. The approximate magnetic field regime that different observational methods can probe is also shown. Credits: Vazza et al. (2017)

Regardless the the origin of the pre-existing seed field, a commonly accepted scenario is that a weak field got amplified via compression and/or turbulent dynamo amplification during structure formation processes. In the dynamo scenario, as a

result of MHD turbulent motions, the kinetic energy is distributed across different magnetic field scales (e.g., Subramanian, Shukurov & Haugen, 2006; Ryu et al., 2012). The radial decrease of magnetic field with cluster radius can be explained as a consequence of turbulent amplification which coupled gas density and magnetic field (e.g., Dolag, Bartelmann & Lesch, 1999; Dolag et al., 2001). The magnetic field growth is exponential in galaxy clusters and only depends on the amount of dissipated kinetic energy so that magnetic fields in clusters completely lose memory of the original seed field (Vazza et al., 2018; Domínguez-Fernández et al., 2019). Observational constraints of cluster magnetic field growth over time were recently presented in Di Gennaro et al. (2020).

Conversely, the primordial and the astrophysical scenarios result in different field strength in the rarefied regions outside clusters (see Fig. 1.7) so that the measure of magnetic fields in filaments and voids are crucial to disentangle the two scenarios (Vazza et al., 2017). Up to date, magnetic fields in the most rarefied region outside galaxy clusters are poorly constrained, with upper limits of few nG and below (e.g., Hackstein et al., 2016; Ravi et al., 2016; Planck Collaboration et al., 2016a; O'Sullivan et al., 2020) to lower limits of $\sim 10^{-15} - 10^{-17}$ G (Neronov & Vovk, 2010; Dolag et al., 2011; Tavecchio et al., 2011).

1.4 Diffuse radio sources in galaxy clusters

The presence of large-scale magnetic fields and relativistic particles in the ICM is unveiled by the presence of diffuse radio sources (see Sec. 1.1.2). These sources were originally classified in three main categories: radio halos, mini-halos and radio relics (Feretti & Giovannini, 1996). Radio halos are roundish Mpc-size sources centrally located in merging galaxy clusters (e.g., Kale et al., 2015). They are usually unpolarized* and they are not directly connected to any optical counterpart. Mini-halos have smaller sizes ($\sim$ 500 kpc) and are typically located in cool-core galaxy clusters (e.g., Giacintucci et al., 2017) which also host a powerful radio-loud central brightest cluster galaxy (BCG). Radio relics have been defined as extended sources that show high levels of polarization ($> 10\%$ at GHz frequencies) and are located in the outskirts of merging galaxy clusters. They often have an arc-like shape (e.g., van Weeren et al., 2010).

In Sec. 1.1.2 the aging time of radio emitting electrons was computed. It was also shown that it is not possible to explain Mpc-scale diffuse emission with elec-

*Currently, only three halos have been reported to be polarized: Abell 2255 (Govoni et al., 2005), MACS J0717.5+3745 (Bonafede et al., 2009a), and Abell 523 Girardi et al. 2016. Whether the polarized emission originates from the radio halo itself, or from polarized radio relics seen in projection on-top of the radio halo emission is still unclear. Hence, actually there are not enough spectral index studies to be able to draw conclusion about the general properties, and those available are limited in fidelity.

trons accelerated at a single location in the ICM. Relativistic electrons need to be (re)accelerated or produced *in-situ* in the ICM (Jaffe, 1977). Acceleration mechanisms connected to structure formation processes (see Sec. 1.2.3) may provide a possible explanation to the diffusion problem. In fact, both radio relics and halos are found in galaxy clusters which are dynamically disturbed, suggesting that cluster mergers play a crucial role in the formation of these sources (Buote, 2001; Cassano et al., 2010b; Golovich et al., 2019b).

Another common feature of diffuse radio sources is that they have steep spectra, i.e. $\alpha > 1$. This indicates that the underlying particle acceleration processes have a low efficiency (e.g., Brunetti & Jones, 2014; Bykov et al., 2019). Spectral index studies are fundamental in order to put constraints on the proposed acceleration models.

The boundaries between different classes of sources, based on their observational features, are not always obvious. The unprecedented detail reached by last-generation radio interferometers, in particular at low-frequencies, unveiled an older electron population emitting at MHz frequencies. These observations revealed cluster sources with complex morphologies (Botteon et al., 2020b) and often connected with radio galaxies or revived AGN fossil plasma sources, also known as phoenices (Mandal et al., 2020). Fossil sources can get blended with other diffuse sources, furnishing them with fossil electrons which are then re-accelerated by shock or turbulence (Sec. 1.2.3). This can complicate the classification, together with projection effects which may cause different classes of sources to overlap along the line-of-sight (e.g., Rajpurohit et al., 2020a). Also, the discovery of Mpc-size ultra-steep-spectrum sources in clusters hosting mini-halos (Savini et al., 2019), suggests the presence of an intermediate stage between mini-halos and giant radio halos, as their host clusters appear to be slightly disturbed (Raja et al., 2020).

The main properties of radio relics and radio halos will be described according to the current nomenclature although the taxonomy of extended radio emission in galaxy clusters is evolving thanks to the advent of new instruments, such as LOFAR (van Haarlem et al., 2013), the *Murchison Widefield Array* (MWA, Tingay et al., 2013) the *upgraded Giant Metrewave Radio Telescope* (uGMRT, Gupta et al., 2017), the *Australian Square Kilometre Array Pathfinder* (ASKAP, Johnston et al., 2007) and *MeerKAT* (Jonas & MeerKAT Team, 2016). In this Thesis, the main focus is on radio relics and on the connection between the merger process and the formation of diffuse radio sources, therefore mini-halos will be not discussed further.

1.4.1 Radio relics

Radio relics are arc-shaped sources on Mpc scale, located at the periphery of some merging galaxy clusters. They are characterized by a steep integrated spectrum (i.e.,

$\alpha = 1 - 1.5$) and strong polarization ($\sim 20 - 50\%$ at 1.4 GHz). At present, there are about 60 radio relics known and they are detected in clusters covering a wide range in mass (see van Weeren et al., 2019, for a recent collection). The occurrence of radio relics was found to be $5 \pm 3\%$ within the GMRT Radio Halo Survey by Kale et al. (2015). The fraction of radio relic hosting clusters found in the second Planck cluster catalog (Planck Collaboration et al., 2016b) in the sky area covered by the first release of the LOFAR Two-meter Sky Survey (LoTSS, Shimwell et al., 2017, 2019) is $15 \pm 8\%$ (van Weeren et al., 2020).

According to simulations, during cluster mergers, shock waves move outwards along the merger axis (see Fig. 1.4) and form pairs of symmetric radio relics, also named double radio relics, that extend in the direction perpendicular to the merger axis (Brüggen et al., 2012; Ha, Ryu & Kang, 2018). Therefore, they should be best observed when the merger occurs in the plane of the sky. About a dozen of double radio relics systems are known. Two examples are shown in Fig. 1.8. In the majority of cases, only one relic is observed and more complex radio morphologies may originate from complicate merger configurations or projection effects (i.e., Owen et al., 2014; Rajpurohit et al., 2018). Radio relics are generally found at distances up to a large fraction of the cluster virial radius from the cluster center. The radial distribution of observed radio relics can be explained by the fact that the dissipated kinetic energy in shocks increases with the distance from the cluster center up to half of the virial radius (Vazza et al., 2012).

There is strong evidence that relics are connected with merger shocks generated during cluster mergers. For several radio relics, the X-ray surface brightness and temperature jumps related to the shock have been identified (e.g., Finoguenov et al., 2010; Akamatsu & Kawahara, 2013; Hoang et al., 2018). Up to date, there are about 20 X-ray detected shocks at the location of radio relics (van Weeren et al., 2019). The connection between mergers and radio relics is corroborated by optical and weak lensing analyses that unveil the internal dynamics of clusters (e.g. Boschin, Barrena & Girardi, 2010; Okabe et al., 2015). A recent and comprehensive optical study of clusters hosting double radio relics is presented by Golovich et al. (2019a,b), who confirmed that the merger axis of these clusters is preferentially near to the plane of the sky. Hence, it is possible that merger axis orientation plays an important role in the detection rate of these sources.

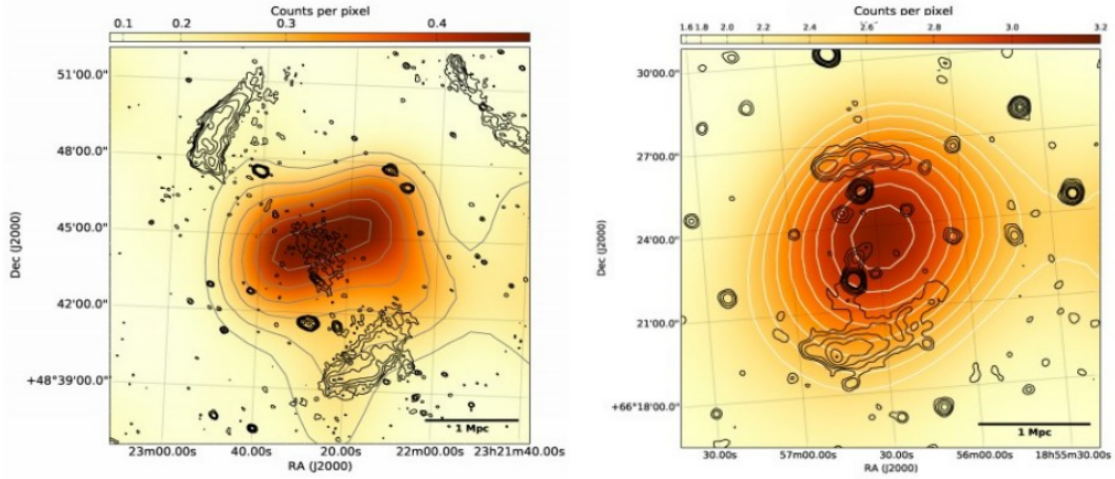

.

Figure 1.8: Double relic systems in the galaxy clusters PSZ1 G108.18-11.53 (left) and PSZ1 G096.89+2417 (right). Black contours show the radio emission overlaid on top of the X-ray image of the cluster. Credits: de Gasperin et al. (2014) and de Gasperin et al. (2015).

The most spectacular example of a radio relic is probably the so called Sausage relic in the CIZA J2242.8+5301 galaxy cluster (van Weeren et al., 2010). It has a remarkable regular arc-shaped structure extending up to ∼2 Mpc with a width of only ∼55 kpc when observed at 610 MHz (Fig. 1.9). It shows very high level of polarization, reaching the $50 - 60\%$ level, and magnetic field vectors are aligned with the relic. Also, this relic shows a very clear steepening trend of the spectral index which increases from the 0.6 of the outer edge to 2.0 across the width of the relic.

A gradual spectral index steepening towards the cluster center is also observed in other radio relics and supports the model of shock acceleration at the outer edge and spectral aging of relativistic electrons in the downstream region (van Weeren et al., 2010). Such as the Sausage, most radio relics also show asymmetric transverse brightness profiles, with a sharp edge on the external side with respect to the cluster center.

Deep high-resolution observations of radio relics have revealed a significant amount of filamentary substructures (e.g. Di Gennaro et al., 2018). Similar structures were found in all relics that have been studied with good signal-to-noise and at high-resolution (i.e., Owen et al., 2014; Rajpurohit et al., 2018). The nature of the filamentary structures is not fully understood: they may trace changes in the magnetic field or be originated by the complex shape of the shock surface. Filaments and threads are also found in highly resolved 3D simulations of cluster radio relics (Wittor et al., 2019; Domínguez-Fernández et al., 2020).

Polarimetric observations of radio relics show that magnetic field vectors are well

aligned and oriented parallel to the shock front, i.e. the relic main axis (Bonafede et al., 2009b, 2012; Pearce et al., 2017). This indicates that the magnetic field is well ordered on the physical scales of radio relics. At the same time, radio relics depolarize at low-frequencies (Pizzo et al., 2011; Ozawa et al., 2015). Hence, observations at frequencies above $\sim$ 1 GHz are best suited to probe their intrinsic polarization properties, as also suggested by highly resolved simulations of cluster radio relics (Wittor et al., 2019).

Scaling relations exist between the relics and host cluster properties. A correlation was found between cluster X-ray luminosity and relic radio power at 1.4 GHz, $P_{1.4\mathrm{GHZ}}$ (Feretti et al., 2012). This correlation likely reflects the underlying correlation between mass an radio power, with $P_{1.4\mathrm{GHZ}} \propto \mathrm{M}_{500}^{2.8}$ (where M_{500} is the mass enclosed within R_{500}) found by de Gasperin et al. (2014). They also found a correlation between the largest linear size (LLS) and the relic distance from the cluster center.

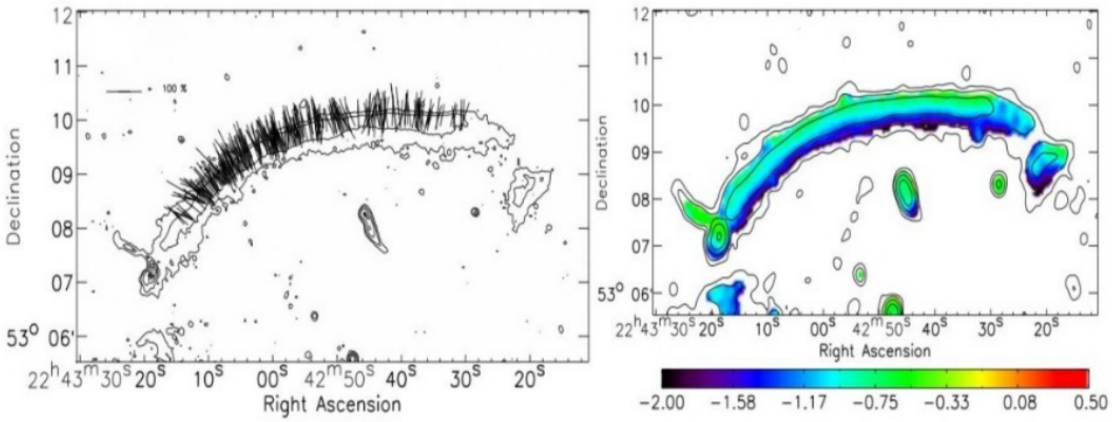

Figure 1.9: Radio polarization and spectral index maps of the Sausage relic. Left: lines represent the polarization electric field vectors. The length of the vectors is proportional to the polarization fraction. A reference vector for 100% polarization is shown in the upper left corner. Right: spectral index map obtained with a power-law fit to measurements at five frequencies between 2.3 GHz and 610 MHz. Credits: van Weeren et al. (2010).

Origin of radio relics

Although there is evidence that relic origin is connected to shock waves generated in the ICM by merger events, the underlying particle acceleration mechanism is still under debate.

A possible acceleration mechanism is the adiabatic compression of confined fossil radio plasma (Enßlin & Gopal-Krishna, 2001; Enßlin & Brüggen, 2002). This mechanism can be used to describe particular relic systems (e.g., Button & Marchegiani, 2020) but it is mainly challenged by two facts. First, in this scenario, the relativistic

plasma should be well confined in the ICM to keep its internal sound speed close to the speed of light since the sound speed would drop as soon as mixing with the thermal ICM occurs. Secondly, the observation of a number of double relics disfavors this scenario because of the low probability to find two symmetric bubble of fossil electrons. Adiabatic compression may play a more crucial role in the formation of the so called radio phoenices which are sources with very steep spectrum ($\alpha > 1.8$) and amorphous morphology (e.g., Mandal et al., 2020).

The alternative mechanism of the DSA has been proposed (e.g., Ensslin et al., 1998; Roettiger, Burns & Stone, 1999). Although this mechanism can explain the general properties of relic emission, two observational features remain unexplained:

(i) the observation of low Mach number shocks. To date, a number of shock fronts have been detected using radio relics as shock tracers (Finoguenov et al., 2010; Urdampilleta et al., 2018, for some collections). Typical Mach numbers of mergers shocks inferred from X-ray observations are between 1.5 and 3, with some exceptions at M>3 (Markevitch et al., 2002; Botteon et al., 2016b; Dasadia et al., 2016). The electron acceleration efficiency predicted by the DSA model for low Mach number shocks is $\ll 1\%$ of the shock injected energy flux (see Sec. 1.2.3). In this regime, the radio power observed from the majority of relic cannot be explained by the classical DSA theory (see Botteon et al., 2020a, and see also the results in Chapter. 3 and published in Stuardi et al. 2019).

(ii) the non-detection of γ-ray emission in merging galaxy clusters. Protons are also expected to be accelerated by merger shocks and to produce γ-rays in the interaction with the thermal gas. The most updated *Fermi* upper limits (Ackermann et al., 2014) lead to a shock acceleration efficiency for protons even lower than what is normally assumed (i.e., below 10^{-3}, Vazza & Brüggen, 2014; Vazza et al., 2016) which is even more problematic compared to the observed radio power;

The standard DSA theory is also challenged by the spectral shape of some relics. The DSA predict an integrated power-law spectrum for radio relics. A clear case in which curved spectral indexes are difficult to reconcile with particle acceleration models is Abell 2256 (Trasatti et al., 2015). The faint relics in the 1RXS J0603.3+4214 cluster (also known as the Toothbrush galaxy cluster) also show a high frequency spectral steepening (Rajpurohit et al., 2020a). A flat (i.e., < 1) integrated spectrum at low-frequencies is also incompatible with the simplest DSA model in a steady state (Trasatti et al., 2015; Kierdorf et al., 2017). However, some of these claims have been recently revised thanks to high frequency observations performed with single dish telescopes that allow to recover the total flux of large structures (e.g., Loi et al., 2020; Rajpurohit et al., 2020b).

Furthermore, a discrepancy between radio and X-ray derived Mach numbers has been often observed (e.g., Rajpurohit et al., 2018). Using the DSA theory it is possible to derive the Mach number directly from the radio spectral index of the observed

emission (inverting Eq. 1.21). A discrepancy exists between the Mach numbers derived with these two different approaches, with the radio-derived Mach numbers being generally higher (e.g., Akamatsu & Kawahara, 2013). Numerical simulations have been performed in order to clarify such inconsistency. Since the acceleration efficiency strongly depends on the Mach number, the CR-energy-weighted Mach number derived by the radio spectral index is expected to be higher than the kinetic-energy-weighted one measured from X-ray emission (Ha, Ryu & Kang, 2018). The emerging scenario is that Mach number variations over shocks (Skillman et al., 2013; Rajpurohit et al., 2020a) and projection effects (Hong, Kang & Ryu, 2015) might mitigate the observed differences.

Following these observational challenges, additional or alternative mechanisms have been proposed, as for example the re-acceleration of pre-existing low-energy relativistic electrons (e.g, Pinzke, Oh & Pfrommer, 2013; Kang & Ryu, 2015, 2016). The origin of such fossil particles could be either in old AGN remnants, or in an electron population accelerated by earlier shock waves. In this scenario, only a fraction of clusters may have adequate seed particle population and, in that case, the acceleration efficiency required to match radio observations would be lower. Furthermore, if the seed population of AGN origin was mostly composed of electrons, the non-detection of γ-ray emission would also be explained. Unfortunately, up to date, the connection between AGN and radio relic could be established only in few cases (e.g., Bonafede et al., 2014; van Weeren et al., 2017). We present an additional case in this Thesis (see Chap. 3, published in Stuardi et al., 2019).

Magnetic fields in radio relics

Recent models have focused on the role of magnetic fields, that in particular configurations, could allow electrons to reach supra-thermal energies via the shock drift acceleration (SDA) process before being injected into the DSA cycle (Sec. 1.2.3). Using particle in cell simulations, Guo, Sironi & Narayan (2014a,b) have shown that, in a quasi-perpendicular pre-shock magnetic field (i.e., when the magnetic field lines are almost perpendicular to the shock normal, hence aligned with the shock front), electrons can be pre-accelerated also by shocks with M=3. This is confirmed by the study of (Kang, Ryu & Ha, 2019) which identified a critical Mach number of 2.3, under which the pre-acceleration is not effective. Caprioli & Spitkovsky (2014) demonstrated that for quasi-perpendicular shocks the proton acceleration is quenched also for M=5 (see also Ha et al., 2018). Although recent studies have confirmed that this might reduce the tension with the upper limits set by the *Fermi* collaboration (Wittor, Vazza & Brüggen, 2017; Ha, Ryu & Kang, 2020; Wittor et al., 2020), the role of the magnetic field and its amplification by low Mach number shocks is still poorly constrained. To this end, obtaining highly resolved information on the polarization of radio emission in relics has the potential of revealing the local topology

of magnetic fields in the electron cooling region.

Shocks may amplify magnetic fields by a number of mechanisms, which are still not well understood, in particular in the low Mach number regime (see Donnert et al., 2018, for a recent review). The possible amplification of the magnetic field components parallel to the shock surface by pure compression was investigated by Iapichino & Brüggen (2012). In this case the ratio of the downstream and upstream magnetic fields is

$$\frac{B_d}{B_u} = \sqrt{\frac{2C^2+1}{3}} \ , \tag{1.25}$$

where C is the compression factor, which is linked to the shock Mach number by Eq. 1.15. This implies that for typical cluster shocks with Mach numbers $M \sim 2-3$ the amplification factor is ∼1.7-2.5. They also studied the possible presence of magnetic field amplification due to the turbulent dynamo in the downstream region. They argue that self-generated vorticity from the shock is not sufficient to drive a turbulent dynamo downstream, but that a turbulent pressure of about $10-30\%$ of the total pressure is required upstream of the shock to explain observed magnetic field lower limits. Ji et al. (2016) also confirmed that the modest magnetic field amplification by low Mach number shocks is mostly compressional and results in a downstream field parallel to the shock surface. A recent model of the Sausage relic explained the downstream magnetic field amplification with a dynamo acting behind the shock with an injection scale of magnetic turbulence of about 10 kpc (Donnert et al., 2016). However, the ordered topology of magnetic fields expected by compressional amplification can explain the large degree of polarization found in some radio relics, thus disfavoring turbulent amplification.

From an observational point of view, the magnetic field amplification in the relic region is still lacking strong evidences. This is also due to the fact that, up to date, the majority of the information about the magnetic field at radio relics are obtained from equipartition estimates which can only give an average value in the relic and cannot be used to constrain the magnetic field amplification. Other methods can be used to study the magnetic field at the position of radio relics, as for example the relic width method (van Weeren et al., 2010). In this case the assumption is that the width of the relic is uniquely determined by the life time of relativistic electrons and the shock downstream velocity. Projection effects, filamentary magnetized structures and multiple shocks detected in radio relics complicate this simplistic view (e.g., Rajpurohit et al., 2018). However, also this method is not able to constrain magnetic field amplification.

Few Faraday rotation studies were performed on radio relics: there are some indications that for radio relics at large projected distances from cluster center the Faraday rotation is mostly caused by the Milky Way foreground, but contribution from the cluster are also observed (e.g., Pizzo et al., 2011; van Weeren et al., 2012b;

Ozawa et al., 2015). We present additional Faraday rotation studies of cluster radio relics in this Thesis (see Chapter 3 and 4). The use of the Faraday rotation of background polarized sources to study the magnetic field of relics gave important results. Johnston-Hollitt & Ekers (2004) found a RM enhancement for two sources observed in the background of the relics in the cluster Abell 3667 (Fig. 1.10, left panel). A Faraday rotation enhancement was also found in the merging group of the Coma by Bonafede et al. (2013) (Fig. 1.10, right panel). These foundings point to a possible magnetic field amplification caused by compression and/or turbulence generated by the merger shock. This problem will be further discussed in Chapter 5.

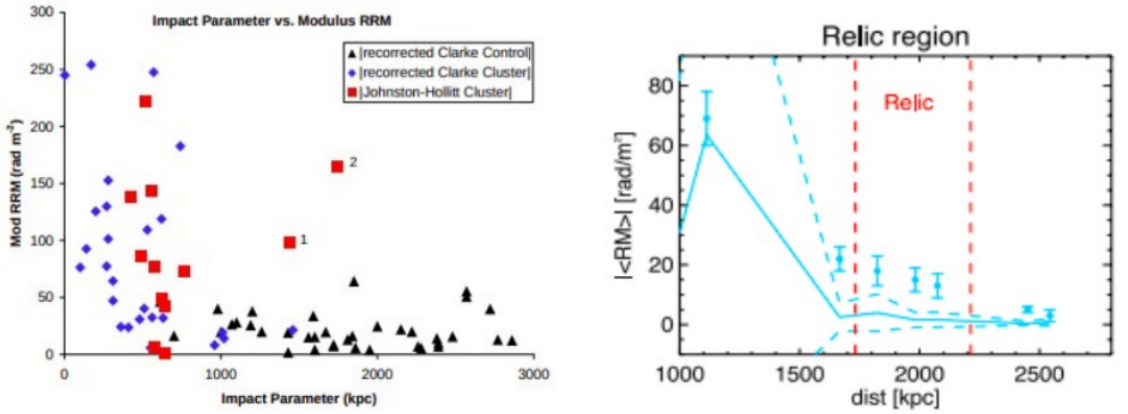

Figure 1.10: Faraday rotation studies performed on sources seen in projection in the background of radio relics. Left: RMs of a large sample of sources (subtracted from the Milky Way foreground) plotted against their distance from the cluster center. The sources marked with numbers are in the background of the relics in the Abell 3667 cluster. Right: RMs of sources in the Coma cluster at the position of the observed radio relic. The solid and dashed lines show the expectations from the magnetic field model derived from the sources at the center of the cluster. Credits: Johnston-Hollitt & Ekers (2004) and Bonafede et al. (2013).

1.4.2 Radio halos

Radio halos permeate the central volume of most massive dynamically disturbed galaxy clusters. They are typically circular, with sizes $\geq$1 Mpc, and their radio surface brightness distribution is generally peaked at the X-ray cluster centroid. The prototype of this class of objects is the radio halo in the Coma cluster (Fig. 1.11) which was detected first by Large, Mathewson & Haslam (1959). Actually, the number of detected radio halos is $\sim$80 (van Weeren et al., 2019) and their are more common in massive clusters. For a mass-selected sample of galaxy clusters Cuciti et al. (2015) found that the halo occurrence fraction is $\sim 60 - 80\%$ for masses $M > 8 \times 10^{14}\ M_{\odot}$ while it drops to $\sim 20 - 30\%$ below this mass.

Radio halos have a steep integrated spectrum, with a reference value of $\alpha = 1.3$ (Feretti et al., 2012). Their spectral index distribution is generally smooth, but some hints of radial spectral steepening has been found in some clusters (e.g., Feretti et al., 2004). Ultra-steep spectrum radio halos with integrated spectral index lower than 1.6 have been also observed (e.g. Dallacasa et al., 2009; Wilber et al., 2018). These features can be explained in the framework of the turbulent re-acceleration model for the formation of radio halos (Cassano et al., 2010a).

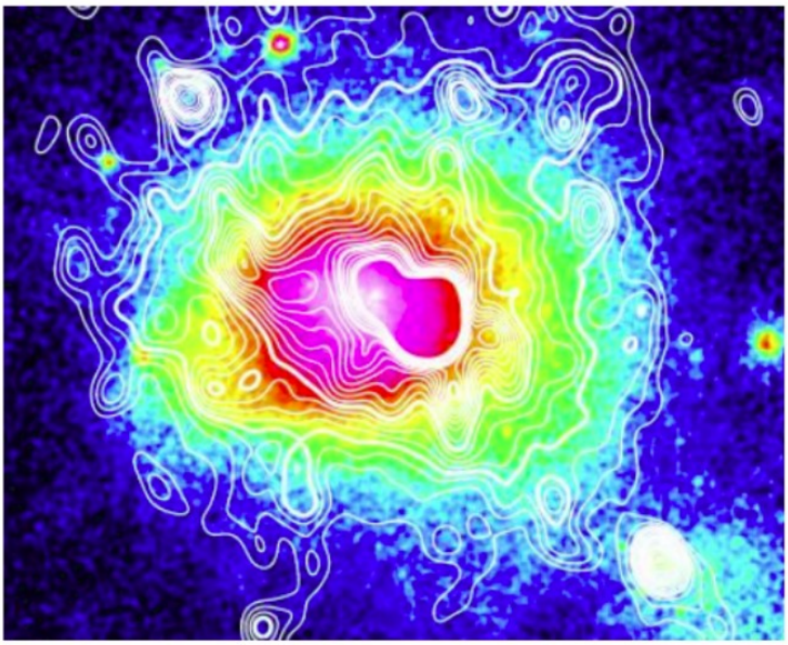

. .

Figure 1.11: The radio halo in the Coma cluster. Radio contours are overlaid over the X-ray emission shown in colors. Credits: Brown & Rudnick (2011).

Origin of radio halos

Is was observed that clusters can be divided into two populations (radio bi-modality): merging systems hosting radio halos, and relaxed systems that do not host detectable large-scale diffuse radio emission (Cassano et al., 2010b). The presence of radio halos in merging galaxy clusters and the close similarity of their emission with the one of the thermal gas, suggest that the energy for particle (re)acceleration could come from the gravitational energy released in the ICM during the process of structure formation (i.e. via turbulence, Brunetti et al. 2009). However, the details of the acceleration mechanism are yet to be understood.

There are two main models that have been proposed: the primary electron (or re-acceleration) model and the secondary electron (or hadronic) model. In the re-acceleration model, a population of mildly relativistic electrons is re-accelerated to

higher-energies by turbulence (see Sec. 1.2.3) induced during merger events (Brunetti et al., 2001; Petrosian, 2001). A prediction of this model is the presence of a larger population of ultra-steep radio halos to be detected at low-frequencies (Cassano et al., 2010a). Conversely, the hadronic model suggests that high energy electron are secondary products of the hadronic interaction between thermal ions and relativistic protons present in the ICM (Dennison, 1980; Blasi & Colafrancesco, 1999). Relativistic protons can accumulate in the ICM because of their negligible energy losses and therefore all galaxy clusters should show diffuse emission in the form of a radio halo. This model is challenged by the non-detection of γ-ray in galaxy clusters, by the correlation found between cluster mergers and radio halos, and by the discovery of ultra-steep spectrum radio halos.

Several scaling relations between the radio and thermal gas properties of the ICM have been studied in the literature (e.g., Enßlin & Röttgering, 2002; Bacchi et al., 2003; Cassano et al., 2007; Rudnick & Lemmerman, 2009). In particular, a steep correlation between the radio power at 1.4 GHz of radio halos and the cluster mass indicates that the cluster mass is an important parameter for halo formation models (Cassano et al., 2013; Cuciti et al., 2015). Cassano et al. (2007) found also a scaling relation between the size of radio halos and their radio power which is motivated in the framework of the re-acceleration scenario.

In some cases the emission from radio relics is spatially connected with that of the radio halo (e.g., Dallacasa et al., 2009; Bonafede et al., 2012; van Weeren et al., 2016a; Hoang et al., 2017). If the connection is real or just a projection effect is still unclear (e.g., Rajpurohit et al., 2020a). One possibility is that in the overlapping region there is a transition from Fermi I to Fermi II re-acceleration process by turbulence that develops in the post shock region (van Weeren et al., 2016a).

Chapter 2

From polarization to magnetic field estimates

2.1 Polarization

Synchrotron radiation is linearly polarized (see Sec. 1.1.2). Therefore, radio polarization observations can directly probe the structure of the projected magnetic field at the source. For example, the alignment of the magnetic field lines observed in radio relics gave important insights on their origin (e.g., Ensslin et al., 1998; van Weeren et al., 2010; Wittor et al., 2020). Polarized emission also allowed the study of the magnetic field structure in radio galaxy jets, lobes and hotspots (e.g., Gabuzda et al., 1992; Guidetti et al., 2011; Johnston-Hollitt et al., 2015).

The intrinsic degree of polarization of the synchrotron emission is described by Eq. 1.13. Typical values of the electron power-law index $\delta \sim 2$ (Sec. 1.2.3) would imply a polarization fraction of approximately 70%, independently on the observing frequency. Observationally, polarization fractions are much lower for many radio sources and normally decreases rapidly with increasing wavelength.

Burn (1966) and Sokoloff et al. (1998) made rigorous discussions on the origin of such wavelength dependent depolarization effects. It was shown that the depolarization can be caused by a complex magnetic field structure whose orientation and strength vary either along the depth of the source and over the angular size of the observing beam. The responsible effect for the observed depolarization is the Faraday rotation. As already introduced in Sec. 1.3.1, this effect can be used to derive information on the magnetic field and thermal particle content of a plasma crossed by polarized emission.

In this Chapter, I will briefly review the definitions that are necessary to understand radio polarization studies and I will describe the techniques used throughout this Thesis to derive magnetic field estimates.

2.1.1 Basic definitions

The polarization state of the electromagnetic radiation can be described using the Stokes parameters: I, Q, U and V (Stokes, 1851). If the radiation is linearly polarized (i.e., $V = 0$) the fractional polarization, p, can be computed as:

$$p = \frac{P}{I} = \frac{\sqrt{Q^2 + U^2}}{I} \ , \tag{2.1}$$

and the polarization angle, χ, is defined as:

$$\chi = \frac{1}{2} \arctan \frac{U}{Q} \ . \tag{2.2}$$

The polarization can be also described as a complex vector (Burn, 1966) of module P and angle χ (see Fig. 2.1):

$$\mathbf{P} = Pe^{2i\chi} = pIe^{2i\chi} = Q + iU \ . \tag{2.3}$$

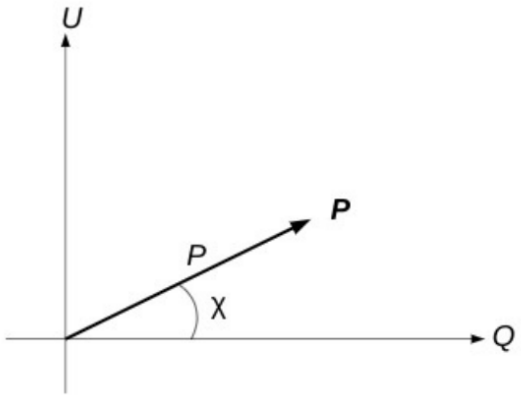

Figure 2.1: Representation of the complex polarization vector.

2.1.2 Faraday rotation

The intrinsic polarization angle of a source, χ_0, defines the direction of the electric vector on the plane of the sky, which is perpendicular to the projected magnetic field at the source ($B_\perp$). For many sources, the polarization angle observed at a certain wavelength λ is not the intrinsic one. In fact, the net component of the magnetic field along the line of sight ($B_\parallel$) is responsible for the Faraday rotation of the radiation passing through a plasma filled with thermal electrons and magnetic fields (see Fig. 2.2). The rotation of the polarization angle is larger at longer wavelengths.

The observed polarization angle at the wavelength λ depends on λ^2:

$$\chi(\lambda^2) = \chi_0 + \phi\lambda^2 \ , \tag{2.4}$$

where, following Burn (1966), the Faraday depth in the source's frame, ϕ, is defined as:

$$\phi = 0.812 \int_{\text{source}}^{\text{observer}} n_e B_{\parallel} \mathrm{d}l \quad \text{rad m}^{-2} \ . \tag{2.5}$$

Here, n_e is the thermal electron density in cm^{-3}, $B_{\parallel}$ is is the magnetic field component parallel to the line-of-sight in μG and dl is the infinitesimal path length in parsecs. A positive Faraday depth implies a magnetic field pointing towards the observer.

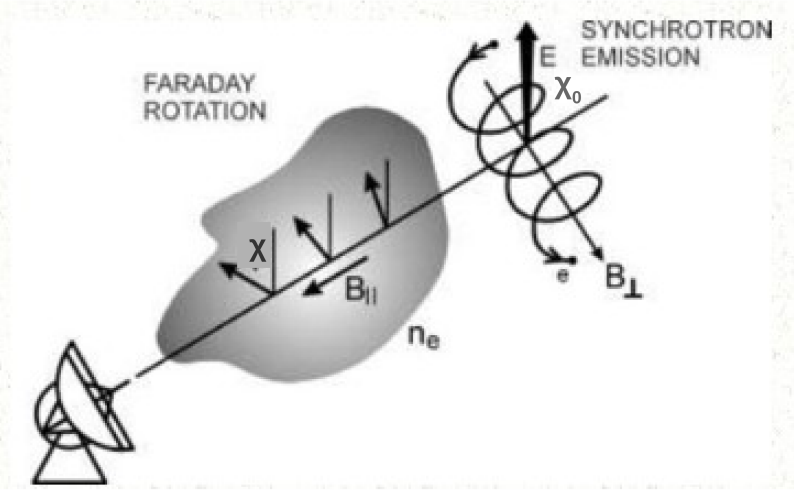

Figure 2.2: The Faraday rotation in a foreground magneto-ionized medium causes the variation of the intrinsic polarization angle, χ_0, of a background synchrotron radiation. Adapted from Beck & Wielebinski (2013).

The Faraday depth in the observer's frame, ϕ_{obs}, is reduced by a factor of $(1+z)^2$ with respect to the the source's intrinsic Faraday depth, where z is the redshift of each Faraday rotating layer along the line of sight. When this correction is taken into account the integral becomes:

$$\phi_{\text{obs}} = 0.812 \int_{z_{\text{source}}}^{0} \frac{n_e(z) B_{\parallel}(z)}{(1+z)^2} \frac{\mathrm{d}l}{\mathrm{d}z} \mathrm{d}z \quad \text{rad m}^{-2} \ . \tag{2.6}$$

Throughout this Thesis, only observed Faraday depth values are considered. However, this correction will be discussed whenever relevant.

Sources may be either Faraday-simple (also referred to as Faraday-thin) or Faraday-complex (Faraday-thick) and this depends on the extent of the source in Faraday

depth, $\Delta\phi$, but also on the observing frequency (Brentjens & de Bruyn, 2005). A source is Faraday-simple if $\lambda^2\Delta\phi << 1$ and can be approximated by a Dirac δ-function in the Faraday depth space (see Fig. 2.3). A source is Faraday-complex if $\lambda^2\Delta\phi >> 1$.

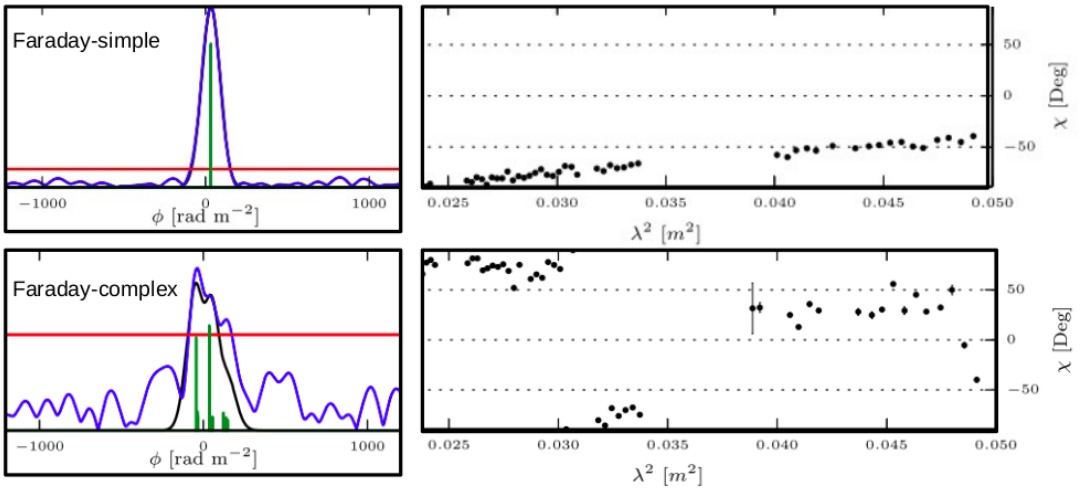

Figure 2.3: A Faraday-simple (top panels) and a Faraday-complex source (bottom panels). The Faraday simple source is represented by a Dirac δ-function in the Faraday depth space and a linear relation can be fitted to the $\chi(\lambda^2)$ plane. Conversely, the Faraday-complex source can be described with a convolution of δ-functions, which results in a larger $\Delta\phi$, and the relation between χ and λ^2 is not linear. Adapted from Anderson et al. (2015).

The Rotation Measure (RM) is generally defined as the coefficient of the linear relation between the polarization angle and λ^2:

$$RM = \frac{\mathrm{d}\chi(\lambda^2)}{\mathrm{d}\lambda^2} \ . \tag{2.7}$$

The RM and the Faraday depth coincide at all wavelengths only when one or several (non emitting) screens lie in between the source and the observer and in the absence of depolarization within the observing beam. This is the case of a Faraday-simple source for which the RM - or ϕ - can be recovered from the linear fit of Eq. 2.4 (see Fig. 2.3). In the case of a single Faraday screen at redshift z the observed RM must be multiplied by $(1+z)^2$ in order to recover the intrinsic RM in the source's frame. Faraday-complex sources with several distinct synchrotron-emitting and Faraday-rotating regions within the measured volume should be treated with more sophisticated techniques because it is not possible to define a single RM value (see Sec. 2.2). However, it is important to have in mind that the simple or complex nature of a source depends also on the observing frequency.

Measuring the Faraday depth of a source it is possible to solve Eq. 2.5 for the

magnetic field strength, if the gas density distribution and the magnetic field topology are known. In the simple case where an external Faraday screen of physical depth L is characterized by constant gas density and uniform magnetic field, the average Faraday rotation is:

$$\langle RM \rangle = 0.812 \; n_e B_{\parallel} L \quad \text{rad m}^{-2} \; . \tag{2.8}$$

In this case, the emission does not suffer depolarization at any observed frequency.

Depolarization occurs when emissions with different values of the polarization angle (i.e. with different χ_0 and/or different $\phi\lambda^2$) are collected together so that the incoherent sum of Stokes Q and U results in the reduction of P. When a large band is used for the observation, *band-width depolarization* can occur, due to the different rotation across the band. Every observation is only sensitive up to a certain maximum value of RM before band-width depolarization becomes significant.

In practice, the magnetic field presents small-scale variation and the gas distribution is not uniform, both along the line of sight and on the plane of the sky. This produces different rotation of the polarization angle for different lines-of-sight. If the magnetic field is regular but its structure is not resolved, the degree of polarization is reduced by an effect generally called *beam depolarization*, which depends on the width of observing beam. The amount of depolarization is related to the RM gradient across the beam. This effect can be used to infer the scale of the magnetic field variations.

The first model to interpret the observed RM variation across sources within or in the background of galaxy clusters was the one with a magnetic field distributed in uniform cells of size Λ_C with random orientations (Lawler & Dennison, 1982; Tribble, 1991b). In this single-scale magnetic field model, the RM distribution is Gaussian with zero mean and dispersion, $\sigma^2_{\rm RM} = \langle RM^2 \rangle$:

$$\sigma^2_{\rm RM} = 0.812^2 \; \Lambda_c \int_{\rm source}^{\rm observer} (n_e B_{\parallel})^2 {\rm d}l \quad \text{rad}^2 \; \text{m}^{-4} \; . \tag{2.9}$$

In the simplest case of uniform cell size, with equal gas density and magnetic field strength but random orientation, Eq. 2.9 can be reduced to:

$$\sigma_{\rm RM} = 0.812 \; n_e B_{\parallel} (\Lambda_C L)^{0.5} \; \text{rad m}^{-2} = 0.812 \; n_e B_{\parallel} N^{0.5} \Lambda_C \; \text{rad m}^{-2} \; , \tag{2.10}$$

where $N = L/\Lambda_C$ is the number of cells. Considering a gas distribution that follows a β-model (Eq. 1.7), Kim, Tribble & Kronberg (1991) and Felten (1996) derived the expression for the RM dispersion at a distance r from the clusters center:

$$\sigma_{\rm RM}(r) = \frac{K B n_0 r_c^{0.5} \Lambda_c^{0.5}}{(1 + r^2/r_c^2)^{(6\beta-1)/4}} \sqrt{\frac{\Gamma(3\beta - 0.5)}{\Gamma(3\beta)}} \; , \tag{2.11}$$

where Γ is the Gamma function and K is a constant whose value depends on the integration path: $K = 624$, if the source is in the background of the cluster, and $K = 441$ if it lies on the plane parallel to the plane of the sky and crossing the cluster center.

If the gas density profile of a galaxy cluster is known through X-ray observations, and Λ_c is inferred, the cluster magnetic field strength can be estimated by measuring $\sigma_{\rm RM}$ from spatially resolved RM images of radio sources. While in many cases the observed RM distribution is almost Gaussian, confirming the random nature of the magnetic field on small scales, the observation of non-zero $\langle {\rm RM} \rangle$ in galaxy clusters suggests the presence of magnetic field fluctuation on hundreds-kpc scales (Murgia et al., 2004). To take into account both small scale and large scale fluctuations it is necessary to consider more advanced magnetic field models (see Sec. 2.4).

2.1.3 Faraday depolarization

Wavelength-dependent Faraday depolarization may be caused by different physical configurations. They can be distinguished on the basis of the behavior of the degree of polarization with λ, RM ad $\sigma_{\rm RM}$ (e.g., Arshakian & Beck, 2011).

Differential Faraday rotation. When a region of space contains relativistic electrons, thermal electrons and regular magnetic fields, the polarization angle of the radiation emitted from the farthest layer of the region is more Faraday-rotated than that from the layer nearest to the observer. This causes depolarization since the emission from all the layers is observed together. In this case the observed degree of polarization at the wavelength λ is:

$$p(\lambda) = p_0 \frac{|\sin(2\langle RM \rangle \lambda^2)|}{|2\langle RM \rangle \lambda^2|} \ , \tag{2.12}$$

where p_0 is the intrinsic degree of polarization of the source.

Internal Faraday dispersion. When a region of space contains relativistic electrons, thermal electrons and turbulent and/or filamentary magnetic fields the emission from turbulent layers is mixed together. In this case the observed degree of polarization depends on the RM dispersion along the line of sight:

$$p(\lambda) = p_0 \frac{1 - e^{-2\sigma_{\rm RM}^2 \lambda^4}}{2\sigma_{\rm RM}^2 \lambda^4} \ . \tag{2.13}$$

This relation is shown in Fig. 2.4 for different values of $\sigma_{\rm RM}$.

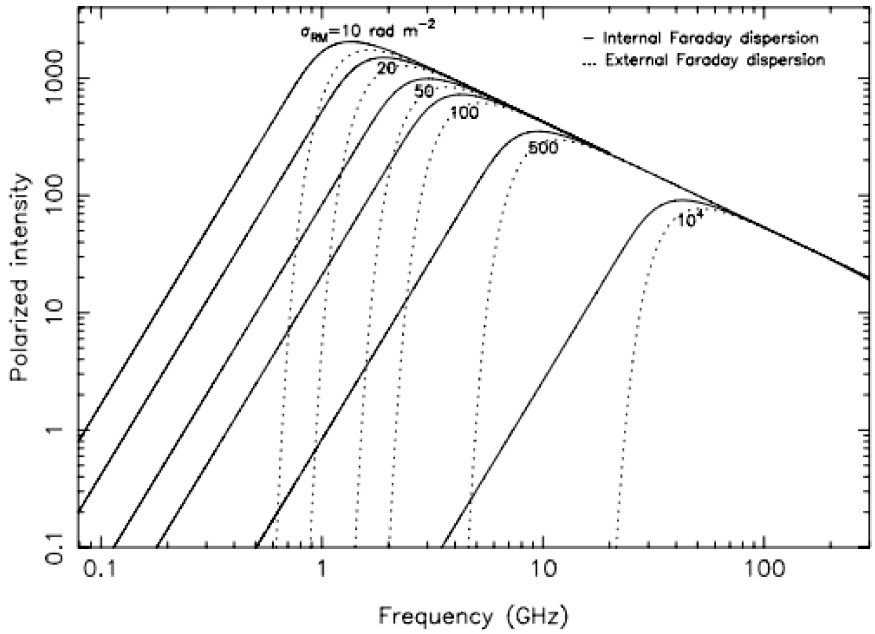

Figure 2.4: Polarized intensity for a total intensity synchrotron emission of spectral index 0.9 and depolarization by internal (solid line) and external (dashed line) Faraday dispersion for different values of $\sigma_{\rm RM}$. Credits: Arshakian & Beck (2011).

External Faraday dispersion. When a region of space contains thermal electrons and turbulent and/or filamentary magnetic fields but not relativistic electrons, the turbulent Faraday screen causes depolarization on background sources because the emission crossing different paths is mixed together in the observing beam (Burn, 1966; Sokoloff et al., 1998). The fractional polarization at λ is given by:

$$p(\lambda) = p_0 e^{-2\sigma^2_{\rm RM}\lambda^4} \ . \tag{2.14}$$

Assuming the presence of an external turbulent Faraday screen it is possible to derive $\sigma_{\rm RM}$ from the measure of the fractional polarization at two wavelength λ_1 and λ_2. If $\lambda_1 < \lambda_2$ the depolarization ratio is:

$$D^{\lambda_2}_{\lambda_1} = \frac{p(\lambda_2^2)}{p(\lambda_1^2)} = e^{-2\sigma^2_{\rm RM}(\lambda_2^4 - \lambda_1^4)} \ , \tag{2.15}$$

and it is always ≤ 1. The depolarization due to external Faraday dispersion can be approximated at long wavelengths with an expression that includes the dependence on the number of uniform magnetic field cells inside the observing beam which leads to $\mathrm{D}^{\lambda_2}_{\lambda_1} \propto N^{-0.5}$ (Tribble, 1991b). This effect is also called beam depolarization, but the latter is used in a more general sense. In fact, beam depolarization can be also caused, for example, by a regular magnetic field where a strong gradient of gas density causes an RM gradient within the beam. In this case the expressions above

do not hold. The beam depolarization is an instrumental effect that can be reduced only with higher angular resolution observations.

2.2 RM synthesis

In Sec. 2.1.2 the notion of Faraday depth was introduced, while in the following the more traditional term RM was used to describe the Faraday effects. This is because it is generally assumed that sources are Faraday-simple, i.e. they can be described by a single value of ϕ which coincides with their RM. In practice, in galaxy clusters the magnetic field is expected to be turbulent and filamentary and the emitting volume of cluster radio sources can be filled with thermal gas. Hence, polarized synchrotron radiation may originate in the same volume that causes Faraday rotation and a single value of ϕ can be insufficient to describe these Faraday-complex sources. Also, different polarized sources could be aligned along the same line-of-sight (e.g., two lobes of a radio galaxy or a radio galaxy and cluster diffuse radio emission), their emission resulting in multiple ϕ values.

The RM synthesis technique developed by Brentjens & de Bruyn (2005) allows to deal with Faraday-complex sources. Following Burn (1966), the authors introduced the Faraday dispersion function (FDF), hereafter also called Faraday spectrum, $\mathbf{F}(\phi)$, which describes the complex polarization vector as a function of the Faraday depth. An example FDF is shown in Fig. 2.5. This represents the polarization flux of three sources observed through the same line-of-sigh as function of the Faraday depth. The knowledge of the Faraday spectrum along a line-of-sight allows the distinction of all the sources and/or layers at different Faraday depths. This technique is indeed also named Faraday tomography.

The wavelength-dependent complex polarization vector, $\mathbf{P}(\lambda^2)$, is recovered through an integral of the Faraday spectrum over all the possible ϕ:

$$\mathbf{P}(\lambda^2) = \int_{-\infty}^{+\infty} \mathbf{F}(\phi) e^{2i\phi\lambda^2} d\phi \ . \tag{2.16}$$

This equation has the form of a Fourier Transform (FT), allowing the relationship to be inverted into:

$$\mathbf{F}(\phi) = \int_{-\infty}^{+\infty} \mathbf{P}(\lambda^2) e^{-2i\phi\lambda^2} d\lambda^2 \ . \tag{2.17}$$

The transformation of $\mathbf{F}(\phi)$ in $\mathbf{P}(\lambda^2)$ is also shown in Fig. 2.5. The contribute of the three polarized sources are mixed in the λ^2 domain. However, in order to retrieve $\mathbf{F}(\phi)$ observations of the polarization at all positive (and negative) λ^2 would be necessary.

In order to extend this method to the more realistic case of a limited sampling in λ^2 space, Brentjens & de Bruyn (2005) introduced a weight function, $W(\lambda^2)$, which

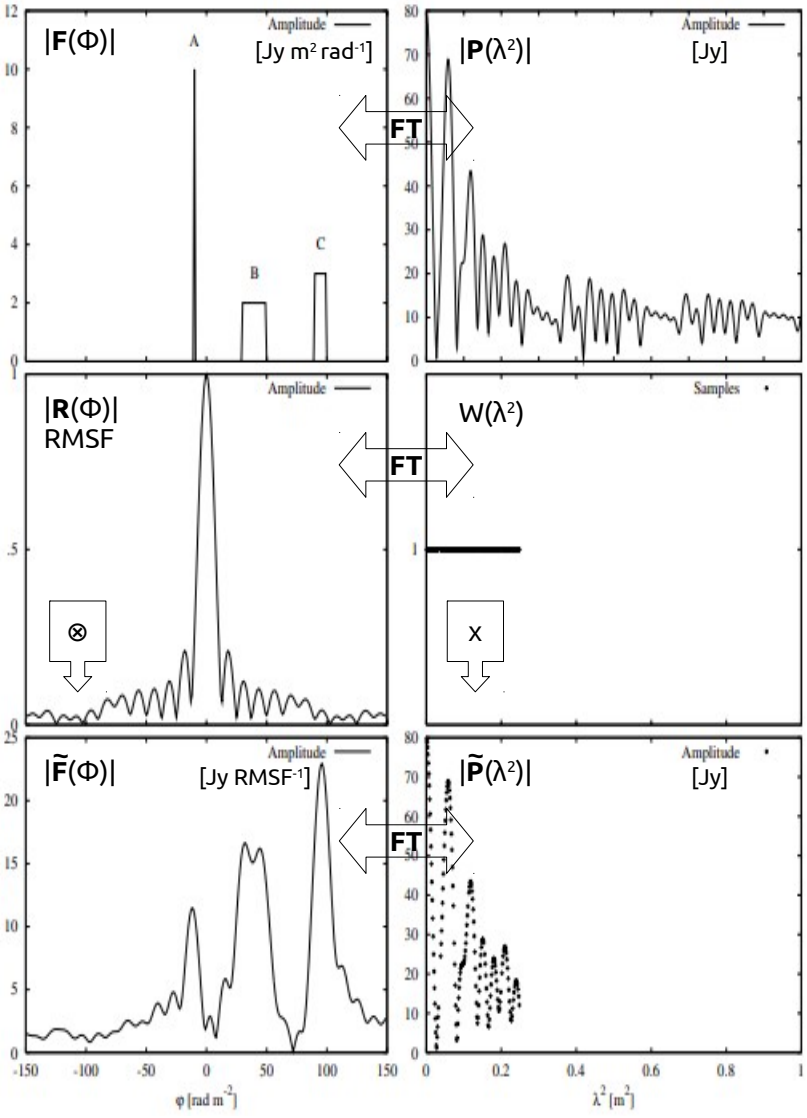

Figure 2.5: Illustrative example of the RM synthesis technique. The left-hand panels show the Faraday depth space while the right-hand panels show the λ^2 space. Each row of the two columns is connected by Fourier Transform relations. The top row shows the input situation with the polarized flux of three sources as function of ϕ (left) and λ^2 (right). The three sources are observed through the same line-of-sight. Source A is Faraday-simple (a Dirac δ-function in Faraday space), source B is multiple RMSFs wide in ϕ, source C is barely resolved by a RMSF. The middle row shows the RMSF on the left and the weight function on the right. The convolution of the top-left and middle-left panels results in the bottom left panel, i.e. the reconstructed Faraday spectrum. The observed polarization, shown in the bottom-right panel, is obtained by multiplying the top-right and the middle-right panels. Units are reported in square brackets. Credits: adapted from Brentjens & de Bruyn (2005).

describes the λ^2 coverage of the experimental setup. Its value is zero for all the λ^2 where measurements are not present, including negative λ^2. Each λ^2 channel of the observation can have equal weight or can be weighted by the inverse of the root mean square (rms) noise in the channel.

The observed polarized flux density is then the product of the polarized flux density of the source and the weight function. Hence, the reconstructed Faraday dispersion function, $\widetilde{\mathbf{F}}(\phi)$, is:

$$\widetilde{\mathbf{F}}(\phi) = K \int_{-\infty}^{+\infty} \mathbf{P}(\lambda^2) W(\lambda^2) e^{-2i\phi\lambda^2} d\lambda^2 = \mathbf{F}(\phi) \otimes \mathbf{R}(\phi) \ , \tag{2.18}$$

where K is a normalization factor, $R(\phi)$ is the Rotation Measure Sampling Function (RMSF) and $\otimes$ denotes convolution. See Fig. 2.5 for an example weight function and the related RMSF.

The RMSF describes the instrumental response in the Faraday space based on the λ^2-coverage of the data. The concept is similar to the one of the observing beam in an interferometric image, which depends on the *uv*-coverage of the observation. The quality of the reconstruction depends mainly on the weight function since it controls the shape of the RMSF: less gaps in the λ^2 sampling reduce the side lobes of the RMSF, while covering a larger range of wavelengths increases the resolution in the Faraday space. In fact, the full width half maximum (FWHM) of the RMSF defines its resolution that, for an observation of total width $\Delta\lambda^2$, is:

$$\delta\phi \approx \frac{2\sqrt{3}}{\Delta\lambda^2} \ . \tag{2.19}$$

The maximum observable Faraday depth (i.e., at which the sensitivity of the observation has dropped to 50%), $|\phi_{\rm max}|$, is controlled by the channel width $\delta\lambda^2$:

$$|\phi_{\rm max}| \approx \frac{\sqrt{3}}{\delta\lambda^2} \ , \tag{2.20}$$

while the largest observable scale in Faraday space, $\Delta\phi_{\rm max}$ (i.e., observable with a 50% sensitivity), is due to the minimum sampled λ^2:

$$\Delta\phi_{\rm max} \approx \frac{\pi}{\lambda^2_{\rm min}} \ , \tag{2.21}$$

Brentjens & de Bruyn (2005) have also shown that the RMSF is better behaved when all polarization vectors are rotated back to their position at the weighted

average of the observed bandwidth, λ_0^2:

$$\lambda_0^2 = \frac{\int_{-\infty}^{+\infty} W(\lambda^2)\lambda^2 \mathrm{d}\lambda^2}{\int_{-\infty}^{+\infty} W(\lambda^2)\mathrm{d}\lambda^2} \ . \tag{2.22}$$

Thanks to the shift theorem of the Fourier theory, this rotation can be performed without any loss of generality. The final form of Eq. 2.18 can be approximated by a sum if $\phi\delta\lambda^2 << 1$ for each of the N channels of width $\delta\lambda^2$ and central frequency λ_i:

$$\widetilde{\mathbf{F}}(\phi) \approx K \sum_{i=1}^{N} \mathbf{P}(\lambda_i^2) W(\lambda_i^2) e^{-2i\phi(\lambda_i^2 - \lambda_0^2)} \ . \tag{2.23}$$

This equation can be implemented in a software in order to perform the RM synthesis. The bottom panels of Fig. 2.5 show the RM synthesis application to the example FDF: the reconstructed Faraday spectrum, $\widetilde{\mathbf{F}}(\phi)$ (bottom-left panel), is obtained applying Eq. 2.23 to the polarization flux measurements performed in small channels within the observing band (bottom-right panel).

The RMSF can be deconvolved from $\widetilde{\mathbf{F}}(\phi)$ using a one dimensional clean that is analytically identical to the one used during aperture synthesis imaging, named RM clean (Heald, 2009). To perform this procedure the RMSF should be known as accurately as possible. The frequency dependence of the primary beam attenuation should be removed before the RM clean and the restoring beam of each channel should be the same to avoid frequency dependent effects. The intrinsic emission spectra of the sources can also be taken into account, if known.

The amplitude of the obtained $\widetilde{\mathbf{F}}(\phi)$ peaks at the Faraday depth ϕ_{peak}, which is the Faraday depth along the path between the observer and the source contributing the most to the polarized emission. If more than one source is seen through the same line-of sight, as in Fig. 2.5, each peak corresponds to a source. From the value of the reconstructed $|\widetilde{\mathbf{F}}(\phi_{\mathrm{peak}})|$ it is possible to recover the polarization fraction of the emission, while from the reconstructed Stokes parameters, $\widetilde{Q}(\phi_{\mathrm{peak}})$ and $\widetilde{U}(\phi_{\mathrm{peak}})$, it is possible to recover the polarization angle at λ_0^2,

$$\chi(\lambda_0^2) = \frac{1}{2} \arctan \frac{\widetilde{U}(\phi_{\mathrm{peak}})}{\widetilde{Q}(\phi_{\mathrm{peak}})} \ . \tag{2.24}$$

The intrinsic polarization angle at the source is obtained by solving Eq. 2.4 for χ_0 with $\lambda^2{=}\lambda_0^2$.

The traditional $\chi(\lambda^2)$ fitting method would be totally inadequate to recover the RM of the complex line-of-sight shown as an example in Fig. 2.5. Hence, the mixed contribution of all the sources would result in a non-linear relation between χ and λ^2, as the one shown in the bottom panels of Fig. 2.3. The possibility to deal with

Faraday-complex sources is one of the advantages of the RM synthesis over the $\chi(\lambda^2)$ fitting method. These include also an improved fidelity and dynamic range.

2.2.1 Uncertainties on ϕ and detection threshold

Brentjens & de Bruyn (2005) computed the statistical errors in the $\phi_{\rm peak}$ estimation, σ_ϕ. They show that, if the rms noise in the Stokes Q and U single frequency channels is equal, $\sigma_{Q,ch} \sim \sigma_{U,ch} \sim \sigma_{ch}$, then the uncertainty on the P estimate is also σ_{ch} and:

$$\sigma_\phi^2 = \frac{\sigma_{ch}^2}{4(N-2)P^2\sigma_{\lambda^2}^2} \ , \tag{2.25}$$

where N is the number of channels used to derive ϕ and $\sigma_{\lambda^2}^2$ is the variance of the λ^2 distribution. If the intrinsic emission spectra of the source is zero, and assuming a uniform coverage in λ^2, Eq. 2.25 can be further simplified to

$$\sigma_\phi = \frac{\delta\phi}{2(P/\sigma_{QU})} \ . \tag{2.26}$$

This is the FWHM of the RMSF divided by twice the signal-to-noise of the detection, since σ_{QU} is derived from the reconstructed $\widetilde{Q}$ and $\widetilde{U}$ after the RM synthesis (Schnitzeler & Lee, 2017). The best way to compute the value of σ_{QU} is formally discussed in Hales et al. (2012). Through this Thesis $\sigma_{QU} = (\sigma_Q + \sigma_U)/2$ where σ_Q and σ_U are computed as the standard deviation in the outer $\sim 20\%$ of the reconstructed $\widetilde{Q}(\phi)$ and $\widetilde{U}(\phi)$ Faraday spectra.

Although Eq. 2.26 is generally used to estimate the uncertainties on ϕ, it should be regarded with caution. It is in fact derived under several simplified assumptions and it was shown to lead to over- or under-estimates of the true errors (Schnitzeler & Lee, 2017).

Hales et al. (2012) derived an analytical relationships to quantify the statistical significance of polarization measurements done with RM synthesis in terms of standard Gaussian statistics. They found that a detection threshold of P/σ_{QU}=6 is required to reach an equivalent Gaussian significance of 5σ. Considering the surveys where the polarization information is obtained from RM synthesis George, Stil & Keller (2012) suggested a detection threshold of $8\sigma_{QU}$. This would correspond to a a false detection rate of 0.06% and to a Gaussian significance level of about 7σ. This conservative choice makes the errors due to the non-Gaussianity of the noise in the Q and U images and to the error in $\phi_{\rm peak}$ estimates negligible. In this Thesis, we will use either 6 or 8 σ_{QU} detection thresholds. Our choices will be discussed and motivated each time in the next Chapters.

2.2.2 Interpretation of Faraday-complex spectra

Although RM synthesis permits the detection of Faraday-complex sources, as the one shown in Fig. 2.3, the interpretation of their spectra is not always straightforward (e.g., Basu et al., 2019). A non trivial point is that the performance of RM synthesis in detecting Faraday-complex sources strongly depends on the frequency coverage of the observation (Brentjens & de Bruyn, 2005). Furthermore, there are several distributions of magnetic fields, thermal electron densities and physical depths that can generate the same observed Faraday spectrum. Also beam depolarization should be considered since it could introduce spatially varying ϕ components that may contribute to the complexity of the Faraday spectrum.

Another problem is the use of the the RM clean procedure to deconvolve the RMSF. Although this procedure helps in reducing secondary lobes when a peak is detected at high signal-to-noise ratio, it is not well suited to detect Faraday-complex sources since it assumes a Dirac δ-function model for every detected component, and it easily diverges at low signal-to-noise values. Some techniques have been proposed to overcome such problems and to optimize the reconstruction of Faraday-complex spectra (Frick et al., 2010; Li et al., 2011; Bell et al., 2013; Cooray et al., 2021). All of them assume a model for the synchrotron emitting and Faraday rotating medium, and nowadays their performances are still tested and debated (see e.g., Sun et al., 2015; Miyashita, Ideguchi & Takahashi, 2016; Schnitzeler, 2018; Ideguchi, Miyashita & Heald, 2018, for a comparison of RM clean with other methods.).

In order to describe a Faraday-complex source with a value of polarized flux and Faraday depth, some choices has to be made. The value corresponding to the $\phi_{\rm peak}$ in the Faraday spectrum is considered to be representative for the Faraday depth of the source. In practice, the peak value represents only the main component of the spectrum. The value of $|\widetilde{\mathbf{F}}(\phi_{\rm peak})|$ is then a fraction of the total emission of the source. To recover the polarized flux of a Faraday-complex source it would be necessary to completely deconvolve the spectrum from the RMSF and then integrate the emission over the whole Faraday depth range where the source is detected. In practice, this is not feasible due to the problems discussed above. As a result, the polarized flux density of Faraday-complex structures estimated from the main peak is lower than the integrated one, and the fractional polarization that is computed with the RM synthesis should be regarded as a lower limit.

2.2.3 Ricean bias

Stokes Q and U images are assumed to be governed by Gaussian noise. As images of polarization intensity are created by summing Q and U in quadrature (Eq. 2.1), the noise statistics in P results in a Rice distribution. This means that also where the polarized signal in Q and U is zero, the resulting P is always positive and this

over-estimation is known as Ricean bias. This bias is particularly important for signal-to-noise ratios lower than 5 (e.g., Simmons & Stewart, 1985).

For band-averaged images the best estimate of the Ricean bias is given by the rms noise in the Q and U images. However, it has been shown that there is a much stronger bias in P images made using RM synthesis due to an additional uncertainty in the $\phi_{\rm peak}$ determination. George, Stil & Keller (2012) shown that a better estimator of the true polarized intensity in this case is given by:

$$P = \sqrt{|\widetilde{\mathbf{F}}(\phi_{\rm peak})|^2 - 2.3\sigma^2_{QU}} \ . \tag{2.27}$$

This correction has been applied throughout this Thesis.

2.3 A-projection

Wide-field imaging techniques are required for low-frequency radio observations in order to accurately measure polarized intensity and RMs across the entire field of view. The primary beam response affect the flux levels across such a wide-field image, but this is usually easily corrected in the Stokes I since the primary beam is symmetric with respect to the phase center. The primary beam response is instead more complex for Stokes Q, U and V since variations of the antenna primary beam pattern as a function of time, frequency, and polarization cause direction dependent effects (Bhatnagar et al., 2008).

The dominant direction-dependent instrumental effect consists in a total intensity flux leakage into the other Stokes. The effect is stronger for Stokes V but the leakage could be relevant also in Q and U, in particular if the source intrinsic polarization level is low. The result is a spurious increase in the observed fractional polarization and an alteration of the polarization angle of sources. The effect becomes more prominent with increasing distance from the phase center. Jagannathan et al. (2017) carried out an analysis of these effects using L band (1-2 GHz) *Jansky Very Large Array* (JVLA) simulations. The authors showed that at the 0.5 gain level of the primary beam the flux leakage from Stokes I to Q and U reaches the 10% of the total intensity. The authors also studied the effect on the RM synthesis and found that, although the instrumental effect is primarily centered around 0 rad m^{-2} it can broaden over a quite large range of Faraday depths. An additional effect is the beam-squint that is caused by the antenna feeds having different pointing centers in the sky. Therefore, wide-field polarimetry requires accurate calibration of the direction dependent, or off-axis, instrumental effects. This correction still poses some challenges to the new generation wide-field polarization surveys such as the Polarization Sky Survey of the Universe's Magnetism (POSSUM) and the VLA Sky Survey (VLASS).

The A-projection algorithm was proposed as an ideal solution for wide-field and wide-band polarization imaging (Bhatnagar et al., 2008; Bhatnagar, Rau & Golap, 2013) and only recently it has been introduced in interferometric imaging software. This is an iterative deconvolution algorithm that corrects direction dependent effects during the imaging process. The correction is done modeling the complex antenna aperture illumination for the two orthogonal polarization products as a function of the parallactic angle and antenna pointing errors. The A-projection both reduces the artifacts around off-axis sources in Stokes I and corrects for the instrumental leakage but it has a very high computational cost. Probably also for this reason, this algorithm has not yet been used in any scientific work based on JVLA observations and it has been validated only for a few usage modes. Furthermore, at the moment of writing, the correction for Stokes Q and U is not yet implemented in the Common Astronomy Software Applications (`CASA`*) package used for JVLA data processing, and therefore we could not apply it to our images. Very recent developments concerning the A-term correction have been done with the imaging software `WSClean`†, but they are steel in a preliminary phase.

The specific way in which we tackled the problem of off-axis flux leakage will be further discussed in Chapters 3 and 4 for JVLA and in Chapters 6 and 7 for LOFAR observations, respectively.

2.4 Magnetic field estimates

In Sec. 2.1.2 it was shown how the observed RM and the RM dispersion, $\sigma_{\rm RM}$, of sources embedded or in the background of a magnetic-ionic medium are determined by its magnetic field strength and structure. These observed quantities can be derived, both, through a depolarization analysis and with the RM synthesis technique, where the RM concept is extended to the more general one of Faraday depth (Sec. 2.2). In Sec. 1.3.1 some of the results achieved with this method in the galaxy cluster science were summarized.

It is important to clarify how the magnetic field estimates are derived from measurements. In fact, because of the random and turbulent nature of magnetic fields and of the number of possible physical scenarios, inverting Eq. 2.5 and Eq. 2.9 is not straightforward unless very simplified assumptions are made. This is the case for Eq. 2.8 and Eq. 2.10. These expressions can be useful to have a first order approximation of the magnetic field strength but should be treated with caution.

The presence of uniform magnetic fields in clusters is in fact contradicted by several observations, both, on single radio galaxies and on polarized cluster diffuse emissions (e.g., Govoni et al., 2006, 2017; Rajpurohit et al., 2018). The structure

*https://casa.nrao.edu/
†https://sourceforge.net/p/wsclean/wiki/Home/

of the magnetic field cannot be neglected, as it manifests itself also in the choice of the value of Λ_C to be used in Eq. 2.11. This was shown to be equal to the magnetic field auto-correlation length which can be computed only if the power spectrum of the magnetic field fluctuations is known (Enßlin & Vogt, 2003; Murgia et al., 2004). Hence, to determine the strength of the magnetic field it is necessary to consider also its 3D structure and this can be done by means of simulations. At the same time simulations allow to consider even more realistic thermal gas distributions

Murgia et al. (2004) developed a code which starts from a 3D model of magnetic field and a gas density distribution to produce mock RM maps. These can be directly compared with observations in order to constrain the parameters of the input model. The magnetic field power spectrum is assumed to be a power-law of index n of the form

$$|B_k|^2 \propto k^{-n} \ , \tag{2.28}$$

where k is the wave number of the fluctuation scale. Broken power-laws have been also explored (Laing et al., 2008; Guidetti et al., 2010). The power spectrum may extend over a large range of spatial scales and different value of the spectral index can be tested. In these simulations it is assumed that the normalization of the power spectrum scales as a function of the thermal gas density:

$$B(r) = \langle B_0 \rangle \left(\frac{n_e(r)}{n_0} \right)^{\eta} \ , \tag{2.29}$$

where $\langle B_0 \rangle$ is the average magnetic field at the center of the cluster and η is the power-law index. The suggestion of a radial decline of the magnetic field strength in clusters comes both from theoretical considerations (e.g., Govoni et al., 2001; Brunetti & Jones, 2014), and from MHD cosmological simulations (e.g. Dolag et al., 2001; Vazza et al., 2018; Domínguez-Fernández et al., 2019). The depolarization effect caused by the tangled magnetic field can be also reproduced and compared with observations (Govoni et al., 2006). These simulations can be analyzed with the RM synthesis technique in order to test its capability to reconstruct cluster parameters (Loi et al., 2019).

Important information on the magnetic field are also derived from MHD cosmological simulations (e.g., Vazza et al., 2017) where, starting from different magnetogenesis scenarios, the magnetic field evolves together with the structure formation processes (see Sec. 1.3.2). Recently, cosmological MHD simulations have reached the resolution to compute magnetic field power spectra down to few kpc scale at different stage of the cluster formation process (Vazza et al., 2018; Domínguez-Fernández et al., 2019). These simulations revealed that the magnetic field spectrum arising from the dynamic of the ICM is more complex than a power-law spectrum (see Fig. 2.6). Vazza et al. (2018) found that the 3D magnetic field distribution depart from a simple Maxwellian distribution and showed that this may have a strong im-

pact on the RM-based estimates of magnetic field strength. In this Thesis, we will make a step forward to integrate these foundings in our magnetic field modeling (see Chapter 4).

Introducing radiating relativistic particles, these simulations are also able to reproduce large scale diffuse radio emission originated during cluster merger and compare their polarization properties with observed ones (Wittor et al., 2019; Rajpurohit et al., 2020a). The RM distributions of simulated diffuse cluster radio emission can be thus directly compared with observations in order to test particle acceleration processes together with magnetic field strength and structure (see Chapter 3).

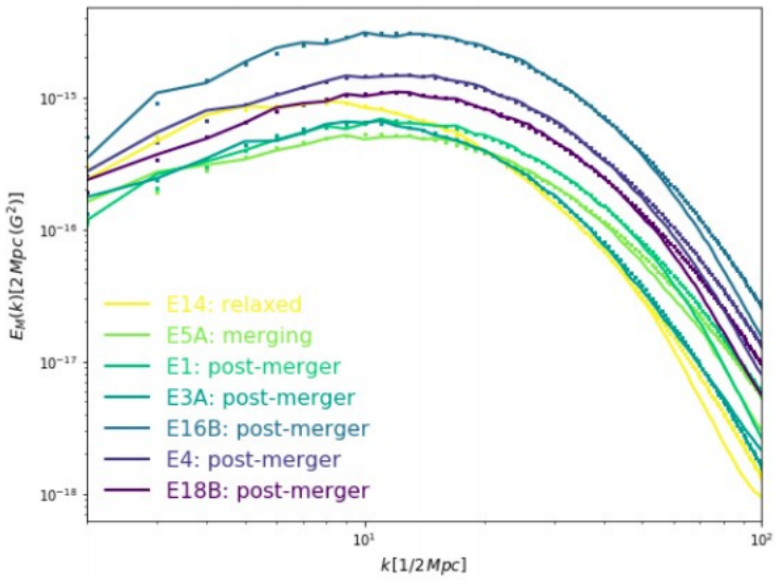

Figure 2.6: Magnetic field power spectra of several clusters in different dynamical states computed from MHD cosmological simulations. Credits: Domínguez-Fernández et al. (2019).

Chapter 3

The origin of radio relics in the RXC J1314.4-2515 galaxy cluster *

Radio relics are thoughts to be generated by shocks developed during cluster mergers but still there are numerous open questions on their origin. The combined information on: *(i)* magnetic fields at relics through radio polarimetric study, *(ii)* discovery of a possible connection between radio relic emission and AGN activity through high-resolution spectral index imaging, and *(iii)* new detection of merger shocks through X-ray data analysis, are the key ingredients to solve the problem of particle acceleration in low Mach number shocks.

Here, we study the radio emission of the galaxy cluster RXC J1314.4-2515. This galaxy cluster shows a number of interesting features: although it is a double relic cluster (i.e., the merger axis is expected to be on the plane of the sky) different works found that a significant component of the merger could lie along the line of sight (Wittman, Cornell & Nguyen, 2018; Golovich et al., 2019b), a central radio halo is spatially connected with the western relic making their nature ambiguous, and the eastern radio relic was suspected to host a radio galaxy (Feretti et al., 2005; Venturi et al., 2007). We decided to carry out a detailed analysis of the extended radio emission of this cluster in order to deepen our knowledge on the origin of radio relic emission.

Throughout this Chapter, we assume a ΛCDM cosmological model, with $H_0 = 69.6$ km s^{-1} Mpc^{-1}, $\Omega_M = 0.286$, $\Omega_\Lambda = 0.714$ (Bennett et al., 2014). With this cosmology $1''$ corresponds to 3.9 kpc at the cluster redshift, z=0.247.

*Based on Stuardi et al. (2019)

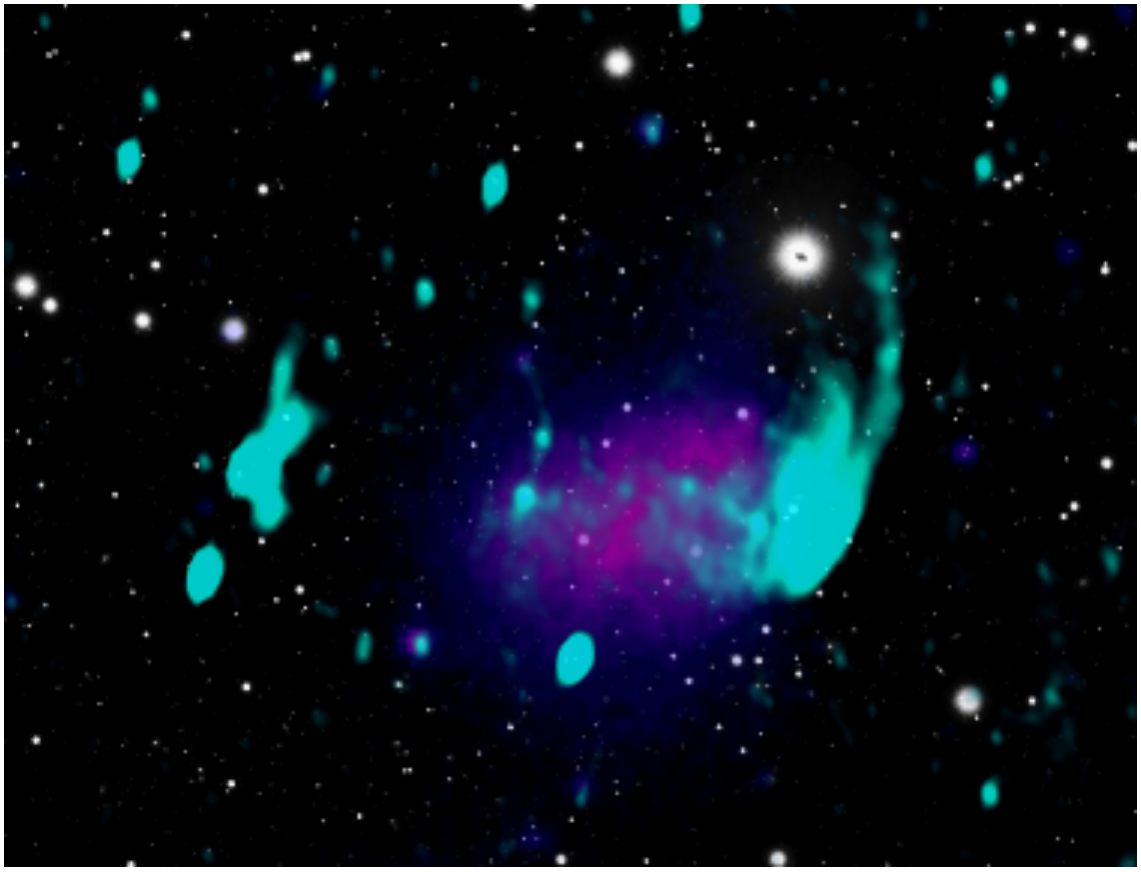

Figure 3.1: *Subaru* r-band image of the RXC J1314.4-2515 cluster (gray-scale) overlaid onto the point-source subtracted X-ray *XMM-Newton* image in the $0.5 - 2.0$ keV band (purple) and the radio JVLA emission at 1.5 GHz (green). The image has illustrative purposes only.

3.1 The double relic galaxy cluster RXC J1314.4-2515

General information on this cluster is listed in Tab. 3.1. An illustrative view of RXC J1314.4-2515 is shown in Fig. 3.1. RXC J1314.4-2515 shows two symmetric radio relics, east and west of the cluster. They were observed with the VLA at 1.4 GHz (Feretti et al., 2005), and with the GMRT at 610 MHz (Venturi et al., 2007) and at 325 MHz (Venturi et al., 2013). The western relic is more extended than the eastern one, and it is connected to a central radio halo. Recently, the galaxy cluster was observed also with the MWA from 88 to 215 MHz (George et al., 2017), leading to an estimate of the integrated spectral index of eastern and western relics: $\alpha_{1.4\mathrm{GHz}}^{118\mathrm{MHz}}$=1.03±0.12 and $\alpha_{1.4\mathrm{GHz}}^{118\mathrm{MHz}}$=1.23±0.09, respectively.

RXC J1314.4-2515 has a disturbed morphology in the X-rays: it is elongated in the east-west direction, suggesting an ongoing merger activity along this axis (Valtchanov et al., 2002). In particular, Mazzotta et al. (2011) found that the western relic is coincident with a shock front, detected through *XMM-Newton* ob-

Table 3.1: Properties of RXC J1314.4-2515. Row 1,2: J2000 celestial coordinates of the X-ray cluster centroid; Row 3: redshift, z; Row 4: X-ray luminosity in the energy band 0.1-2.4 keV; Row 5: estimate of the hydrostatic mass. References: (1) Piffaretti et al. (2011), (2) Valtchanov et al. (2002), (3) Planck Collaboration et al. (2016b).

R.A. (J2000)	$13^{h}14^{m}28^{s}.0$	(1)
Dec. (J2000)	-25°15′41″	(1)
z	0.247	(2)
$L_{X(0.1-2.4keV)}$	$9.9{\cdot}10^{44}$ erg s^{-1}	(1)
M_{500}^{SZ}	$6.7{\cdot}10^{14}M_{\odot}$	(3)

servations, with Mach 2.1±0.1. They noticed that this shock front is M-shaped, with the nose of the front tilted inward, which they proposed may be produced by the material in-falling along a filament. In the X-ray image, a sub-cluster in the south direction is also visible, with a stream of gas suggesting accretion by the northern main cluster (see Fig. 3.3).

Valtchanov et al. (2002) found a bi-modal distribution of the galaxies in this cluster both in velocity space (∼1700 km s^{-1} separation) and in projected space. This was recently confirmed by Golovich et al. (2019b), who found also that the two merging sub-clusters have ∼1500 km s^{-1} line of sight velocity difference, suggesting that the merger axis has a substantial component along the line of sight. Recently, matching the observed projected separation and relative radial velocities between sub-clusters with cosmological N-body simulations, Wittman, Cornell & Nguyen (2018) constrained the angle between the sub-cluster separation vector and the line of sight. While in other double relic clusters the merger axis is found on the plane of the sky, for RXC J1314.4-2515 they obtained a maximum likelihood at 42°, although angles up to 90° cannot be ruled out.

The median Galactic RM in the region of RXC J1314.4-2515 measured with an angular resolution of 8° is -30±2 rad m^{-2} (Taylor, Stil & Sunstrum, 2009). We used this value throughout the polarization analysis because we found the same median value outside the galaxy cluster in our field. This value is also consistent with the most updated estimate by Oppermann et al. (2012) and Hutschenreuter & Enßlin (2020).

3.2 Data analysis

3.2.1 Radio observations

The cluster has been observed with the JVLA in the L-band (1-2 GHz) in A, B, C and D configurations. These observations have a total bandwidth of 1024 MHz, subdivided into 16 spectral windows of 64 MHz each (with 64 channels at frequency

resolution of 1 MHz). We also reduced and analyzed archival data in S-band (2-4 GHz) in DnC configuration, covering a total of 2048 MHz in 16 spectral windows of 128 MHz each (64 channels of 2 MHz channel^{-1} frequency resolution). Both data sets have full polarization products. Observing date, time, rms noise (σ) and restoring beam of radio observations are listed in Tab. 3.2.

Calibration

For calibration and total intensity imaging we used the `CASA 5.3.0`[†] package. We started the calibration process from data pre-processed by the VLA `CASA` calibration pipeline[‡] which performs basic flagging and calibration on Stokes I continuum data. Then, we derived delay (i.e., a phase slope across frequency due to the differences in the signal paths from antenna feeds to correlator), bandpass, gain/phase, leakage and polarization angle calibrations and applied them to the target. The source 3C 286 was used as a bandpass, absolute flux density and polarization angle calibrator for all the observations. We used the Perley & Butler (2013) flux density scale and we followed the NRAO polarimetry guide for polarization calibration[§]. In particular, we performed a polynomial fit to the values of linear polarization fraction and angle tabulated in Perley & Butler (2013) for 3C 286, to obtain a frequency-dependent polarization model. J1248-1959 was used as a phase calibrator for observations in A and B configurations in L-band, and for the S-band observations, while J1311-2216 was used for the observations in C and D configurations (L-band). To correct for the instrumental leakage, an unpolarized source was used: J1407+2827 and 3C 147 for the L- and S-band observations, respectively.

Radio frequency interference (RFI) was removed by statistical flagging algorithms also from the cross correlation products. At the end of the flagging process, some spectral windows seriously affected by RFI were entirely removed. We flagged the frequency ranges: 2116-2244 MHz in the S-band observations; from 1520 MHz to 1584 MHz in A configuration; from 1072 MHz to 1136 MHz and from 1520 MHz to 1648 MHz in B configuration; 1136-1264 MHz and 1520-1584 MHz in C configuration; from 1136 MHz to 1328 MHz and from 1520 MHz to 1648 MHz in D configuration. After RFI removal, we averaged the data sets in time down to 10 seconds to speed up the imaging process and we re-weighted the visibilities according to their scatter.

[†] https://casa.nrao.edu/
[‡] https://science.nrao.edu/facilities/vla/data-processing/pipeline
[§] https://science.nrao.edu/facilities/vla/docs/manuals/obsguide/modes/pol

Table 3.2: Details of radio observations. Column 1: central observing frequency; Column 2: name of the frequency band; Column 3: array configuration; Column 4: date of the observation; Column 5: observing time; Column 6: `robust` parameter used for the Briggs weighting scheme (Briggs, 1995) during imaging process; Column 7: size of the Gaussian taper used in the imaging process. If "–", no taper has been used; Column 8: FWHM of the major and minor axes of the restoring beam of the final image; Column 9: 1σ rms noise of the total intensity image; Column 10: reference of the figures in this Chapter. Rms noise and beam shape of the images obtained with a combination of different configurations are reported under the horizontal line.

Freq. (GHz)	Band	Array Conf.	Obs. Date	Obs. Time (hr)	Robust	Taper	Beam	rms Noise (σ) (mJy/beam)	Fig.
1.5	L	A	2018 Mar. - 2018 Apr.	5.5	0.5	–	$2''\times1''$	0.011	3.2
1.5	L	B	2017 Oct.	2.0	0.5	–	$7''\times4''$	0.018	
1.5	L	C	2017 Jun.	2.0	0.5	–	$24''\times11''$	0.035	3.10,3.11
1.5	L	D	2017 Feb.	0.5	0.5	–	$74''\times33''$	0.3	
3.0	S	DnC	2014 Sept.	6.0	0.5	–	$17''\times13''$	0.012	3.5, 3.10,3.11
1.5	L	B+C			0.5	–	$9''\times5''$	0.015	3.2
1.5	L	C+D			0.5	–	$25''\times11''$	0.014	3.4
1.5	L	B+C+D			0.0	$15''\times15''$	$17''\times14''$	0.035	3.6,3.7
1.5	L	A+B+C+D			0.5	$8''\times8''$	$15''\times8''$	0.016	3.3

Imaging and self-calibration

We used the multi-scale multi-frequency de-convolution algorithm of the `CASA` clean (Rau & Cornwell, 2011) for wide-band synthesis-imaging. We set two terms for the Taylor expansion (`nterms` = 2) in order to take into account both the source spectral index (likely a power-law) and the primary beam response. We also used a w-projection algorithm to correct for the wide-field non-coplanar baseline effect (Cornwell, Golap & Bhatnagar, 2008) with an appropriate number of w-projection planes for each data set. We generally used the Briggs weighting scheme with the `robust` parameter set to 0.5. We highlight in Tab. 3.2 the cases in which a different weighting scheme has been used.

There are two bright sources in the target field, one south-west of the cluster and the other to the north-east. The latter falls at the edge of the primary beam in L-band observations, causing problems for the self-calibration procedure. We set `nterms` = 3 to individually image these sources. Then, we used the peeling technique (Noordam, 2004) to subtract them out of the images with direction-dependent gain solutions derived for each one. Some artifacts around the brightest source in the south are still present in the final images but their effect on the cluster emission is negligible. We used the peeling technique to subtract two variable sources before combining data at various configurations observed in different dates.

The combination of various antenna configurations differently flagged in frequency could in principle cause imaging artifacts due to uneven uv-coverage. First, we imaged each configuration individually. Then, we combined the visibilities of different configurations and we imaged them together. We compared the obtained images to exclude the presence of strong artifacts.

Finally, cycles of self-calibration were performed to refine the antenna-based phase gain variations on the target field. The residual amplitude errors due to the calibration are estimated to be ~ 5 %. The local rms noise of the images is reported in Tab. 3.2. The final images were corrected for the primary beam attenuation using the `widebandpbcor` task in `CASA`.

The S-band observations were performed on two pointings roughly centred on the east (E) and west (W) relic. We separately performed data reduction, peeling and imaging of the two fields. Then, we joined the two final images correcting for the primary beam attenuation of both pointings.

In Fig. 3.2, radio contours at 1.5 GHz in the combined B and C (B+C) configurations are overlaid to the optical image of RXC J1314.4-2515 composite of *Subaru* r- and g-band. A zoom of the E relic with A configuration high-resolution contours is also shown in Fig. 3.2. In Fig. 3.3 the radio contours obtained combining all the L-band observations (A+B+C+D) are overlaid on the X-ray *XMM-Newton* image of the cluster. The L-band image obtained combining C and D (C+D) configurations

is shown in Fig. 3.4. The S-band image in DnC configuration is shown in Fig. 3.5.

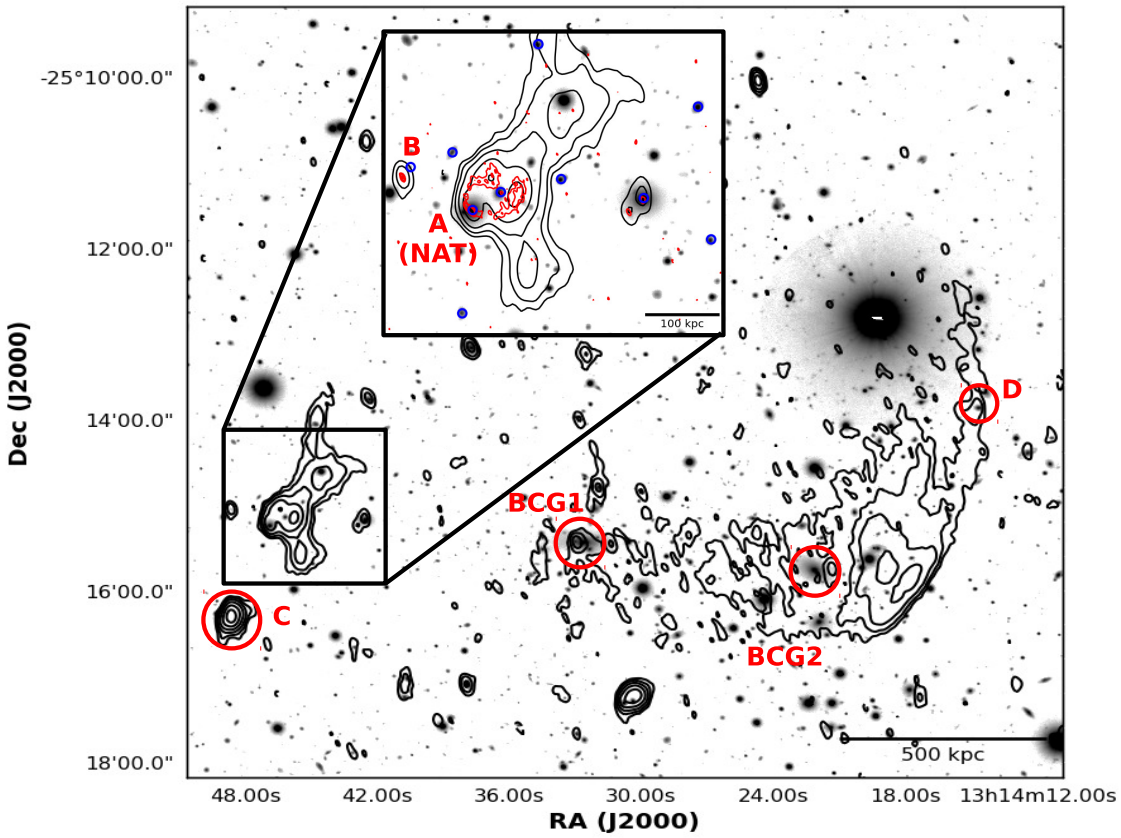

Figure 3.2: *Subaru* r- and g-band image of the cluster RXC J1314.4-2515 with black radio contours overlaid. Contours are obtained combining B and C configurations and the restoring beam is $9'' \times 5''$. Black contours start from 3σ, with σ=0.015 mJy beam^{-1}, and they are spaced by a factor of two. A zoom in the region of the E radio relic at 1.5 GHz is displayed in the top inset panel. Black contours are in B+C configuration, same as above; red contours are from A configuration with a restoring beam of $2'' \times 1''$, and they start at 3σ, with σ=0.011 mJy beam^{-1}, spaced by a factor of two. Blue circles mark optically identified cluster members. Red letters and circles mark the sources with optical counterparts quoted in the text. *BCG* 1 is the brightest cluster galaxy of the main sub-cluster; *BCG* 2 is the one of the western sub-cluster; *A* and *B* are cluster members; *C* and *D* do not have redshift estimates (Golovich et al., 2019a,b)

3.2.2 X-ray observations

We retrieved from the *XMM-Newton* Science Archive two observations on RXC J1314.4-2515 (ObsID: 0501730101 and 0551040101), accounting for a total exposure time of $\sim$ 110 ks. The data sets were processed using the *XMM-Newton* Scientific Analysis System (`SAS v16.1.0`) and the Extended Source Analysis Software (`ESAS`) data reduction scheme (Snowden et al., 2008) following the working flow described by

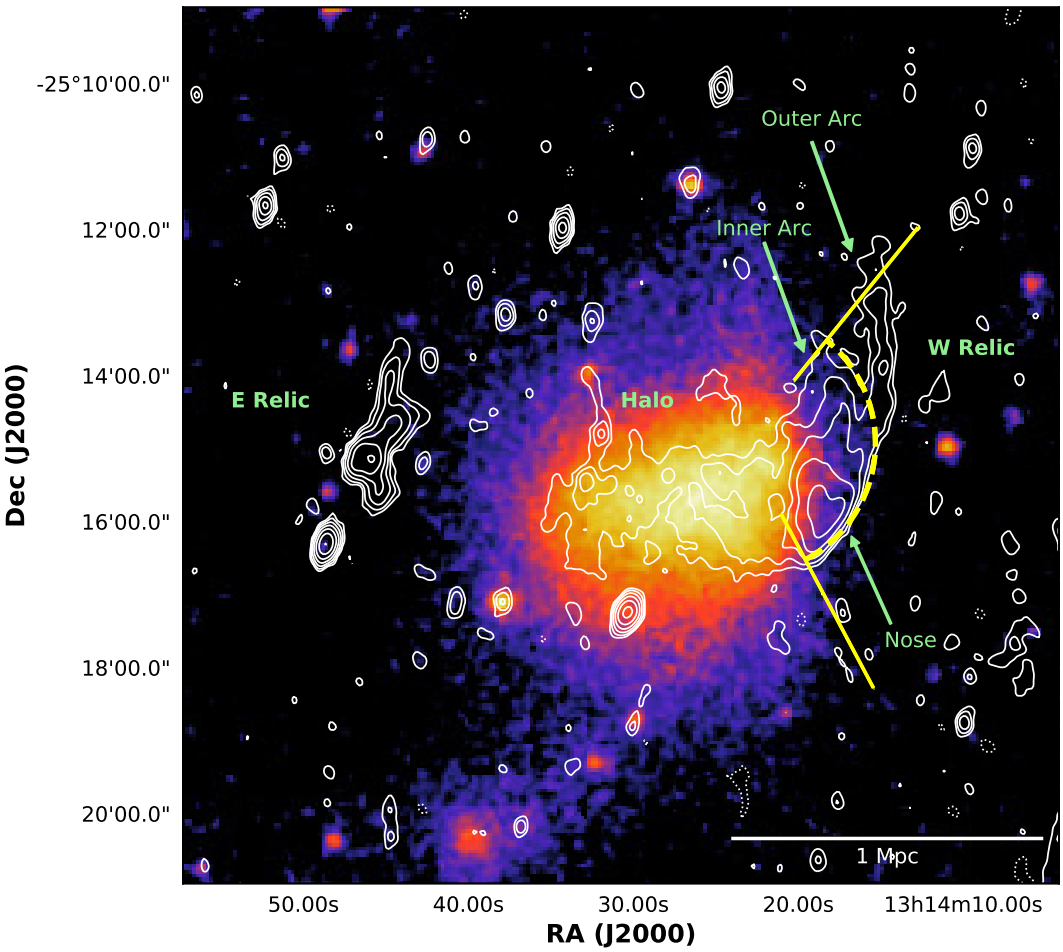

Figure 3.3: X-ray *XMM-Newton* image of the cluster RXC J1314.4-2515 with white radio contours overlaid. Contours are from A+B+C+D configurations at 1.5 GHz and start at $\pm 3 \times 0.016$ mJy beam^{-1}. They are spaced by a factor of two and negative contours are dotted. The restoring beam is $15'' \times 8''$. The X-ray image is smoothed with a Gaussian kernel of $5''$. The yellow dashed line marks the position of the X-ray detected shock and the yellow sector encloses the region used to extract the surface brightness profile (see Sec. 3.5.2).

Ghirardini et al. (2019a). We combined the count images and corresponding background and exposure maps of each ObsID to produce a single background-subtracted image also corrected for the effects of vignetting and exposure time fluctuations. The image in the $0.5 - 2.0$ keV band is shown in Fig. 3.3.

After the excision of contaminating point sources, we performed surface brightness and spectral analyses in the region of the western radio relic. The cluster emission was described with a thermal model with fix metallicity of 0.3 $Z_{\odot}$ (e.g. Werner et al., 2013) and taking into account the Galactic absorption in the direction of the cluster as reported in Kalberla et al. (2005). The background was carefully treated by modelling both the astrophysical and instrumental components (see Ghirardini

et al., 2019a, for more details on the procedure).

3.3 Study of the continuum emission

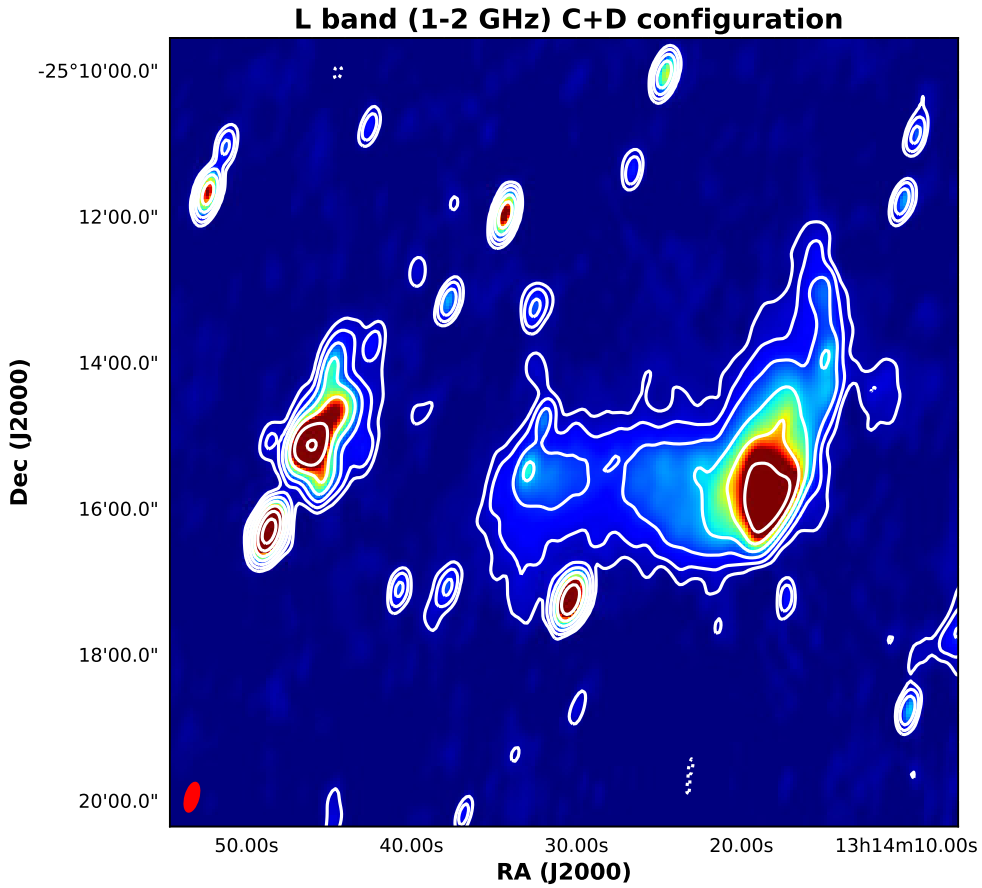

Figure 3.4: Lowest resolution image of the cluster in C+D configuration at 1.5 GHz. White contours are overlaid, starting from $\pm 3\sigma$, with σ=0.014 mJy beam^{-1}, and they are spaced by a factor of two. Negative contours are dotted. The restoring beam of $25'' \times 11''$ is shown in red in the left-hand corner and has a physical size of ∼70 kpc.

3.3.1 Description of radio sources

The eastern and western relics have a different shape but they are at about the same projected distance of ∼750 kpc from the central brightest cluster galaxy of the main sub-cluster (BCG 1, at redshift z=0.246, see Fig. 3.2). A comparison between radio and X-ray images (Fig. 3.3) shows that the two relics are on the opposite sides of the cluster while the radio halo overlaps with the X-ray emission. There is a shift between the peak of X-ray surface brightness and the position of the BCG 1, as may be expected from an interacting system (Rossetti et al., 2016). The X-ray emission

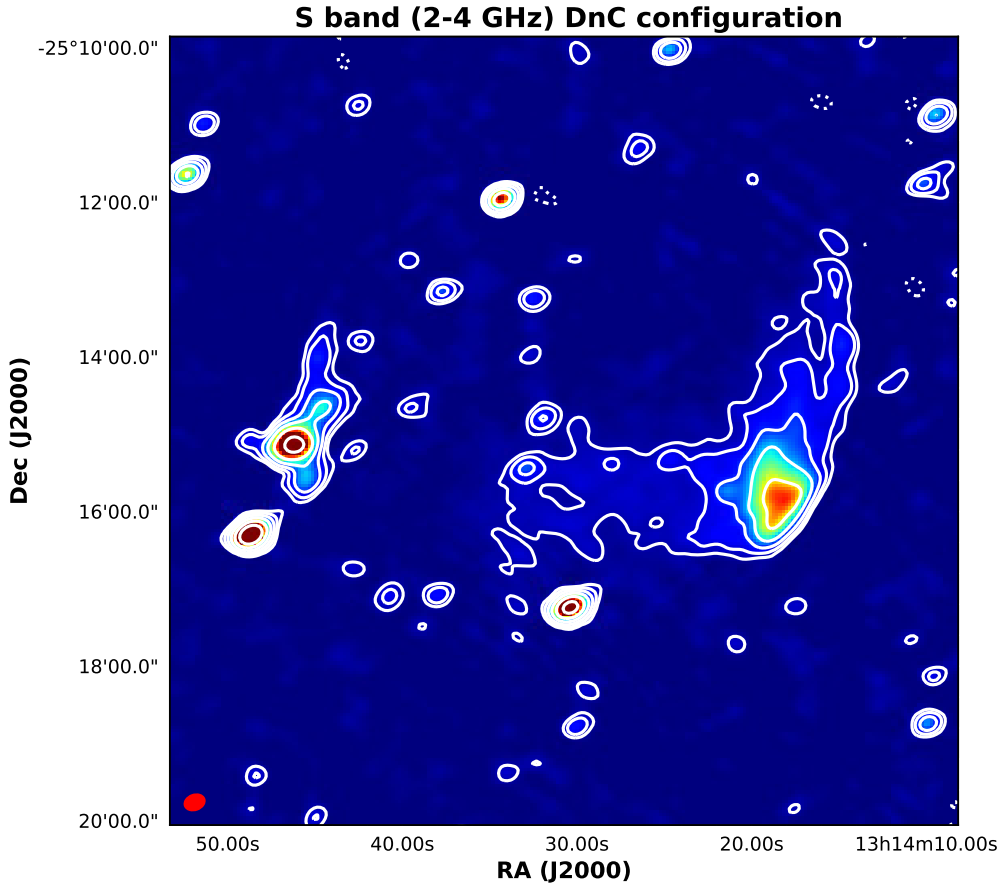

Figure 3.5: DnC configuration image at 3 GHz. White contours start by $\pm 3\sigma$, with σ=0.012 mJy beam^{-1}, and they are spaced by a factor of two. Negative contours are dotted. The restoring beam is $17'' \times 13''$ and it shown in red at the left-hand corner. It has a physical size of ∼58 kpc.

is elongated along the east-west merger axis and it is brighter on the western side of the cluster. At the position of the nose of the W relic, the X-ray emission has a sharp drop where a shock was first detected by Mazzotta et al. (2011). We confirm and discuss the shock detection in Sec. 3.5.2. A stream of gas that follows the profile seems to connect the main cluster with a southern sub-cluster but in this region we did not detect any diffuse radio emission.

The eastern relic

The eastern relic has a largest linear size of $\sim$ 500 kpc. Its morphology and a plausible association with optical sources made Feretti et al. (2005) cautious about its identification with a radio relic. With high-resolution A configuration imaging we discovered that a narrow angle tail radio galaxy (NAT, e.g. Miley, 1980) is embedded in the diffuse emission (marked with *A* in Fig. 3.2). This radio galaxy is a cluster

member at redshift z=0.242 (Golovich et al., 2019a,b). The diffuse emission is clearly related to the NAT but it extends well beyond radio galaxy lobes in the N-S direction and its largest size is perpendicular to the E-W merger axis. In Sec. 3.5.1 we discuss the relic-AGN connection using spectral index and polarization analyses. Another radio galaxy without redshift estimate (C in Fig. 3.2) lies to the south of the E radio relic, at a projected distance of ∼200 kpc.

The E relic lies in a region of low X-ray surface brightness that prevents the possible detection of a shock related to the relic emission (see Fig. 3.3.)

The western relic and the radio halo

The dominant radio feature of RXC J1314.4-2515 is in the western part of the cluster. The faint diffuse emission of the halo with a roundish shape of radius ∼ 65″ (i.e., 250 kpc) is visible at the centre of the cluster in Fig. 3.3. The emission broadens and brightens to the west. Then it bends to the north and two arcs detach from the brightest region of the W relic along the N-S direction. The innermost one extends for approximately 140″, corresponding to ∼550 kpc, and it is the brightest one. The outermost arc is more extended, reaching a largest linear size of 970 kpc and a transverse size in the thinnest part of ∼80 kpc. The inner arc seems to follow the sharp X-ray profile in the west side of the cluster, while the longest one lies outside the region where the X-ray shock was detected. No clear optical counterpart could be associated with this radio emission. A point-like radio source without redshift estimate lies along the outermost arc (labelled with D in Fig. 3.2). All these features are observed also in the S-band image in Fig. 3.5.

3.3.2 Spectral index study

Using archival S-band data, we performed the spectral analysis of the extended emission to locate the site of particle acceleration.

We computed the spectral index between 1.5 and 3 GHz based on the combined L-band (B+C+D in Tab. 3.2) and S-band observations. We imaged the L-band observations with the same uv-range as the S-band data (0.19-23.7 kλ). We used the same pixel size and baseline interval, and set data weights in order to reach a similar beam size as in the S-band. After cleaning, we convolved the two images to the same Gaussian beam with FWHM of 18.5″ and we corrected them for the primary beam response. We have checked the position of a number of point-like sources in the two data sets to exclude any significant astrometric offset between them.

For the W relic and the halo, we computed the spectral index excluding point-like sources. We first imaged both S- and L-band data sets excluding short baselines (i.e., < 3.5 kλ) which are sensitive to extended emission (i.e., larger than 90″ correspond-

ing to 350 kpc). Then, we subtracted from the original visibilities the corresponding model components and we made new images using all the baselines at the resolution of 18.5″. This procedure was also applied to the E relic, but since the emission of the NAT is extended, it is impossible to properly separate the contribution of the tail from the relic. Hence, we decided not to subtract the radio galaxy. This choice allows us to study the spectral index behaviour from the core of the NAT to the lobes, and to investigate its connection with the diffuse source.

We computed the average flux density and spectral index of the E relic (and of the NAT radio galaxy) and of the W relic and the radio halo emission (sources subtracted) between 1.5 and 3 GHz. The values are reported in Tab. 3.3. The uncertainties on the flux density measurements, S, are computed as:

$$\sigma_S = \sqrt{(\delta S \times S)^2 + (\sigma \times \sqrt{n_{\rm beam}})^2} \ , \tag{3.1}$$

where $\delta S = 5$ % is the calibration error, σ is the rms noise listed in Tab. 3.2 and $n_{\rm beam}$ is the number of beams in the sampled region. These uncertainties were then propagated to the spectral index.

We extrapolated the radio power at 1.4 GHz from the 1.5 GHz flux density measurement, considering a luminosity distance $D_L = 1253.3$ Mpc (Wright, 2006) and using the spectral indices for the k-correction. The uncertainties on flux densities were propagated to the radio power. The sum of the radio power of the two relics (sources subtracted) is consistent with the relation found by de Gasperin et al. (2014) between the radio power of double radio relics and the cluster mass.

Finally, we computed the spectral index for each pixel with value $> 3\sigma$ in both frequency bands. We show the spectral index map of the E relic in Fig. 3.6. We propagated the uncertainties on the flux densities pixel by pixel on the spectral index. The error map of the spectral index for the E relic is shown in the bottom panel of Fig. 3.6, while the spectral index image of the western region and its error map are shown in Fig. 3.7.

Spectral index images obtained from interferometric data should be treated with caution, since the value of α that we computed in each pixel is not independent of the neighbouring pixels. Furthermore, some artifacts (due to slightly different sampling of the baselines and to imaging artifacts in the two original images) could affect spectral index images, in particular at the edge of extended emission or where point-like sources were subtracted out. We can recover the spectral index variations with higher significance by integrating the flux over regions larger than the beam size. Regions were chosen by following the features observed in the spectral index maps and with the goal of obtaining a signal-to-noise ratio higher than 3 in each region. Spectral index profiles of the E relic and of the W relic and the halo emission are shown in Fig. 3.8 and Fig. 3.9, respectively.

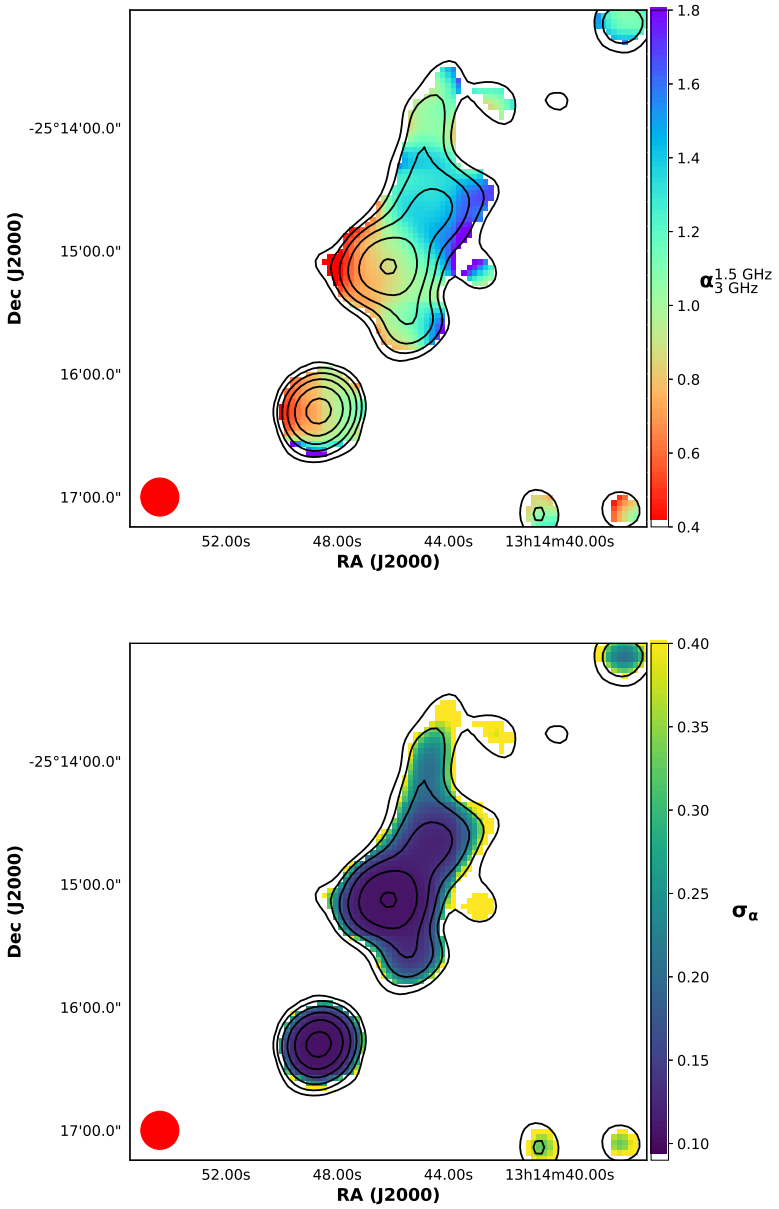

Figure 3.6: Top panel: spectral index image of the E relic region between 1.5 and 3 GHz. The 1.5 GHz total intensity contours (B+C+D configuration) are overlaid in black: the levels start at 3σ, with σ=0.04 mJy beam^{-1}, and are separated by a factor of two. Bottom panel: error map of the spectral index image with the same contours overlaid. The restoring beam of the two images is shown in the left-hand corner and its size is $18.5'' \times 18.5''$.

The eastern relic

The integrated spectral index found in the E relic, including the NAT, is in agreement with the one obtained by George et al. (2017) with a power-law fit of the spectrum

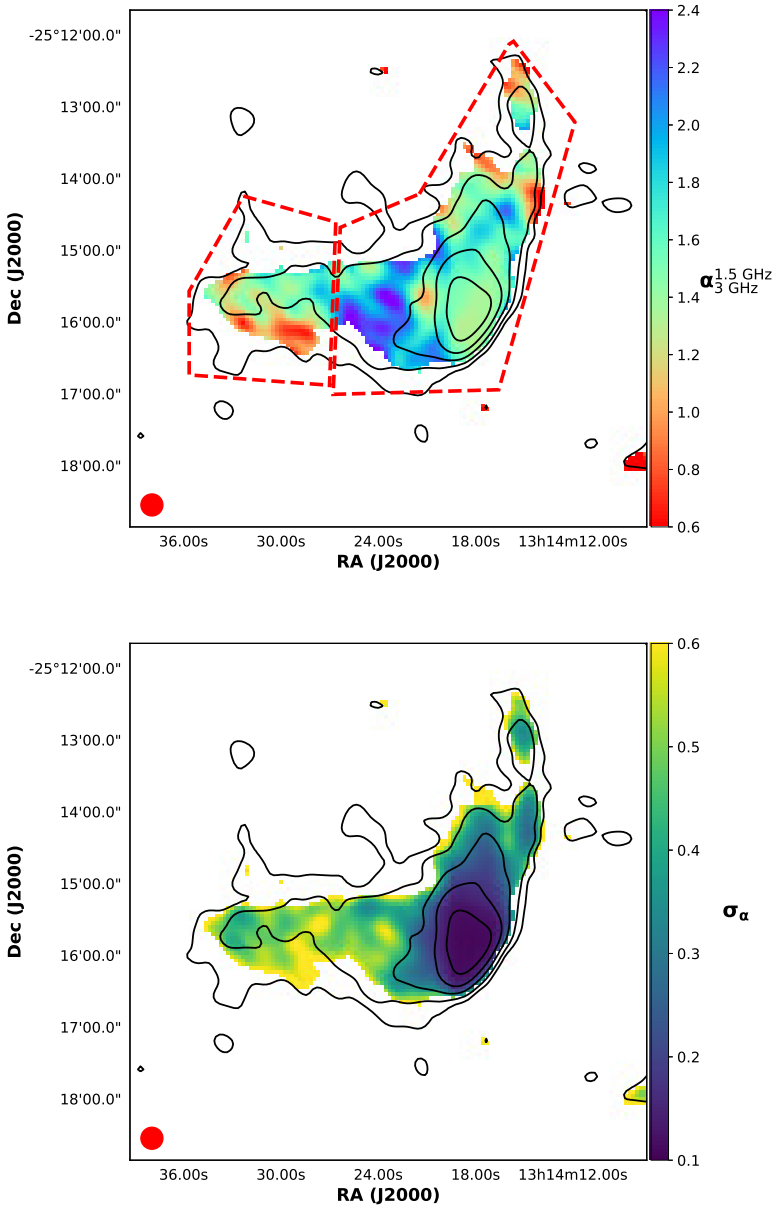

Figure 3.7: Top panel: spectral index image of the W relic and halo region computed between 1.5 and 3 GHz. Point-like sources were subtracted. The two dashed red polygons mark the flux density extraction regions for the halo and the West relic. Bottom panel: error map of the spectral index image. Contours and restoring beam are as in Fig. 3.6.

between 118 MHz and 1.4 GHz, $\alpha_{1.4\mathrm{GHz}}^{118\mathrm{MHz}}$=1.03±0.12. No spectral curvature is thus observed for this relic up to 4 GHz.

The spectral index image is shown in Fig. 3.6. It is not trivial to identify a single spectral gradient of the whole extended emission. A steepening trend is visible from the core of the radio galaxy to its lobes but it is possible to draw a steepening trend

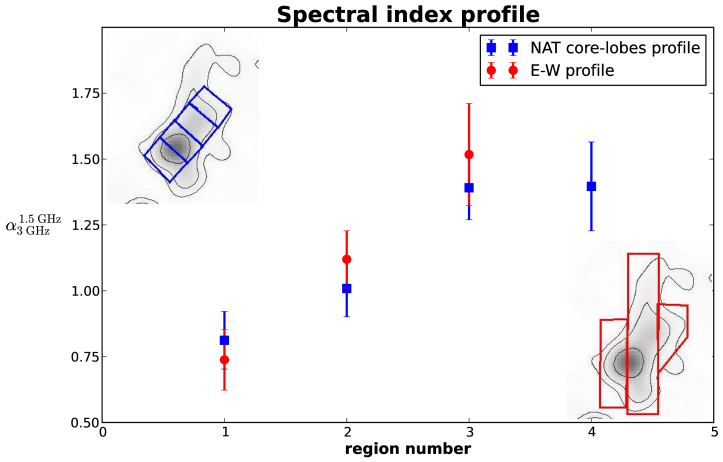

Figure 3.8: Spectral index profiles in the E relic. The spectral index is computed in the regions shown in the inset panels and numbered following the profiles. The regions used for the red profile (plotted with round marks) are shown in the top-left inset panel and are numbered from E to W. The regions used for the blue profile (plotted with square marks) are shown in the bottom-right inset panel and are numbered from the core in the SE to the lobes in the NW. We drew the regions in order to avoid point-like sources surrounding the extended emission.

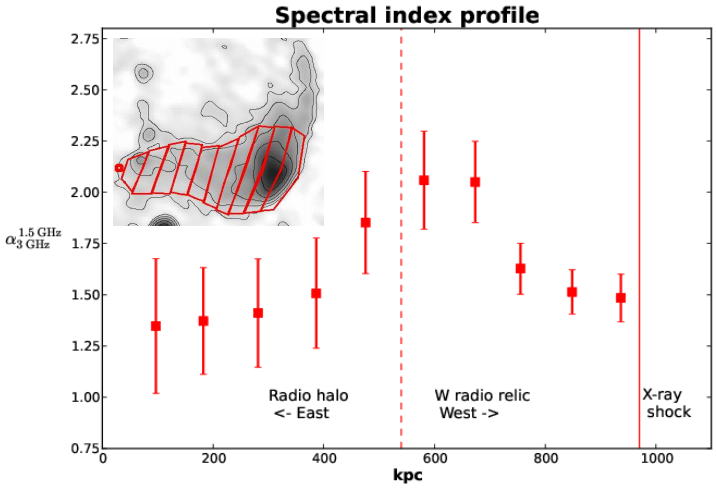

Figure 3.9: Spectral index profile in the W relic and halo region where point-like sources were subtracted. The origin of the x axis coincides with the position marked with the red point in the inset panel. The solid red line shows the position of shock front detected in X-ray while the dashed line separates the W relic and halo region.

Table 3.3: Flux density, spectral index between 1.5 and 3 GHz and radio power of extended sources measured from the images used for the spectral index study. We separated the region of the W relic and the halo on the basis of the spectral index profile as described in Sec. 3.3.2. The "*" stands for point-like sources subtracted.

Source	Freq. (GHz)	Flux Density (mJy)	$\alpha_{3\ \mathrm{GHz}}^{1.5\ \mathrm{GHz}}$	$P_{1.4\ \mathrm{GHz}}$ (10^{24}W/Hz)
E relic	1.5	11.3±0.6	1.0±0.1	2.3±0.1
	3	5.6±0.3		
W relic*	1.5	33±2	1.6±0.1	7.9±0.5
	3	10.9±0.8		
Halo*	1.5	5.3±0.3	1.3±0.2	1.16±0.07
	3	2.1±0.2		

also from E to W. The first trend is expected if the only radio galaxy originates the emission while the second is expected from the acceleration of particles from a shock wave propagating outwards from W to E. If these two trends were both present they would be mixed in the spectral index map, due to the physical superimposition and of the resolution of our image.

In Fig. 3.8 we trace both the expected trends and the spectral index profiles are displayed in different colours. The blue profile follows the core-lobes direction as can be derived from the high resolution A configuration image at a position angle of -45° (see Fig. 3.2). The flattest spectral index corresponds to the core of the radio galaxy in the first blue region, with $\alpha_{3\mathrm{GHz}}^{1.5\mathrm{GHz}}$=0.8±0.1. The spectral index steepens toward the tails of the radio galaxy and in the fourth region, furthest away from the core, it remains constant. The fact that the northern and southern edges of the emission do not follow the core-lobes direction and show a flatter spectral index (Fig. 3.6) than the fourth region of the profile, indicates that the propagation of jets has been perturbed and/or that another mechanism is possibly accelerating particles.

With the red boxes we traced the E-W profile (avoiding nearby point-like sources in the W and E of the extended emission). A clear steepening trend is observed also in this direction. This is suggestive of an acceleration process that is active along the whole length of the E relic and not only originating in the core of the radio galaxy. This scenario is further discussed in Sec. 3.5.1.

The western relic and the radio halo

We computed the spectral index profile of the western emission region using ten regions between the centre of the cluster to the region of the shock detected in the X-ray (see Fig. 3.9). The emission of point-like sources was subtracted out of the images as explained in Sec. 3.3.2.

In the region close to the shock front, the spectral index is $\alpha_{3\mathrm{GHz}}^{1.5\mathrm{GHz}}$=1.5±0.1. In

Sec. 3.5.2 we derive the Mach number of the underlying shock wave assuming the DSA mechanism and compare it to the one derived from X-rays (see also Sec. 1.2.3).

The spectral index steepens towards the cluster centre, reaching a peak value of $\alpha_{3\mathrm{GHz}}^{1.5\mathrm{GHz}}$=2.1±0.2 at ∼400 kpc from the shock front. A steepening trend is expected in the downstream of a shock wave where energetic particles cool down, and it is often observed in radio relics (e.g. Hoang et al., 2017).

Toward the halo region, the spectral index flattens again and reaches a value of ∼ 1.3. The trend is clear also from Fig. 3.7. The spectral profile strongly resembles the one observed in the Toothbrush radio relic (van Weeren et al., 2016a). The flattening of the spectrum can be explained by the presence of another mechanism re-accelerating particles in the central region of the cluster. This is further discussed in Sec. 3.5.3.

The profile flattens and remains almost constant in the four central regions. According to the spectral index profile, we disentangled the region of the relic from that of the radio halo. We assumed that the steepening of the spectrum up to $\alpha_{3\mathrm{GHz}}^{1.5\mathrm{GHz}}$ ∼2 is due to the aging of particles in the region downstream the shock. We considered as radio halo the region where the spectral index flattens again. In Fig. 3.7 we show the two approximate regions with red dashed polygons. In Tab. 3.3 we reported average spectral index and radio power of W relic and radio halo.

George et al. (2017) derived a spectral index of $\alpha_{1.4\mathrm{GHz}}^{118\mathrm{MHz}} = 1.23 \pm 0.09$ for the western relic subtracting the flux density of the radio halo extrapolated from the 610 MHz measurement. We instead derived two distinct integrated values: in the halo $\alpha_{3\mathrm{GHz}}^{1.5\mathrm{GHz}} = 1.3 \pm 0.2$ and in the relic $\alpha_{3\mathrm{GHz}}^{1.5\mathrm{GHz}} = 1.6 \pm 0.1$. We can also estimate the spectral index of the halo between 610 MHz and 1.5 GHz using the work of Venturi et al. (2007) and integrating over the same physical region: $\alpha_{1.5\mathrm{GHz}}^{610\mathrm{MHz}} = 1.1 \pm 0.1$. Our spectral index estimates within the uncertainties are consistent with those measured by Venturi et al. (2007) at 610 MHz and by George et al. (2017).

3.4 Polarized intensity study

3.4.1 Polarized intensity imaging

We made use of `WSClean 2.6`[¶] (Offringa et al., 2014) for the polarization intensity imaging. This imager exploits a w-stacking algorithm as a faster alternative to w-projection and allows multi-scale, multi-frequency and auto-masking algorithms (Offringa & Smirnov, 2017).

We imaged 1-2 GHz A, B, C configurations data and 2-4 GHz data in DnC configuration to sample different spatial scales and frequencies. We also used together L-band B+C and S-band DnC data to cover the whole frequency band 1-4 GHz.

[¶] https://sourceforge.net/p/wsclean/wiki/Home/

The images were cleaned down to 3σ level using the `auto-masking` option. We used 64 frequency sub-bands of 16 MHz each for the data in L-band, and 16 sub-bands of 128 MHz for the S-band data. The different sub-band width is required to avoid bandwidth depolarization at the lowest frequency. For the whole 1-4 GHz band we used 96 frequency sub-bands of 32 MHz each. The restoring beam was forced to be the same in each frequency sub-band, matching the lowest resolution one. The parameters used for each image are listed in Tab. 3.4.

We used `join-channels` and `join-polarizations` options to make Stokes I, Q, U image cubes and full-bandwidth images, as recommended in the `WSClean` documentation. Each image was corrected for the primary beam calculated for the central frequency of the sub-band. We restricted our analysis to a circular region of radius $\sim 6'$ (i.e., $\sim$1.4 Mpc) around the L-band pointing centre so that the effect of direction-dependent gain, polarization leakage in Q and U and beam squint are negligible (Jagannathan et al., 2017). We quantified the leakage from Stokes I to V to be ≤ 2 % within the closest $6'$ to the image centre. This constrains the leakage to Stokes Q and U to be within 1 % of I. We caution however about the usage of similar data for sources showing lower fractional polarization (<5 %) and further away from the beam centre.

3.4.2 RM synthesis

We performed RM synthesis on the Q and U image cubes using `pyrmsynth`[‖] and we obtained the cubes in the Faraday space. We thus recovered the reconstructed Faraday dispersion function, or Faraday spectrum, $\widetilde{F}(\phi)$, in each pixel (i.e. each line of sight).

Faraday cubes were created between ± 600 rad m^{-2} and using bins of 2 rad m^{-2}. This range is motivated by our sensitivity to large values of ϕ. Using Eq. 2.19, 2.20 and 2.21 we can estimate the resolution in Faraday space, $\delta\phi$, the maximum observable Faraday depth, $|\phi_{\rm max}|$, and the largest observable scale in Faraday space, $\Delta\phi_{\rm max}$. The parameters for each observation are listed in Tab. 3.4.

Notice the different resolutions and $\Delta\phi_{\rm max}$ values of our measurements. The values of $|\phi_{\rm max}|$ to which we are sensitive are well above the value expected from galaxy clusters (see, e.g., Bonafede et al., 2010, 2013; Böhringer, Chon & Kronberg, 2016). In this galaxy cluster, we observed $|\phi_{\rm peak}|<100$ rad m^{-2} both in the L- and in the S-band observations, so that the lower $|\phi_{\rm max}|$ obtained combining L- and S-band does not limit our measurements. In the combined data set, with a central frequency of 2.5 GHz, we reach the highest resolution in Faraday space and we are sensitive to polarized emission spread over large Faraday scales.

We first run `pyrmsynth` on the entire central region cleaning the spectrum down

[‖] https://github.com/mrbell/pyrmsynth

Table 3.4: Details of polarized intensity images. Column 1: observing frequency range, i.e. first and last frequency sub-bands; Column 2: name of the frequency band; Column 2: array configuration; Column 3: $\delta\nu$ is the frequency sub-band width; Column 4: σ_{QU} is the best estimate for the rms noise in polarization obtained as $(\sigma_Q + \sigma_U)/2$; Column 5: FWHM of the major and minor axes of the restoring beam of the image cubes; Column 6: resolution in the Faraday space; Column 7: maximum observable Faraday depth; Column 8: largest observable Faraday-scale; Column 9: reference of the figures in this Chapter.

Freq. Range (GHz)	Band	Array Config.	$\delta\nu$ (MHz)	Beam	σ_{QU} (mJy/beam)	$\delta\phi$ (rad m^{-2})	$\lvert\phi_{\rm max}\rvert$ (rad m^{-2})	$\Delta\phi_{\rm max}$ (rad m^{-2})	Figure
1.015-2.023	L	A	16	$2.5''\times2.5''$	0.004	45	535	143	
1.015-2.023	L	B	16	$11''\times5''$	0.005	45	535	143	
1.015-2.023	L	C	16	$25''\times 25''$	0.007	45	535	143	3.10, 3.11
2.050-3.947	S	DnC	128	$25''\times 25''$	0.004	188	598	543	3.10, 3.11
1.022-3.995	S+L	B+C+DnC	32	$25''\times25''$	0.004	37	288	558	3.12, 3.13

to five times the noise level of full-bandwidth Q and U images (see Heald, 2009, for the RM clean technique). We imposed an average total intensity spectral index α=1 on the entire field. We noticed the RM cleaning process was improved by the use of α=1 instead of the default α=0, although it comes from an average estimate for the entire field and it is assumed to be constant at each Faraday depth. We measured the local rms noises σ_Q and σ_U in the slices of $\widetilde{Q}(\phi)$ and $\widetilde{U}(\phi)$ at 500 rad m^{-2} $<$ $|\phi|$ $<$ 600 rad m^{-2} i.e. outside the sensitivity range of our observations. Since $\sigma_Q \sim \sigma_U$, we estimated the noise of polarization observation as $\sigma_{QU} = (\sigma_Q + \sigma_U)/2$ (see also Hales et al., 2012). This value is reported in Tab. 3.4 for each measurement set. Then, we selected pixels with a peak in the Faraday spectrum above a threshold of $8\sigma_{QU}$, following George, Stil & Keller (2012), which corresponds to a false detection rate of 0.06 % and to a Gaussian significance level of about 7σ according to Hales et al. (2012). This conservative choice accounts for the Ricean bias, the non-Gaussian noise in the Q and U images, and the additional bias due to error in $\phi_{\rm peak}$ estimates. We run again `pyrmsynth` only on these pixels, cleaning the spectrum down to $8\sigma_{QU}$ level.

We computed polarization intensity images using the peak of the Faraday dispersion function and correcting for the Ricean bias as per Eq. 2.27. We then obtained fractional polarization images dividing the P images (with the $8\sigma_{QU}$ threshold) by the full-band Stokes I images with a cutoff of three times the rms noise. We also obtained $\phi_{\rm peak}$** images with the same cutoff. From the reconstructed values of Q and U at $\phi_{\rm peak}$ we can also recover the intrinsic polarization angle (i.e., corrected for the value of RM determined by $\phi_{\rm peak}$), χ_0, as:

$$\chi_0 = \chi(\lambda_0^2) - \phi_{\rm peak}\lambda_0^2 = \frac{1}{2}\arctan\frac{\widetilde{U}(\phi_{\rm peak})}{\widetilde{Q}(\phi_{\rm peak})} - \phi_{\rm peak}\lambda_0^2 \ , \tag{3.2}$$

where λ_0 is 19.7 cm, 11.9 cm and 10 cm for the L, S+L and S-band, respectively.

Fractional polarization and magnetic field vector images of the L-band C configuration and S-band are shown in Fig. 3.10 and Fig. 3.11 for the E and W relics, respectively. We also obtained B configuration L-band images but, for the purpose of this work, we are more interested in the polarized diffuse emission of the relics, more visible in the C configuration image. We obtained only few pixels above the $8\sigma_{QU}$ cutoff with the A configuration L-band image. Fractional polarization and magnetic field vector images obtained from the whole frequency band 1-4 GHz are shown in the upper panel of Fig. 3.12. We show the same quantities obtained at different frequency bands to show the importance of combining multi-band observations for

**Note that these values are not corrected for the redshift of the cluster, and thus they represent the Faraday rotation in the observer's frame. The intrinsic values would be a factor 1.6 higher and the difference will be accounted for in Sec. 3.5.5, when these values are used to derive B and n_e at the position of the W relic.

this analysis.

The Faraday depth image of RXC J1314.4-2515 resulting from the combined S+L-band data set is shown in Fig. 3.13. We show only the S+L-band map since we obtained a good trade-off between resolution in Faraday space and sensitivity. Thanks to the wide and contiguous frequency coverage of our observations, we can identify some regions of the W relic which clearly show Faraday-complex structures. In this case, the value of $|\widetilde{F}(\phi_{\rm peak})|$ and of $\phi_{\rm peak}$ are not sufficient to describe the polarization and rotation effect experienced by the radiation since the polarized emission would be spread at different values of ϕ and affected by Faraday depolarization. For this reason, the results of RM synthesis in the southern region of the W relic (i.e., the nose) should be regarded with caution. Faraday-complex structures are separately discussed in Sec. 3.5.6.

The RM value of the Galactic foreground (i.e., -30 rad m^{-2}) was subtracted out: we will refer to the cluster Faraday depth, ϕ_{cl}, to indicate foreground subtracted values.

We computed σ_ϕ following Eq. 2.26 and we added in quadrature the error of 2 rad m^{-2} on the estimate of the Galactic foreground by Taylor, Stil & Sunstrum (2009) to obtain $\sigma_{\phi_{cl}}$. The error map is shown in the bottom panel of Fig. 3.13. From σ_ϕ we derived the error on the polarization angle by propagating the uncertainties on the quantities in Eq. 3.2 as:

$$\sigma^2_{\chi_0} = \sigma^2_\chi + \sigma^2_\phi \lambda^4_0 = \frac{\sigma^2_{QU}}{4P^2} + \left(\frac{\delta\phi}{2P/\sigma_{QU}}\right)^2 \lambda^4_0 \, . \tag{3.3}$$

These uncertainties for the vector map for the S+L-band data set are shown in the bottom panel of Fig. 3.12.

As pixel values are not independent of each other, in the text we will refer to beam-averaged quantities, which are the average values of ϕ_{cl} over beam-size regions, weighted by the signal-to-noise ratio of pixels. To a first approximation, in the case of Faraday-simple sources, the distribution of RM values in each beam has a Gaussian distribution for signal-to-noise ratios higher than 8 (George, Stil & Keller, 2012) and its variance is not due to a physical variation of the Faraday rotating medium, but to the underling noise in the Faraday spectrum, which shifts the position of the peak. Hence, we calculated also the standard deviation of neighbouring pixels in a region equivalent to the beam area to estimate the RM uncertainties.

The eastern relic

In the B configuration we detected polarized emission arising only from a barely resolved source in the south-east of the E relic (source C in Fig. 3.2) and from two regions close to the lobes of the NAT radio galaxy embedded in the relic.

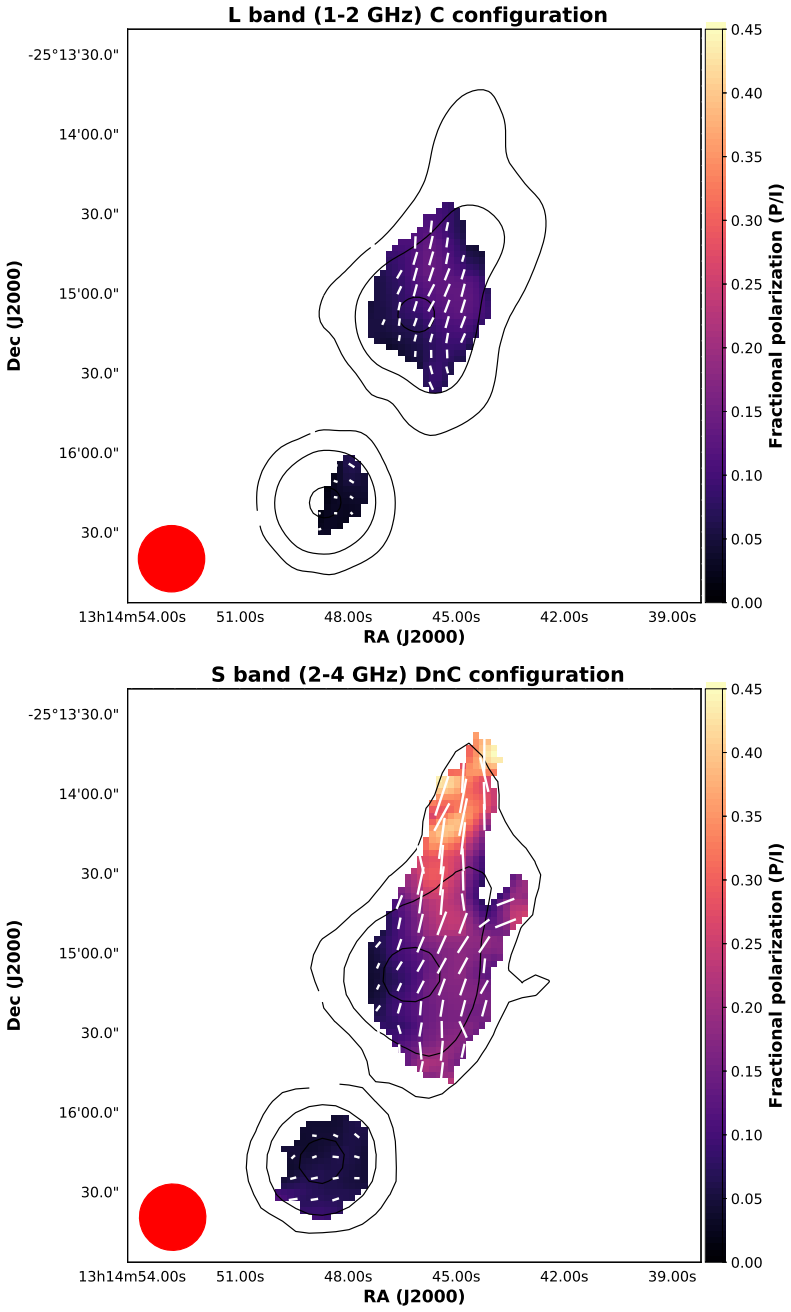

Figure 3.10: Fractional polarization (color scale) and magnetic field vectors (white lines) of the E radio relic: L-band data in C configuration (top panel) and S-band data (bottom panel). An $8\sigma_{QU}$ detection threshold was imposed polarization and values were corrected for the Ricean bias. See Tab. 3.4 for details on the images. The length of white vectors is proportional to the fractional polarization. Black contours are from the total intensity images in the same frequency band and configuration. The restoring beam is $25'' \times 25''$ in both images. Contour levels start from 3 times the rms noise (0.08 mJy beam^{-1} and 0.03 mJy beam^{-1} for the L- and S-band respectively) and are spaced by a factor of four.

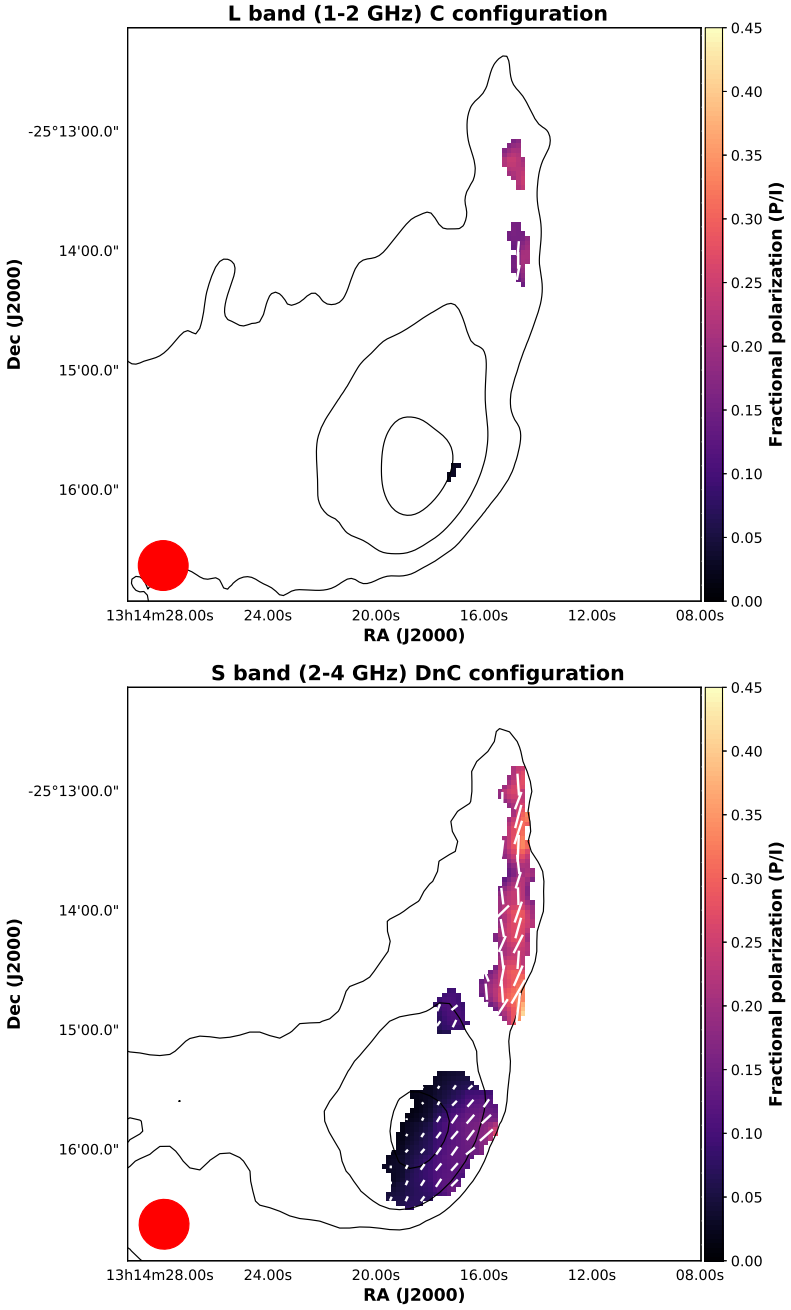

Figure 3.11: Same as Fig. 3.10 for the W relic.

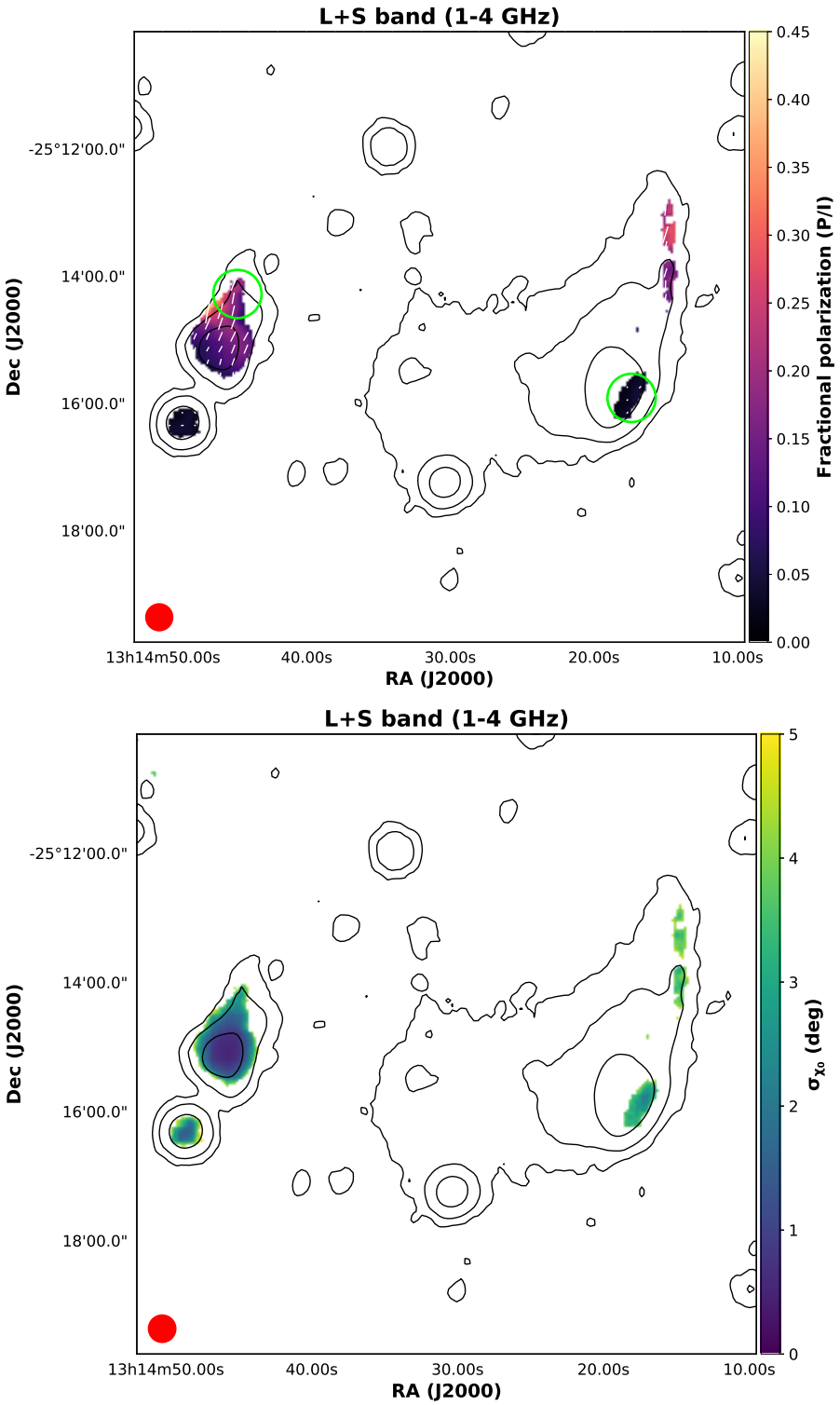

Figure 3.12: Top panel: fractional polarization (color scale) and magnetic field (white lines) with a $8\sigma_{QU}$ detection threshold for the 1-4 GHz data in B+C+DnC configuration (see Tab. 3.4 for image details). Fractional polarization values were corrected for the Ricean bias. The green circles mark the regions used for the Faraday depolarization study in Sec. 3.5.6. The length of white vectors is proportional to the fractional polarization. Bottom panel: error map of the polarization angle. In both panels the black contours are from the total intensity image with a restoring beam of $25'' \times 25''$, shown in the left-hand corner of the image. They start from 3 times the rms noise of 0.02 mJy beam^{-1} and are spaced by a factor of four.

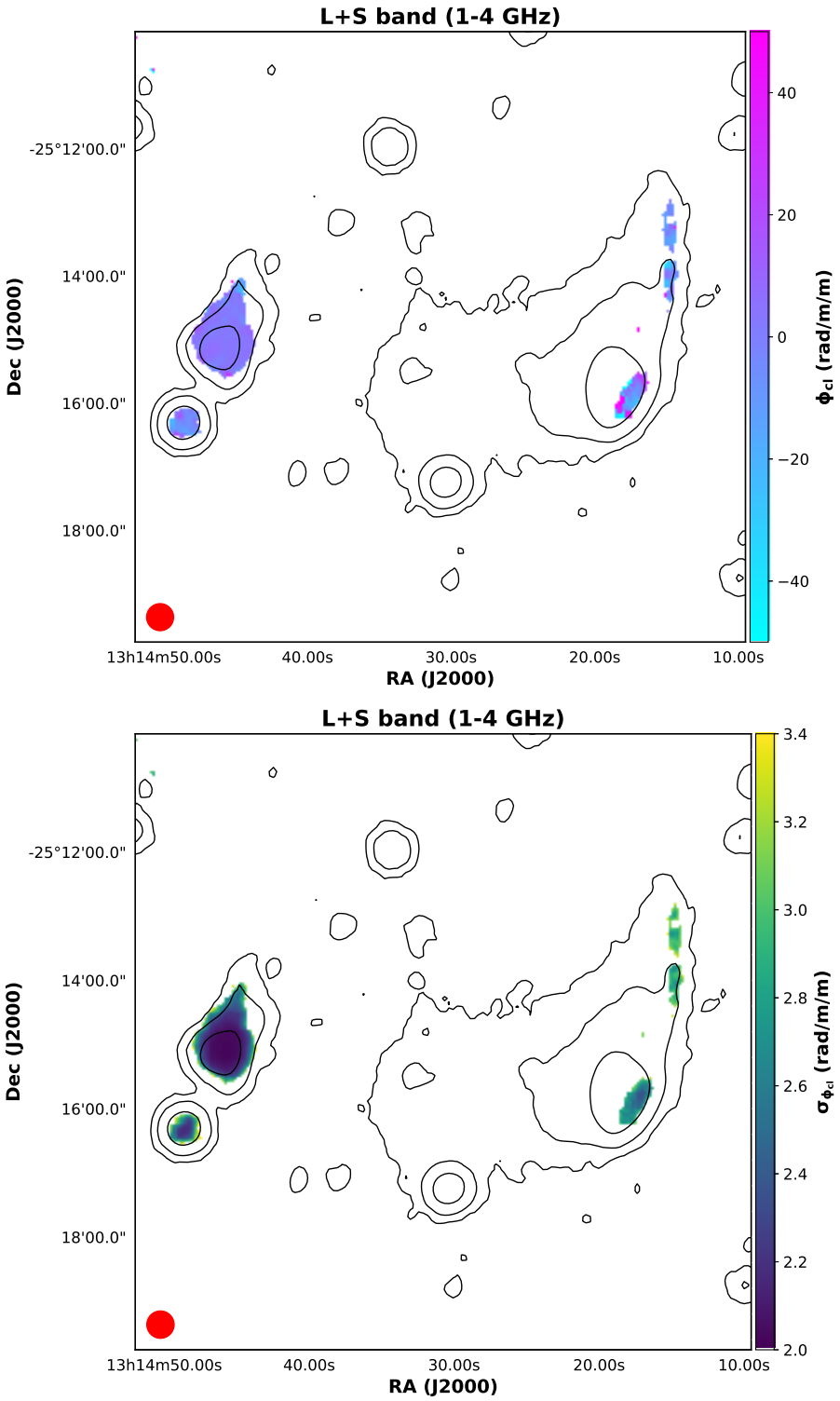

Figure 3.13: Top panel: value of ϕ_{cl} on a pixel by pixel basis with a $8\sigma_{QU}$ detection threshold for the 1-4 GHz image in B+C+DnC configuration. Bottom panel: error map of the ϕ_{cl} image. Black contours and restoring beam are the same as Fig. 3.12.

In the S-band and L-band C configuration images (Fig. 3.10), the average polarization fraction of the source C is 4.3±0.4 % and 3.6±0.4 %, respectively. The polarization fraction is 3.6±0.3 % also in the combined S+L-band image (Fig. 3.12). The weighted average ϕ_{cl} of this source derived from the Faraday depth map of Fig. 3.13 is -4 rad m^{-2} while the standard deviation is 9 rad m^{-2}.

The E relic shows a resolved polarized emission in the C configuration L-band and in the S-band images (Fig. 3.10). The fractional polarization observed in the L-band is lower than what is detected in other radio relics, while in the S-band it is consistent with the literature (van Weeren et al., 2019). The region of the core of the NAT radio galaxy in the eastern edge of the relic is polarized at an average 9.9±0.9 % level in the S-band. The fractional polarization increases in the region of the lobes and in the N-S direction. In particular, in the S-band image we detect polarized emission from the E radio relic, reaching a polarization fraction of $\sim$ 45 % in the northern part of the relic. The magnetic field is oriented almost in the direction of the radio lobes of the galaxy and then bends to be aligned in the N-S direction along the radio relic. The same is observed in Fig. 3.12.

The values of average ϕ_{cl} within beam-size regions located in the E relic are almost constant ranging between 2 and 4 rad m^{-2} with a standard deviation of $\sim$3 rad m^{-2}. Only in the northern side of the relic the average ϕ_{cl} changes to -3 rad m^{-2} with a standard deviation of 11 rad m^{-2}.

All the values of ϕ_{cl} measured are consistent with zero considering the standard deviation as the uncertainty, meaning that the electron density and the magnetic field in this region of the cluster are not responsible for the Faraday rotation effect which is mainly due to the external screen of our Galaxy. This is confirmed by the moderate Faraday depolarization detected in this region which can be explained by the low thermal electron density (see Fig. 3.3).

The western relic and the radio halo

The western side of RXC J1314.4-2515 does not show polarization in the B configuration image. Few pixels with a signal-to-noise ratio in polarization higher than 8 appear in the thinnest part of the outer W relic in the L-band C configuration image. Here the degree of polarization reaches the 25 % level but it is measured only in few pixels (Fig. 3.11). Hence, the fractional polarization observed in the L-band is lower than what expected from the literature also for the W relic (see van Weeren et al., 2019, and references therein).

In the S-band, we found a totally different situation (see Fig. 3.11). Almost all of the outer arc shows high levels of intrinsic fractional polarization reaching a value of $\sim$ 40 % in the northern part. The average fractional polarization in the northern arc is 24±4 %. The magnetic field lines are almost aligned along the radio relic arc.

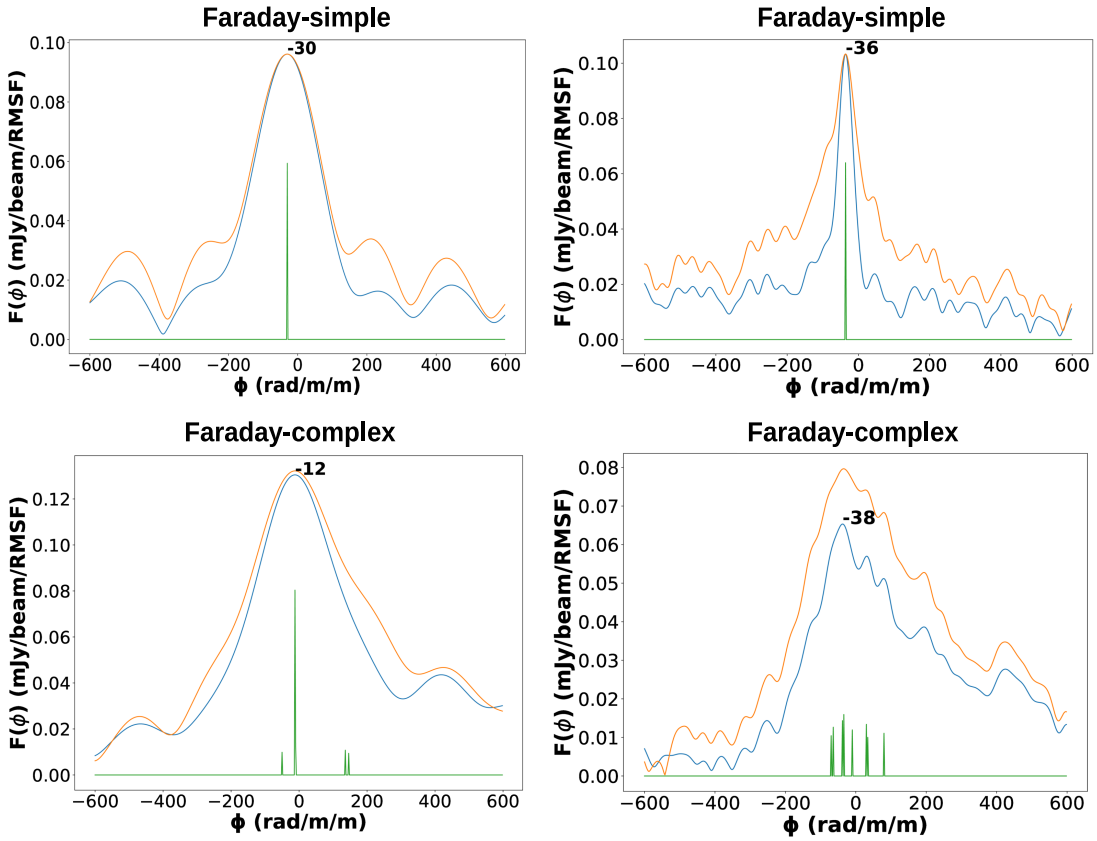

Figure 3.14: Faraday dispersion function of two representative pixels in the 2-4 GHz band observation (left column) and in the whole 1-4 GHz band (right column). The orange line is the dirty spectrum. the blue is the clean spectrum and in green the clean components. The pixel in the first row has a Faraday-simple structure while the one in the second row has a Faraday-complex structure, barely resolved in the first column and resolved as a convolution of peaks in the second one.

In Fig. 3.13, the values of ϕ_{cl} in the northern part of the relic are scattered between -44 rad m^{-2} and 42 rad m^{-2}. A spot of polarized emission, without any optical counterpart, is also detected along the inner arc at 10±3 % level of polarization and with values of ϕ_{cl} reaching 50 rad m^{-2}.

Also the southern part of the arc (i.e., the nose) shows polarization with an average value of 7.6±0.6 % in the S-band and of 3.0±0.3 % in the S+L combined data set. In the S-band, the fractional polarization increases, from $\sim$ 2 % in the inner region to $\sim$ 25 % at the shock front detected in the X-rays (see right panel of Fig. 3.11). In the whole southern region the ϕ_{cl} values in the S+L-band are in the range between -82 and 78 rad m^{-2}.

The emission coincident with the shock region, detected only in the S- and S+L-band observations, clearly shows a Faraday-complex emission unveiled by a broadening of the Faraday spectrum larger than the FWHM of the RMSF (i.e., at least larger than 150 rad m^{-2}, see Fig. 3.14). The strong Faraday depolarization between S- and L-band in this region is probably explained by the higher thermal electron density in respect to the E relic (Kierdorf et al., 2017). This is further discussed in Sec. 3.5.6.

The emission that extends from the W relic toward the central region of RXC J1314.4-2515 does not show any polarized emission. The upper limit on the fractional polarization in this area is 17 %, in agreement with literature results for other radio halos (e.g. Feretti et al., 2012).

3.5 Discussion

3.5.1 AGN-relic connection in the eastern relic

The NAT radio galaxy in Fig. 3.2 is a cluster member, and its lobes extend for $\sim$ 90 kpc fading into the radio relic which extends in the N-S direction. Although the detection of a shock related to the E relic emission is prevented by the low X-ray surface brightness (see Fig. 3.3) the combined information gained from the spectral index and the polarized intensity study support the idea that a shock wave is at the origin of the extended eastern emission together with the AGN activity. Since pairs of shock waves propagating along the merger axis are generated during cluster mergers, a shock wave moving outwards from W to E is in fact expected to be present at the position of the relic.

Assuming a magnetic field between 0.1 and 10 μG, as observed in other galaxy clusters (e.g., Govoni & Feretti, 2004), the lifetime of relativistic electrons that emit at 3 GHz at redshift 0.247 due to synchrotron and inverse Compton losses is $\leq 10^8$ yr (van Weeren et al., 2019, Eq. 3). Considering a plasma diffusion and/or bulk velocity of $\sim 10^5$ m s^{-1} (either due to AGN jet activity or to the merger shock) these

high-energy electrons are already aged after distances of few tens kpc. The observed emission at 3 GHz spreads over 500 kpc and implies that another mechanism is actively energizing the electrons. We suggest that the re-acceleration originates in the shock front as suggested by the E-W spectral steepening (see Sec. 3.3.2).

Low-energy electrons with Lorentz factor $\gamma < 10^2$ have radiative lifetimes larger than the Hubble time. During a maximum AGN lifetime of $\sim$1 Gyr these electrons can travel distances of hundreds kpc in the ICM. Hence, it is plausible that the AGN may have supplied the low-energy electrons re-accelerated by the shock.

In the northern region of the E radio relic, we measured an integrated spectral index of $\alpha_{3\mathrm{GHz}}^{1.5\mathrm{GHz}}$=1.2$\pm$0.2, flatter than the value reached in the region of the lobes of the radio galaxy (i.e., 1.4 ± 0.2, see Fig. 3.8). The flattening of the spectral index at the edge of the E relic could indicate that the particles are first injected by AGN jets in the ICM, where they lose energy due to synchrotron and Inverse Compton losses in the radio galaxy lobes, before being re-accelerated by a shock wave. A similar scenario was invoked by Bonafede et al. (2014) for PLCKG287.0+32.9. Recently, van Weeren et al. (2017) reported the clearest connection known to date between an AGN and a relic in Abell 3411 - Abell 3412.

If spectral index of the pre-existing population is flatter than the one that could be produced by the shock, the spectrum is amplified and retains the spectral index of the pre-existing population (e.g Gabici & Blasi, 2003; Kang & Ryu, 2011). In the opposite case, the post-shock electron population has the spectral index of the DSA and loses the memory of the injection spectrum. Since we observe a flatter spectrum in the northern edge compared to the lobes region, also considering the uncertainties on the spectral index values, we are in this latter case. The sampled regions have sizes > 50 kpc, thus the electron population should have already reached the equilibrium with the energy losses (continuous injection model, Kardashev, 1962). Hence, the Mach of the shock can be derived from the integrated spectral index inverting Eq. 1.21:

$$M = \sqrt{\frac{\alpha + 1}{\alpha - 1}} \, . \tag{3.4}$$

This implies that, if a shock wave is re-vitalizing the aged particles from the AGN lobes, its Mach number would be $M = 3 \pm 1$.

Furthermore, polarization vectors suggest that the projected magnetic field lines follow the AGN jets and then are bent along the north-south direction (see 3.11). A shock wave propagating from W to E along the merger axis (i.e. the line connecting the two sub-clusters) would be able to align the magnetic field lines in the N-S direction. A shock wave with $M \sim 3$ can in fact amplify the magnetic field components parallel to the shock front of a factor 2.5 (see, Iapichino & Brüggen, 2012, and Sec. 1.4.1), so that the resulting magnetic field on the plane of the sky would have a

preferential direction aligned with the N-S shock front. As a result, the polarization fraction of the emission is enhanced and reaches values of ~ 50 %. The fact that the highest polarization is observed in the same northern region where we found a flattening of the spectrum, suggests that in this region the shock wave could be the active acceleration process. Where the emission of the radio galaxy dominates, the fractional polarization is lower, as expected for radio galaxies. This further indicates that the plasma could be a mixture of radio-emitting particles accelerated by the AGN jets and of plasma tracing a shock-wave with highly ordered magnetic fields.

The Faraday depth values of the cluster that we derived from the NAT and the radio relic (i.e., ϕ_{cl} in Fig. 3.13) are in agreement and consistent with zero within the uncertainties. This indicates that in both the sources the Faraday rotation is only caused by the external screen of our Galaxy and thus, in the regions of the cluster where they lie, the ICM has similar properties (i.e. either low thermal electron density and/or low magnetic field).

We can obtain an equipartition estimate of the magnetic field in the region of the E relic (see Sec. 1.3.1). We integrated the synchrotron luminosity between 10 MHz and 10 GHz. Assuming that all the relic volume is occupied by magnetic fields and have a width of 500 kpc along the line of sight, the equipartition magnetic field is estimated to range from 0.9 to 2.7 μG, depending on the k value for the ratio between the energy density of relativistic protons and electrons. The upper bound comes from the assumption of $k = 10^2$, as is usually inferred for the Milky Way (Schlickeiser et al., 2002), while the lower bound is for $k = 1$. A similar electron to proton ratio is implied by our modeling of the W Relic, at variance with standard DSA model (see Sec. 3.5.5). This magnetic field value should be used with caution because it is based on some working and simplified assumptions. Considering our uncertainties on the RM determination, an ordered magnetic field with this strength along the line of sight would have been detected if the electron density was higher than 10^{-5} cm^{-3}.

Overall, our analysis of the spectral index and polarization properties of the NAT and E relic supports the idea that remnants of radio lobes from AGN are strongly related to the origin of radio relics providing a fossil, low-energy (i.e., $\gamma < 10^2$) electron population (Markevitch et al., 2005; Kang & Ryu, 2016). An increasing number of systems where the AGN-relic connection is well supported by observations has been discovered in the past years (e.g. Bonafede et al., 2014; van Weeren et al., 2017). Currently, for the majority of radio relics, this connection is not established and the source of fossil electrons is yet to be discovered. Low-frequency radio observations are fundamental to unveil the remnant electron population and, together with complementary high-frequency observations, to probe if re-acceleration is powered by merger shocks.

3.5.2 Relic-shock connection in the western relic

Our deep JVLA images show intriguing features in the western radio relic, that appear constituted by two arcs in Fig. 3.3. A peculiar morphology is also observed in the X-rays, where a shock front with an unusual "M" shape was reported (Mazzotta et al., 2011). We re-analyzed the archival *XMM-Newton* observations and used our new radio images to study the connection between the shock and the radio relic.

We used `PROFFIT v1.5` (Eckert, Molendi & Paltani, 2011) to extract a number of surface brightness profiles following the "M" shape of the shock. We then decided to focus our analysis in the yellow sector reported in Fig. 3.3 which better highlights the discontinuity and encloses the brightest part of the radio relic. We adopted a broken power-law model to fit the data in such a region, as this model shape is generally used to describe density discontinuities in the ICM such as shocks and cold fronts (e.g. Markevitch & Vikhlinin, 2007). The best-fitting model convolved for the *XMM-Newton* point spread function (see Eckert et al., 2016a, for details) is reported in Fig. 3.15 and appears in good agreement with the data. The surface brightness jump is observed to be co-spatially located with the outer edge of the nose-inner arc of Fig. 3.3 and it would imply a shock with Mach number $M = 1.7^{+0.4}_{-0.2}$ as from the Rankine-Hugoniot density jump conditions. To confirm the shock nature of the edge, we extracted and fitted spectra downstream and upstream the front, obtaining temperatures of $kT_d = 8.2^{+2.3}_{-1.3}$ keV and $kT_u = 3.2^{+2.3}_{-1.2}$ keV, respectively. In this case, the Rankine-Hugoniot temperature jump conditions provide a Mach number of $M = 2.4^{+1.1}_{-0.8}$, consistent with that derived from the surface brightness analysis. The Mach number that we measured is in agreement with the value of 2.1 ± 0.1 reported in Mazzotta et al. (2011).

In Sec. 3.3.2 we measured a spectral index $\alpha^{1.5\mathrm{GHz}}_{3\mathrm{GHz}}$=1.5±0.1 in the region of the nose close to the X-ray detected shock. For the consideration of the previous section this value can be considered as the integrated spectral index of particles which are accelerated via DSA by a shock moving outwards, and than reach the equilibrium with energy losses as in the continuous injection model (Kardashev, 1962). The corresponding Mach number is given by Eq. 3.4 that implies M=2.2±0.2. This value is consistent with the one derived from the X-rays.

The detection of a shock front coincident with a radio relic strongly supports the relic-shock connection and allows to evaluate the efficiency of particle acceleration in cluster outskirts.

The sector chosen for X-ray analysis maximizes the surface brightness jump which bounds the radio emission of the inner arc of the relic and is part of the "M" shape structure observed by Mazzotta et al. (2011). Conversely, the outer arc of the relic lies in front of this feature, which is also located in a region where the X-ray brightness is too low for a proper characterization in surface brightness. The

presence of this feature and of a possible, still undetected, underlying shock supports the idea of a complex merger dynamic.

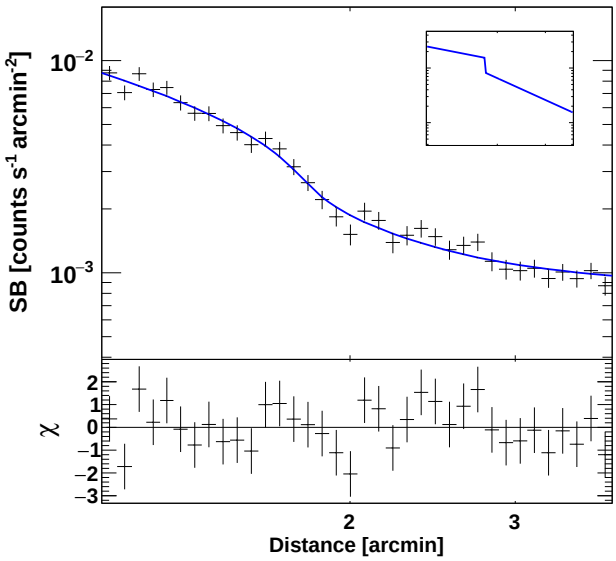

Figure 3.15: *XMM-Newton* surface brightness profile in the $0.5-2.0$ keV band extracted in the yellow sector shown in Fig. 3.3. The best-fitting broken power-law model provides a good description of the data ($\chi^2 = 32$ for 31 d.o.f) and the discontinuity, located at a radial distance of $1.81^{+0.06}_{-0.05}$ arcmin from the centre of the sector, is coincident with the outer edge of the radio emission. The profile is convolved with the *XMM-Newton* point spread function. The inset panel shows the corresponding 3D gas density model.

3.5.3 Particle re-acceleration in the radio halo

The radio halo in RXC J1314.4-2515 is not a classical giant (i.e., $\geq$1 Mpc) radio halo since its extension reaches a maximum of 550 kpc in the W-E direction. Cassano et al. (2007) found a scaling relation between the size of radio halos and their radio power. This relation is motivated in the framework of the re-acceleration scenario in which relativistic electrons are re-energized *in situ* by mechanisms associated with the turbulence originated during cluster merger (see Sec. 1.4.2). Using their relations, we found that, for the halo radio power at 1.4 GHz, listed in Tab. 3.3, the expected halo radius, defined as $\sqrt{R_{\rm min} \times R_{\rm max}}$, $R_{\rm min}$ and $R_{\rm max}$ being the minimum and maximum radii measured on the 3σ radio contours, is 409^{+26}_{-35} kpc. The average radius of the halo in RXC J1314.4-2515 is instead 250 kpc. Hence, this halo is slightly smaller than what would be expected. This is not an observational effect due to missing short baselines since with the JVLA D configuration it is possible to recover emission on a scale of several Mpc at the cluster redshift, if present.

The radio emission permeating the central region of RXC J1314.4-2515 is spatially connected to the W radio relic although they show different spectral index

trend and polarization properties. The halo emission shows a smooth spectral index distribution with an average value of 1.3±0.2 (Fig. 3.7). Instead, the radio relic shows a typical steepening of the spectrum in the downstream region. The spectral index profile of the whole western extended emission (see Fig. 3.9) is similar to the one observed in the Toothbrush radio relic by van Weeren et al. (2016a) and Rajpurohit et al. (2018), with a steepening between the relic and the halo, followed by flattening of the spectrum. This spectral index distribution suggests a link between different mechanisms of particle acceleration. The flattening of the spectral index in the halo region may be due to the re-acceleration of aged electrons previously accelerated by the shock in the W relic. If this is the case, this cluster indicates that the seed electrons necessary for turbulent re-acceleration to work could be supplied by shock waves that also inject turbulence in the cluster core (van Weeren et al., 2016a).

It is well-established that the radio power of giant radio halos scales with the cluster X-ray luminosity, and thus with the cluster mass (e.g. Feretti et al., 2012). The SZ effect (Sec. 1.1.1) has also been used as a proxy of the cluster mass to derive a well-defined scaling relation between the radio power and cluster mass (Cassano et al., 2013). The radio halo hosted in RXC J1314.4-2515 follows this relation. If we consider the halo emission as detached from the relic on the basis of the spectral index profile, the radio halo luminosity at 1.4 GHz is $1.16\pm0.07\cdot10^{24}$ W Hz^{-1} (see Tab. 3.3) while the one expected from the correlation is $2.2^{+0.7}_{-0.5}\cdot10^{24}$ W Hz^{-1}. Despite its small size, the radio power originating from this radio halo is in agreement within the 3σ confidence level of the correlation.

3.5.4 Projection effects and polarization

Although projection effects are expected to be minimal in double relic clusters, they are probably playing a role in the observed properties of this system. Golovich et al. (2019b) derived that RXC J1314.4-2515 has a large line of sight velocity difference between the merging clusters, which they found is atypical for double relic systems. The viewing angle of the merger θ (i.e. the angle between the line of sight and the merger axis) was constrained by means of a comparison with simulated cluster by Wittman, Cornell & Nguyen (2018). They found that $\theta > 37°$ within the 68 % confidence interval.

In the absence of optical observations, polarization data can also be used to get an independent constraint on the merger axis. Ensslin et al. (1998) developed a simplified relation which links the observed average polarization of a radio relic with its viewing angle, given its integrated spectral index. This relation is derived under a number of assumptions and it does not take into account the effects due to beam and Faraday depolarization. In spite of this, it could be used to derive a lower limit on the viewing angle (e.g. Hoang et al., 2018).

Referring to the S-band measurements, in the northern part of the E relic the average polarization fraction is 41±6 % and $\alpha_{3\mathrm{GHz}}^{1.5\mathrm{GHz}} = 1.2 \pm 0.2$. This implies a viewing angle of $\sim 62°$. For the W relic we considered only the northern arc, since the southern nose of the shock is experiencing stronger internal Faraday depolarization as discussed in Sec. 3.5.6. The arc is polarized on average at 31±3 % and we can use a spectral index of $\alpha_{3\mathrm{GHz}}^{1.5\mathrm{GHz}}$ =1.5±0.1 as derived at the edge of the relic: the viewing angle is therefore ∼55°. A value of around 60° can thus be considered as a lower limit for the viewing angle of the merger.

With the fractional polarization value of relics we can also derive the Mach number of the underlying shock as done in Kierdorf et al. (2017). Here the polarization is derived for relics seen perfectly edge-on assuming a weak upstream magnetic field that is tangled and compressed on small scales at the shock front. Under these assumptions, a fractional polarization of 41±6 % corresponds to a Mach number of ∼1.7 for the E relic while for a fractional polarization of 31±3 %, as in the W relic arc, M ∼1.4. These values are both lower than the Mach numbers that we estimated from the spectral index and X-ray analysis. This supports the idea that projection effects may lower the observed fractional polarization of the relics.

3.5.5 Comparison with a simulated radio relic

In the following, we compare our results with mock X-ray and radio images of a simulated radio relic. The 3D cubes of simulated quantities can be integrated along different directions, changing the angle θ and obtaining projected images of the simulated cluster at different viewing angles. This comparison allows us to: *(i)* check if the values of RM obtained in the simulation can be compared to the observed ones, with the aim of deriving a rough estimate of the magnetic field in the region of the diffuse radio emission and to constrain the electron acceleration efficiency at the shock *(ii)* test the viewing angle using realistic geometrical conditions and introducing the effects of beam depolarization and Faraday rotation, both external and internal (see Sec. 2.1.3).

We used a high-resolution cosmological MHD simulation of a galaxy cluster produced with the adaptive mesh refinement code ENZO (Bryan et al., 2014), as in Vazza et al. (2018). The cluster has a virial mass of $M_{100} \approx 1.3 \cdot 10^{15} M_{\odot}$ at $z = 0.05$. The maximum spatial resolution in the simulation is 3.95 kpc/cell. However, in the region where a simulated radio relic is used for a comparison with our observations the effective resolution is 7.9 kpc/cell.

At the beginning of the simulation ($z = 30$), we assumed a uniform magnetic field value $B_0 = 0.1$ nG along each coordinate axis, which mimics a primordial magnetic field and is below the upper limits from the analysis of the CMB (e.g. Subramanian, 2016). The field is then amplified in the course of the cluster formation process,

both due to gas compression (for $z > 1$) and small-scale dynamo (for $z \leq 1$) and finally reaches a typical magnetic field strength of $\sim 2 - 5$ μG in the cluster core, and of $\sim 0.1 - 0.3$ μG at the cluster virial radius, showing a tangled 3D magnetic field with a typical scale of ~ 50 kpc (see Domínguez-Fernández et al. 2019 for more details on the simulation).

We followed an approach similar to (Wittor et al., 2019) to compute the polarized emission of the simulated radio relic. Therefore, we used a velocity jump method as in Vazza, Brunetti & Gheller (2009b) to detect and flag shock waves in the simulation and for each flagged cell, we computed the integrated polarized emission following the model by Burn (1966, Eq. 1). We follow the formalism of Hoeft & Brüggen (2007, Eq. 29) to compute the downstream radio profile of an electron population injected at the shock via DSA and that cools via synchrotron and IC. We evaluated the profile at nodes on the simulation grid along the shock normal. For the frequency range probed in this work, the electron cooling length is of a few kpc and hence most profiles are computed within one simulation cell. Therefore, we assume a homogeneous magnetic field and downstream temperature for each profile. Analogous, we compute the downstream profiles of the perpendicular and parallel component of the radio emission, that determine the intrinsic degree of polarization (Eq. 2.2).

In order to match the observed radio power of RXC J1314.4-2515 the acceleration efficiency by Hoeft & Brüggen (2007) is not enough for this weak shock. Following Vazza et al. (2015), we included also the effect of re-accelerated particles by shocks, which is expected to dominate over the contribution from freshly injected particles for $\mathcal{M} \leq 3$ shocks (e.g. Pinzke, Oh & Pfrommer, 2013). We include both internal and external Faraday rotation, directly using the three-dimensional magnetic field from the simulation.

We selected a galaxy cluster (SIM for short) in a post-merger state at redshift 0.05. We found that the 2D projection of this cluster at a viewing angle of 70° matches the observed properties: *(i)* the selected cluster shows a shock front in the X-rays, with an "M" shaped morphology, similar to the one detected in RXC J1314.4-2515, *(ii)* a radio relic ∼900 kpc long traces the shock front at a distance of ∼500 kpc from the X-ray centroid, with a region of the relic lying beyond the bulk of the shock, where the X-ray luminosity decreases, *(iii)* the average Mach number at the shock is similar to the one detected in RXC J1314.4-2515. The main characteristics of the simulated cluster are listed in Tab. 3.5, with the same quantities estimated for RXC J1314.4-2515 for comparison. The 2D projected gas density and maximum magnetic field strength along each line of sight are shown in Fig. 3.16. The simulated magnetic field shows filament and complex substructures. The average width of magnetic field filaments in Faraday space is few tens rad m^{-2} thus they cannot be resolved at the maximum resolution in Faraday space that we reach combining L-

Table 3.5: Quantities of interest in the comparison between the observed RXC J1314.4-2515 (RX1314) and the simulated cluster (SIM). Column 1: cluster name; Column 2: radio power at 3 GHz. The flux density was extracted from a region of the same physical size (i.e., $\sim 1.5 \cdot 10^5$ kpc^2) in both clusters; Column 3: the X-ray luminosity of RXC J1314.4-2515 from Piffaretti et al. (2011) (given without uncertainties) was used to compute the luminosity of RXC J1314.4-2515 in the range 0.5-2 keV using WebPIMMS (https://heasarc.gsfc.nasa.gov/cgi-bin/Tools/w3pimms/w3pimms.pl). The luminosity of SIM was computed as the sum in the whole cube; Column 4: thermal electron density at the shock front. From the density profile derived in Mazzotta et al. (2011) we listed the post-shock electron density with an uncertainty derived from their profile. For SIM we computed an average value in the post-shock region and we used the standard deviation as uncertainty. Column 5: Mach number of the shock. We list the value derived in Sec. 3.5.2 for RXC J1314.4-2515. For SIM, we computed an average value in the cells within the shock region where $M>2$, and we used the standard deviation of the distribution as uncertainty.

Cluster	P_{3GHz} (10^{23} WHz^{-1})	L_X (10^{44}ergs^{-1})	n_e (10^{-3}cm^{-3})	M
RX1314	11.5±0.6	8.91	0.7±0.05	$1.7^{+0.4}_{-0.2}$
SIM	11.1±0.4	5.65	3.7±0.9	2.2±0.2

and S- band data.

By comparing the simulated radio power from the relic at 3 GHz to the observed one of RXC J1314.4-2515, we find that an electron acceleration efficiency of $\xi_e \geq 1000\%$ (referred to the kinetic energy flux of shocked cells) is needed, meaning that the kinetic energy of this shock would not be enough to explain our 3 GHz observation of RXC J1314.4-2515. This value obviously requires something beyond the standard DSA, and as argued in other works, it can be attained only if a pre-existing population of fossil electrons (with $\gamma = 10^2 - 10^3$) was present upstream of the merger shock which produced the western radio relic in RXC J1314.4-2515 (Markevitch et al., 2005; Pinzke, Oh & Pfrommer, 2013; Kang & Ryu, 2015; Botteon et al., 2016a; Eckert et al., 2016b). Our modeling suggests that this is reasonable, provided that the injection of fossil electrons happened no longer than $\sim$ 1Gyr before the $M \approx 2$ shock crosses the region where the western radio relic is now visible.

The origin of such fossil population is not clear as it could be for the E relic. It could originate from an AGN that is no longer active or from previous shocks or turbulence generated in the cluster formation process. Considering that the typical time scale for turbulent acceleration larger than 1 Gyr on scales of 500 kpc (Brunetti & Jones, 2014) the observed radio halo cannot have supplied already aged electron in the region where the W relic is observed. Fossil electrons have $\gamma = 10^2 - 10^3$ and to detect them and discover their origin we would need low frequency observation in the MHz regime.

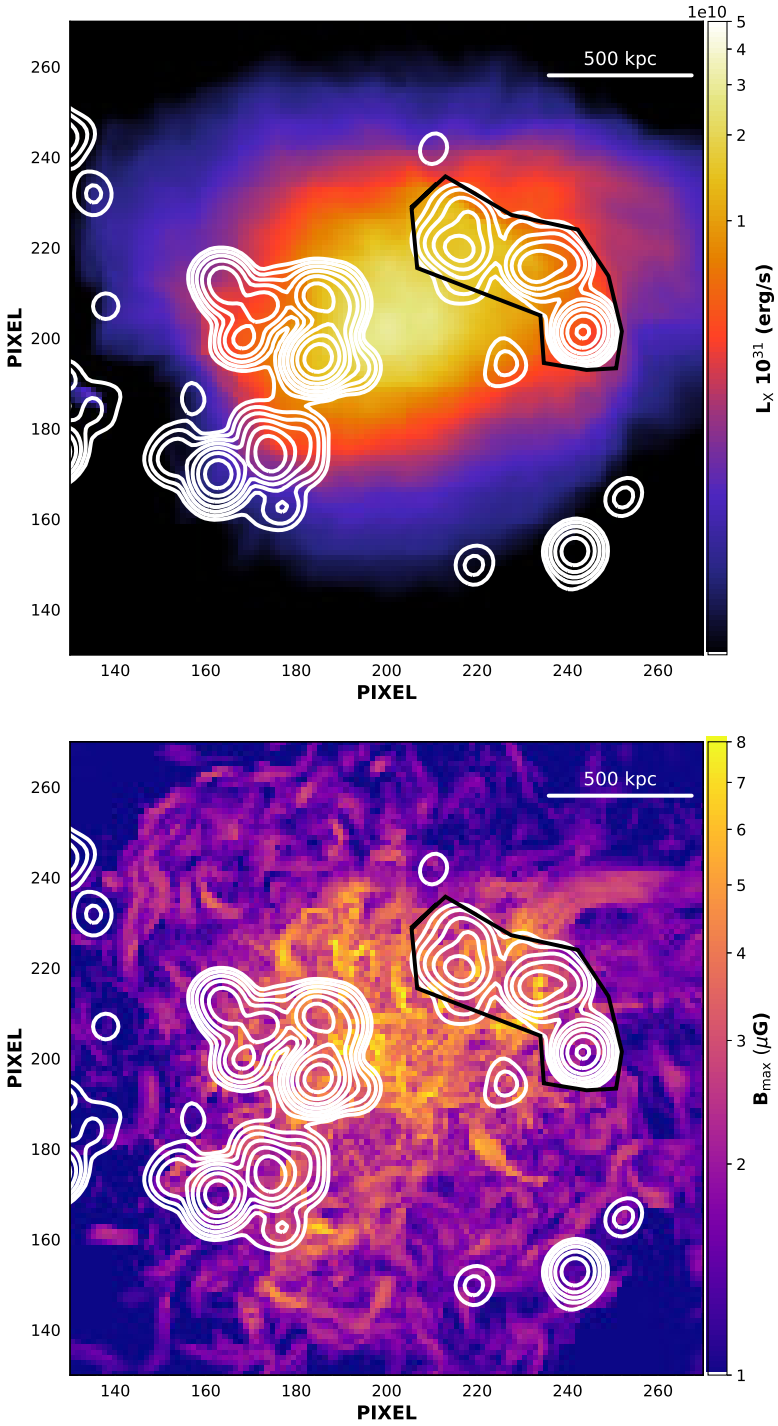

Figure 3.16: Top panel: X-ray luminosity map of the simulated cluster (SIM), with 3 GHz radio contours overlaid. Contours start at $1.8 \cdot 10^{20}$ W Hz^{-1} and are spaced by a factor of two. The viewing angle is 70°. The resolution of the image is the same of the simulation (i.e., 15.8 kpc per pixel) while the radio power image was smoothed with a Gaussian kernel of ∼80 kpc. Bottom panel: maximum magnetic field along each line of sight (pixel) of the 3D simulated cluster for a 70° viewing angle. Radio contours are the same as in the top panel. In both panels the black region is the one used to extract the relic radio power.

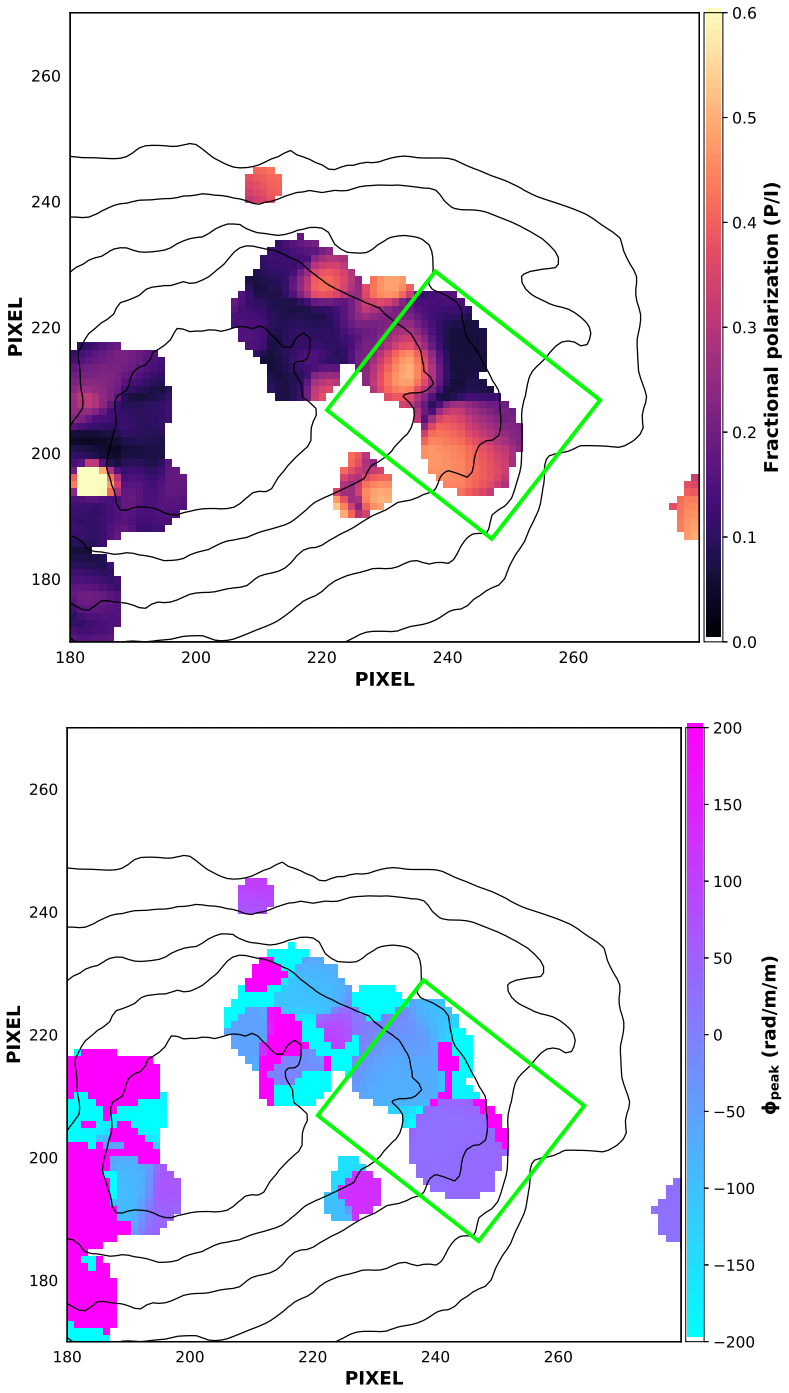

Figure 3.17: Top panel: Fractional polarization (top panel) and Faraday depth (bottom panel) of the radio diffuse emission in SIM in the 2-4 GHz band. A threshold is imposed to have the same total intensity dynamical range of our observation in the region of the relic. Black contours are from the X-ray luminosity image in the energy band 0.5-2 keV: they start at 10^{40} erg/s and they are spaced by a factor of two. The green box shows the region where we extracted the average fractional polarization and $|\phi_{\rm peak}|$ values

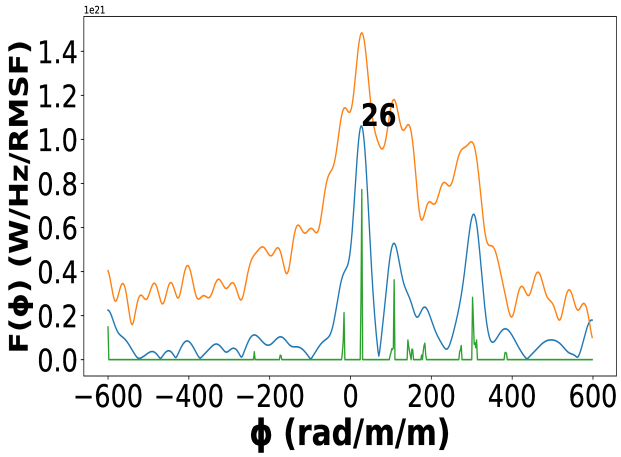

Figure 3.18: Same image as the bottom-right panel of Fig. 3.14 but for the simulated radio relic.

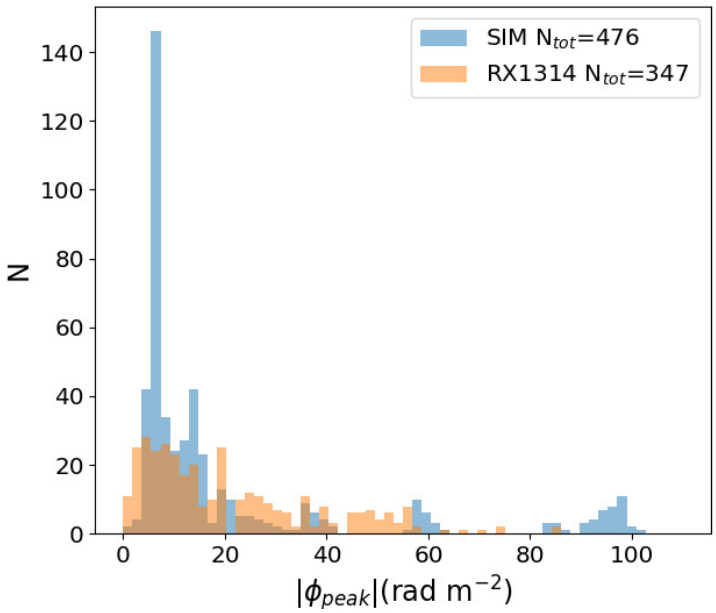

Figure 3.19: Distribution of Faraday depths. The $|\phi_{\rm peak}|$ values of the simulation were reduced by a factor 5 to be compared with the observation, due to the different thermal electron density. For the observation (RX1314), the values are obtained in the northern region of the W relic arc in the S-band measurement. For the simulation (SIM) the values are extracted in the region marked with the green box in Fig. 3.17.

Since the average synchrotron power of a relativistic electron population is $\langle P_S \rangle \propto \gamma^2 B^2$ (if $B \leq 3.2\ \mu G\ (1+z)^2$ as in our case here), in principle either a higher magnetic field, or a larger acceleration efficiency (and/or a higher density of seed fossil

electrons) are needed to match the observation. However, as we shall see, the polarization properties of the west relic can be used to constrain the magnetic field amplitude, which in turn sets a lower limit on the amount of necessary particle re-acceleration (or higher efficiency).

We performed RM synthesis on the simulated data. We obtained Stokes I, Q and U 2D projections in the same frequency range and sub-bands of our measurements in the S-band. We smoothed all images with a Gaussian kernel of the physical size of the restoring beam of the S-band image (i.e., FWHM ∼80 kpc). With the same procedure described in Sec. 3.4.2 we obtained images of $\phi_{\rm peak}$ and $P = |\widetilde{F}(\phi_{\rm peak})|$ and we obtained the linear degree of polarization map by dividing the polarization and total intensity smoothed images. Fractional polarization and $\phi_{\rm peak}$ images for the 2D projection at θ=70° are shown in Fig. 3.17. In all the images we imposed a threshold in order to obtain the same dynamical range of our observations in total intensity.

Also from the simulation we obtained Faraday-complex spectra in some regions of the relic. In order to produce a high resolution Faraday spectrum of the simulated relic, we also performed the RM synthesis on the simulated data between 1 and 4 GHz reaching a resolution of 37 rad m^{-2} as in the S+L-band measurement. The high resolution spectrum of a representative pixel is shown in Fig. 3.18. The Faraday spectrum is shown together with the clean components found during the RM clean procedure and the final cleaned Faraday spectrum. Several filaments are clearly separated after the RM clean. The filaments in the simulation appear to be spread over $\sim$ 300 rad m^{-2} in Faraday depth and they have different luminosity.

We can use as a benchmark the average fractional polarization and the distribution of $\phi_{\rm peak}$ values in the most external region of the relic, marked with the green box in Fig. 3.17. We chose a region where we obtained Faraday-simple spectra in the S-band as in the northern arc of the W relic of RXC J1314.4-2515, thus we can more easily compare the results of the RM synthesis. The average fractional polarization for $\theta \sim 70°$ in the smoothed image is 32 % and it is consistent with what we obtained from the observation at the same physical resolution (i.e., 31 ± 3 % in the western relic). This value takes into account the depolarization due to the smoothing of the polarization vectors on physical scales between 15 and 80 kpc since the simulated magnetic field has important sub-structure on such scales.

In SIM, we found higher values of $\phi_{\rm peak}$ compared to the $\phi_{\rm cl}$ values obtained in RXC J1314.4-2515 in the S-band, but the thermal electron density in the region of the shock is on average ∼5 times lower in RXC J1314.4-2515 than in SIM (see Tab. 3.5). To make a fair comparison on the effect of the magnetic field on the Faraday rotation in the two clusters, we compare in Figure 3.19 the distribution of Faraday depths obtained in the simulation reduced by a factor of 5 with the observed one (foreground subtracted). The average and median values of the two

distributions are consistent within the uncertainties. At the cluster's redshift the Faraday depth values are a factor 1.6 higher but the two distributions are still compatible. This indicates that the magnetic field in the relic region in RXC J1314.4-2515 is already of the order of the simulated one (i.e., $\sim 1\mu$G), and hence that only a higher (re)acceleration efficiency can explain the power radio emission from the W relic. We notice that while the role of re-accelerated fossil electrons has been already proposed as key ingredient to explain observed radio relics (e.g, Pinzke, Oh & Pfrommer, 2013; Kang & Ryu, 2015, 2016), this is the first time in which we can constrain its importance by simultaneously fixing the uncertainties on the magnetic field in the relic region, thanks to polarization data and simulations.

In spite of similar median values, the two distributions in Fig. 3.19 are very different. For this comparison we used the peak values of S-band spectra in the green region of Fig. 3.17, where Faraday spectra are not resolved and show a single component. The simulated distribution is thus dominated by the emission of the brightest filament at a certain Faraday depth and the narrower distribution compared to the data is due to the fact that the same filament dominates in the sampled spatial region. The broader distribution of RM values found in the northern arc of the radio relic shows that various emitting structures at different Faraday depths are co-spatially located in a region equivalent to the one considered in the simulation.

3.5.6 Faraday-complex emission

As reported in Sec. 3.4.2, we observed Faraday-complex emission in the nose of the W relic. This means that linearly polarized emission originates from different layers of the radio relic which experienced different amounts of Faraday rotation. Faraday complex structures were observed also in the Toothbrush radio relic (van Weeren et al., 2012b). In this region, we observed features in the Faraday dispersion functions spread over a range of 150-250 rad m^{-2}.

As an example, in Fig. 3.14, the S- and S+L-band Faraday dispersion function (i.e. Faraday spectrum) is shown for two pixels. The first row shows a Faraday-simple source (i.e., a pixel at the position of the source labelled with C in Fig. 3.2), the second row a Faraday-complex one (i.e., a pixel in the nose region).

The RM clean found a single component in the spectrum of the Faraday-simple source, both with the S- and S+L-band resolution. In the S-band, the Faraday-complex pixel is observed as a single peak but with a FWHM slightly larger than the RMSF resolution (i.e., $\delta\phi$ =188 rad m^{-2}): some cleaned components are found, within a range of 200 rad m^{-2}. Instead, in the S+L-band measurement, where we have higher resolution in Faraday space, the RM clean on the Faraday-complex spectrum found several components, with a similar flux density, and a width of 150 rad m^{-2}.

The shape of a complex Faraday spectrum is indicative of the medium generating the emission. A single broad feature in the Faraday-spectrum originates from a regular distribution of magnetic fields and thermal electron density while a series of peaks are expected if filamentary magnetic fields structures are overlaid along the same line of sight. In both cases the Faraday rotation occurs in the emitting region. Our simulation suggested that we should expect a series of peaks in our case since the magnetic fields has filamentary structures with a width in Faraday space lower than 40 rad m^{-2} (see Fig. 3.16 and Fig. 3.18).

On the basis of the spectrum shown in the bottom right panel of Fig. 3.14 it is hard to distinguish between a single broad feature or a convolution of several Faraday-simple spectra originating from different filaments (see also Sec. 2.2.2). For this reason we also studied the wavelength dependence of the degree of polarization. If filamentary and complex structures of magnetic field originate the complex Faraday spectrum, internal Faraday depolarization is expected (see Arshakian & Beck, 2011, and also Sec. 2.1.3). The dispersion of RM values that we detected in our unresolved structures should be the same as the turbulent dispersion causing the depolarization, $\sigma_{\rm RM}$.

We imaged the Q and U data cubes between 1 and 4 GHz into 20 frequency sub-bands of 150 MHz each and we smoothed the data to 30″resolution to increase the signal-to-noise ratio. We calculated the fractional polarization of each sub-bands separately. The depolarization trend computed in the region of the nose, marked with a green circle in the top panel of Fig. 3.12, is shown in Fig. 3.20. We fitted both internal and external Faraday depolarization as modeled in Arshakian & Beck (2011). Both depend on RM dispersion, $\sigma_{\rm RM}$, and wavelength (Eq. 2.13 and 2.14). Internal Faraday depolarization well represents our data with a $\sigma_{\rm RM}$ of 94±7 rad m^{-2}. This shows that the depolarization is occurring in the same emitting volume. We note that the dispersion value is of the same order of magnitude of the range of Faraday depths that we detected with the RM synthesis. Several magnetic field filaments along the line of sight in a turbulent ionized gas are likely the origin of the Faraday-complex structures and of depolarization in the nose region.

We studied the depolarization trend also in the northern region of the E relic, marked with the green circle in the upper panel of Fig. 3.12. In this case, the RM dispersion for internal and external Faraday depolarization are 12±2 rad m^{-2} and 7±1 rad m^{-2}, respectively, and the reduced χ^2 is 1.2 for both. Under the simplified assumption that the magnetic field is the same at the position of the two relics, the ratio of $\sigma_{\rm RM}$ is equal to the ratio of the thermal electron densities along the line of sight (from Eq. 2.10). This would imply that the thermal electron density in the region of the E relic is 0.13 ± 0.02 or 0.16 ± 0.02 times lower than in the W relic region, considering only internal or external depolarization, respectively. Overall this is in agreement with the upper limit from the X-rays and with the estimate

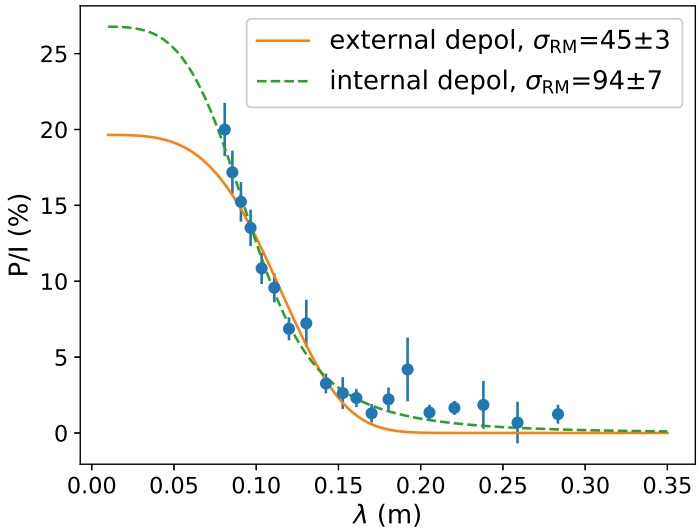

Figure 3.20: Depolarization profile of the nose of the western relic. Fractional polarization was computed in each sub-band separately. Green dashed line is the fitted internal depolarization model while the orange line is the external depolarization model.

made in Sec. 3.5.1. Anyway, simulations probed that every shock has a peculiar and complex morphology that does not allow a simplified and general description (Hoeft et al., 2011).

When the Faraday spectrum is unresolved, the peak value of the spectrum represents the total polarized flux density of the source in Jy/beam, integrated along the Faraday spectrum. Conversely, in the case of a resolved Faraday-complex emission, the peak value represents only the main component of the spectrum, and it is a fraction of the total emission of the source. As a result, the polarized flux density of Faraday-complex structures estimated from the main peak is lower than the integrated one, and the fractional polarization that we compute with the RM synthesis should be regarded as a lower limit.

For the purpose of this work, we decided to use the information that we obtained directly from the RM synthesis technique as it is implemented in `pyrmsynth`. In the pixels where we observed a Faraday-complex spectrum, we considered as integrated polarization that one obtained from the peak of the S-band data, where the broad feature is only partially resolved. In this way, we have the best possible estimate for the polarized flux density. Instead, we used S+L-band data to recover the RM value of the brightest component ($\phi_{\rm peak}$) with higher precision. This value should be used with caution for Faraday-complex spectra.

3.6 Conclusions

In this work, we performed a detailed study of the radio emission of the merging galaxy cluster RXC J1314.4-2515 in the frequency range 1-4 GHz. We exploited a variety of JVLA observations: full polarization A, B, C and D configurations between 1 and 2 GHz (L-band) and DnC configuration archival data in the 2-4 GHz S-band. We performed both spectral analysis and RM synthesis on the entire cluster field, and in particular on two radio relics and the central radio halo. This study allows us to investigate possible scenarios for the origin of the extended radio emission observed in RXC J1314.4-2515.

Our results can be summarized as follow:

1. New multi-configurations JVLA data offer unprecedented view of RXC J1314.4-2515 at 1.5 GHz. We detected the two relics and the central radio halo. The western relic shows interesting substructures: two arcs depart from the X-ray detected shock, one of the two being ∼900 kpc long and extending toward the outer region of the cluster. The eastern relic embeds a NAT radio galaxy, member of the cluster.

2. This study revealed a possible connection between the AGN activity and the extended emission of the E radio relic. The spectral index profile supports a re-acceleration scenario in which a seed population of mildly relativistic particles, pre-accelerated by AGN jets, are subsequently re-accelerated by merger driven shock waves. Polarization properties of the entire eastern system suggest that the shock waves were able to align the magnetic field lines along the shock plane, but we did not find Faraday rotation caused by the cluster magnetic field in this region. Only very deep X-ray observations could proof the presence of a shock underlying the eastern radio relic.

3. Spectral index profiles and polarization properties, allowed us to disentangle the contributions of the relic and the halo to the western diffuse emission. The relic shows a typical spectral steepening downstream of the X-ray detected shock, while a different acceleration process should be able to re-energize particles in the radio halo region. The polarization properties support this scenario: only the radio relic is detected in polarized intensity at 3 GHz.

4. We discovered Faraday-complex emission in the northern region of the W relic. This indicates the presence of thermal gas and complex magnetic field morphology within the relic volume. The fractional polarization in the region is low (i.e., on average 8.5 ± 0.6 % at 3 GHz) due to internal Faraday depolarization. We obtained very different RM dispersion from the depolarization trend of the two relics. However, deriving constraints on underlying magnetic field would require a more detailed knowledge of the gas thermal density, projection effects, and shock-wave morphology.

5. We studied the X-ray shock coincident with the inner arc of the western radio

relic. We derived a Mach number consistent with that found by Mazzotta et al. (2011) (i.e., $M = 1.7^{+0.4}_{-0.2}$ from the X-ray surface brightness jump and $M = 2.4^{+1.1}_{-0.8}$ from the temperature jump). The Mach number derived from the radio spectral index assuming DSA mechanism is consistent with the one derived from the X-ray analysis.

6. We made a detailed comparison of the total intensity and polarization properties of the W relic with a radio relic generated within a cosmological simulation. Considering the polarization properties of simulated radio relics is fundamental to disentangle the contributions of relativistic electrons and magnetic fields to the total radio power. We tested a possible viewing angle of $\sim 70°$. The consistency check pointed out that the simulation is able to reproduce the observed fractional polarization and the RM of the western relic with a magnetic field of $\sim 1\mu$G in the relic region and important sub-structures on scales between 15 and 80 kpc. The required electron acceleration efficiency to match the observed radio power provides the need of significant re-acceleration of fossil electrons.

In the future, to resolve and interpret Faraday-complex structures, we could exploit the SKA-MID[††], which will reach a resolution in Faraday space of ~ 5 rad m^{-2}, spanning the frequency range between 350 MHz and 14 GHz. A deeper understanding of the physical interpretation of such structures should be also reached thanks to the comparison with simulation (Loi et al., 2018). The combination of radio polarimetric studies, high-resolution spectral index imaging, total intensity radio observation at 50-350 MHz and deep X-ray observations of merger shocks, promises to shed new light on particle acceleration processes occurring in the ICM, on the role played by the fossil plasma and on the properties of the magnetic field at merger shocks.

[††]https://www.skatelescope.org/

Chapter 4

The intra-cluster magnetic field in the Abell 2345 galaxy cluster *

Magnetic fields are ubiquitous in galaxy clusters but their radial profile, power spectrum and connection to cluster properties are poorly known. Merging galaxy clusters hosting diffuse polarized emission in the form of radio relics offer a unique possibility to study the magnetic fields in these complex systems.

Here, we study the magnetic field in the merging galaxy cluster Abell 2345 using JVLA observations in the 1-2 GHz band, *XMM-Newton* observations, and numerical simulations of the cluster magnetic field. Abell 2345 is highly disturbed and hosts two radio relics. The aim of this work is to constrain the magnetic field profile in the cluster, up to the peripheral regions where the relics are located. Using recent results from MHD cosmological simulations, we produce mock RM images and compare them with observed RM data. This work improves our understanding on how the RMs derived from relics can be used in order to derive general information on the magnetic fields in the cluster, as well as to constrain the magnetic fields at the relics and its amplification.

Throughout this Chapter, we assume a ΛCDM cosmological model, with $H_0 = 69.6$ km s^{-1} Mpc^{-1}, $\Omega_M = 0.286$, $\Omega_\Lambda = 0.714$ (Bennett et al., 2014). With this cosmology 1″ corresponds to 3.043 kpc at the cluster redshift, z=0.1789.

*Based on Stuardi et al. (2021)

4.1 The double relic galaxy cluster Abell 2345

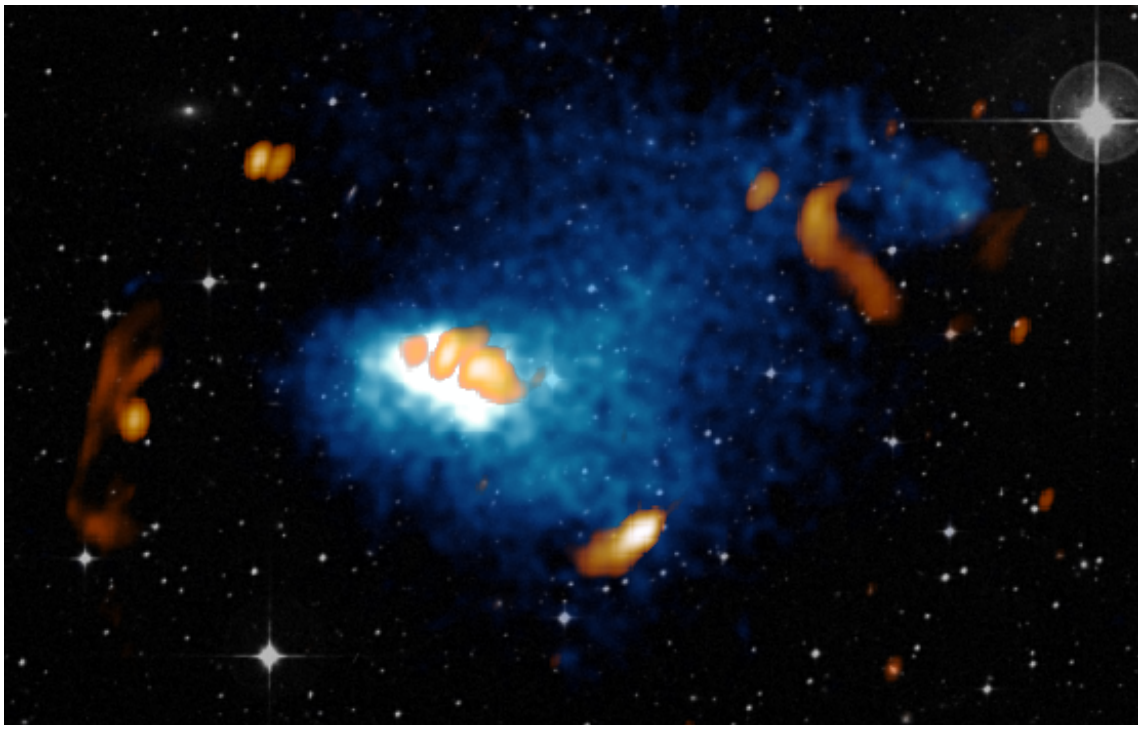

Figure 4.1: Second Digitized Sky Survey (DSS2) optical image of the A2345 cluster (gray-scale) overlaid onto X-ray emission from *XMM-Newton* in the 0.3-2 keV band (point-source subtracted, in blue) and radio JVLA emission at 1.5 GHz (orange). The image has illustrative purposes only.

Abell 2345 (A2345, z=0.1789, Boschin, Barrena & Girardi 2010) is a rich galaxy cluster, cataloged as one of the brightest X-ray clusters within the ROentgen SATellite (ROSAT) All Sky Survey (Ebeling et al., 1996). An illustrative image of A2345 is shown in Fig. 4.2 while the main properties of this cluster are listed in Tab. 4.1.

A detailed X-ray study of A2345 is still missing, but several authors pointed out its disturbed morphology as shown by ROSAT, *Chandra* and *XMM-Newton* observations (e.g., Lovisari et al., 2017; Golovich et al., 2019a). Rossetti et al. (2016) found a significant offset of $\sim$ 200 kpc between the X-ray peak of A2345 and its BCG (at the J2000 coordinates: $21^{\rm h}27^{\rm m}13^{\rm s}.7$, -12°09′47″), confirming a highly disturbed X-ray morphology.

The presence of diffuse radio emission in the A2345 cluster was discovered by Giovannini, Tordi & Feretti (1999). Using images of the National Radio Astronomy Observatory (NRAO) VLA Sky Survey (NVSS), two candidate radio relics were observed in the outskirts of this cluster, on opposite sides with respect to the cluster center: to the east (E relic) and to the west (W relic). A detailed radio analysis of this cluster, including spectral index and polarization analysis, was performed by

Table 4.1: Properties of A2345. Row 1,2: J2000 celestial coordinates of the X-ray cluster peak; Row 3: redshift; Row 4: X-ray luminosity in the energy band 0.1-2.4 keV; Row 5: estimate of the hydrostatic mass from Sunyaev-Zeldovich effect observation. References: (1) This work, (2) Boschin, Barrena & Girardi (2010), (3) Lovisari et al. (2020), (4) Planck Collaboration et al. (2016b).

R.A. (J2000)	$21^{h}27^{m}12^{s}.6$	(1)
Dec. (J2000)	-12°09′46″	(1)
z	0.1789	(2)
$L_{X[0.1-2.4keV]}$	2.91×10^{44} erg s^{-1}	(3)
M_{500}^{SZ}	$5.91\times10^{14}M_{\odot}$	(4)

Bonafede et al. (2009b). The authors used VLA observations at 325 MHz and 1.4 GHz. The W relic revealed a peculiar morphology with a faint filamentary structure extending toward the cluster outskirts. The spectral index image of this radio relic shows a steepening toward the cluster outskirts, opposite to other radio relics, which steepen toward the cluster center (see Sec. 1.4.1). Together with the comparison with the ROSAT image, this observation suggested that the W relic was produced by a complex merger between different sub-groups. The E relic instead, elongated along the north-south direction, can be more easily explained by a major merger along the main E-W axis. At 1.4 GHz and at the resolution of $23'' \times 16''$ the authors found a mean fractional polarization of the E relic of ~ 22 %, reaching values up to 50 % in the eastern region. The W relic instead shows a mean fractional polarization of ~ 14 %, with regions of higher fractional polarization (~ 60 %) in the northwestern part of the relic. Bonafede et al. (2009b) also estimated the equipartition magnetic field in the W and E relic to be 1.0 and 0.8 μG, respectively. Recently, George et al. (2017) computed the integrated spectral indices of the two relics between 118 MHz and 1.4 GHz, obtaining values consistent with the work of Bonafede et al. (2009b): $\alpha = 1.29\pm0.07$ for the E relic and $\alpha = 1.52\pm0.08$ for the W relic.

Several weak lensing analyses were performed on this cluster. A small field-of-view, centered on the main eastern sub-cluster of A2345, was analyzed by Dahle et al. (2002). Although they noticed numerous substructures in the ROSAT image, suggestive of a dynamically disturbed system, the weak lensing analysis resulted in a density distribution peaked roughly around the BCG. These results were confirmed by a subsequent study by Cypriano et al. (2004), where the galaxy cluster was fitted by an isothermal ellipsoid, with the main axis oriented along the E-W direction. A weak lensing study on a larger field-of-view, comprising the entire cluster up to the virial radius, found instead numerous substructures for which it was classified as complex (Okabe et al., 2010). In this latter study, a spherically symmetric morphology was discarded.

Boschin, Barrena & Girardi (2010) performed an extensive optical study of the

A2345 cluster to unveil its internal dynamics. The presence of three clumps (E, NW and SW) emerged from this analysis, with the E one being the more massive component and coincident with the mass peak recovered by the weak lensing analysis. The authors suggested a complex merger history: a major merger along the E-W direction with a component along the line-of-sight gave origin to the E relic, while a minor merger along the N-S direction and parallel to the plane of the sky could be at the origin of the peculiar shape of the W relic. More recently, Golovich et al. (2019a,b) repeated a similar study confirming the results of Boschin, Barrena & Girardi (2010).

4.2 Data analysis

4.2.1 Calibration and total intensity imaging

A2345 has been observed with the JVLA in the L-band (1.008-2.032 GHz) B- and C-configurations. The bandwidth covers 1024 MHz, subdivided into 16 spectral windows of 64 MHz each (with 64 channels of 1 MHz frequency resolution). The observations have been performed with full polarization products. Central frequency, observing date and time of radio observations are listed in Tab. 4.2.

We used the `CASA 5.6.2`[†] package for the data reduction and total intensity imaging processes. Data were pre-processed by the VLA `CASA` calibration pipeline, that performs flagging and calibration procedures which are optimized for Stokes I continuum data. Then, we derived final delay, bandpass, gain/phase, leakage, and polarization angle calibrations. The sources used for the bandpass, absolute flux density, and polarization angle calibrations were 3C 286 and 3C 138. We used the Perley & Butler (2013) flux density scale for wide-band observations. We followed the NRAO polarimetry guide for polarization calibration[‡]: a polynomial fit to the values of linear polarization fraction and polarization angle of 3C 286 and 3C 138 was used as frequency-dependent polarization model. The source J2131-1207 was used as phase calibrator for all the observations. The unpolarized sources J1407+2827 and 3C 147 were used as instrumental leakage calibrators. The calibration tables were finally applied to the target.

Radio frequency interference (RFI) was removed manually and using statistical flagging algorithms also from the cross-correlation products. Some spectral windows were entirely removed: those centered at 1.168, 1.232 and 1.552 GHz (i.e, spectral windows 2, 3, and 8) in B-configuration observations, and those centered at 1.232, 1.552 and 1.616 GHz (i.e., spectral windows 3, 8 and 9) in C-configuration. After RFI removal, we averaged the data sets in time down to 6 s and in frequency with

[†] https://casa.nrao.edu/
[‡] https://science.nrao.edu/facilities/vla/docs/manuals/obsguide/modes/pol

Table 4.2: Details of radio observations. Column 1: central observing frequency; Column 2: array configuration; Column 3: date of the observation; Column 4: total on-source observing time; Column 5: Full Width Half Maximum (FWHM) of the major and minor axes of the restoring beam of the final total intensity image obtained with `robust`=0.5; Column 6: 1σ rms noise of the total intensity image; Column 7: reference to the figures in this Chapter.

Freq. (GHz)	Array Conf.	Obs. Date	Obs. Time (hr)	Beam	σ (mJy/beam)	Fig.
1.5	B	2017 Nov. & Dec.	4.0	$3.3''\times4.8''$	0.015	Fig. 4.3, 4.4, 4.5
1.5	C	2017 Jun.	1.5	$11''\times18''$	0.07	Fig. 4.2, 4.4, 4.5

channels of 4 MHz, in order to speed up the imaging and self-calibration processes. We computed new visibility weights according to their scatter.

Data have been imaged using the multi-scale multi-frequency de-convolution algorithm of the `CASA` task `tclean` (Rau & Cornwell, 2011) for wide-band synthesis-imaging. As a first step, we made a large image of the entire field ($\sim 1^\circ \times 1^\circ$). We used a three Taylor expansion (`nterms` = 3) in order to take into account both the source spectral index and the primary beam response at large distances from the pointing center. We also used the w-projection algorithm to correct for the wide-field non-coplanar baseline effect (Cornwell, Golap & Bhatnagar, 2008). We set 128 and 64 w-projection planes for the B- and C-configuration data set, respectively. At this first stage, we used the uniform weighting scheme in order to minimize the synthesized beam side-lobes level, as well as to better image sources with high signal-to-noise ratios. The large images were then improved with several cycles of self-calibration to refine the antenna-based phase gain variations. During the last cycle amplitude gains were also computed and applied. The two observations performed in B-configuration were self-calibrated together.

The second step was to subtract from the visibilities all the sources external to the field of interest ($\sim 20' \times 20'$). This was done, both, to reduce the noise generated by bright sources in the field and to speed up the subsequent imaging processes. Since the subtraction is not applied to cross-correlation products, polarized sources will be present outside the field of interest. This is not a problem since, both, the polarized flux density and the number of polarized sources are lower. After the subtraction, we used only two Taylor terms, we reduced the number of w-projection planes, and we set Briggs weighting scheme with the `robust` parameter set to 0.5. The latter choice was done to better image the extended emission. We performed a final cycle of phase and amplitude self-calibration. The final images were corrected for the primary beam attenuation using the `widebandpbcor` task in `CASA`. The residual calibration errors on the amplitude are estimated to be ~ 5 %. The restoring beam and the local root mean square (rms) noise in the central region of the final images, σ, are listed in Tab. 4.2.

4.2.2 Polarization imaging

To produce Stokes I, Q and U images for the polarization analysis, we used `WSClean 2.8.1`[§] (Offringa et al., 2014; Offringa & Smirnov, 2017).

We produced both full-band and sub-band images. The latter, with a frequency resolution of 16 MHz each, were used for the RM synthesis (see Sec. 4.2.3). The Stokes Q and U images were cleaned together using the `join-channels` and `join-polarizations` options. Full-band Stokes I was used as a mask for the RM synthesis and to compute the fractional polarization. We used the Briggs weighting scheme with `robust` = 0.5. The restoring beam was forced to be the same in the full-band image and in each frequency sub-band, matching the lowest resolution one (i.e., at 1.02 GHz). Each sub-band image was corrected for the primary beam calculated for the central frequency of the sub-band. The parameters describing the images used for the polarization analysis are listed in Tab. 4.3.

Some frequency sub-band were discarded due to their higher noise with respect to average rms noise in the sub-bands: in Tab. 4.3 we list the number of sub-bands used for the RM synthesis for each configuration.

4.2.3 RM synthesis

In the following, we will refer to the Faraday depth, ϕ, to describe the Faraday space in which the RM synthesis is performed, but we will use the more common term RM to describe the actual value derived applying this technique. This is possible because we detected only Faraday-simple sources, which are not resolved in Faraday space (see Sec. 2.2).

We performed the RM synthesis on the $Q(\nu)$ and $U(\nu)$ sub-band images with `pyrmsynth`[¶]. We used equal weights for all the sub-bands and we imposed a spectral correction using an average spectral index $\alpha = 1$. We obtained the reconstructed $\widetilde{Q}(\phi)$ and $\widetilde{U}(\phi)$ cubes in the Faraday space. Thus, in each pixel of the image, we obtained the reconstructed Faraday dispersion function, or Faraday spectrum, $\widetilde{F}(\phi)$. Faraday cubes were created between $\pm$1000 rad m^{-2} and using bins of 2 rad m^{-2}.

We used Eq. 2.19, 2.20 and 2.21 to compute the resolution in Faraday space, $\delta\phi$, the maximum observable Faraday depth, $|\phi_{\rm max}|$, and the largest observable scale in Faraday space, $\Delta\phi_{\rm max}$. These parameters depend on the observational bandwidth and on the width of the sub-bands, which are listed in Tab. 4.3. Therefore, in our case:

[§] https://sourceforge.net/p/wsclean/wiki/Home/
[¶] https://github.com/mrbell/pyrmsynth

Table 4.3: Details of polarized intensity images. Column 1: array configuration; Column 2: central frequency of the first sub-band used for the RM synthesis; Column 3: central frequency of the last sub-band used for the RM synthesis; Column 4: width of the frequency sub-band used for the RM synthesis; Column 5: number of sub-bands used in the RM synthesis (excluding the flagged ones); Column 6: FWHM of the major and minor axes of the common restoring beam imposed to the sub-band and full-band images used for the polarization analysis (see Sec. 4.2.2); Column 7: 1σ rms noise of the full-band total intensity image; Column 8: average rms noise of polarized intensity images resulting from the $\widetilde{Q}(\phi)$ and $\widetilde{U}(\phi)$ spectra obtained with the RM synthesis. The average is computed over the image of the values of σ_{QU} obtained for each unmasked pixel as $(\sigma_Q + \sigma_U)/2$ (see Sec 4.2.3); Column 9: reference to the figures in this Chapter.

Array Conf.	ν_i (GHz)	ν_f (GHz)	$\delta\nu$ (MHz)	Sub-bands	Beam	σ (mJy/beam)	$<\sigma_{QU}>$ (mJy/beam/RMSF)	Fig.
B	1.015	2.023	16	48	$8'' \times 8''$	0.02	0.009	Fig. 4.8, 4.9
C	1.015	2.023	16	49	$30.5'' \times 30.5''$	0.05	0.02	Fig. 4.2, 4.8, 4.9

$$\delta\phi \sim 45 \text{ rad m}^{-2} , \tag{4.1}$$

$$|\phi_{\max}| \sim 535 \text{ rad m}^{-2} , \tag{4.2}$$

$$\Delta\phi_{\max} \sim 143 \text{ rad m}^{-2} . \tag{4.3}$$

We masked the $Q(\nu)$ and $U(\nu)$ sub-band images using the full-band total intensity image: we thus run `pyrmsynth` only for those pixels above 3σ in total intensity. We also performed the RM clean down to the same threshold (see Heald, 2009, for the RM clean technique). For each pixel we measured the noise of $\widetilde{Q}(\phi)$ and $\widetilde{U}(\phi)$ computing the rms, σ_Q and σ_U, in the external ranges of the spectrum: at $|\phi| > 500$ rad m^{-2}. This Faraday depth range is chosen to be outside of the sensitivity range of our observations (defined by $|\phi_{\max}|$) and to avoid contamination from residual side-lobes of the sources. Since $\sigma_Q \sim \sigma_U$, we estimated the noise of each pixel of the polarization observations as $\sigma_{QU} = (\sigma_Q + \sigma_U)/2$ (see also Hales et al., 2012). By definition, σ_{QU} is in units of Jy/beam/RMSF, where Rotation Measure Sampling Function (RMSF) represents the instrumental response in the Faraday space, similarly to the observing beam in the image domain (see also Sec. 2.2). In Tab. 4.3, we list the average value of σ_{QU} for all the unmasked pixels in each observation.

We fitted pixel-by-pixel a parabola around the main peak of the Faraday spectrum. We thus obtained the RM in the observer's frame (i.e., the Faraday depth at the peak, ϕ_{peak}, not corrected for the redshift of the cluster) and polarized intensity ($|\widetilde{F}(\phi_{\text{peak}})|$) images from the coordinates of the parabola vertex in each pixel. For our analysis, we considered only pixels with a peak in the Faraday spectrum above a threshold of $6\sigma_{QU}$. This corresponds to a Gaussian significance level of about 5σ (see Hales et al., 2012).

The pixel-wise uncertainty on ϕ_{peak} (and thus on the RM value in the single pixel), σ_ϕ, is derived with Eq. 2.26.

We computed polarization intensity images using the peak of the Faraday dispersion function, and correcting for the Ricean bias as explained in Sec. 2.2.3. We then obtained fractional polarization images dividing the P images (with the $6\sigma_{QU}$ threshold) by the full-band Stokes I images (masked at the 3σ level).

Our polarization images are not corrected for direction-dependent effects caused by the variation of the antenna primary beam pattern (see Sec. 2.3). These effects can cause beam squint and off-axis flux leakage from the total intensity to the other Stokes parameters (Bhatnagar, Rau & Golap, 2013). The strongest effect is visible in the Stokes I and V images. We estimated that in our images the V/I ratio increases with the distance from the pointing center, going from 1%, at a distance of $2'$, to 4% at $12'$. This constrain the leakage to Stokes Q and U to be within 2% of the

total intensity flux within the field of interest. This spurious contribution can be important for polarized sources with low fractional polarization. Therefore, we will not discuss the fractional polarization obtained for the sources observed in our field whenever it is below the 5% level. The instrumental leakage is centered on 0 rad m^{-2} (see Jagannathan et al., 2017). Hence, we will consider the RMs as not affected by polarization leakage when |RM|>45 rad m^{-2} (i.e., when the detected sources are at a distance of more than one RMSF from 0 rad m^{-2}). RMs below this threshold can differ from the true value by about 5% (Jagannathan et al., 2017). Hence, in this case, a 5% uncertainty is added to the value computed with Eq. 2.26.

4.2.4 X-ray data analysis

A2345 was observed by *XMM-Newton* in April 2010 during rev. 1900 (ObsID: 0604740101) with a total exposure time of 93 ks. The observation was performed in full frame mode for the MOS cameras and extended full frame mode for the pn detector, all using the thin filter.

Observation data files (ODFs) were downloaded from the *XMM-Newton* archive and processed with the `XMMSAS 16.0.0` software for data reduction (Gabriel et al., 2004). We used the tasks `emchain` and `epchain` to generate calibrated event files from raw data. We excluded all the events with `PATTERN>4` for pn data and with `PATTERN>12` for MOS data. In addition, bright pixels and hot columns were removed in a conservative way by applying the expression `FLAG==0`. We discarded the data corresponding to the periods of high background induced by solar flares using the two-stage filtering process extensively described in Lovisari, Schindler & Kapferer (2011). The remaining exposure times after cleaning are 47.5 ks for MOS1, 51.5 ks for MOS2, and 25.5 ks for pn. Point-like sources were detected using the task `edetect-chain` and excluded from the event files. The background event files were cleaned by applying the same `PATTERN` selection, flare rejection criteria, and point-source removal used for the observation events. The resulting image is shown in Fig. 4.2.

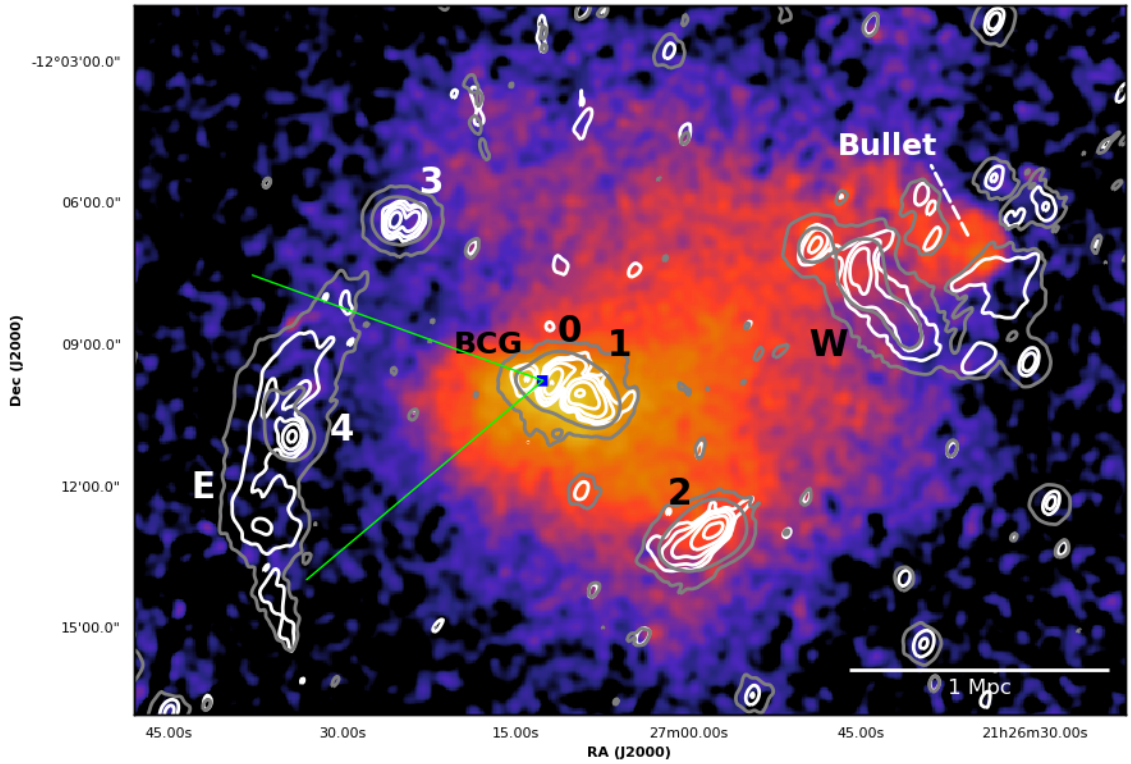

Figure 4.2: X-ray *XMM-Newton* point-source subtracted image of the cluster Abell 2345 (0.3-2 keV) with 1.5 GHz radio contours overlaid. Contours are from the C-configuration observation: white contours have a a restoring beam of $11''\times18''$, while gray contours show the same data set with a restoring beam of $30.5''\times30.5''$. White contours start at 3σ and are spaced by a factor of four, where σ is the value listed in Tab. 4.2. Gray contours show only the 3σ and 48σ levels and σ is the value listed in Tab. 4.3. The five radio galaxies detected in polarization are marked with numbers, while the eastern and western relics are marked with the letters "E" and "W", respectively. The blue square marks the position of the X-ray surface brightness peak, at the J2000 coordinates: $21^{h}27^{m}12^{s}.6$, $-12°09'46''$. Green lines show the boundaries of the sector used to extract the surface brightness profile and to model the thermal electron density distribution.

The X-ray morphology of A2345 is strongly disturbed and an average surface brightness profile would result in a poor description of the thermal environment of each source. The deviation from spherical symmetry is stronger in the north-western side of the cluster and far away from the BCG, confirming weak lensing studies (e.g., Cypriano et al., 2004). We used the background-subtracted and exposure-corrected images in the 0.3-2 keV energy band to extract the surface-brightness profiles in a sector centered on the X-ray peak, and encompassing the radio sources of interest. In particular, we are interested in the sector containing the E relic in order to study the magnetic field profile up to the relic region. This sector is also the less disturbed one (see Fig. 4.2).

A double β-model was used for fitting:

$$S_X(r) = S_{X,1}\left[1+\left(\frac{r}{r_{c,1}}\right)^2\right]^{-3\beta_1+0.5} + S_{X,2}\left[1+\left(\frac{r}{r_{c,2}}\right)^2\right]^{-3\beta_2+0.5}, \quad (4.4)$$

where the central surface brightness, $S_{X,i}$, the core radius, $r_{c,i}$, and the β_i parameter of each component were left free to vary.

Under the assumption of spherical symmetry, the electron density profile in the sector can be obtained combining spectral (i.e., using the normalization of an APEC model obtained by fitting a spectrum extracted in the sector) and imaging analysis (i.e., the best-fits values of the double β-model), as described in Lovisari, Reiprich & Schellenberger (2015) (see also Hudson et al., 2010). For a double β-model the thermal electron density profile is:

$$n_e(r) = \left\{n_{e,1}^2\left[1+\left(\frac{r}{r_{c,1}}\right)^2\right]^{-3\beta_1} + n_{e,2}^2\left[1+\left(\frac{r}{r_{c,2}}\right)^2\right]^{-3\beta_2}\right\}^{0.5}, \quad (4.5)$$

where $n_{e,1}$ and $n_{e,2}$ are the central densities of the two components. Indeed, due to the complex structure of A2345 the assumption of spherical symmetry is a source of uncertainty in our modeling. However, we note that using a narrow sector for the calculation of the profile helps to mitigate this effect.

4.3 Results

The *XMM-Newton* image of A2345 is shown in Fig. 4.2, overlaid with C-configuration total intensity contours. The central core is elongated in the NE-SW direction while a northern bullet-like component has a peak in the NW and shows an elongated tail toward the eastern direction.

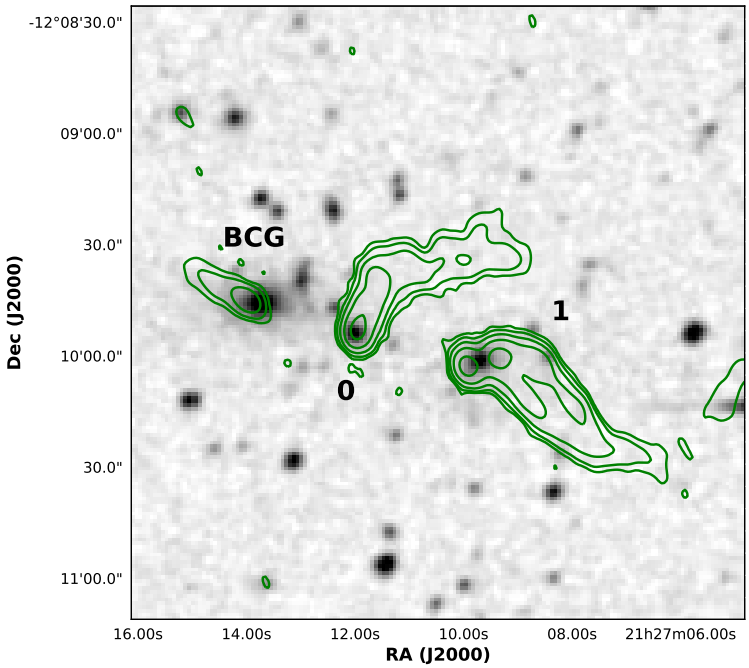

Figure 4.3: Optical DSS2 image of the central region of A2345 with 1.5 GHz radio contours overlaid. Contours are from the B-configuration observation with a restoring beam of $3.3'' \times 4.8''$. Contours start at 3σ and are spaced by a factor of four. The value of σ is listed in Tab. 4.2. The three central sources are marked with the same labels of Fig. 4.2.

Three radio sources lie nearby the X-ray surface brightness peak (see Tab. 4.1) and are all resolved in the B-configuration observation (see Fig. 4.3). The eastern one is the BCG identified by Boschin, Barrena & Girardi (2010), at redshift z=0.181, the other two (marked as source 0 and source 1) are tailed radio sources. The source 0 is a narrow angle tail radio galaxy (NAT, e.g. Miley, 1980) while the presence of two warm-spots and of two distinguishable tails suggest the wide angle tail (WAT) classification for the source 1 (e.g., Missaglia et al., 2019). Another tailed radio galaxy (marked as source 2 in Fig. 4.2) lies 5.2′ (i.e., ∼950 kpc) away from the BCG to the SW direction. These classes of sources are commonly found at the center of merging galaxy clusters, where the dynamic pressure resulting from their motion through the surrounding ICM swept back their jets (Sakelliou & Merrifield, 2000). The tails of these sources point toward different directions, suggesting that they are on different radial orbits around the main potential well (see also Fig. 4.3).

The E radio relic is elongated along the N-S direction with a largest linear size of 1.41 Mpc (7.7′). It lies at a distance of ∼1 Mpc from the BCG, in a region of low X-ray surface brightness. The high-resolution image of the relic is shown in Fig. 4.4, overlaid on the optical image from the Second Digitized Sky Survey (DSS2, McLean et al., 2000). This image reveals the internal filamentary structure of the

relic, representing a great improvement with respect to the observations performed by Bonafede et al. (2009b). In particular, a bright internal arc-like structure, with a linear size of 250 kpc and a transverse size of ∼25 kpc, is detached from the main large scale arc. A double lobed source is detected in the down-stream region of the relic, marked as source 4 in Fig. 4.2.

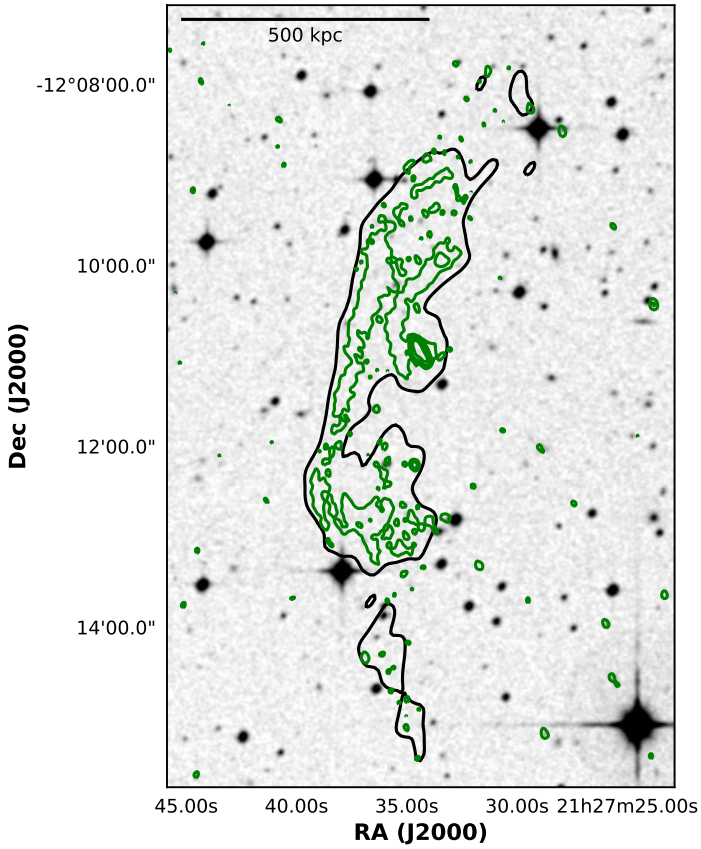

Figure 4.4: Optical DSS2 image of the E relic with 1.5 GHz radio contours overlaid. Green contours are from the B-configuration observation. They have a restoring beam of $3.3'' \times 4.8''$, start at 3σ and are spaced by a factor of four. The value of σ is listed in Tab. 4.2. The black contour is the 3σ level of same C-configuration observation shown with white contours in Fig 4.2.

The W radio relic has a peculiar morphology, as already noticed by Bonafede et al. (2009b). It lies at a distance of ∼1.3 Mpc from the central BCG. In our high-resolution image (see Fig. 4.5) it shows a main structure elongated for 455 kpc (2.5′) in the NE-SW direction. At the northern edge this structure is connected with an arc-like filament elongated in the perpendicular direction. It is difficult to judge whether this arc is purely diffuse emission, or a radio galaxy with a faint counterpart visible in the DSS2 image. There are diffuse patches of radio emission also toward the outskirts of the cluster. The faint outer emission is visible also in the upper-right corner of Fig. 4.2 and it surrounds the NW X-ray peak. Although at low

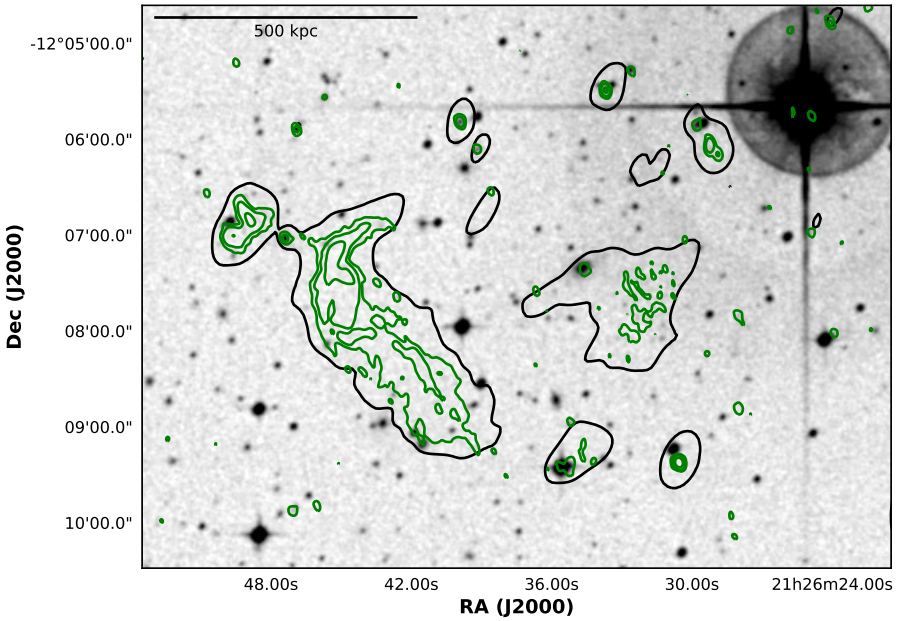

Figure 4.5: Same as Fig: 4.4 for the W relic.

resolution this emission gets blended with a number of point-like sources, we checked that the flux measured from the low resolution image has a higher flux density (38.5 mJy) with respect to the sum of the flux densities measured from single point-like sources detected in the high resolution image (3.9 mJy). In particular, the largest patch of emission coincides with the position of the bullet-like X-ray structure, likely generated by a sub-cluster motion toward W.

4.3.1 Polarized radio galaxies

The polarization analysis of the B-configuration observation allowed the detection of five radio galaxies within the field (marked with numbers from 0 to 4 in Fig. 4.2). Sources 0, 1 and 2 are confirmed cluster members (Boschin, Barrena & Girardi, 2010), while 3 and 4 are likely background radio sources. For each of them, we computed a pixel-wise average RM, <RM>, using only pixels detected with a signal-to-noise ratio higher than 6, as specified in Sec. 4.2.3. We computed the RM dispersion, $\sigma_{\rm RM}$, for each source as $\sqrt{\sigma^2_{\rm RM,obs} - {\rm med}(\sigma_\phi)^2}$, where $\sigma_{\rm RM,obs}$ is the observed standard deviation of the pixels and med(σ_ϕ) is the median error of the RM estimate at each pixel. The value of med(σ_ϕ) is $\sim 1-3$ rad m^{-2} for all the sources. The estimates of <RM> and σ_{RM} are listed in Tab. 4.4. Moreover, we listed the median RM value of each source and the median absolute deviation (MAD), which are good estimators in the case of low statistics and presence of outliers due to low signal-to-noise in the

sampled regions. We also listed in Tab. 4.4 the number of resolution beams, $n_{\rm beam}$, sampled by each source in polarization with a $6\sigma_{QU}$ detection threshold. Finally, the pixel-wise RM distribution of each source is shown in Fig. 4.6.

4.3.2 Polarization properties of the relics

The two relics are detected in polarization at both high (i.e., B-configuration) and low (i.e., C-configuration) resolution. The extended emission is better recovered with the C-configuration observations, in particular for the E relic. The RM and fractional polarization images of the relics are shown in Fig. 4.8 and 4.9. The same information obtained for polarized sources are listed in Tab. 4.5 for the relics, at both resolutions. The RM distributions of the relics in the B- and C-configuration observations are shown in Fig. 4.7.

For the relics, that have negligible polarized flux leakage because of their high polarization, we also computed their average fractional polarization. We integrated the total intensity (I) and polarized (P) flux densities over the area covered by pixels detected above the $6\sigma_{QU}$ detection threshold in polarization and we computed P/I. The uncertainty on the fractional polarization was computed as $P/I \cdot \sqrt{(\sigma_P/P)^2 + (\sigma_I/I)^2}$ with the error on the flux densities estimated as

$$\sigma_{\rm flux} = \sqrt{(\delta f \cdot {\rm flux})^2 + ({\rm noise} \cdot \sqrt{n_{\rm beam}})^2}\,, \tag{4.6}$$

where flux $= I$, P and noise $= \sigma$, $<\sigma_{QU}>$ for total intensity and polarized flux densities, respectively. δf is the residual calibration error on the flux (5 % for JVLA data) and $n_{\rm beam}$ is the number of beam in the sampled region.

From the obtained values of Q and U at $\phi_{\rm peak}$ we recovered the intrinsic polarization angle, χ_0, corrected for the RM determined by $\phi_{\rm peak}$ as in Eq. 3.2, where $\lambda_0 = 19.7$ cm. Hence, the distribution of magnetic field vectors at the relics can be displayed.

The E relic shows few polarized regions above the $6\sigma_{QU}$ threshold in the B-configuration image (Fig. 4.8, left panels). Most of the detected pixels coincide with the internal thin arc of this relic. The fractional polarization reaches the 65% level here, and the average value is 34 ± 3 %. Magnetic field vectors are mainly perpendicular to the main axis of the polarized emission in this region. The Faraday depth ranges between -28 and 45 rad m^{-2} with a median RM of -2 rad m^{-2} and MAD(RM) $= 5$ rad m^{-2}. In the low-resolution C-configuration observation the extended emission of this relic is better sampled (see Fig. 4.8, right panels). The polarized emission covers the entire relic, except for the northern region. The average fractional polarization is lower than at higher resolution (i.e., 18 ± 1 %) but it reaches the 70% in the southern part. We notice a decrease of the fractional polarization where the total intensity high-resolution image shows more substructures. In

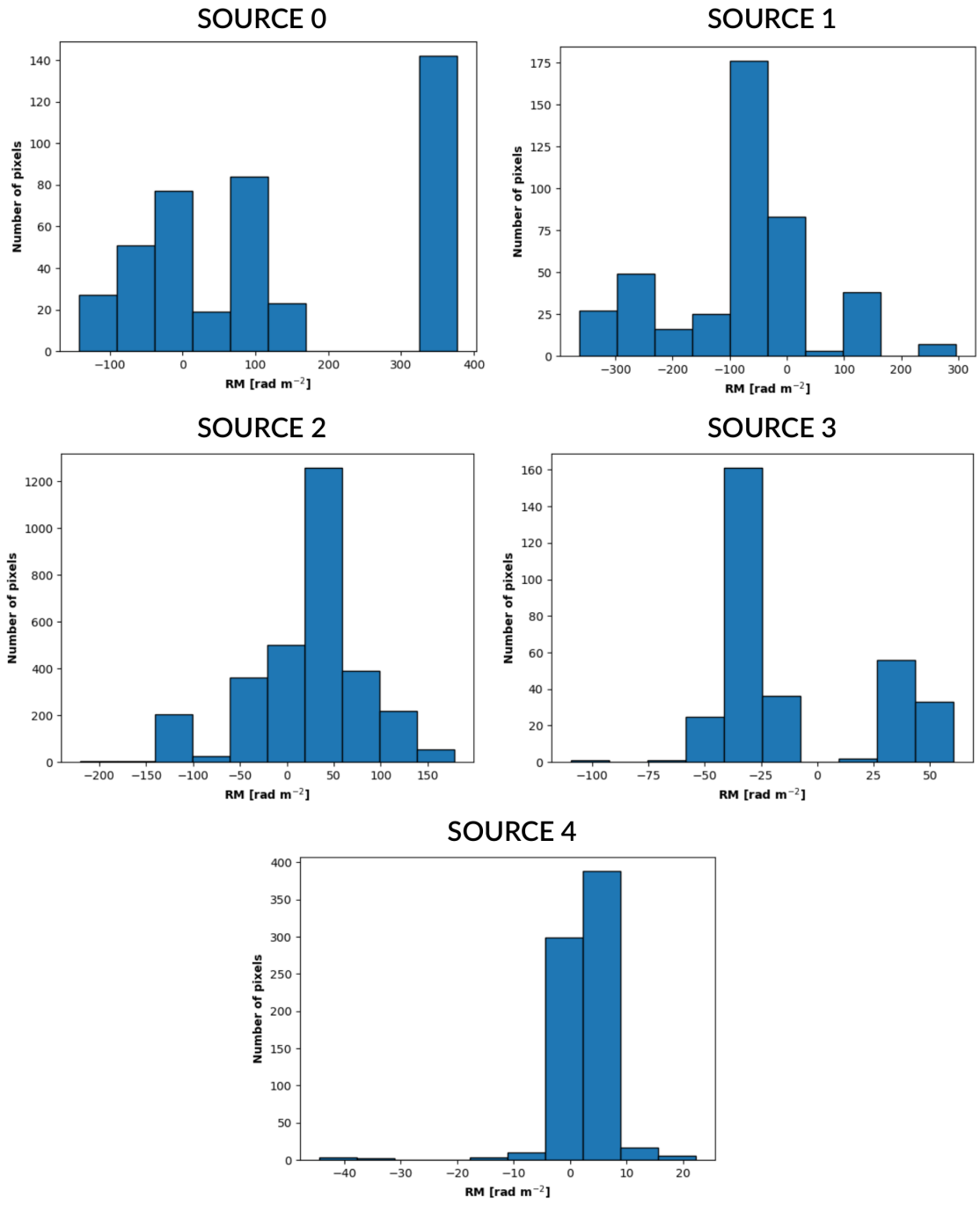

Figure 4.6: RM distribution of the five sources detected in polarization in the B-configuration observation. All the considered pixels are above the $6\sigma_{QU}$ detection threshold.

Table 4.4: Polarization properties of the sources detected in polarization in the B-configuration observation. Column 1: identification number of the source as shown in Fig. 4.2; Column 2,3: J200 celestial coordinates of the source measured at the position of the brightest polarized pixel; Column 4: redshift of the source from Boschin, Barrena & Girardi (2010); Column 5: average RM of the source; Column 6: standard deviation of the RM distribution after the subtraction of med(σ_ϕ); Column 7: median RM of the source; Column 8: median absolute deviation of the RM distribution; Column 9: median of the uncertainty on $\phi_{\rm peak}$, σ_ϕ, for the considered pixels; Column 10: number of resolution beams covered by the pixels detected above a $6\sigma_{QU}$ detection threshold in the B-configuration observation, rounded to a whole number; Column 11: distance of the source from the X-ray surface brightness peak. All the statistical quantities are computed using only pixels with signal-to-noise ratio higher than 6 in polarization.

Source	R.A. (deg)	Dec. (deg)	z	<RM> (rad m^{-2})	$\sigma_{\rm RM}$ (rad m^{-2})	med(RM) (rad m^{-2})	MAD(RM) (rad m^{-2})	med(σ_ϕ) (rad m^{-2})	$n_{\rm beam}$	Distance (kpc)
0	321.800	-12.165	0.180	128	173	107	179	3	3	37
1	321.789	-12.167	0.179	-80	131	-62	57	3	3	154
2	321.738	-12.214	0.176	25	61	38	31	1	20	911
3	321.850	-12.107	-	-11	35	-28	9	2	2	816
4	321.893	-12.181	-	2	5	3	1	1	5	1015

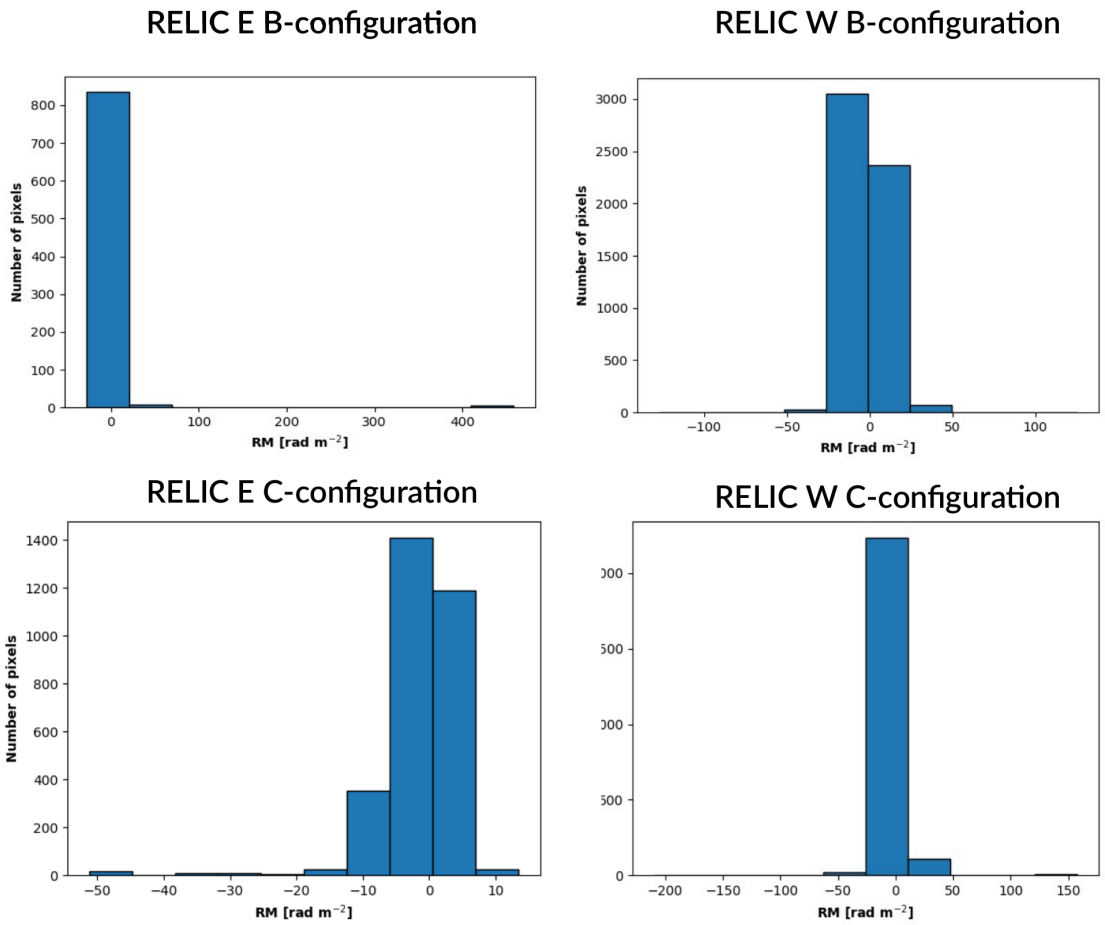

Figure 4.7: RM distribution of the relics considering all pixels above the $6\sigma_{QU}$ detection threshold.

Table 4.5: Polarization properties of the relics. Column 1: Array configuration; Column 2: name of the relic as identified in Fig. 4.2; Column 3: average RM of the source; Column 4: standard deviation of the RM distribution after the subtraction of med(σ_ϕ); Column 5: median RM of the source; Column 6: median absolute deviation of the RM distribution; Column 7: median of the uncertainty on $\phi_{\rm peak}$, σ_ϕ, for the considered pixels; Column 8: average fractional polarization with statistical uncertainties quoted in the $\pm1\sigma$ range; Column 9: number of resolution beams covered by the pixels detected above a $6\sigma_{QU}$ detection threshold, rounded to a whole number; Column 10: distance of the relic from the X-ray surface brightness peak. All the statistical quantities are computed using only pixels with signal-to-noise ratio higher than 6 in polarization.

Array Conf.	Relic	<RM> (rad m^{-2})	$\sigma_{\rm RM}$ (rad m^{-2})	med(RM) (rad m^{-2})	MAD(RM) (rad m^{-2})	med(σ_ϕ) (rad m^{-2})	P/I (%)	$n_{\rm beam}$	Distance (Mpc)
B	E	1	41	-2	5	3	34±3	6	1.0
B	W	-1	9	-2	4	2	24±2	37	1.3
C	E	-1	6	-0.2	2	2	18±1	18	1.0
C	W	-4	13	-5	3	2	12.6±0.9	14	1.3

particular, in the region surrounding the internal thin arc, the decrease of polarized emission coincides with strong variation of the Faraday depth. At low-resolution, magnetic field vectors are well aligned on the scales of the emission and they are mainly perpendicular to the main axis of the relic. This is opposite to what observed in other radio relics (e.g., van Weeren et al., 2010) and could be connected to the magnetic field distribution in the plasma before the shock passage (this topic will be also discussed in Dominguez-Fernandez et al. in prep.). In the southern region of the relic, that shows higher fractional polarization, RM variations are smoother than in the northern part. Therefore the depolarization is likely to be caused by substructures in the shock surface or the magnetic field within the beam. The median RM of the E relic at low-resolution is consistent with zero.

The polarized emission of the W relic is patchy and reaches the 75% level in the northern region in the B-configuration observation (Fig. 4.9, top panels). This emission could be associated to the lobe of a radio galaxy, but such a high level of fractional polarization is suggestive of a very ordered magnetic field which is expected in radio relics. The magnetic field vectors are also indicative of a compressive process in the northern region since they are well aligned along the same direction. The RM distribution in this region is smooth, while it is less homogeneous in the central part, indicating the presence of more substructures that causes depolarization. There is a sharp change in the direction of field vectors at the boundary between these two emission regions. Projection effects could pay a role in the observed polarization properties. The average fractional polarization is 24 ± 2 %. The degree of polarization decreases at low resolution but still reaches the 70% in the northern part, with an average value of 12.6 ± 0.9 %. It is interesting that, at low resolution, the patch of emission in front of the bullet-like X-ray structure (see Fig. 4.2) appears to be polarized with a maximum polarization fraction of 73%. This may suggest the presence of a shock which is ordering the magnetic field lines and thus increasing the fractional polarization in this region. This is supported by the alignment of magnetic field vectors in the direction parallel to the putative shock front. An X-ray surface brightness jump is also visible at this position in Fig. 4.2. The median RM is -2 rad m^{-2} in the B-configuration observation, while it is -5 rad m^{-2} in the C-configuration. The MAD(RM) is 4 rad m^{-2} in the B-configuration observation and 3 rad m^{-2} in C-configuration.

In general, the obtained fractional polarization is consistent with the work of Bonafede et al. (2009b). The resolution achieved in this previous work was in fact intermediate between the ones of our high and low resolution images and the fractional polarization obtained by the authors has an intermediate value. This is expected since a larger amount of depolarization is generated when the polarized emission is mixed inside a larger observing beam. The differences in the average fractional polarization and in the morphology of the detections observed between B-

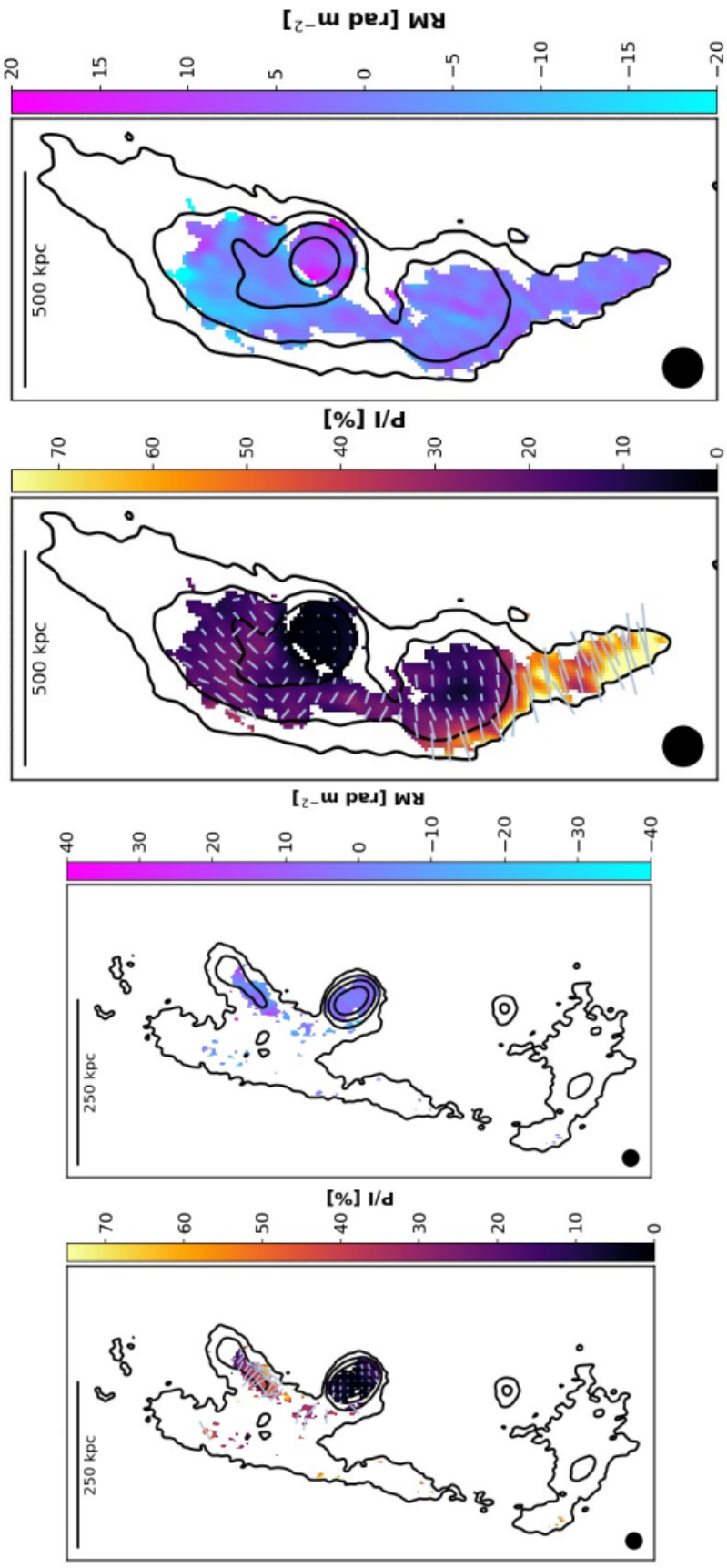

Figure 4.8: Fractional polarization and RM images of the E radio relic in the B- and C-configuration observations. Magnetic field vectors are shown over the fractional polarization images and their length is proportional to the factional polarization value. The $6\sigma_{QU}$ detection threshold was imposed in polarization and only pixels above this threshold are shown. Black contours show the total intensity image used to compute the fractional polarization, start from 3 times the rms noise and are spaced by a factor of four (more details on the images in Tab. 4.3).

and C-configuration are consistent with beam depolarization and with the different sensitivity obtained with the change in resolution.

The Faraday spectra detected from the two relics are Faraday-simple, meaning that they show a single peak with a FWHM coincident with the resolution of our observation in Faraday space (i.e., $\delta\phi \sim 45$ rad m^{-2}). As an example, the Faraday spectra of the brightest polarized pixels in the E and W relics are shown in Fig. 4.10. Several layers of radio-emitting plasma are expected to be present in radio relics and they may be unveiled by the RM synthesis (see, e.g., Stuardi et al., 2019). In this case, it is possible that the emitting layers of the relics are not resolved and that we detect only an external Faraday rotating screen.

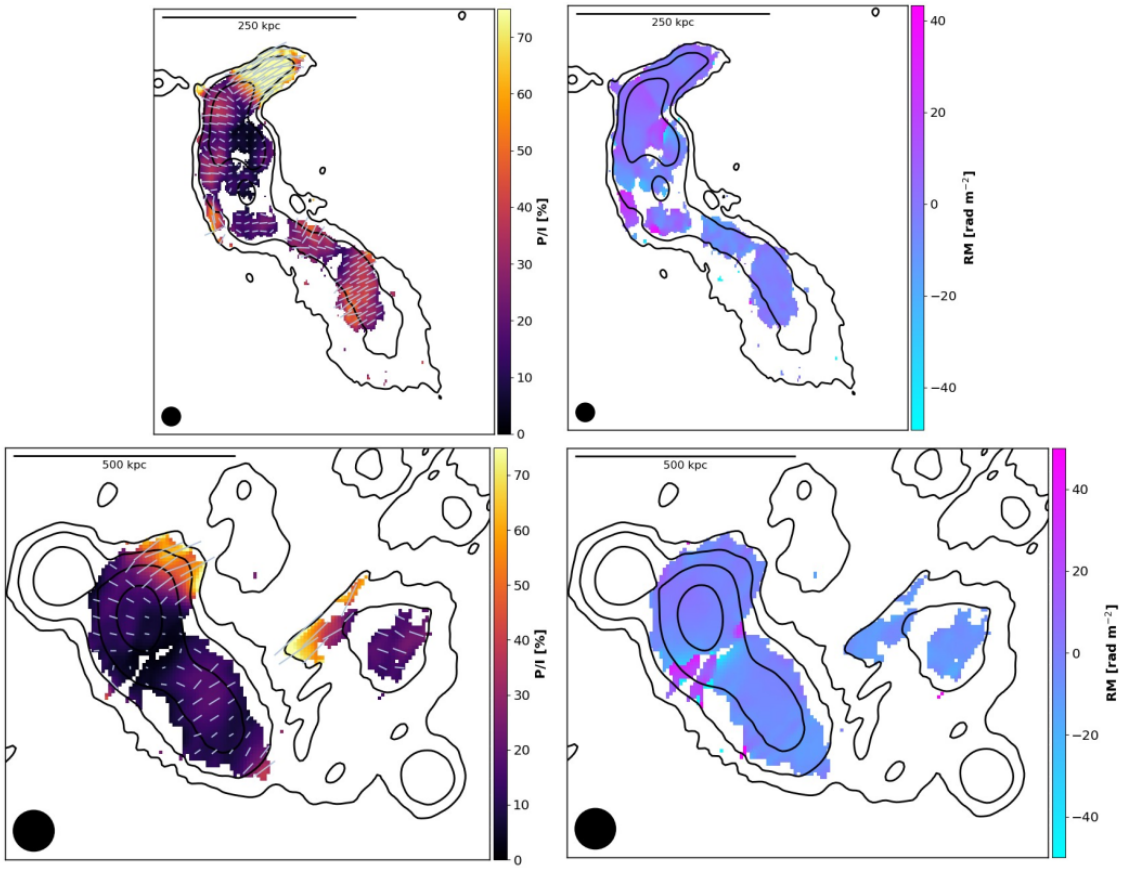

Figure 4.9: Same as Fig. 4.8 for the W relic.

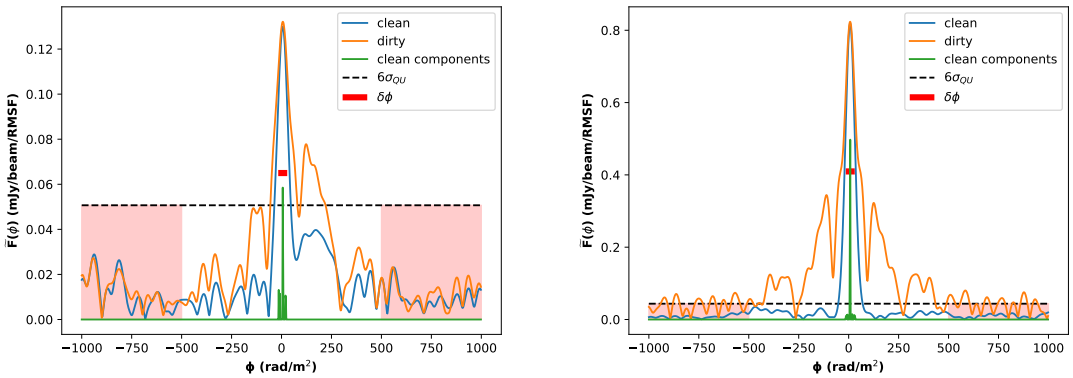

Figure 4.10: Faraday spectra of the brightest polarized pixels of the E relic (left panel) and of the W relic (right panel). The orange line is the dirty spectrum, the blue line is the spectrum after the RM clean, and the green lines show the cleaned components. For reference, the $6\sigma_{QU}$ detection threshold is plotted with a black dotted line and the red shadowed regions show the range of the spectrum where σ_{QU} was computed. The width corresponding to the resolution in Faraday space is plotted at the half-maximum of the spectrum to show that the emission is Faraday-simple.

4.3.3 The Galactic contribution

The mean RM value of the Galactic foreground in the region of the cluster is consistent with zero (i.e., -0.2±5.2 rad m^{-2}, Hutschenreuter & Enßlin, 2020). Therefore, the Galactic contribution will not be subtracted out from our measurements. Nevertheless, when studying the RM distribution of sources in the cluster, the Galactic RM variance generated by the turbulence of the inter-stellar medium on the angular scales of the cluster should be considered. The Galactic RM variance has a strong dependence on angular separation and Galactic latitude (Simonetti, Cordes & Spangler, 1984; Simonetti, 1992). The largest angular distance between two polarized sources in our sample (i.e., the distance between the relics) is $\sim 13'$. Although sub-degree angular scales are not well sampled by actual studies, the amount of Galactic RM variance on $\sim 10' - 15'$ scales is of the order of $\sim$10 rad m^{-2}, depending on the Galactic latitude (Stil, Taylor & Sunstrum, 2011). For example, using the analytical formula derived by Anderson et al. (2015), Eq. 20, we can estimate the Galactic RM variance to be ~ 7 rad m^{-2} at $13'$. The standard deviation computed between the <RM> of the sources in A2345 (considering also the relics) is instead $\sim$57 rad m^{-2}, and thus this value cannot be entirely attributed to the Milky Way.

The median RM computed for the relics and from source 4 in the B-configuration observation is consistent with the Galactic mean RM. In the C-configuration, the med(RM) of the W relic is larger but still consistent with the Galactic one, due to the large uncertainty on the latter. Local enhancement of the RM within the regions of the relics are likely due to the local ICM and can be regarded as a small

fluctuation around the mean, which is instead determined by the Faraday rotation within our Galaxy. The RM dispersion, or the MAD(RM), computed on the scales of the sources (i.e., angular scales below 2.5′, which is the angular extent of the E relic) are thus more indicative of the cluster magnetic field.

4.3.4 RM profiles

The radial profiles of the |<RM>|, |med(RM)|, $\sigma_{\rm RM}$, and MAD(RM) values of the sources detected in polarization in the A2345 cluster are shown in Fig. 4.11. The radial distance of each source is computed as the projected distance between the X-ray peak and the brightest polarized pixel detected at the source position.

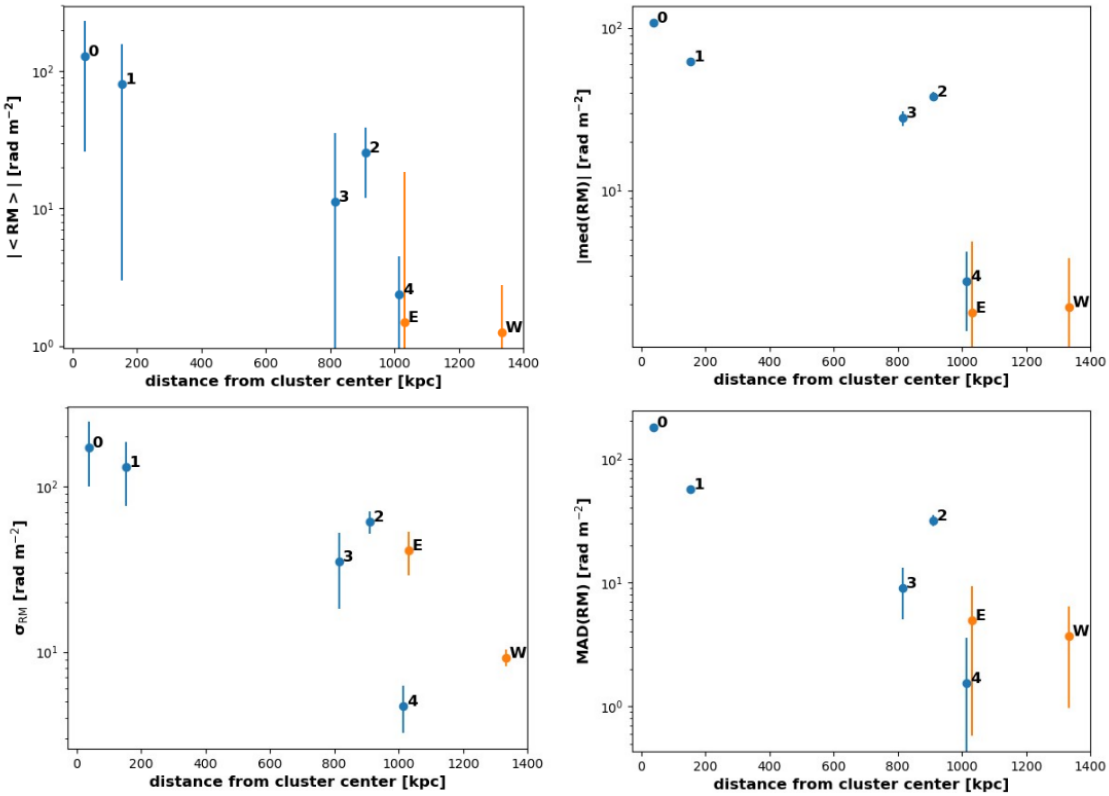

Figure 4.11: |<RM>|, |med(RM)|, $\sigma_{\rm RM}$, and MAD(RM) of the sources in the cluster computed in the B-configuration plotted against the projected distance of each source from the X-ray peak. The uncertainties plotted for |<RM>| and $\sigma_{\rm RM}$ are the $\pm 1\sigma$ computed considering $n_{\rm beam}$ independent samples for each source. The uncertainties plotted for |med(RM)| and MAD(RM) are derived from the median error on the single RM measurement, med(σ_ϕ). The five sources detected in polarization are numbered as in Fig. 4.2 and the eastern and western relics are marked with the letters "E" and "W", respectively.

All the profiles clearly show a radial trend moving from the cluster center. This trend is expected if the Faraday rotation is mainly caused by the magneto-ionized

medium of the cluster that produces a stronger effect on the sources seen in projection closer to the cluster center (see, e.g., Böhringer, Chon & Kronberg, 2016; Stasyszyn & de los Rios, 2019). As we noticed in Sec. 4.3.3, the Galactic contribution on the angular scales of the observed trend is expected to be negligible. The observed radial decrease of, both, RM and RM dispersion also disfavors the interpretation of the RM as due to the local environment of the radio sources. A layer of gas at the edge of the radio emitting plasma or in its close surroundings was proven to cause RM smaller than $\sim$20 rad m^{-2} (e.g., Guidetti et al., 2012; Kaczmarek et al., 2018). Although a local contribution to the observed RM cannot be totally excluded, it is unlikely to be dominant over the ICM contribution (see also, Ensslin et al., 2003). Furthermore, we observed Faraday-simple spectra which follows the expectations for an external Faraday screen. Following these considerations, we argue that the RM radial profile is likely to originate from the ICM, and thus that it can be used to infer the properties of the ICM magnetic field.

Due to the complex X-ray morphology of A2345, the radial trend does not always follow a decrease in the X-ray surface brightness, and thus, of the thermal electron density integrated along the line-of-sight. Since we are more interested in the scaling of RM with this latter quantity, we also plotted the $|<\mathrm{RM}>|$, $|\mathrm{med(RM)}|$, σ_{RM}, and MAD(RM) values against the X-ray surface brightness measured at the position of each source (see Fig. 4.12). We observe decreasing RM trends with decreasing X-ray surface brightness, as it is expected in the case the trend is caused by the ICM that has a larger column density closer to the cluster center. Also these profiles can be used to constrain the properties of the ICM magnetic field.

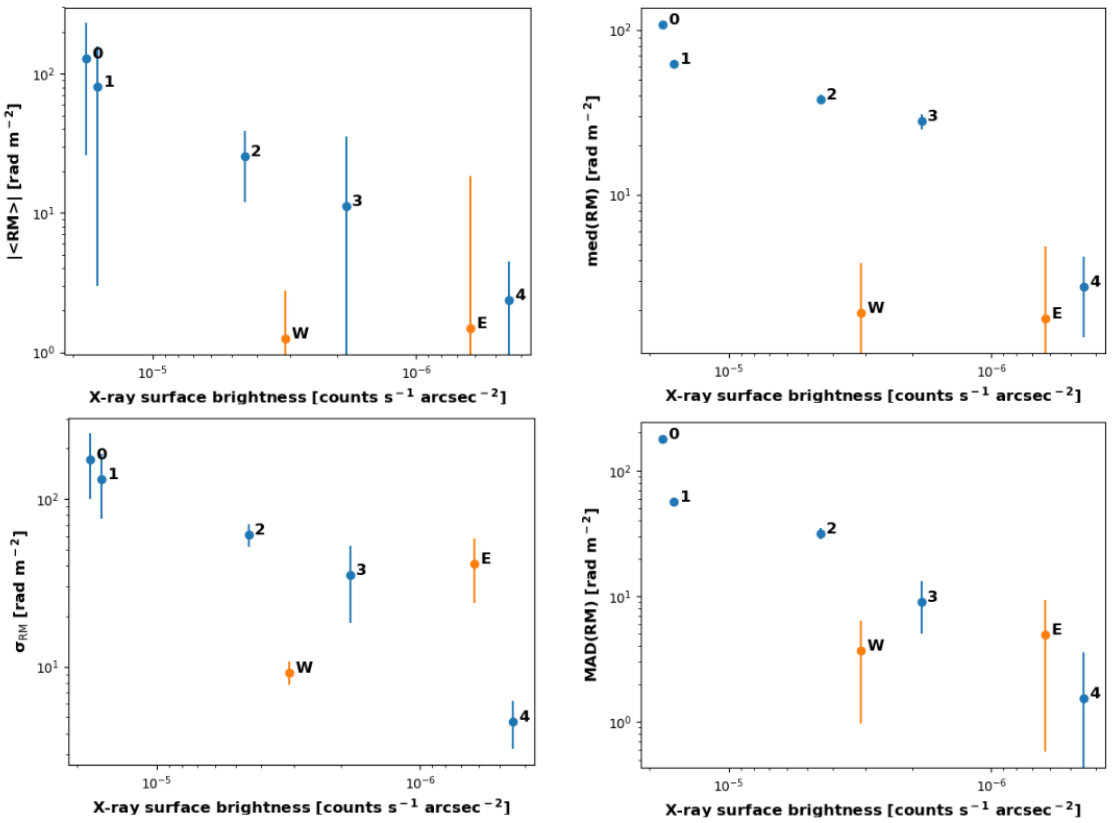

Figure 4.12: |<RM>|, |med(RM)|, σ_{RM}, and MAD(RM) of the sources in the cluster computed in the B-configuration plotted against the X-ray surface brightness at the position of each source. Uncertainties and labels are the same as in Fig. 4.11.

Among the shown profiles, we decided to focus on the median absolute deviation, MAD(RM). This choice is motivated by the fact that, in the simplest idealized model of ICM composed by cells of uniform size, equal thermal electron density, equal magnetic field strength and random orientation of the B vector, the RM dispersion is directly proportional to the cluster magnetic field (Tribble, 1991b). Furthermore, we already noticed in Sec. 4.3.3 that, while the mean RM observed in the external regions of the cluster can be attributed to the Galactic RM, the Milky way is not expected to contribute to the RM dispersion on the angular scales of the observed sources. The MAD is a good estimator for the RM dispersion and it is more resistant to outliers than σ_{RM}. Hence, only the MAD will be compared with our simulated RM maps.

4.4 Cluster magnetic field modeling

The determination of the cluster magnetic field properties from the RM measurements relies on the knowledge of, both, the thermal electron density and the mag-

netic field structure. In order to avoid simplistic assumptions, often used to solve the integral in Eq. 2.5, we produced synthetic RM maps by taking into account realistic 3D models of the thermal electron density and of the magnetic field of a galaxy cluster. These RM maps can then directly be compared to observations, where the magnetic field model parameters can be constrained with a statistical approach.

This method has been proven to be successful for the study of the magnetic field in clusters (Murgia et al., 2004; Govoni et al., 2006; Guidetti et al., 2008; Bonafede et al., 2010; Vacca et al., 2012; Bonafede et al., 2013; Govoni et al., 2017). However, to our knowledge, it has never been applied to the RM measurements of a radio relic. Only in Bonafede et al. (2013) the RMs of seven sources seen in projection through the radio relic in the Coma cluster were used to probe the magnetic field properties in the relic and in the infall region. Using the RM of the relic itself can provide additional information on cluster magnetic fields.

Moreover, this is the first time in which this study is performed using the RM synthesis technique. The RM synthesis technique is in fact sensible to the internal Faraday rotation which is expected to be present in radio relics where layers of radio emitting plasma are mixed with the thermal gas (see, e.g., Stuardi et al., 2019). The peak of the Faraday spectrum obtained at the relics is thus the sum of the polarized emission at each Faraday depth occupied by the emitting layers of the relic. In our case, we detected a Faraday-simple emission from the relics and this means that the single emitting layers are not resolved (see Sec. 4.3.2 and Fig. 4.10). However, it is important to understand if the RM distribution observed at the relics can be used to probe the global magnetic field properties in the cluster.

In this Section, we will apply this method to the RMs obtained from the central source 0, the more external source 4 and the E relic. Since the X-ray morphology of the cluster is strongly disturbed (see Sec. 4.2.4), a unique thermal electron density model, which would allow us to combine the RMs observed from all the sources and study their radial dependence, would be inaccurate. Hence, we decided to carry out the main analysis on the galaxy cluster region occupied by the E relic, using the thermal electron density profile obtained in this cluster sector. This is also the less disturbed region of the cluster, thus the assumption of the spherical symmetry is more suitable. We will reproduce the MAD(RM) profile and compare it to observations, in order to constrain the magnetic field profile from the center of the cluster up to the relic region.

We will also study the MAD(RM) dependence from the X-ray surface brightness in order to be able to use the measurements obtained from all the sources together, with the expense of a larger uncertainty on the cluster geometry.

4.4.1 Simulations of RM maps

We used a modified version of the MiRo code described in Bonafede et al. (2013). We implemented important changes on the modeling of the magnetic field power spectrum, following recent results from cosmological MHD simulations (Domínguez-Fernández et al., 2019). The code firstly produces a mock 3D thermal electron density distribution based on X-ray observations. Then, it produces a 3D distribution of the magnetic field, based on an analytical power spectrum within a fixed range of spatial scales. The magnetic field is scaled by the density profile and then normalized. Hence, the generated cluster magnetic field is tangled on both small and large scales, and it decreases radially. Finally, the code computes the cluster 2D RM map integrating the thermal electron density and magnetic field profile along one axis, solving Eq. 2.5. We describe in more detail each of these steps.

1. The thermal electron density distribution is built on the basis of the surface brightness profile derived in Sec. 4.2.4. For our statistical analysis we chose the sector of the E relic, i.e. between the position angles 160° and 220° (shown in Fig. 4.2), and we extracted the $n_e(r)$ profile following the double β-model (see Eq. 4.5). The six parameters of the double β-model were given as input in the simulation together with the size of the box and the pixel resolution (i.e., $\sim 2^3$ Mpc^3 sampled with 512^3 pixels of 4 kpc size). The center of the box was chosen to be the origin of the profile as computed from the X-ray surface brightness peak.

2. The magnetic field power spectrum is derived from the work of Domínguez-Fernández et al. (2019). Using cosmological MHD simulations, the authors studied the evolution of the magnetic field in a set of highly resolved galaxy clusters. The authors found that the one-dimensional magnetic spectra of all the analyzed clusters can be well fitted to the same equation despite of the different cluster dynamical states:

$$E_B(k) \propto k^{3/2}\left[1 - \mathrm{erf}\left(B \ln \frac{k}{C}\right)\right], \tag{4.7}$$

where $k = \sqrt{\sum_i k_i^2}$ (with i=1,2,3) is the wavenumber corresponding to the physical scale of the magnetic field fluctuation (i.e., $\Lambda \propto 1/k$), B is a parameter related to the width of the spectrum and C is the wavenumber corresponding to the peak of the spectrum. Both B and C are found to depend on the dynamical state of the cluster while they only marginally depend on its mass (see Domínguez-Fernández et al., 2019, for a discussion on those parameters).

This parameterization allows us to use a more realistic power spectrum than those used in other work, where a Kolmogorov power-law spectrum is generally

assumed (e.g., Murgia et al., 2004). Indeed the turbulent dynamo, that is thought to be responsible for the amplification of the magnetic field in clusters, does not produce a power-law power spectrum for the magnetic field (see, e.g. Schober et al., 2015, for a recent review). Instead, the slope of the power spectrum obtained from highly resolved MHD simulation is compatible with the Kazantsev model of dynamo for low wavenumbers, $E_B(k) \propto k^{3/2}$, and rapidly steepens from $\propto k^{-5/3}$ to $\propto k^{-2}$ or less after the peak of the spectrum (Domínguez-Fernández et al., 2019).

We used the B and C parameters of one of the merging clusters in the set at $z = 0$ [‖]. The fit is performed in the innermost $\sim 2^3$ Mpc^3 region of the cluster using a $\sim 512^3$ grid with a resolution of ~ 4 kpc. This corresponds to a maximum fluctuation scale $\Lambda_{\rm max} = 1$ Mpc and a minimum scale $\Lambda_{\rm min}$ ∼8 kpc. The parameters derived from the fit are B=1.054 and $C = 4.354$ Mpc^{-1} (corresponding to a power-spectrum peaking at ∼230 kpc). In our simulations we used the same box size, resolution and range of scales on which the fit was performed.

In order to obtain a divergence-free turbulent magnetic field, with the power spectrum described by Eq. 4.7, we first selected the corresponding power spectrum for the vector potential $\widetilde{\mathbf{A}}(\mathbf{k})$ in Fourier space $E_A(k) \propto k^{-2} E_B(k)$ (Tribble, 1991b; Murgia et al., 2004). For each pixel in Fourier space the amplitude, $A_{k,i}$, and the phase of each component of $\widetilde{\mathbf{A}}(\mathbf{k})$ are randomly drawn. $A = \sqrt{\sum_i A_{k_i}^2}$ is extracted from a Rayleigh distribution with scale parameter $E_A(k)$, while the phases are uniformly distributed between 0 and 2π. The magnetic field vector in Fourier space is then $\widetilde{\mathbf{B}}(\mathbf{k}) = \mathbf{ik} \times \widetilde{\mathbf{A}}(\mathbf{k})$ and has the desired power spectrum. $\widetilde{\mathbf{B}}(\mathbf{k})$ is transformed back into real space using an inverse Fast Fourier Transform algorithm. The resulting magnetic field, $\mathbf{B}$, has components B_i following a Gaussian distribution, with $< B_i >= 0$ and $\sigma_{B_i}^2 =< B_i^2 >$.

3. The radial profile of the magnitude of the magnetic field is expected to scale with the thermal electron density (e.g., Murgia et al., 2004; Bonafede et al., 2010). A radial decrease of the magnetic field strength is also observed by MHD simulations (e.g., Dolag, Bartelmann & Lesch, 1999; Marinacci et al., 2015; Vazza et al., 2018; Domínguez-Fernández et al., 2019). Therefore, we imposed that the cluster magnetic field scales with the thermal electron density following a power-law:

$$|\mathbf{B}(r)| \propto n_e(r)^{\eta} \ , \tag{4.8}$$

where η is a free parameter, as in Bonafede et al. (2013).

[‖] See Tab. 1 in Domínguez-Fernández et al. (2019) and cluster with ID E5A

4. The normalization of the magnetic field distribution is finally obtained imposing that the magnetic field averaged over the cluster volume (i.e., $\sim 2^3$ Mpc^3) is $B_{\rm mean}$. This is equivalent to fixing the value of σ_{B_i}. The value of $B_{\rm mean}$ is the second parameter to be determined in the comparison with observations. This approach is slightly different from previous work where the normalization was performed fixing the average magnetic field value within the core radius or at the cluster center. This approach was preferred due to the greater complexity of the thermal electron density distribution found in A2345 with respect to other clusters. For comparison, we will also refer to the average magnetic field within the 200 kpc radius, $\langle B_0 \rangle$, computed over a set of ten random simulations having the same $B_{\rm mean}$. Within ten simulations the value of $\langle B_0 \rangle$ has standard deviation below the 5%.

Our magnetic field model considers a total of two free parameters, that can be finally determined comparing with our observations, namely η and $B_{\rm mean}$. The use of semi-analytical simulations including both the thermal electron density model obtained from the X-ray analysis and the power spectrum derived from MHD simulations give us the possibility to explore a wide range of magnetic field radial profiles.

Finally, we created a simulated RM map. The thermal electron density and the magnetic field along one axis (arbitrary chosen to be the z axis of the cube) are numerically integrated according to Eq. 2.5. The integration is performed from the center of the cluster, thus assuming that the sources and the relic lie on the plane parallel to the plane of the sky and crossing the cluster center. The resulting RM map has a size of $\sim 2^2$ Mpc^2 and a resolution of 4 kpc. The map is then convolved with a Gaussian kernel with FWHM equivalent to the restoring beam of the observed RM image (listed in Tab. 4.3).

The RM profile can easily be computed from a single mock RM image considering annuli of increasing radius. As an example, we show the median RM profiles computed for two different combinations of η and $B_{\rm mean}$, namely [0.5,1] and [1.5,0.1], in Fig. 4.13. The change of η is responsible for a change in the slope of the RM profile while a change of $B_{\rm mean}$ affects the overall normalization. We also compare these profiles with those obtained using a simple Kolmogorov power spectrum for the magnetic field. The Kolmogorov power spectrum is computed between $\Lambda_{\rm min}$ = 8 kpc and $\Lambda_{\rm max}$ = 230 kpc. The auto-correlation length, i.e. the characteristic scale of magnetic field fluctuations, is $\sim$ 100 kpc for the Kolmogorov power spectrum while it is $\sim$230 kpc in our simulations. With this arbitrary choice we decided to minimize the differences between the two spectra since $\Lambda_{\rm max}$ coincides with the peak of the magnetic power spectrum described by Eq. 4.7. We notice that, for the same magnetic field profile, the Kolmogorov power spectrum produces, on average, lower values of median RM by a factor $\sim$2. This means that the same observational RM radial trend would be fitted with a higher magnetic field for a

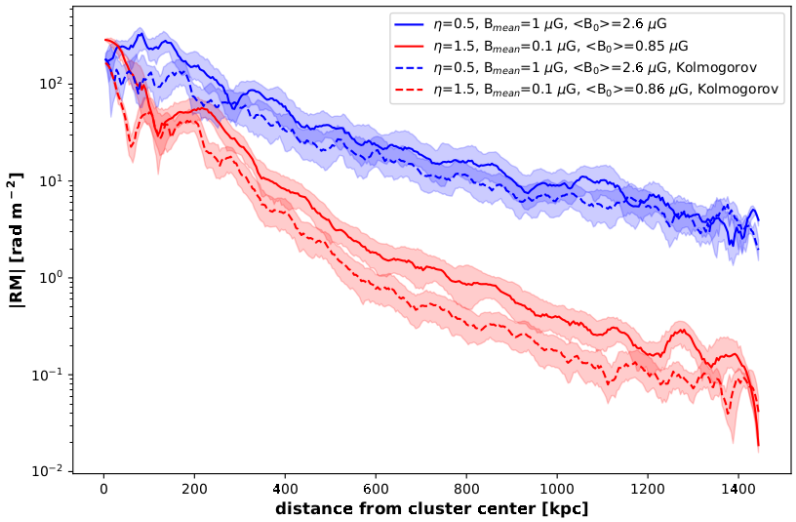

Figure 4.13: Comparison between RM profiles computed from different magnetic field models. The lines show the median |RM| profile with 35% and 65% boundaries computed from the simulated RM maps within annuli of increasing radius in a single random realization. The parameters of the models are listed in the label and the dashed lines refer to the same model computed with a magnetic Kolmogorov power spectrum.

power-law Kolmogorov spectrum, with respect to the one that would be fitted by our model. Considering the model with $B_{\rm mean} = 0.1$ μG, the RM profile obtained with the Kolmogorov power spectrum appears steeper: in this case, a fit performed with this model would underestimate the η parameter. This comparison confirms that, in order to derive detailed cluster magnetic fields properties, it is essential to use a more realistic magnetic power spectra.

Given the random nature of the magnetic field distribution, the RM and RM dispersion in a certain position of the cluster vary depending on the initial random seed of the simulation for different realizations of the same model. To better compare the observed and simulated quantities, the RM image can be also clipped at the distance of a source from the cluster X-ray peak and blanked following the shape of the given source. Hence, the same observational sampling bias is introduced in the simulated quantities.

4.4.2 Constraining magnetic field properties

In order to asses the best match between observation and simulations, we build a set of simulations varying $B_{\rm mean} = 0.05, 0.1, 0.5, 1$ μG and $\eta = 0.5, 1, 1.5, 2$. For each combination of the two parameters we build ten realization starting from different random seeds. The RM maps were convolved with a FWHM of 24 kpc corresponding to the $8''$ resolution of the B-configuration observation. From each simulation we extracted the mock RM image at the distance and with the shape of each source, as

described in Sec. 4.4.1.

As explained in Sec. 4.3.4, we decided to carry out the comparison between observation and simulation using the values of the median absolute deviation, MAD(RM). In this case the best match with observation is obtained for the minimum of the quantity:

$$q = \sum_{i=0,4,\mathrm{E}} \left(\frac{\mathrm{MAD(RM)_{i,obs}} - \langle \mathrm{MAD(RM)_{i,sim}} \rangle}{\mathrm{errMAD(RM)_{i,obs}}} \right)^2 , \tag{4.9}$$

where $i = 0$, 4, E refers to the three sources and the average is computed over the ten different realizations of the same magnetic field model. The error on the observed MAD is computed as $\mathrm{errMAD(RM)_{i,obs}} = \sqrt{2}\mathrm{med}(\sigma_\phi)$ (the MAD is the difference between two single RM estimates which are affected by the same median error). The resulting q parameters for the explored combinations of η and B_{mean} are shown in the top panel of Fig. 4.14.

The minimum is reached for η=1 and $B_{\mathrm{mean}} = 0.5$ μG. This magnetic field model has an average central magnetic field $\langle B_0 \rangle = 2.8 \pm 0.1$ μG (where the average is computed over the ten random realizations and the uncertainty is the standard deviation). The average magnetic field at the relic (i.e., computed in a spherical shell of 200 kpc radius at a distance of 1 Mpc from the center) is $\sim$0.3 μG.

The best MAD(RM) profile derived from simulations is compared with observed values in the top panel of Fig. 4.15. In the same plot, we also show two simulated MAD(RM) profiles obtained with the same B_{mean} (i.e., 0.5 μG) but with different η.

We repeated the same test on q including in the profile the E relic observation performed with the C array. In this case the maps were convolved with a FWHM of 96 kpc, corresponding to the 30.5″ resolution beam. The results (not shown here) are very similar to the results obtained without including this observation, and they constrain the same magnetic field model.

As we noticed in Sec. 4.3.4, each sector of A2345 shows a different X-ray surface brightness profile and thus a different underlying density distribution. Therefore, it is not possible to fit the same radial profile including all the sources. Instead, it is possible to exploit the dependence of MAD(RM) from the observed X-ray surface brightness (see Fig. 4.12). Independently of the underlying thermal gas density distribution, the X-ray surface brightness observed at the position of each source is a good proxy for the thermal electron column density at that position. A large uncertainty is represented by the unknown position of each source along the line-of-sight within the X-ray emitting volume.

In order to test our model with a larger number of observational points, we extracted the simulated RM images of each source at the radial distance derived from the observed X-ray surface brightness, i.e. inverting Eq. 4.4. This method

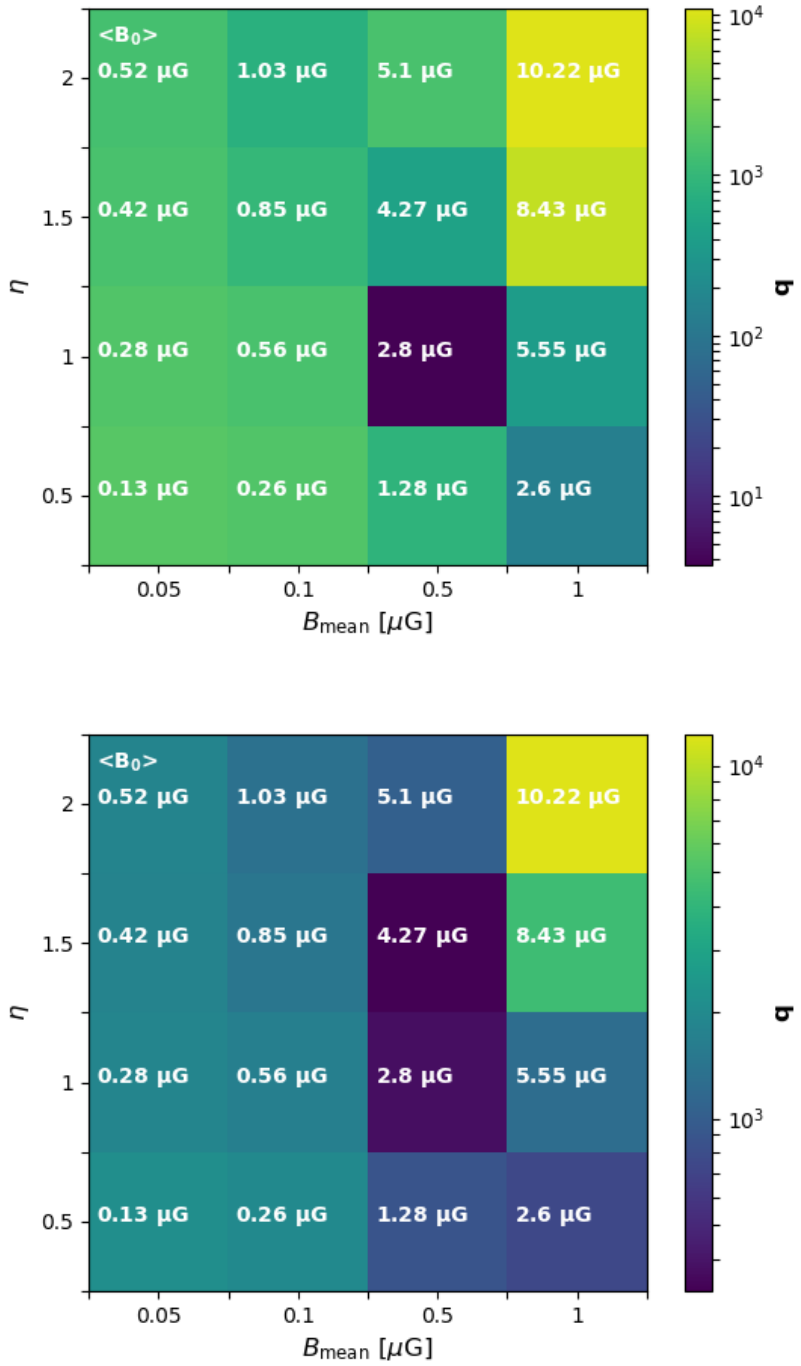

Figure 4.14: Plots of the q statistics derived for the radial MAD(RM) profile (upper panel) and for the profile against X-ray surface brightness (bottom panel) for several combinations of the model parameters η and $B_{\rm mean}$. For each model we show the value of the average magnetic field computed for ten different realizations in the central volume of the cluster within 200 kpc radius.

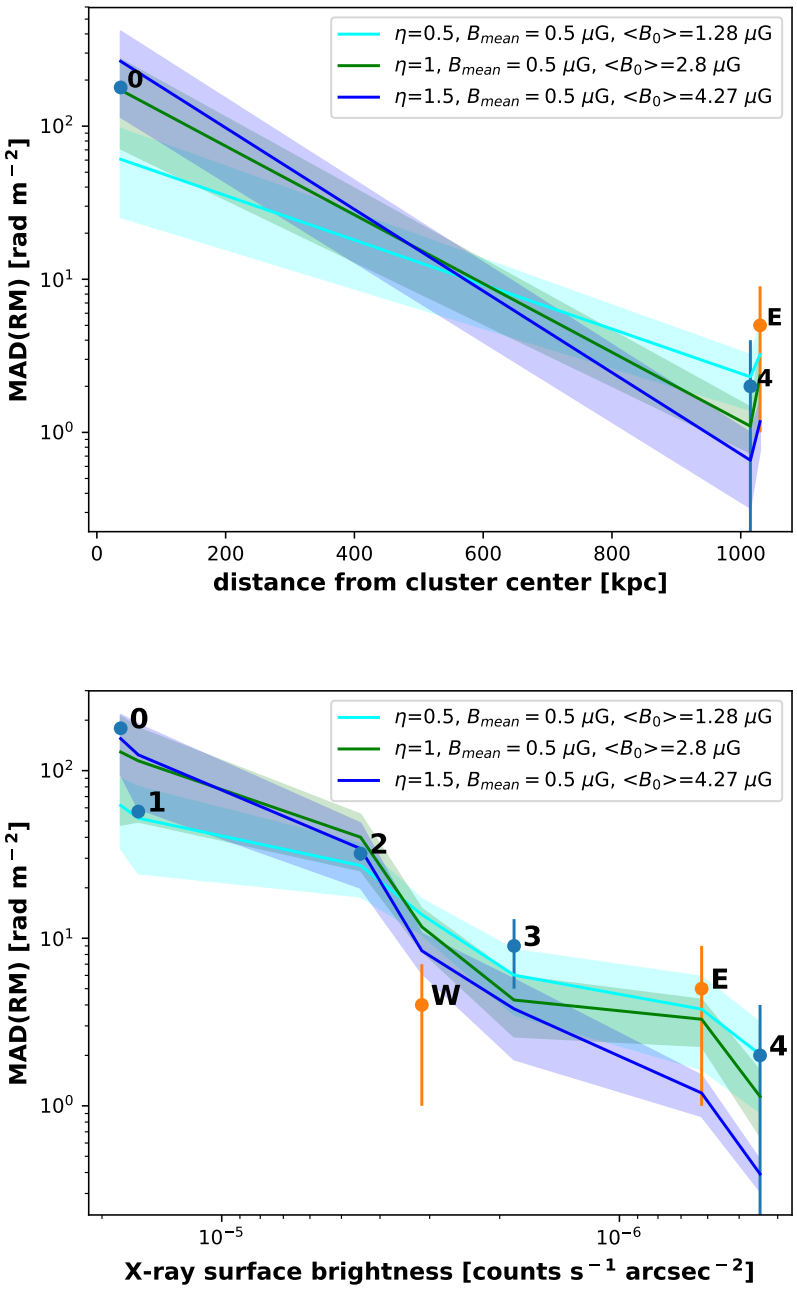

Figure 4.15: Simulated MAD(RM) profiles compared with observations. Lines show the average obtained from ten different realizations of the same model with shadowed areas showing the standard deviation. In the sector containing the E relic the profiles are plotted against the radial distance from the X-ray peak (top panel). The profiles computed using all the detected sources are plotted against the X-ray surface brightness (bottom panel), as explained in Sec. 4.4.2. The best model is the green one.

allows us to enlarge the statistics, at the expense of a larger uncertainty in the adopted density model. We computed the new values of MAD(RM) for all the combination of $B_{\rm mean} = 0.05, 0.1, 0.5, 1$ μG and $\eta = 0.5, 1, 1.5, 2$ and we computed the q parameter (see Eq. 4.9), with i = 0, 1, 2, 3, 4, E, W. In this case, the best-fitting model is the one with $\eta = 1.5$ and $B_{\rm mean} = 0.5$ μG but a very similar q value is obtained for $\eta = 1$ (see bottom panel of Fig. 4.14).

The three models with $B_{\rm mean} = 0.5$ μG and η = 0.5, 1, 1.5 are compared with the observed MAD(RM) profile plotted against the X-ray surface brightness in the bottom panel of Fig. 4.15. Although the minimum q is obtained for the model with $\eta = 1.5$, this seems to be mainly due to the MAD(RM) value of the central sources while peripheral sources are better described by the model with $\eta = 1$. This confirms that this latter model better describes the magnetic field profile in the radio relic sector, and that the same magnetic field profile is able to reasonably reproduce the RMs observed in the entire cluster.

To summarize, we found that a magnetic field tangled on scales between 8 and 1000 kpc, following a power spectrum defined by Eq. 4.7 with a peak at ∼230 kpc, best describes our data with a central magnetic field $\langle B_0 \rangle = 2.8 \pm 0.1$ μG and $\eta \sim 1$**. The average magnetic field at the position of the E relic is thus constrained to be ∼ 0.3 μG.

It is necessary to notice that our simulations assume spherical symmetry and that the RM computation further assumes that all the observed sources and relic are aligned on the same plane. A recent work by Johnson et al. (2020), identified these assumptions as one of the principal uncertainties on the determination of cluster magnetic fields from Faraday rotation measurements. The authors stated that RM-estimated central magnetic field strengths suffer for an uncertainty of a factor ∼3 due to the, still, unknown parameters of the the model used to interpret RM measurements. Another source of uncertainty in our modeling is introduced by the assumption that the ICM magnetic field strength follows a Maxwellian distribution. In fact, cosmological MHD simulations demonstrated that the 3D magnetic field distribution shows strong departures from a simple Maxwellian distribution and that this may have a strong impact on the RM-based estimate of the central magnetic field strength (Vazza et al., 2018). In order to verify this hypothesis, we would need RM information from a larger fraction of the sky area cover by the cluster. With the lack of the necessary statistic, the assumption of a magnetic field distribution other than the Gaussian would only add more free parameters to our model. Taking note of these considerations, it is clear that the uncertainty on the value of $\langle B_0 \rangle$ = 2.8 μG is larger than the one derived from the standard deviation between the ten realizations of the same model.

**We notice that, in this case, the z-correction for the RM values would be negligible and have not been considered

4.5 Discussion

Under the assumption that the RM and $\sigma_{\rm RM}$ radial profiles observed in the A2345 galaxy cluster are dominated by Faraday rotation in the ICM, we constrained the magnetic field profiles that, within the framework of our model, may better reproduce the observations.

Several statistical studies demonstrated that the Faraday rotation of sources seen in projection within clusters decreased with the radial distance from the cluster center (e.g., Clarke, Kronberg & Böhringer, 2001; Johnston-Hollitt & Ekers, 2004; Böhringer, Chon & Kronberg, 2016; Stasyszyn & de los Rios, 2019). Fewer of these kinds of analyses were performed on single clusters, since current facilities allow the detection of few polarized sources per square degree (see, e.g., Rudnick & Owen, 2014). The RM radial trend we observed in the A2345 galaxy cluster is a single-cluster confirmation of previous statistical studies, as was also found in Abell 514 (Govoni et al., 2001)

One of the first attempts to unveil the magnetic field profile and power spectrum of a single cluster was performed by Murgia et al. (2004), who used RMs from three galaxies observed within Abell 119. Similar work was performed on Abell 2255, Abell 2382 and Abell 194 (Govoni et al., 2006; Guidetti et al., 2008; Govoni et al., 2017). Other studies were performed exploiting the presence of a central radio halo or a single extended polarized radio source observed at high angular resolution (Vacca et al., 2010, 2012). Another notable exception is the Coma galaxy cluster that, thanks to its proximity, spans more than one degree in projected size. Its intra-cluster magnetic field was studied with great detail using the RMs of 14 radio galaxies and with a method similar to the one we adopted in this work (Bonafede et al., 2010, 2013). In this work, the intra-cluster magnetic field was described with a Kolmogorov power spectrum on scales between 2 and 34 kpc. The best-fit parameters were found to be $\langle B_0 \rangle = 4.7$ μG and $\eta = 0.5$. The authors also inferred that the magnetic field should be amplified by a factor of ~ 3 throughout the entire merging region where the Coma radio relic is observed.

We list the main results of the aforementioned work in Tab. 4.6 and we include the results obtained in Sec. 4.4.2. We computed the average magnetic field strength in the central $\sim$1 Mpc^3 of the simulated cube. This value is only computed for reference, since in our case we only modeled a sector of the cluster. The parameters of the magnetic field profile obtained by each work are also plotted in Fig. 4.16.

The values obtained for $\langle B_0 \rangle$ range between 1.3 and 11.7 μG and do not correlate with the mass of the galaxy cluster. The value of η we obtained in this work agrees with the ones obtained in the literature. In most of the previous work, the value of $\eta = 0.5$ was assumed, and only in the case of Coma it was derived from a comparison with observations. In fact, if the magnetic field strength decreases

Table 4.6: Comparison of results in literature. Column 1: galaxy cluster name; Column 2: mass estimate within r_{500}. All the estimates refer to the hydrostatic mass from Sunyaev-Zeldovich effect observations (Planck Collaboration et al., 2016b), apart from the poor galaxy cluster Abell 194 for which we used the X-ray mass estimate from Lovisari, Reiprich & Schellenberger (2015); Column 3: redshift; Column 4: dynamical state of the cluster based on literature search. When the classification is uncertain a "(?)" symbol is used; Column 5: magnetic field power spectrum index in the expression $|B_k|^2 \propto k^{-n}$. In this work the magnetic field power spectrum is assumed as explained in Sec 4.4.1; Column 6 and 7: minimum and maximum scale of the magnetic field power spectrum fluctuations; Column 8: average magnetic field at the cluster center; Column 9: average magnetic field in a $\sim$1 Mpc^3 volume; Column 10: radial slope of the magnetic field profile; Column 11: Reference paper. A value is marked with an asterisk when it is assumed and fixed in the model rather than derived from observed parameters.

Galaxy cluster	M_{500} ($10^{14} M_\odot$)	z	Dynamical state	n	$\Lambda_{\rm min}$ (kpc)	$\Lambda_{\rm max}$ (kpc)	$\langle B_0 \rangle$ (μG)	$\langle B_{\rm 1Mpc^3} \rangle$ (μG)	η	Ref.
Abell 119	3.4	0.04	merging	2	6*	770*	5	1.5	0.9	Murgia et al. (2004)
Abell 2255	5.4	0.08	merging	2-4	4*	512*	2.5	1.2	0.5*	Govoni et al. (2006)
Abell 2382	2.0	0.06	relaxed (?)	11/3	6*	35	3.3	1	0.5*	Guidetti et al. (2008)
Coma	7.2	0.02	merging	11/3	2	34	4.7	2	0.5	Bonafede et al. (2010)
Abell 665	8.9	0.18	merging	11/3*	2*	34	1.3	0.75	0.5*	Vacca et al. (2010)
Abell 2199	2.9	0.03	relaxed	2.8	0.7	35	11.7	0.2	0.9	Vacca et al. (2012)
Abell 194	0.3	0.02	relaxed	11/3*	1*	64	1.5	0.3	1.1	Govoni et al. (2017)
Abell 2345	5.9	0.18	merging	Eq. 4.7	8*	1000*	2.8	1.2	1.0	This work

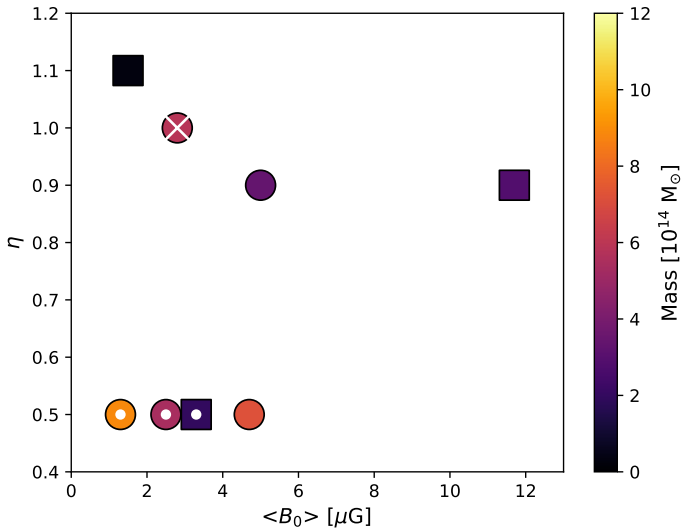

Figure 4.16: Comparison with η and B_0 values found in the literature. Square markers show relaxed clusters while circles show merging clusters. The value obtained in this work is marked with an "X" while clusters for which the value of $\eta = 0.5$ was assumed a priori are marked with a filled white circle. The values are listed in Tab. 4.6.

as the square root of the thermal electron density, the gas is at the equilibrium since the magnetic energy density decreases as the gas energy density. Higher values of η lead to a higher central magnetic field and to a stronger radial decrease of the magnetic energy density. However, it shall be stressed that the $\langle B_0 \rangle$ and η parameters reported from the literature were derived with rather varied approaches to the 3D modeling of magnetic fields, and, in particular, our work here is the first to assume a power spectrum that departs from a simple power-law, in agreement with small-scale dynamo simulations. Furthermore, the largest scale of our spectrum, derived from MHD simulations, is 1 Mpc, which is ∼30 times larger than the largest scale obtained for the power spectrum in the Coma cluster, and has a peak at ∼230 kpc. Also the physical condition of the galaxy cluster can play a role since it is still not clear if the more massive and relaxed clusters have a larger central magnetic field with respect to merging systems (van Weeren et al., 2019; Stasyszyn & de los Rios, 2019).

In our magnetic field model we assumed a unique magnetic field power spectrum to describe the entire volume of the cluster. In particular, the power spectrum was retrieved from the cosmological MHD simulation of a merging galaxy cluster (Domínguez-Fernández et al., 2019). However, it is possible that existing shocks change the magnetic power spectrum. This would be a possible scenario for the observed relic. Recently, Domínguez-Fernández et al. (2020) studied the impact of shocks on the magnetic power spectrum. This study used MHD simulations of

Mach number 2-3 shocks propagating through a turbulent ICM 200^3 kpc^3 box. In this work, the authors concluded that the turbulence created after the shock passage may have an impact of the local magnetic field power spectrum. In particular, after the shock passage, the power spectrum shifts the power spectrum on physical scales $\gtrsim$ 50 kpc to larger scales (i.e, lower wave-numbers) while leaving scales below 10 kpc largely unaffected. In this case, the intra-cluster magnetic field profile would be best represented by the RM dispersion profile since this is determined by magnetic field fluctuation on scales smaller than the sources size. Furthermore, a global power spectrum model may not be sufficient to describe the magnetic field profile in the entire cluster when a merger is occurring, as was also pointed out by Govoni et al. (2006).

We also obtained an estimate of the magnetic field strength at the E relic. Assuming equipartition Bonafede et al. (2009b) obtained an estimate of 0.8 μG for the E relic. This value is 2.7 times larger than the one that we obtained for the model with $B_{\rm mean}$=0.5 μG (i.e., 0.3 μG). This discrepancy can be motivated by the large number of assumptions that should be taken into account in the equipartition estimate and that could have lead to an overestimation of the magnetic field. In any case, no physical reason for relics to be at the equipartition exists. On the other hand, it is also possible that projection effects play a role and that the RMs we obtained from the relic only sample the intra-cluster medium outside a thin shell in front of the relic. In this case, our magnetic field would be underestimated. Another important source of uncertainty is the assumption of spherical symmetry in the determination of the electron density profile. A discrepancy between the magnetic field values obtained from the equipartition estimate and with the RM analysis in radio relics was already observed (e.g., Ozawa et al., 2015).

No evident RM jump was found at the position of the E relic, as for the Coma radio relic. In any case, with the current modeling we cannot investigate if magnetic field amplification occurs in the relic region, as found for the Coma cluster, since we miss observational point in the upstream region. It should be noted that, while the Coma relic is located in a sector where the group NGC 4839 is falling in the main cluster, the E relic in A2345 is in a low-density region where no apparent accretion is currently ongoing. Therefore, a similarity between the two systems is not guaranteed.

We did not attempt the modeling of the magnetic field profile in the W relic sector since an analytical description of the thermal electron density in this region is not trivial. Geometrical uncertainties could be the cause of the discrepancy between the observed MAD(RM) value of this relic and the model derived from the X-ray surface brightness profile (see Fig. 4.15, bottom panel).

4.6 Conclusions

We investigated the intra-cluster magnetic field of the merging galaxy cluster Abell 2345 by using polarization observations of cluster radio sources and relics. We present new JVLA observations of this galaxy cluster in the 1-2 GHz L-band, with the angular resolution ranging from 3″ to 30.5″. These images reveal the complex internal structure of the two radio relics to the east (E relic) and to the west (W relic) of the cluster. In addition, we detected 5 sources seen in projection within a radius of 1 Mpc from the cluster center.

We applied RM synthesis and derived the average RM and its dispersion of each polarized source. We also analyzed a *XMM-Newton* archival observation which show a clearly disturbed morphology. The average RM radial profiles show a decreasing trend centered on the X-ray peak of the cluster, with the values obtained at the location of the most external source and of the relics being consistent with the Milky Way foreground. A decreasing trend is also observed as a function of the X-ray surface brightness.

We created 3D simulations of the galaxy cluster sector containing the E radio relic, including, both, a thermal electron density analytical profile derived from X-ray observations and a 3D magnetic field model based on MHD cosmological simulations (Domínguez-Fernández et al., 2019). We derived mock RM maps and compared the resulting RM median absolute deviation, MAD(RM), to observed values in order to constrain the parameters of the magnetic field model. This method relies on the assumption that all the observed polarized sources lie at the same distance along the line-of-sight and that the origin of the observed MAD(RM) decrease with the projected cluster radius is caused by the Faraday rotation in the ICM.

We find that in our best model the magnetic field linearly decreases with the thermal electron density, with a power-law index $\eta = 1$. This value is larger than the one obtained in cosmological simulations and for the Coma cluster, i.e. $\eta \sim 0.5$ (Bonafede et al., 2010; Vazza et al., 2018). This implies that the magnetic field is not in equilibrium with the thermal gas. The best model has an average central magnetic field $\langle B_0 \rangle = 2.8 \pm 0.1$ μG while the average magnetic field at the position of the E relic is $\sim$ 0.3 μG. This value is $\sim$2.7 times lower than the equipartition estimates. The same model, derived for the E relic sector, is also able to describe the decrease of MAD(RM) with the X-ray surface brightness which is observed for all the sources in the cluster.

We compared our results with the literature, finding a good match, despite the variety of approaches used to obtain magnetic field estimates in galaxy clusters with different properties. Even with the large uncertainties that remains in the derivation of cluster magnetic field properties from RM data, a great improvement is constituted by the use of a realistic power spectrum derived from MHD cosmolog-

ical simulations. In order to achieve a general understanding of the magnetic field structure (radial profile, power spectrum, connection to cluster properties) a larger number of this kind of studies should be performed. In particular, this is the first time that this analysis is performed using polarization and RM synthesis data of a cluster radio relic and more studies would help in confirming our findings.

Chapter 5

A polarization study of double radio relics

Magnetic fields are expected to be amplified by shocks through several mechanisms, like compression of plasma assuming ideal MHD conditions, or turbulent dynamo in the downstream region (see Sec. 1.4.1). While the non-linear evolution of strong shocks is expected to lead magnetic field amplification, it is still not clear if this can happen also in the low Mach number regime (Brunetti & Jones, 2014). Observational constraints to the magnetic field amplification in cluster radio relics are still missing. This is partly due to the fact that the methods used to estimate the magnetic field at the relics (e.g., the equipartition) are only able to derive average estimates. The Faraday rotation effect is the only method that can constrain the magnetic field amplification, by comparing the RMs of sources observed in the pre- and post-shock region. So far, this method has been applied only to the Coma cluster, where no jump has been detected in the relic with respect to the pre-shock region but a magnetic field amplification was observed in the whole cluster region affected by gas accretion (Bonafede et al., 2013). Higher RMs with respect to an average RM profile in galaxy clusters were also detected for sources observed in the background of the relics in the Abell 3667 (Johnston-Hollitt & Ekers, 2004).

Usually, the orientation of the magnetic field is derived by correcting the polarization vector for the Faraday rotation derived from $\chi(\lambda^2)$ fitting or, in the absence of RM estimates, for the value of the Galactic contribution. However, internal Faraday rotation is expected within the relic itself and this has been rarely taken into account. Indeed, before the advent of spectro-polarimetric receivers, it was not possible to derive the Faraday depth of the relics. The RM synthesis is an important tool to unveil the internal magnetic field structure of radio relics.

During my PhD, I approached the first systematic radio polarization study of clusters with double relics. The final goal is to constrain the magnetic field strength, structure and possible amplification in a sample of galaxy clusters, where shock waves have been detected in X-ray and/or double radio relics are observed. The full

Table 5.1: Selected double relic galaxy clusters. Column 1: name of the cluster; Column 2: J2000 celestial coordinates retrieved from the NASA/IPAC Extragalactic Database (NED, https://ned.ipac.caltech.edu/); Column 3: redshift, z, retrieved from NED with the exception of 8C 0212+703 for which an updated redshift is provided by Zhang et al. (2020); Column 4: reference paper for the radio total intensity analysis.

Cluster	R.A.	Dec	z	Reference
8C 0212+703	$02^h17^m01^s$	$+70°36'.3$	0.180	Brown & Rudnick (2011)
Abell 1240	$11^h23^m32^s$	$+43°06'.5$	0.159	Bonafede et al. (2009b)
Abell 2146	$15^h56^m09^s$	$+66°21'.4$	0.234	Hlavacek-Larrondo et al. (2018)
Abell 2345	$21^h27^m11^s$	$-12°09'.5$	0.176	Bonafede et al. (2009b)
Abell 3365	$05^h48^m13^s$	$-21°56'.1$	0.093	van Weeren et al. (2011a)
CIZA J2242.8+5301	$22^h42^m53^s$	$+53°01'.1$	0.192	van Weeren et al. (2010)
MACS J1149.5+2223	$11^h49^m35^s$	$+22°24'.2$	0.544	Bonafede et al. (2012)
MACS J1752.0+4440	$17^h52^m01^s$	$+44°40'.8$	0.366	van Weeren et al. (2012a)
PLCK G287.0+32.9	$11^h50^m49^s$	$-28°04'.6$	0.390	Bonafede et al. (2014)
PSZ1 G096.89+24.17	$18^h56^m54^s$	$+66°20'.1$	0.300	de Gasperin et al. (2014)
PSZ1 G108.18-11.53	$23^h22^m29^s$	$+48°46'.5$	0.335	de Gasperin et al. (2015)
RXC J1314.4-2515	$13^h14^m28^s$	$-25°15'.7$	0.247	Venturi et al. (2007)
ZwCl 0008.8+5215	$00^h11^m25^s$	$+52°31'.7$	0.104	van Weeren et al. (2011b)
ZwCl 2341.1+0000	$23^h43^m39^s$	$+00°16'.7$	0.270	van Weeren et al. (2009)

sample is made of 14 galaxy clusters observed with the JVLA in L band (1-2 GHz). In this Chapter, I will describe this project and show some preparatory work and preliminary results.

5.1 Sample selection and observations

Numerical simulations predict that double relics are visible when the merger axis of the clusters is almost perpendicular to the line-of-sight (e.g. Skillman et al., 2013). This is confirmed by optical studies which unveiled the internal geometry of several double relic galaxy clusters (Golovich et al., 2019a,b). Hence, we can reasonably assume that for the majority of these systems the geometry of the merger is known, and projection effects are minimized. Furthermore, when the merger axis is in the plane of the sky, X-ray and optical observations are easier to interpret and compare with radio data. For these reasons we focused our analysis on a list of clusters with detected double relics above declination $-30°$ (see Tab. 5.1). The limit on the declination is dictated by the JVLA that is well suited for high-resolution observations of radio galaxies but also has good sensitivity to the largest scales of the radio relics emission.

L band (1-2 GHz) observations were required in order to achieve high accuracy in the RM determination through RM synthesis. Observations were performed with B (A for sources at declination $< -15°$ 1), C, and D array configurations. In

particular, B configuration observations are necessary to avoid beam depolarization and to derive the RM of sources in the background of the relics and in the pre-shock region. C and D observations permit to derive the Faraday Rotation, fractional polarization and polarization angle of the relics. Some data were already stored in the JVLA archive, while the remaining targets were observed for 20 h in A array, 33 h in B array, 18 h in C array, and 8 h in D array, for a total of 79 h. These observations have a total bandwidth of 1024 MHz, subdivided into 16 spectral windows of 64 MHz each (with 64 channels at frequency resolution of 1 MHz) centered at 1.5 GHz. Full polarization products were recorded.

A the moment of writing, part of the data has been processed following the calibration and imaging procedures described in Chapters 3 and 4. Preliminary results are shown in the next Section for the 8C 0212+703, and ZwCl 2341.1+0000 galaxy clusters. The analyses performed on RXC J1314.4-2515 Abell 2345 are fully described in Chapters 3 and 4, respectively. The final goal is to obtain polarization and Faraday rotation information for all the 14 galaxy clusters, both from relics and background sources, using the RM synthesis method. Due to time constraints, this project cannot be entirely carried out during a PhD project, because processing and data analysis are particularly time-consuming. When completed, this work will allows us to corroborate the results obtained for RXC J1314.4-2515 and Abell 2345. Stronger constraints to the magnetic field amplification by low Mach number shocks will be obtained by comparing values of RM derived from background sources in the pre-shock and post-shock regions with magnetic field models as done in Bonafede et al. (2013).

X-ray observations, performed either with *Chandra* and/or with *XMM-Newton*, are available for all the targets. This will allows us to use realistic models for the thermal electron density distribution to disentangle its contribution to the RM from the one of the intra-cluster magnetic field. Our data will be compared with state-of-the-art cosmological MHD simulations of galaxy clusters that include magnetic field evolution, shocks and turbulence (e.g., Vazza et al., 2018; Domínguez-Fernández et al., 2019; Wittor et al., 2019; Domínguez-Fernández et al., 2020).

5.2 Preliminary analyses

The main motivation for working on a well defined sample of galaxy clusters is that the number of background polarized sources detected in single clusters is generally low (i.e., < 5). Using the equation provided by (Rudnick & Owen, 2014) to compute the number of polarized sources above a certain detection limit at 1.4 GHz, we obtain that for a putative σ_{QU} of 5 μJy (which is expected for our L-band observations in the B configuration) and a detection threshold of $6\sigma_{QU}$ the number of expected polarized sources per square degree is 8. This number decreases to 5 for a $8\sigma_{QU}$

detection threshold. This is a very raw estimate because the number of detected sources also depends on the resolution beam due to the beam depolarization effect. In the redshift range of our sample, galaxy clusters cover an area of the sky way smaller than one square degree and radio relics (considering both the pre- and the post-shock region) occupy only a fraction of this area. Therefore, for each cluster in our sample we expect 1-2 polarized sources around radio relics*.

As a preparatory analysis, we checked NVSS images of all the selected clusters. This survey has lower sensitivity and resolution (i.e., 45″) with respect to our observations but it provides a lower limit on the number of polarized sources that can be used for our analysis. We created 1.4 GHz fractional polarization images (Eq. 2.1) using only the pixels with signal-to-noise higher than 3 both in the total intensity and in the polarized flux density images. These images are shown in Fig. 5.1, where polarized sources are labeled. This check confirmed that we can expect to detect a total of a least 8 sources in the area covered by radio relics and almost the same number of sources sources in the surroundings. A literature search for radio relics in our sample with polarization data already published, confirmed that at least one polarized source can be detected in the radio relics region of each cluster. The most problematic area is the pre-shock region where few sources are detected and, moreover, the sensitivity of our observations drops due to the limited field of view. However, estimates about the RM in the outskirts of clusters can be obtained through statistical Faraday rotation studies of background sources (see Sec. 7).

Beside the poor statistics, this study is challenged by the still-lacking A-term correction for off-axis polarized flux leakage, as discussed in Sec. 2.3. While this is a second order correction for radio relics, which show high levels of fractional polarization, it can be important for radio galaxies that generally have fractional polarization levels below the 5%. Although, there are ways to tackle the off-axis leakage problem without lost of reliability (as shown in Chapters 3 and 4), a study that want to reach a high fidelity in RM determination on a wide-field through RM synthesis needs to take into account the A-correction. This will be addressed once the correction will be implemented in the data processing tools used for JVLA observations. We are working in close contact with the people that are responsible for this and, as soon as the correction will be implemented, we will apply it to our data.

In the following, I will show preliminary results obtained for two galaxy clusters in our sample. These analyses were carried out with different purposes. In the case of 8C 0212+703, the analysis was triggered by recent discovery obtained from

*The Coma radio relic studied in Bonafede et al. (2013) is an exceptional case because, due to its proximity, it has three polarized sources seen in projection through the relic and two in the pre-shock region.

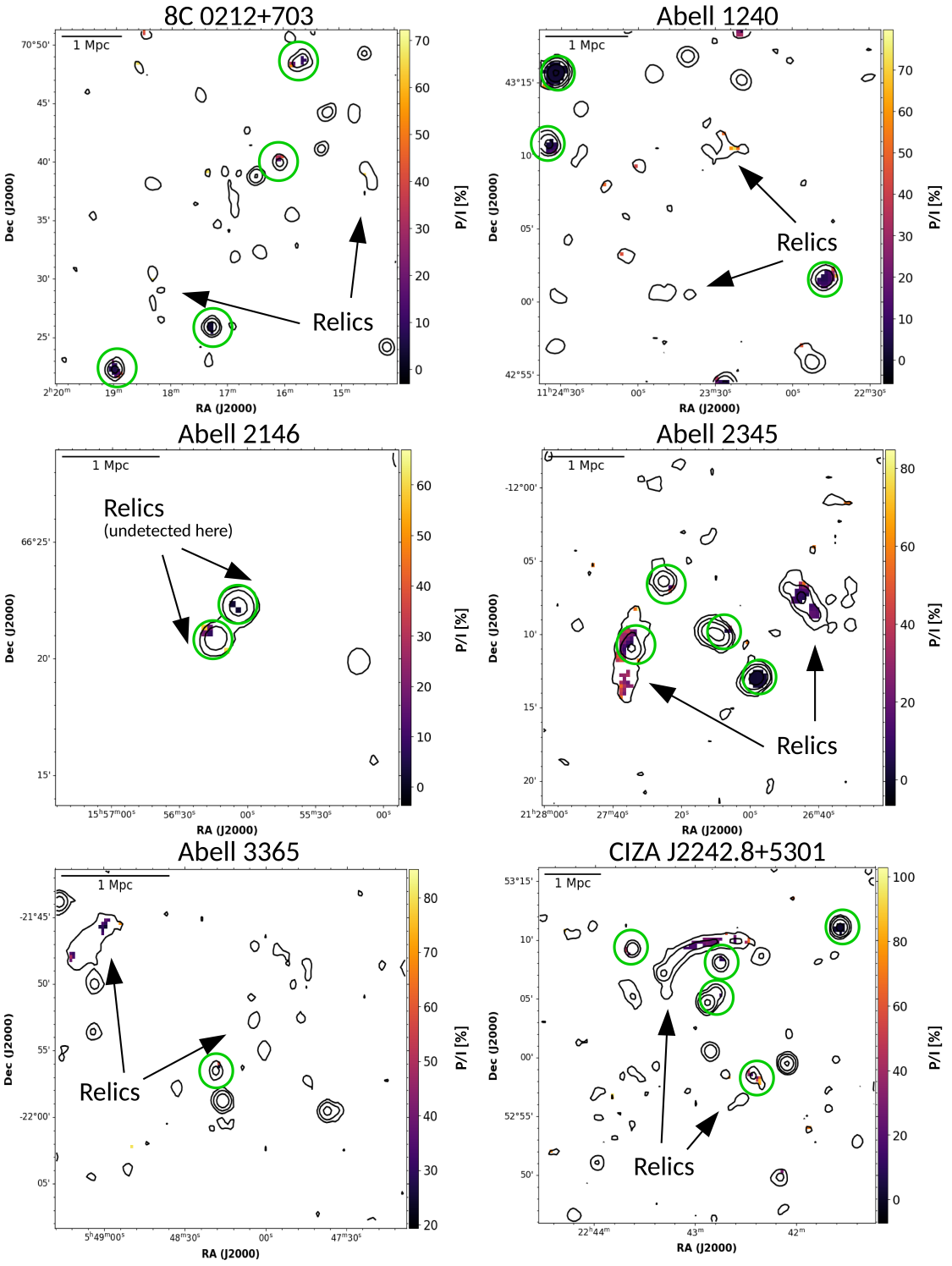

Figure 5.1: Fractional polarization images of the 14 double relic galaxy clusters. Contours show the total intensity image and start from the 3σ level. Polarized sources are marked with green circles.

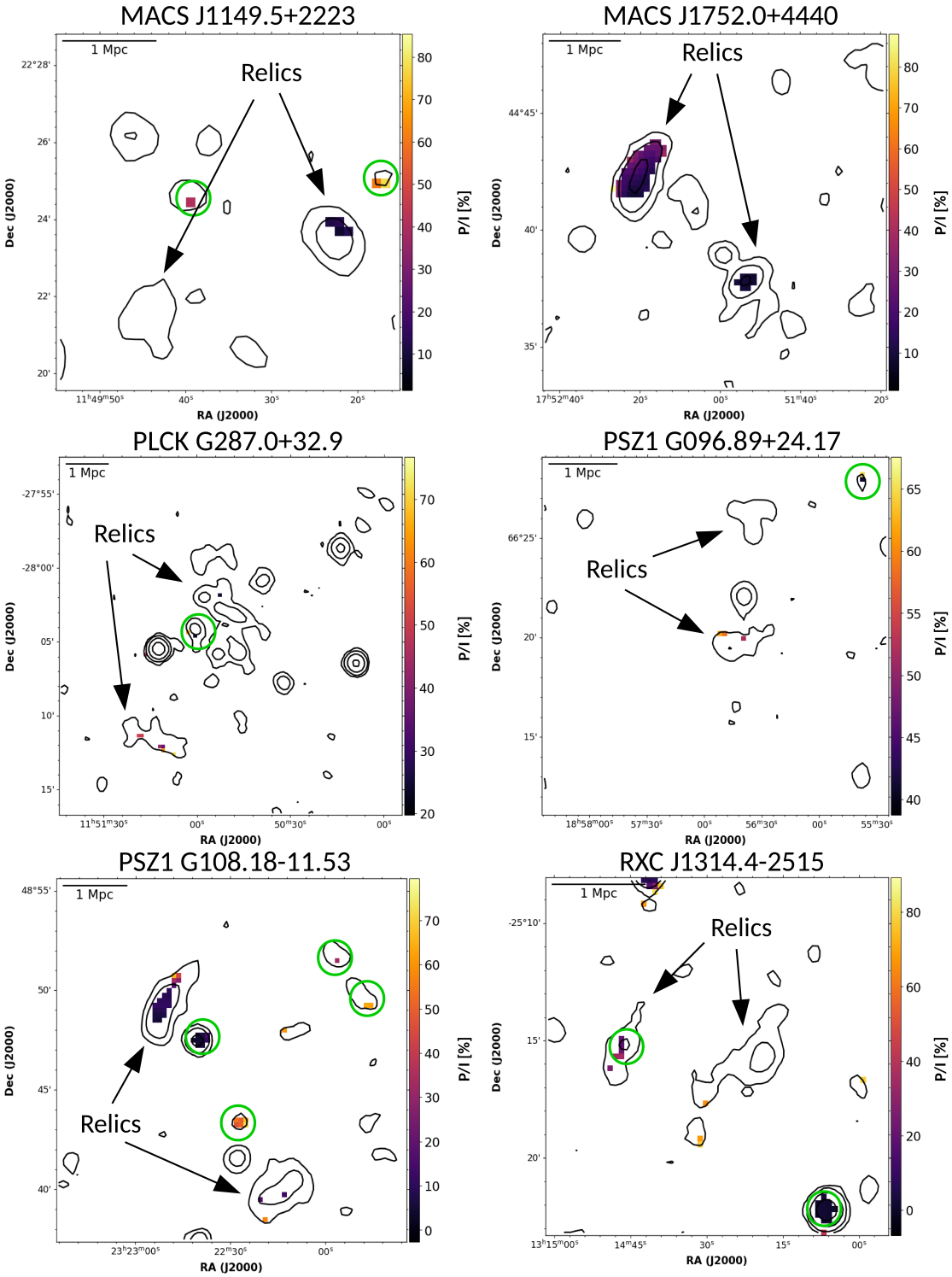

Figure 5.1 (continued)

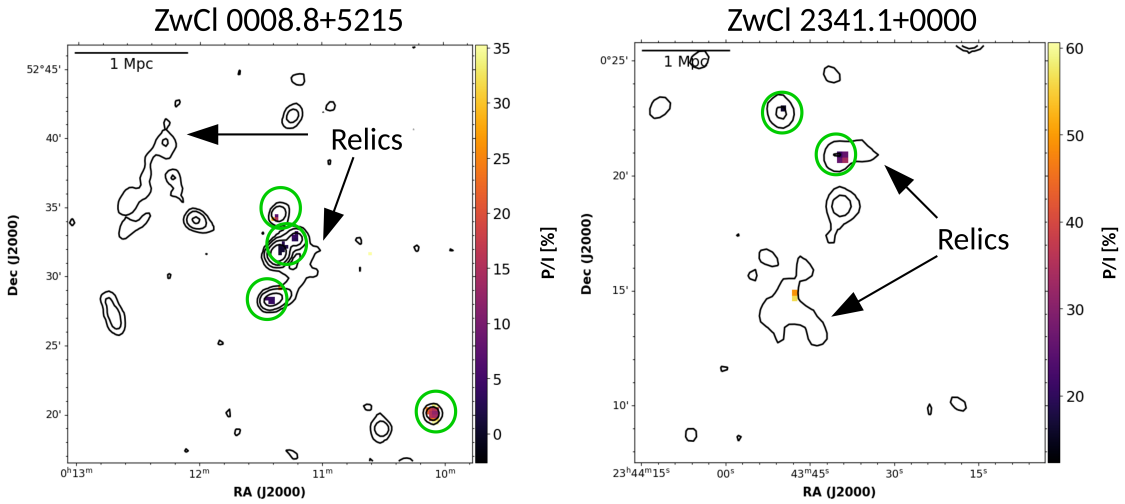

Figure 5.1 (continued)

the the X-ray observation of this cluster. In the case of the ZwCl 2341.1+0000 galaxy cluster, a preliminary inspection of the polarized emission was driven by the presence of a polarized source clearly detected within the northern radio relic in the NVSS image (see Fig. 5.1 (continued)) and by the lack of literature work showing polarization data of this cluster.

5.2.1 New insights from the ClG 0217+70 galaxy cluster

JVLA data that I have analyzed for the cluster ClG 0217+70 have been used in two publications that I have coauthored: Zhang et al. (2020) and Hoang et al. (in prep.). In this Section, I will describe the main results of these works

In Zhang et al. (2020), we presented an X-ray analysis of the merging galaxy cluster ClG 0217+70 (also known as 8C 0212+703). In order to obtain an image of the radio extended emission observed in this cluster with a resolution comparable with that of *Chandra* observations, we performed standard data reduction and imaging procedures on our C configuration JVLA data (not shown in the published letter).

Observations were carried out on June 2017 and were performed on two pointings roughly centered on the two relics. This observational setting was chosen to avoid the attenuation due to the antenna primary beam in the interesting regions of the cluster. The observing time on each relic was 2 hours. We separately performed data reduction, imaging and self-calibration of the two fields. Finally, we made a mosaic of the two final images correcting for the primary beam attenuation of both pointings. The total intensity emission of this cluster at 1.5 GHz is shown in Fig. 5.2 and detailed information on the image are given in the caption.

ClG 0217+70 hosts a central radio halo and numerous diffuse sources in its pe-

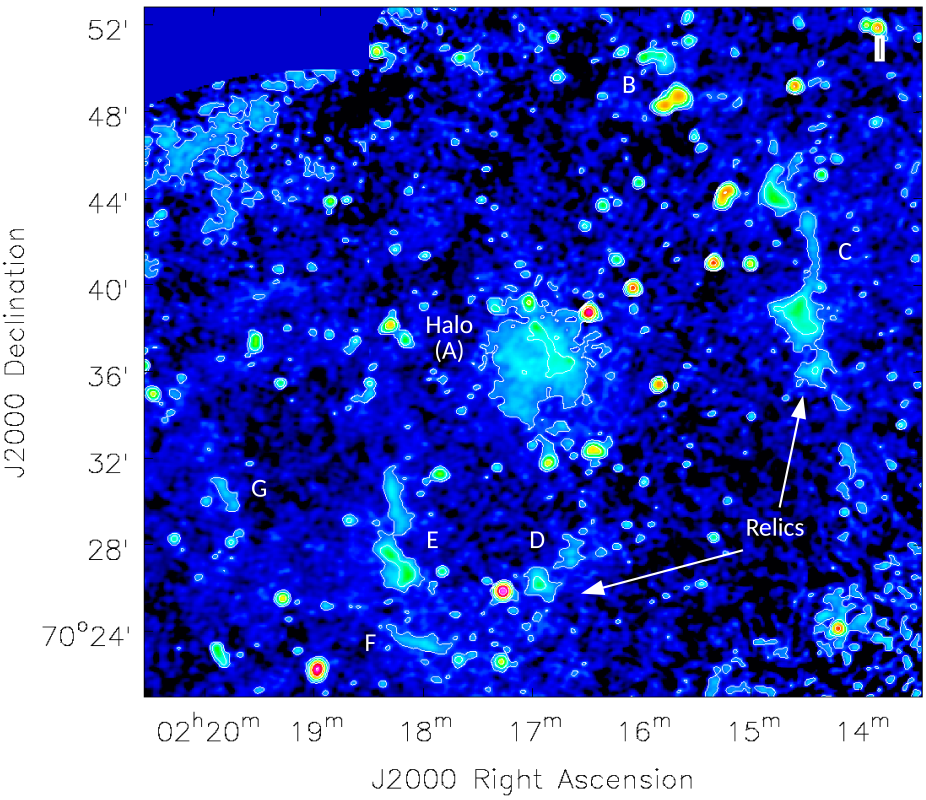

Figure 5.2: JVLA mosaic of the ClG 0217+70 galaxy cluster in C configuration at 1.5 GHz. White contours are overlaid, starting from 3σ and spaced by a factor of four, with σ=0.03 mJy beam^{-1}. The restoring beam is $20'' \times 20''$. The candidate radio relics and the other diffuse sources are labeled following the notation used in Brown & Rudnick (2011).

ripheral regions (labeled with letters from B to G in Fig. 5.2). These sources were classified as radio relics by Brown & Rudnick (2011) on the basis of low-resolution L-band VLA observations. High-resolution observations allowed us to better resolve the morphology of these sources and to perform a comparison with optical images. A more complete source classification, together with high-resolution spectral index maps created with LOFAR observations, will be presented in a forthcoming paper (Hoang et al. in prep.). Among the relic candidates, sources C, D, E, and G are not associated with any optical galaxy, and sources C, E, F, and G show a spectral steepening towards the cluster center. This latter founding suggests the association of these sources with shocks propagating outwards in the ICM. In particular, source E could be associated with an extended radio galaxy with lobes interacting with a shock. Instead, source B is likely a tailed radio galaxy not associated with the relic emission.

In Zhang et al. (2020), archival *Chandra* observations were used to measure the redshift of the cluster that was incorrectly set to $z = 0.0655$ due to sparse optical

data. The position of the Fe emission line obtained through the X-ray spectral analysis yielded instead $z = 0.180 \pm 0.006$. The updated redshift estimate allowed us to revise the scaling relations found for the radio halo observed in this cluster. In fact, the radio halo hosted in ClG 0217+70 was previously know as one of the few outliers in the X-ray to radio luminosity scaling relation, which is expected in the turbulent re-acceleration scenario as a consequence of the relation between the mass of the cluster and the radio halo emission (see Sec. 1.4.2). The updated radio and X-ray luminosities are well in agreement with the expected relation. Furthermore, using the updated redshift, the halo largest linear size reaches 1.6 Mpc and the sizes of source C is above 2 Mpc.

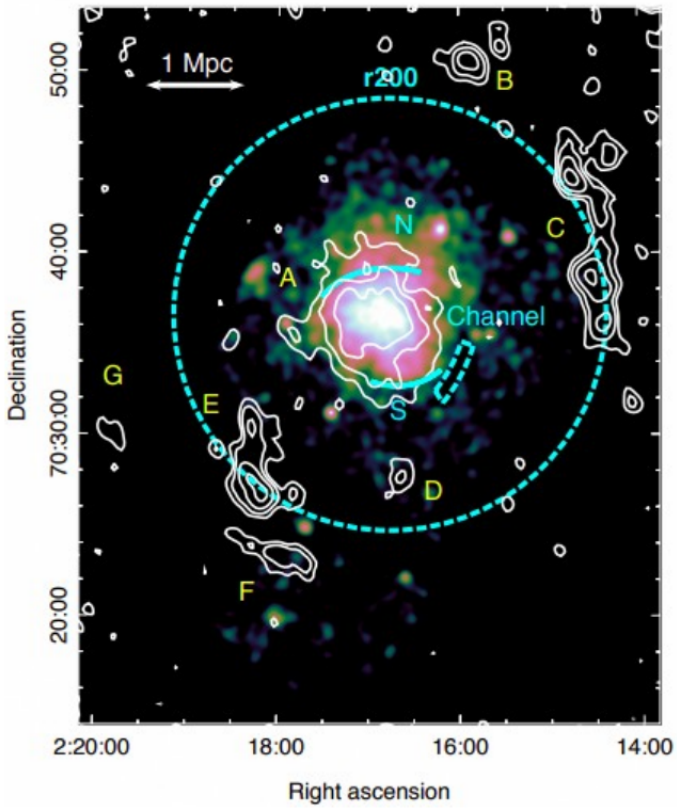

Figure 5.3: The 1-3 keV *Chandra* image of the ClG 0217+70 galaxy cluster with point-source subtracted 1.4 GHz VLA radio contours (resolution beam $49.5'' \times 43.1''$). The northern and southern X-ray discontinuities are marked with solid cyan lines. Individual diffuse radio sources are labeled with letters as in Fig. 5.2. Credits: Zhang et al. (2020).

The X-ray analysis also yielded important information on the dynamical state of the cluster. ClG 0217+70 is dynamically disturbed and show two X-ray surface brightness discontinuities at ∼460 kpc and ∼680 kpc toward the north and south of the core, respectively (see Fig. 5.3). The X-ray discontinuities coincide with sharp changes in the radio halo surface brightness. However, the thermodynamic

properties of these jumps are still unclear due to the short exposure time of the X-ray observations. An X-ray channel was also tentatively detected to the west of the radio halo: this decrease of the X-ray surface brightness has a length of about 700 kpc and a width of ∼200 kpc. If confirmed, this feature could be either a compressed and heated region between the main cluster and an in-falling group, or a region where non-thermal pressure, in the form of turbulent motions and/or enhanced magnetic fields, displaced the thermal gas.

5.2.2 Polarized sources in the ZwCl 2341.1+0000 galaxy cluster

ZwCl 2341.1+0000 has been classified as a double radio relic cluster by van Weeren et al. (2009). The GMRT image at 610 MHz (shown in the right-hand panel of Fig. 5.4) revealed two radio relics located on the opposite sides of the cluster. The X-ray emission is elongated in the NW-SE direction, coincident with the main merger axis suggested by the position of the two radio relics. ZwCl 2341.1+0000 has also been observed at 1.4 GHz with the VLA in D configuration (Giovannini et al., 2010). These observations revealed an additional ∼2.2 Mpc-size central radio emission that has an unclear origin. Proposed scenarios are the ones of a filamentary structures between clusters, a giant radio halo between the relics, or the merging of two clusters both hosting a central radio halo. Both X-ray, optical and weak lensing analyses probed the complex, dynamically disturbed and filamentary nature of this cluster (Boschin, Girardi & Barrena, 2013; Ogrean et al., 2014; Benson et al., 2017) which is also the second more massive system in the Saraswati supercluster (Bagchi et al., 2017).

A polarization study of ZwCl 2341.1+0000 is still missing but NVSS images revealed the presence of a polarized source overlapping with the northern radio relic emission (see Fig. 5.1 (continued)). Hence, we decided to derive polarization and Faraday rotation information from archival B configuration observations of this cluster. Observations were performed on March 2015 (PI Van Weeren) for a total observing time of 2.5 hours. We performed imaging and self-calibration following the procedures described in Sec. 4.2.1. The 1-2 GHz total intensity image of ZwCl 2341.1+0000 with a resolution of $4.3'' \times 3.4''$ is shown in the left-hand panel of Fig. 5.4. Detailed information on the final image are given in the caption.

Since the high-resolution observation excludes the shortest baselines, the two radio relics are resolved out and only few patches of faint diffuse emission are visible. However, numerous tailed and bent radio sources are detected within the field and nearby the relics.

We produced sub-band Q and U images and performed the RM synthesis, as described in Sec. 4.2.1 and 4.2.3. Two sources are detected in polarization above the $6\sigma_{QU}$ detection threshold. The RM map was derived fitting a parabola around

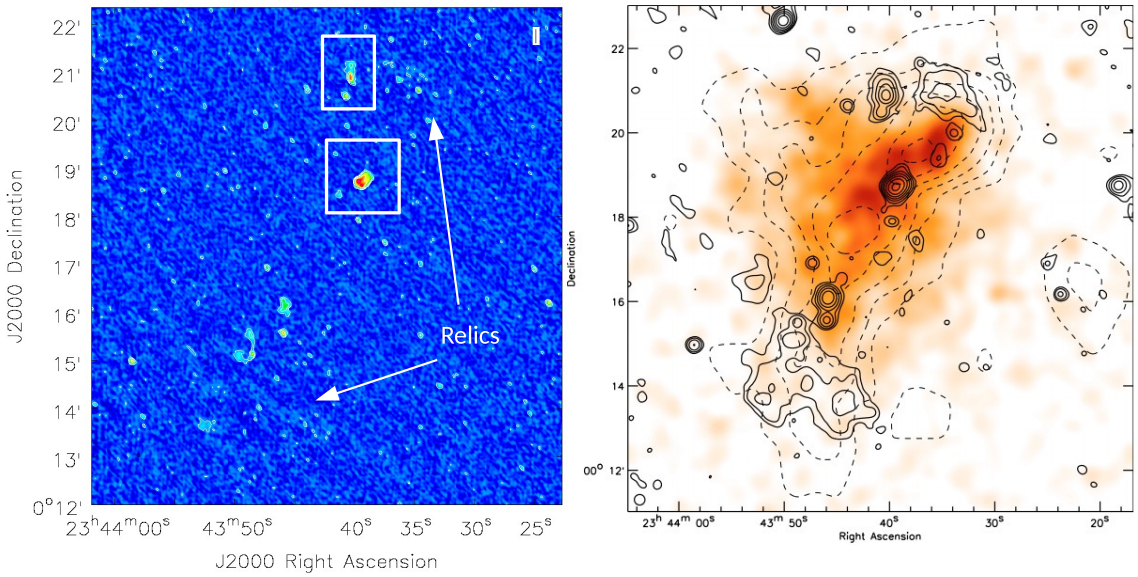

Figure 5.4: Left panel: JVLA total intensity image of the ZwCl 2341.1+0000 at the central frequency of 1.5 GHz (Stuardi et al. in prep.). The image has a restoring beam of $4.3'' \times 3.4''$ and contours are drawn starting from the the 3σ level (with σ=0.012 mJy beam^{-1}) and increasing by a factor of four. The position of the relics is shown and the two polarized sources detected are marked with white squares. Right panel: *Chandra* X-ray image of the cluster in the 0.5-3.0 keV energy band with point-sources subtracted. Black solid contours show the GMRT radio emission at 610 MHz GMRT. Dashed lines show the galaxy isodensity contours from SDSS. Credits: van Weeren et al. (2009).

the main peak of the Faraday spectrum obtained for each detected pixel. The two sources are marked with white squares in Fig. 5.4 and their RM images are shown in Fig. 5.5. In particular, we detected the source that was observed in the NVSS image (left panel) and another source closer to the central region of the cluster (right panel). The latter shows high RM values which are scattered between -79 and 50 rad m^{-2} and only few pixels are detected. The tailed radio galaxy detected close to the northern radio relic shows instead lower and less scattered values of RM with a median value of -19 rad m^{-2}. This behavior is expected because the two radio galaxies are located in different environments, with the one closer to the center lying in a denser region where the Faraday rotation is stronger. In order to derive firm conclusions, a deeper investigation is needed.

The Galactic RM at the position of ZwCl 2341.1+0000 is -9±4 rad m^{-2} (Hutschenreuter & Enßlin, 2020). Hence, not all the Faraday rotation observed from the sources can be ascribed to the Milky Way foreground and a contribution from the large-scale magnetic field of the cluster is favored. Once again, it is not possible to study magnetic field amplification caused by merger shocks using the observations of a single cluster because the number of detected sources is too low and, moreover, there are not polarized sources detected in the pre-shock region. Only the use of

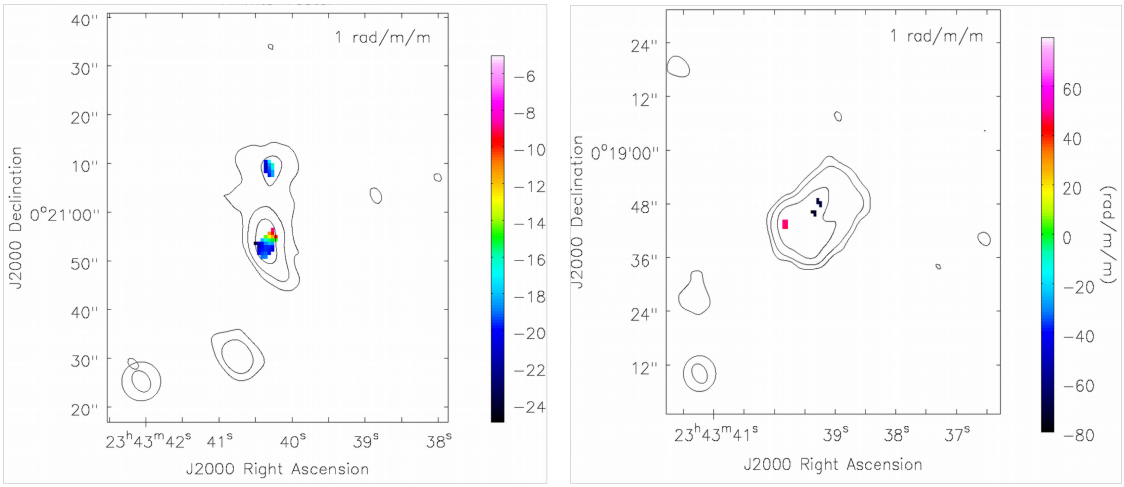

Figure 5.5: RM images of the two detected radio galaxies. The insets show the regions marked with white squares in Fig. 5.4. The RM are shown only for pixels above the $6\sigma_{QU}$ detection threshold. Black contours are the same as in the left panel of Fig. 5.4. The RM image has a restoring beam of $8'' \times 8''$.

a large sample will increase the statistics and this will permit us to constrain the magnetic field amplification by low Mach number shocks.

Chapter 6

Polarimetric observations at low radio frequencies

Radio polarimetric observations below 1 GHz open up a new window for the study of large-scale magnetic fields. In Sec. 2.2 we showed that the accuracy in the RM reconstruction through RM synthesis (i.e., the $\delta\phi$ parameter) depends on the total coverage in wavelength-squared. Therefore, observations at low frequencies can reach the best RM accuracy. This translates into a better magnetic field reconstruction through Faraday rotation measurements. There is, however, a downside because the Faraday depolarization is a wavelength-dependent effect (see Sec. 2.1.3): the decrease in fractional polarization depends on λ^2 in the case of differential Faraday rotation and on λ^4 in the cases of internal and external Faraday dispersion. Hence, the number of detectable polarized sources decreases with increasing wavelength, mainly in high densities and magnetic fields environments. However, when the polarized signal is detected, in the most rarefied regions, long-wavelengths allow to observe the depolarization caused by very small RM gradient and/or by a small amount of RM dispersion which would not cause depolarization at cm-wavelengths.

The LOFAR Two Metre Sky Survey (LoTSS, Shimwell et al., 2017, 2019) offers a unique possibility for polarization studies at 100 MHz-frequencies. This ongoing survey covers the entire northern sky with the LOFAR High-Band Antenna (HBA) at frequencies from 120 to 168 MHz. The first LoTSS data release (DR1) consists of images at $6''$ resolution and a sensitivity of $\sim$70 μJy/beam. It covers 424 deg^2 in the region of the Hobby-Eberly Telescope Dark Energy eXperiment (HETDEX) Spring field (i.e., 2% of the northern sky). The observing time for each pointing is $\sim$8 hours and the FWHM of the primary beam is $\sim 4°$.

Polarization observations in the 120-168 MHz band provide exceptional Faraday rotation measure accuracy (Brentjens, 2018; Van Eck, 2018). Using Eq. 2.26 it is easy to compute that, for a signal-to-noise ratio of 8 in polarization (i.e., $P/\sigma_{QU} = 8$),

LoTSS HBA observations provide σ_ϕ ∼0.08 rad m^{-2} while σ_ϕ is about 3 rad m^{-2} for JVLA L band observations (1-2 GHz). However, there are still some technical challenges that need to be addressed to perform polarization observations with LOFAR. The absolute polarization cannot be calibrated yet and, at the moment, the polarization leakage correction is not implemented. The latter causes the presence of a spurious peak at the level of ~ 1.5 % of the total intensity in the Faraday spectra centered on 0 rad m^{-2}. Thanks to the small $\delta\phi$ of LoTSS observations, it is possible to avoid the instrumental leakage contamination just excluding a small range of the spectrum, i.e. $-3 < \phi < 1$ rad m^{-2} (see also Chapter 7). Finally, residual errors in the ionospheric RM correction were found to be of the order of 0.1-0.3 rad m^{-2} across the 8 hours observations (Van Eck et al., 2018). These errors cause additional depolarization when visibilities are integrated over time.

Despite the technical challenges, preliminary efforts to build a polarization catalog with LOFAR were successfully performed (Mulcahy et al., 2014; Van Eck et al., 2018; Neld et al., 2018). LOFAR polarization capabilities have been recently shown to be well suited for the study of magnetic fields for different science cases ranging from the interstellar medium (Van Eck et al., 2019) to the cosmic web (O'Sullivan et al., 2019, 2020).

Another aspect that needs to be taken into account when observing at 100 MHz-frequencies is the selection effect caused by the Faraday depolarization. Depolarization is less severe in low-density ionized environments, which are characterized by weak magnetic fields with large fluctuation scales (compared to the resolution of the observations), since it depends on the magnetic field and thermal electron density along the line of sight as well as on their spatial gradient within the synthesized beam (see Sec. 2.1.3). For example, a source observed by the LoTSS with a peak total intensity of 1 Jy beam^{-1} and a 20% intrinsic fractional polarization level can be detected in polarization with a signal-to-noise larger than 6 only if the RM dispersion within the beam is lower than ∼0.4 rad m^{-2} (considering $\sigma_{QU} = 0.1$ mJy beam^{-1} and external depolarization with $p(\lambda) \propto e^{-2\sigma^2_{\rm RM}\lambda^4}$). Sources that lie within or behind a medium with larger RM dispersion would remain undetected. This is the case of galaxy cluster centers where we expect typical $\sigma_{\rm RM} \gg 1$ rad m^{-2} (using, as reference values, B∼1 μG, $n_e \sim 10^{-3}$ cm^{-3}, Λ_C ∼1 kpc and L ∼1 Mpc in Eq. 2.10). Therefore, polarization in the sub-GHz regime is mainly expected from sources that populate low-densities and weak magnetic fields environments, identified with the extreme outskirts of galaxy clusters, filaments and voids of the cosmic web.

In this Chapter, I will describe two studies of polarization at 100 MHz-frequencies, one focused on the Coma radio relic and the other on the investigation of the magnetic fields in the cosmic web. The former was performed as part of my PhD project and it will be included in a forthcoming publication (Bonafede et al. in prep.), the latter is strictly connected to the work described in Chapter 7 and it has been re-

cently published in a paper to which I contributed as a co-author (O'Sullivan et al., 2020).

6.1 Observing the Coma radio relic in polarization with LOFAR

The Coma cluster is a well studied merging system at redshift 0.023. Indeed, the Coma radio halo was the first diffuse source ever detected in the ICM (Large, Mathewson & Haslam, 1959). A radio relic was also observed at the western periphery of this cluster (Ballarati et al., 1981; Giovannini, Feretti & Stanghellini, 1991). Since then, a number of observational multi-wavelength campaigns have been carried out on this cluster making it a milestone for galaxy clusters science. X-ray observations suggested the presence of a filamentary structure south-west of the Coma cluster, associated with the western NGC 4839 galaxy group and with the relic (Simionescu et al., 2013; Lyskova et al., 2019). Recent studies have explored the large-scale structure around the Coma cluster discovering hints of gas accretion from the cosmic web along a filament connecting Coma to another merging system (Malavasi et al., 2020; Mirakhor & Walker, 2020). Ogrean & Brüggen (2013) and Akamatsu et al. (2013) found a possible shock with Mach number $\sim$2, in a region spatially coincident with the relic.

The relic in the Coma cluster is one of the best candidates for magnetic field studies: it is nearby, thus it has a large angular extent ($\sim 0.^{\circ}5$) and a high flux density (260 mJy at 1.4 GHz). Previous studies have constrained the magnetic field strength and structure in the cluster and relic region using VLA observations of background radio sources (Bonafede et al., 2010, 2013).

Low-resolution (i.e., $\sim 900''$) observations of the Coma radio relic at 1.4 GHz performed with the Green Bank Telescope (Brown & Rudnick, 2011) have shown low levels of fractional polarization in the relic region ($12 - 17$ %). Previous studies found values of fractional polarization between 25 and 40 % at 4.75 GHz and between 20 and 30 % at 2.7 GHz (Andernach, Feretti & Giovannini, 1984, with the Effelsberg telescope at resolution $\sim 260''$). Since higher fractional polarization values are often observed from radio relics, depolarization effects are likely present. Higher-resolution observations at lower frequencies can help to disentangle between beam depolarization and Faraday depolarization effects. Hence, LoTSS observations can be a good tool to search for polarization from the Coma radio relic. This search is also motivated by the fact that radio relics are typically brighter at lower frequencies thanks to their steep spectral index.

The data used in this work consist of two LoTSS pointings which have been calibrated and imaged following the procedures described in Bonafede et al. (2020). The Coma cluster observed at LOFAR frequencies is shown in Fig. 6.1 where the

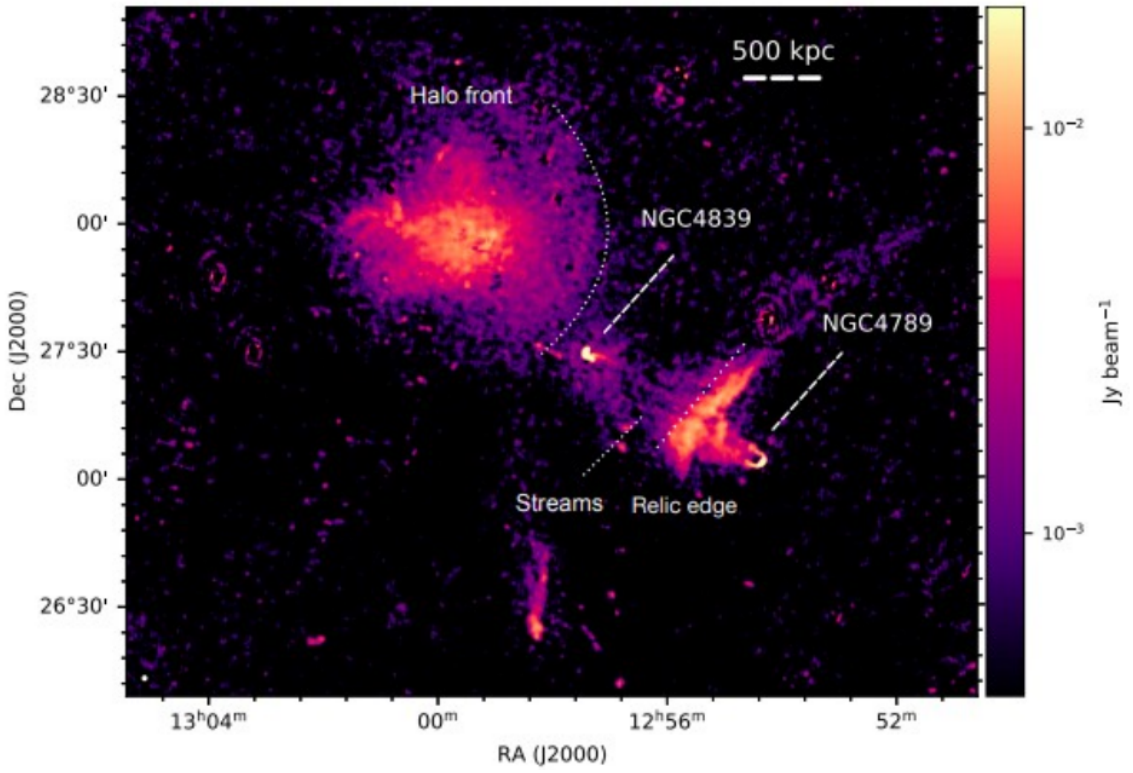

Figure 6.1: The Coma cluster observed at 144 MHz with LOFAR. The bridge emission is visible in between the halo and the relic and the most important radio features and sources are labeled. Credits: Bonafede et al. (2020).

emission of the bridge connecting the NGC 4839 group to the Coma cluster is also visible. The main results achieved in Bonafede et al. (2020) are focused on the radio bridge and will be described in the following Section, while the detailed study of the radio relic emission will be the subject of a forthcoming paper.

The Coma radio relic was present in both pointings at different distances from the pointing center. Polarization imaging and RM synthesis were separately performed for the two pointings since, as already mentioned, the absolute polarization angle has not been calibrated [*]. Q and U sub-band images of ∼98 kHz each with 20″ restoring beam were made in the 120-168 MHz band. Imaging has been performed with DDFacet [†] (Tasse et al., 2018). The Q and U images were not deconvolved because this procedure was not implemented in DDFacet at the time of writing.

We performed the RM synthesis applying a threshold of 1 mJy beam^{-1} in the total intensity map, corresponding to a 5σ Gaussian significance. This was done to speed up the process and considering that no fractional polarization $< 50\%$ could be detected for sources with lower surface brightness due to the LoTSS sensitivity. The observing band-width and the chosen channelization imply the theoretical values: $\delta\phi$=1.2 rad m^{-2}, $\Delta\phi_{\rm max}$=0.96 rad m^{-2} and $|\phi_{\rm max}|$=171 rad m^{-2} (computed using Eq. 2.19, 2.21, and 2.20). Since $\Delta\phi_{\rm max} < \delta\phi$ no Faraday-complex structures can be observed.

At first, we have applied the RM synthesis in the range $\phi < |500|$ rad m^{-2} on channels of 0.5 rad m^{-2}. Since there were not significant peaks (i.e. with signal-to-noise above 8) outside the range $\phi < |200|$ rad m^{-2} we repeated the RM synthesis with a finer ϕ channelization of 0.2 rad m^{-2} in the range $\phi < |200|$ rad m^{-2}. We did not perform RM clean because the signal-to-noise was too low.

The first results we have obtained is that, in both pointings, there were no pixels with signal-to-noise above 8 in the whole relic region. We decided to compare the RM obtained from the two pointings in order to asses if, although with low significance, the same RM values would be recovered in both pointings with a $6\sigma_{QU}$ detection threshold. The results of this consistency check are that no one pixel was found to be polarized in both pointings, most of the polarized neighboring pixel in the two pointings had very different $\phi_{\rm peak}$ values, and the distribution of $\phi_{\rm peak}$ values in the two pointings was scattered on the entire Faraday range (see Fig. 6.2).

We conclude that we did not detect polarization from the Coma radio relic above 1 mJy beam^{-1} at the central frequency of 144 MHz with LoTSS observations. Using the average surface brightness in total intensity in the relic region (∼ 2.5 mJy beam^{-1}), it is possible to compute the upper limit of ∼ 40 % to the fractional polarization of the Coma radio relic at 144 MHz.

[*] A technique to stack Stokes Q and U data cubes for deep LOFAR observations was recently discussed in Herrera Ruiz et al. (2020)

[†] https://github.com/mhardcastle/ddf-pipeline

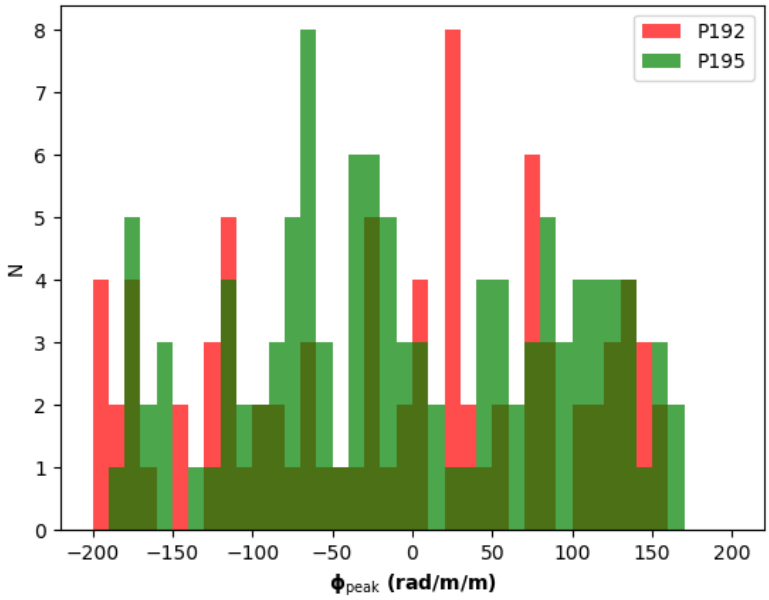

Figure 6.2: Distribution of $\phi_{\rm peak}$ (RM) values found in the two pointings (P195 and P192) in the relic region with a detection threshold of $6\sigma_{QU}$.

This result confirms the presence of a strong internal and/or external Faraday depolarization. The depolarization could be caused either by a turbulent magneto-ionic material filling the region where the relic is located and/or by the complex geometry of the magnetic field in the relic, as shown by cosmological simulations in shocked regions (e.g., Wittor et al., 2019).

As a further probe, we also checked other few bright radio relics observed in the second LoTSS data release, but none of them shows polarization with signal-to-noise higher than 8. The RM dispersion or RM gradient caused by the intra-cluster magnetic field prevents the detection of polarized emission at 100 MHz-frequencies even in in the outskirts of galaxy clusters. Being already an important result, this suggests to search for sources further away from galaxy clusters to observe polarization at these frequencies (see Chapter 7).

The radio bridge in the Coma cluster

In Bonafede et al. (2020), we analyzed the emission of the radio bridge connecting the Coma cluster to the NGC 4839 galaxy group. The discovery of bridges of radio emission connecting clusters and merging groups (Bonafede et al., 2018) or massive clusters in a pre-merger state (Govoni et al., 2019; Botteon et al., 2020c) is very recent, and it was made possible by low-frequency instruments. In the case of Coma, the bridge is connected by streams of emission with the radio relic, its

surface brightness peaks on the NGC 4839 group and decreases towards the radio halo (see Fig. 6.1).

The radio emission in the bridge can be only partially explained by the cooling of particles in the downstream of the shock that formed the radio relic. Additional (re)acceleration mechanisms have to be invoked. Archival Westerbork Synthesis Radio Telescope (WSRT) observations at 326 MHz were used to constrain the spectral index in the bridge that is a fundamental information to understand the origin of the radio emission. The average spectral index in the bridge is $1.4 \pm 0.2 \leq \alpha \leq 1.6 \pm 0.2$ and the emission appears to be clumpier at 326 MHz than at 144 MHz. Another important information is obtained from the spatial correlation of radio and X-ray emission. This was investigated using archival ROSAT observations that revealed a moderate positive correlation, which is expected if the radio emission is volume-filling as the X-ray emission.

Simplified energetic considerations showed that the radio bridge may originate from the turbulent particle re-acceleration at work in the dynamically active region of the NGC 4839 group. Cosmological simulations were used in order to investigate this scenario. Assuming the presence of seed electrons with an initial non-thermal to thermal energy ratio of 3×10^{-4}, the emission from the simulated radio bridge was found to be in general agreement with observational properties. The seed electron population could have been supplied by cluster radio galaxies. The combination of turbulent motions injected by accretion processes and of the presence of a considerable amount of seed particles in the medium could explain the Coma radio bridge emission.

6.2 New constraints on the magnetization of the cosmic web

Low-frequency polarization observations of background radio sources are key tools for the of study large-scale magnetic fields. This concept triggered the studies published in O'Sullivan et al. (2020) and in Stuardi et al. (2020). The latter work will be fully described in Chapter 7.

In O'Sullivan et al. (2020), we investigated the properties of the extra-galactic magnetic field through its Faraday rotation effect on background sources. In particular, we considered the RM difference (ΔRM) between polarized physical pairs (i.e., double-lobed radio galaxies) and non-physical pairs (i.e., two close sources due to projection effects) observed within the LoTSS second data release (see Fig. 6.3). This method allowed us to statistically disentangle the contribution of extra-galactic magnetic fields to the RM difference between non-physical pairs, from the one due to the Milky Way.

We found that there is no significant difference between the ΔRM distributions of physical and non-physical pairs when observed at 144 MHz, constraining the extra-

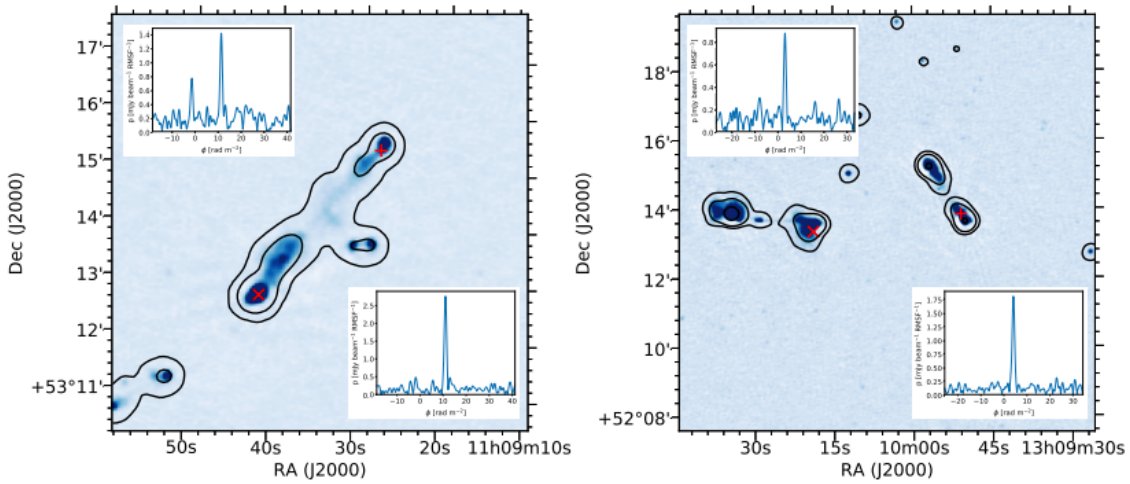

Figure 6.3: Example of a physical pair (left) and a non-physical pair (right). The cross and plus symbols represent the location of the peak polarized intensity from which the RM is taken and the correspondent Faraday spectra are shown in the top left and bottom right insets, respectively. Credits: O'Sullivan et al. (2020).

galactic RM contribution to be <1.9 rad m^{-2}. In order to translate this upper limit into a limit on the co-moving cosmological magnetic field strength, we compared the observational constraint with the RM difference computed from a numerical simulation. We modeled an inhomogeneous Universe, with an initial cosmological magnetic field evolving with the local gas density variations. The comparison resulted in an upper limit of 4 nG on the co-moving cosmological magnetic field on Mpc scales. The observations were also compared with cosmological MHD simulations to investigate different magnetogenesis scenarios (see Sec. 1.3.2). The astrophysical scenario and a primordial scenario with a seed field of B<0.5 nG were found to be consistent with the data, while stronger primordial fields or models involving dynamo amplification are disfavored.

Once again, low-frequency observations proved to be fundamental. This is unveiled by the comparison with similar studies performed at higher radio frequencies (e.g., Vernstrom et al., 2019, at 1.4 GHz). These studies found an higher ΔRM excess for non-physical pairs with respect to physical pairs. Conversely, the small extra-galactic contribution observed at 144 MHz suggests that the dominant contribution to the ΔRM excess observed at 1.4 GHz is due to the magneto-ionic material local to the radio sources. Due to the Faraday depolarization effects, low-frequency observations naturally select sources for which the local RM contribution is lower, and therefore they are ideal to study the weak magnetization of the cosmic filaments and voids far from galaxy cluster environments.

Chapter 7

The intergalactic magnetic fields probed by giant radio galaxies *

Giant radio galaxies (GRGs) are physically large radio sources that extend well beyond their host galaxy environment. Their polarization properties are affected by the poorly constrained magnetic field that permeates the intergalactic medium on Mpc scales. A low frequency (< 200 MHz) polarization study of this class of radio sources is now possible with LOFAR.

Here, we investigate the polarization properties and Faraday rotation measure of a sample of 239 GRGs detected in the LoTSS. This is the first low frequency polarization study of a large sample of radio galaxies selected on their physical size. We explore the magneto-ionic properties of their under-dense environment and probe intergalactic magnetic fields using the Faraday rotation properties of their radio lobes.

Throughout this Chapter, we assume a ΛCDM cosmological model, with $H_0 = 67.8$ km s^{-1} Mpc^{-1}, $\Omega_{\rm M} = 0.308$, and $\Omega_\Lambda = 0.692$ (Planck Collaboration et al., 2016b).

7.1 Giant radio galaxies

A lower limit of 1 Mpc in size was historically adopted to define GRGs, assuming $H_0 = 50$ km s^{-1} (Willis, Strom & Wilson, 1974). Nowadays the general consensus is to use a limiting size of 0.7 Mpc in order to maintain the classification within the revised cosmology (e.g., Dabhade et al., 2017; Kuźmicz et al., 2018). GRGs are mostly FR II radio galaxies, with lobes that extend well beyond the host galaxy and local environment and that also expand into the surrounding IGM. They are

*Based on Stuardi et al. (2020)

particularly interesting objects for the study of different astrophysical problems, ranging from the evolution of radio sources (Ishwara-Chandra & Saikia, 1999) to the ambient gas density (Mack et al., 1998; Malarecki et al., 2015; Subrahmanyan et al., 2008). In particular, Faraday rotation and polarization properties of the lobe and hotspot emission can be used to study the nature of intergalactic magnetic fields (O'Sullivan et al., 2019). In the future, giant radio galaxies will also be targeted with the SKA to probe the warm-hot intergalactic medium (WHIM, Peng, Chen & Strom, 2015).

GRGs are a small subclass of radio galaxies: they constitute about 6 % of the complete sample of 3CR radio sources (Laing, Riley & Longair, 1983). Until recently, only a few hundred GRGs had been reported (e.g., Kuźmicz et al., 2018, and references therein). Only now, last-generation interferometers have started to demonstrate that the number of GRGs has been significantly underestimated in the past due to the limited sensitivity of traditional instruments to low surface brightness emission (Brüggen et al., 2020; Delhaize et al., 2020). The LoTSS is one of the best surveys to identify GRGs thanks to its high sensitivity to low surface brightness sources, the high angular resolution, and the high quality associations with optical counterparts including redshifts. Recently, Dabhade et al. (2020) reported a large catalog of 239 GRGs, of which 225 are new findings from the LoTSS first data release (DR1). Optical and infrared identifications and redshift estimates are available for the entire sample (Williams et al., 2019; Duncan et al., 2019).

In Chapter 6 we discussed the power of polarization studies in the sub-GHz regime, for which GRGs are preferential targets. Previous work probed the strong polarization of the lobes of GRGs at low radio frequencies (e.g., Willis, Wilson & Strom, 1978a; Bridle et al., 1979; Tsien, 1982; Mack et al., 1997). One of the first objects observed in polarization by LOFAR was the double-double giant radio galaxy B1834+620 (Orrù et al., 2015) and, recently, a polarization study of the giant radio galaxy NGC 6251 was performed with LOFAR (Cantwell et al., 2020). Machalski & Jamrozy (2006) also showed that GRGs are less depolarized at 1.4 GHz than normal-sized radio galaxies, indicating the presence of less dense gas surrounding their lobes. Hence, the lobes of GRGs are probably one of the best targets for polarization studies at low frequencies (O'Sullivan et al., 2018a). While previous GRG polarization studies were based on single sources, or at most tens of objects, which were observed with different facilities, LOFAR allowed us to perform the first study on a large sample of hundreds of GRGs that were selected and analyzed consistently.

A low density ($\sim 10^{-5} - 10^{-6}$ cm^{-3}) WHIM permeates the large scale structure of the Universe from the extreme outskirts of galaxy clusters to filaments (Davé et al., 2001). Previous studies demonstrated that lobes of GRGs evolve and interact with the WHIM (Mack et al., 1998; Chen et al., 2011). In these regions, the

inter-galactic magnetic field is expected to range from 1 to 100 nG, with the true value being important to discriminate between different magneto-genesis scenarios (Brüggen et al., 2005; Vazza et al., 2017; Vernstrom et al., 2019). While the detection of both thermal and nonthermal emission of the WHIM is still an observational challenge (Vazza et al., 2019), GRGs are potentially indirect probes of these poorly constrained regions of the Universe (Subrahmanyan et al., 2008). RM and depolarization information derived from the polarized emission of GRGs can yield tomographic information about this extremely rarefied environment (O'Sullivan et al., 2019).

7.2 Data analysis

Our work is based on the data from LoTSS, which are fully described by Shimwell et al. (2017, 2019) and presented in Chapter 6. Although our work is mainly based on the GRG catalog by Dabhade et al. (2020), which is located in the DR1 region, we make use of the updated data products from the upcoming LoTSS second data release (DR2, Tasse et al., 2020).

7.2.1 Calibration and data reduction

We refer the reader to Shimwell et al. (2017) for the full details on the calibration and data reduction. Here we summarize only the main steps.

For our analysis, we used images at 20″ and 45″ resolution. The choice of a restoring beam that is larger than 6″ (used for the LoTSS DR1) was meant to maximize the sensitivity to the extended emission of the lobes. The 20″ resolution images from the upcoming LoTSS DR2 pipeline (Tasse et al., 2020) were used to identify polarized sources and record the position, polarized flux density, fractional polarization, and RM of the pixels with the highest signal-to-noise ratio (see Sec. 7.2.3). The 45″ resolution images of the detected sources were instead necessary to be compared with images at 1.4 GHz and to perform the depolarization analysis (see Sec. 7.2.4). We used two different strategies for calibration and imaging at the two resolutions to cross-check the reliability from the `ddf-pipeline`[†] (Tasse, 2014; Tasse et al., 2018; Shimwell et al., 2019) output and also to enable deconvolution in Stokes Q and U at 45″. We obtained a reliable calibration and imaging performance with both procedures, which are described in the following.

Direction-dependent calibration was performed using the `ddf-pipeline`. Calibrated data were used for the total intensity images at 20″ resolution in order to better resolve the morphological properties of the sources. These data were also used to image Stokes Q and U frequency channel cubes at 20″ resolution.

[†]https://github.com/mhardcastle/ddf-pipeline

We made low resolution 45″ images of the GRGs that were detected in polarization at 20″ (see Sec. 7.2.3). Only direction-independent calibration was performed using `PREFACTOR 1.0`[‡] (van Weeren et al., 2016b; Williams et al., 2016). This procedure is robust, because of the absence of any large direction-dependent artifacts in the Q and U images, and allowed us to deconvolve the emission at 45″ without rerunning the entire calibration on the full LoTSS field where a GRG had been detected. The root mean square noise level was on average one order of magnitude larger at 45″ than at 20″ due to the uv-cut and down-weighting of data on the longer baselines. The direction-independent calibrated data were phase-shifted to the source location and averaged to 40 s (from 8 s) to speed up the imaging and deconvolution process (as in, e.g., Neld et al., 2018; O'Sullivan et al., 2019).

The ionospheric RM correction was applied with `RMextract`[§] (Mevius, 2018). Residual ionospheric RM correction errors are estimated to be $\sim$ 0.05 rad m^{-2} between observations and $\sim 0.1-0.3$ rad m^{-2} across the 8h observations (Sotomayor-Beltran et al., 2013; Van Eck et al., 2018).

7.2.2 Polarization and Faraday rotation imaging

The Q and U images at 20″ resolution were not deconvolved because this procedure was not implemented in the `ddf-pipeline` at the time of writing. Although some of the RM structure for the brightest polarized sources is dominated by a spurious structure, this should not affect our analysis since we used the RM value at the peak of the polarized emission. We used `WSClean 2.4`[¶] (Offringa et al., 2014) to deconvolve the Q and U images at 45″ resolution in order to directly compare with polarization images from the NVSS at 1.4 GHz (Condon et al., 1998). In 90 % of the cases, we obtained consistent RMs at 45″ and 20″. We found a larger scatter in the values obtained at low resolution, which is as expected due to the larger beam and higher noise.

We created 480 Q and U frequency channel images with 0.1 MHz resolution between 120 and 168 MHz with a fixed restoring beam (20″ or 45″). The primary beam correction was applied to each channel. The total intensity (I) image was created using the entire band at the central frequency of 144 MHz and then corrected for the primary beam. All of the pixels below 1 mJy beam^{-1} in total intensity (for which no fractional polarization $<$ 50 % can be detected due to the LoTSS sensitivity) were masked out to speed up the subsequent analysis.

We performed RM synthesis (Brentjens & de Bruyn, 2005) on the Q and U per-channel cubes using `PYRMSYNTH`[‖] to obtain the cubes in the Faraday depth (ϕ) space.

[‡]https://github.com/lofar-astron/prefactor
[§]https://github.com/lofar-astron/RMextract
[¶]https://sourceforge.net/p/wsclean/wiki/Home/
[‖]https://github.com/mrbell/pyrmsynth

In these cubes, every pixel contains the Faraday spectrum along the line of sight, that is, the polarized intensity at each Faraday depth (see Sec. 2.2). An example Faraday spectrum extracted from the peak of polarized intensity of a source is shown in Fig. 7.1. RM clean was also performed on the 45″ cubes (Heald, 2009).

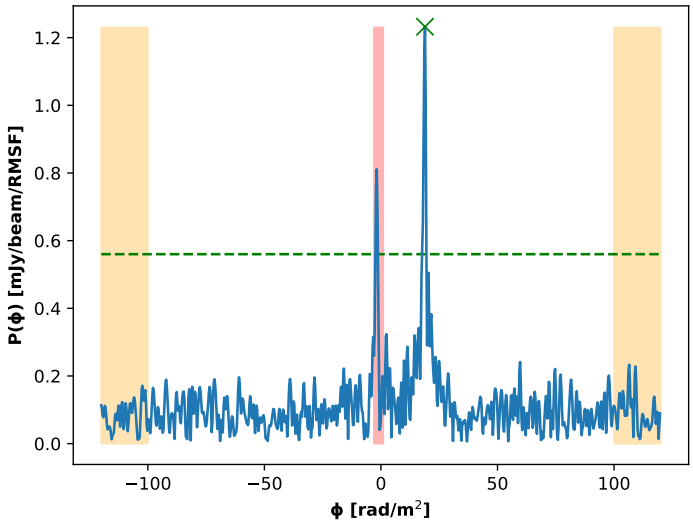

Figure 7.1: Example Faraday spectrum. In particular, this is the Faraday spectrum obtained at the polarized peak position of the lobe "b" of GRG 2 (see Tab. 7.2). The red shadowed area shows the region of the spectrum excluded due to the instrumental leakage contamination. The orange areas show the range used to compute the root mean square noise from the Q and U Faraday spectra. The green dashed line highlights the 8σ detection threshold. The green "X" marks the position of the peak from which we derived the RM and P values of the pixel.

Considering the LoTSS bandwidth and the adopted channelization, and using Eq. 2.19, 2.20 and 2.21, we can estimate our resolution in Faraday space, $\delta\phi = 1.16$ rad m^{-2}, the maximum observable Faraday depth, $|\phi_{\rm max}| = 168$ rad m^{-2}, and the largest observable scale in Faraday space, $\Delta\phi_{\rm max} = 0.97$ rad m^{-2}. As a consequence, with LoTSS, we can only detect emission that is unresolved in Faraday depth. Faraday cubes were created between -120 and 120 rad m^{-2} and sampled at 0.3 rad m^{-2}. The Faraday range was chosen considering that RM values for sources at high Galactic latitude (above $b > 55°$) and outside galaxy cluster environments are a few tens of rad m^{-2} (see, e.g., Böhringer, Chon & Kronberg, 2016).

The LOFAR calibration software (i.e., `PREFACTOR 1.0`) does not allow instrumental polarization leakage correction so that peaks appear in the Faraday spectrum at the level of ~ 1.5 % of the total intensity in the range of $-3 < \phi < 1$ rad m^{-2} (see Fig. 7.1). This asymmetric range is due to the ionospheric RM correction that shifts the leakage peak along the Faraday spectrum (Van Eck et al., 2018). We thus

excluded this range in order to avoid contamination from the instrumental leakage as was done by other authors (e.g., Neld et al., 2018; O'Sullivan et al., 2019). This method systematically excluded all real polarized sources within this Faraday depth range from this analysis. We fit, pixel-by-pixel, a parabola around the main peak of the Faraday spectrum outside of the excluded range. We obtained the RM and polarized intensity (P) images from the position of the parabola vertex in each pixel. Hence, we obtained the RM values in the observer's frame, i.e. not corrected for the redshift of the rotating Faraday screen which is unknown *a priori*. For each pixel, we computed the noise, σ_{QU}, as the standard deviation in the outer 20 % of the Q and U Faraday spectra and we imposed an initial $6\sigma_{QU}$ detection threshold, which ensures an equivalent 5σ Gaussian significance (Hales et al., 2012). We also computed the fractional polarization (p) images by dividing the polarization image P obtained from the RM synthesis by the full-band total intensity image I (with a 3σ detection threshold, where σ is the local root mean square noise). We computed the fractional polarization error map by propagating the uncertainties on P and I images.

The RM error map was computed dividing $\delta\phi$ by twice the signal-to-noise ratio of the detection as per Eq. 2.26. the computed error does not include the systematic error from the ionospheric RM correction ($\sim$0.1 rad m^{-2}, Van Eck et al., 2018).

7.2.3 Source identification

Using the 20″ images, we compiled a catalog of polarized sources in the LoTSS. Each source is represented by the pixel with the highest signal-to-noise ratio within a $\sim$5-beam-size region above the $6\sigma_{QU}$ threshold. For each source, we listed the sky coordinates, the polarization signal-to-noise level, the fractional polarization, the RM value, and the separation from the pointing center in degree. When the same source was detected in several pointings of the survey, we selected the image with the highest signal-to-noise ratio and which was closest to the pointing center.

We cross-matched our catalog with the catalog of 239 GRGs in the LoTSS DR1 compiled by Dabhade et al. (2020) by choosing different radii to match the angular size of the sources. The cross-match resulted in 51 GRGs showing radio emission that is coincident with at least one entry in the polarization catalog. Through a careful visual inspection, we excluded 15 sources for which polarization was detected in less than four pixels with a signal-to-noise ratio lower than 8 and only in one pointing of the survey (or in two pointings but with different RM values). The final detection threshold in polarization is thus $8\sigma_{QU}$: This conservative choice is motivated by both the literature (see, e.g., George, Stil & Keller, 2012; Hales et al., 2012) and by our experience with RM synthesis data. The 36 GRGs that were clearly detected in polarization are listed in Tab. 7.1. The GRG numbers refer to the source numbers in the Dabhade et al. (2020) catalog. In Tab. 7.1, we also added 3C 236: It is one

of the largest radio galaxies known (Willis, Strom & Wilson, 1974) and, although it was not present in the LoTSS DR1, it was recently observed by LOFAR (Shulevski et al., 2019). Hereafter, we refer to this source as GRG 0.

Table 7.1: Polarized GRGs. Column 1: progressive GRG identification number from Tab. 2 in Dabhade et al. (2020); Column 2 and 3: J2000 celestial coordinates of the host galaxy. The reference is Dabhade et al. (2020) for all of the GRGs, apart from GRG 0 for which we refer to Becker, White & Helfand (1995); Column 4: redshift (z); Column 5 and 6: angular and projected linear size; Column 7: Fanaroff-Riley type (Fanaroff & Riley, 1974). GRG 136 has a peculiar morphology and thus it is not classified; Column 8: the letter indicates if the GRG is detected as a double ("d") or a single ("s") source in polarization. Polarized emission was detected from the core and/or inner jets region only in the case of GRG 117.

GRG	R.A. (deg)	Dec (deg)	z	Ang. size (arcsec)	Lin. size (Mpc)	FR	Remark
1	164.273	53.440	0.460^a	153	0.92	II	d
2	164.289	48.678	0.276^a	439	1.9	II	d
7	164.575	51.672	0.415^a	330	1.86	II	s
19	167.402	53.230	0.288^b	230	1.03	II	d
22	168.381	46.371	0.589^b	112	0.76	II	d
44	174.882	47.357	0.518^a	312	2.0	II	s
47	178.000	49.849	0.891^a	96	0.77	II	s
51	180.345	49.427	0.205^b	345	1.2	I	d
57	182.692	53.490	0.448^a	119	0.71	I	s
64	184.576	53.456	0.568^c	183	1.23	II	d
65	184.708	50.438	0.199^a	210	0.71	II	d
77	186.493	53.161	0.811^c	147	1.14	II	d
80	187.498	53.546	0.523^c	137	0.88	II	s
83	188.210	49.107	0.690^a	256	1.87	II	s
85	188.756	53.299	0.345^d	683	3.44	II	d
87	189.202	46.068	0.615^b	125	0.87	II	d
91	190.052	53.577	0.293^a	164	0.74	II	d
103	195.396	54.136	0.313^b	168	0.79	II	d
112	197.620	52.228	0.650^b	197	1.41	II	s
117	199.144	49.544	0.563^b	126	0.84	II	core
120	200.124	49.280	0.684^a	113	0.82	II	d
122	200.902	47.497	0.440^b	180	1.05	II	s
136	203.345	53.547	0.354^b	173	0.88	-	s
137	203.549	55.024	1.245^a	91	0.78	II	s
144	204.845	50.963	0.316^b	174	0.83	II	d
145	205.263	49.267	0.747^c	113	0.85	II	d

148	206.065	48.764	0.725[b]	202	1.51	II	s
149	206.174	50.383	0.763[a]	123	0.93	II	s
165	210.731	51.458	0.518[c]	135	0.87	II	d
166	210.813	51.746	0.485[c]	228	1.41	II	d
168	211.421	54.182	0.761[c]	116	0.88	II	d
177	213.535	48.699	1.361[b]	107	0.92	II	d
207	220.033	55.452	0.584[c]	238	1.62	II	s
222	222.739	53.002	0.918[a]	184	1.48	II	d
233	226.190	50.502	0.652[c]	201	1.44	II	d
234	226.553	51.619	0.611[a]	262	1.82	II	s
0*	151.507	34.903	0.1005[e]	2491	4.76	II	d

[a] Spectroscopic redshifts from the Sloan Digital Sky Survey (SDSS, York et al., 2000).
[b] Redshifts from the LoTSS DR1 value-added catalog (Williams et al., 2019; Duncan et al., 2019).
[c] Photometric redshifts from the SDSS.
[d] Spectroscopic redshift from O'Sullivan et al. (2019).
[e] Spectroscopic redshift from Hill, Goodrich & Depoy (1996).
* GRG 0 is 3C 236 that was added to the Dabhade et al. (2020) catalog for this analysis.

7.2.4 Faraday depolarization

We used the images of the NVSS in order to estimate the amount of Faraday depolarization between 1.4 GHz and 144 MHz. To match the NVSS resolution, we used the 144 MHz images at 45″. We find that 8.5 % of the sources detected at 144 MHz are not detected by the NVSS due to the lower sensitivity of this survey compared to LoTSS. For some sources, the polarized emission is not exactly co-spatially located at the two frequencies but always separated by less than a single beam-width of 45″ (see Sec. 7.6).

For each component (i.e., lobes and hotspots of single and double detections as well as the core and/or inner jets of GRG 117), we estimated the depolarization factor, $D^{144\ \mathrm{MHz}}_{1.4\ \mathrm{GHz}}$, as the ratio between the degree of polarization at 144 MHz (at the peak polarized intensity location at 45″) and the degree of polarization in the NVSS image at the same location. When there was an offset between LOFAR and NVSS detection, we chose the brightest LOFAR pixel in the overlapping region to compute the depolarization factor. With this definition, $D^{144\ \mathrm{MHz}}_{1.4\ \mathrm{GHz}}=1$ means no depolarization, while lower values of $D^{144\ \mathrm{MHz}}_{1.4\ \mathrm{GHz}}$indicate stronger depolarization.

7.3 Results

The 37 GRGs are displayed in Fig. 7.9. Contours show the total intensity. The left-hand panel is the total intensity image at 20″ resolution, the central panel is

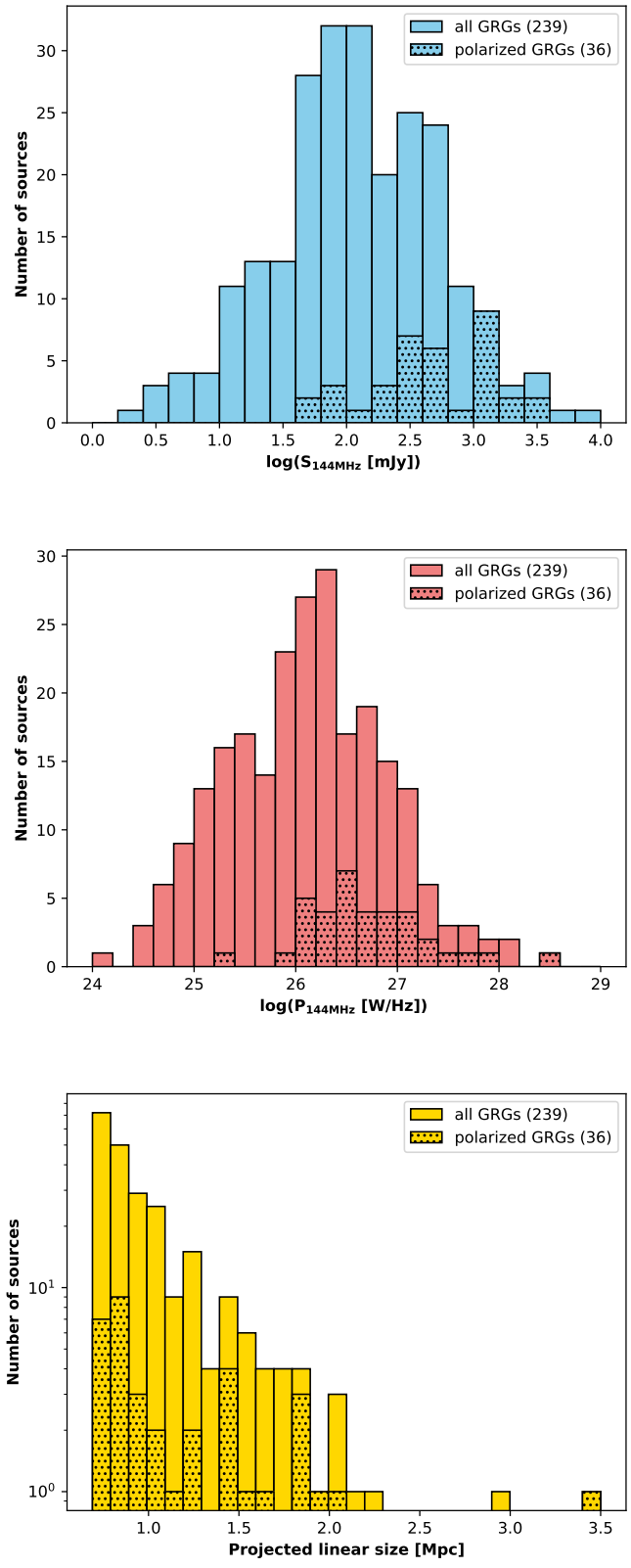

Figure 7.2: Flux density (top), radio power (center), and projected linear scale (bottom) distributions of the LoTSS DR1 GRG catalog (Dabhade et al., 2020) compared with the 36 GRGs detected in polarization at 144 MHz within this sample.

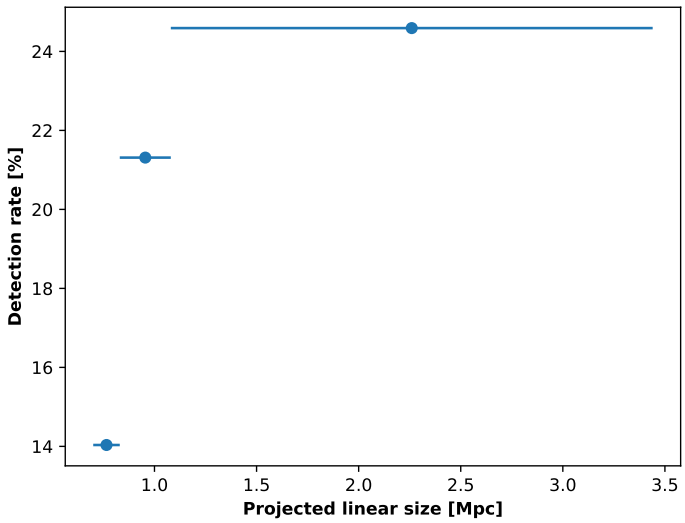

Figure 7.3: Detection rate as function of the projected linear size of the GRGs from the distribution shown in the bottom panel of Fig. 7.2. The widths of the bins were computed to contain the same total number of sources (∼60). The markers are positioned at the center of each bin and the error bars show the bin width.

the LOFAR fractional polarization at 45″ resolution, and the right-hand panel is the NVSS fractional polarization at 45″.

We note that 3C 236 (GRG 0) was not present in the original GRG catalog by Dabhade et al. (2020). Since it was selected only because its polarization at low frequencies was studied in previous work (e.g., Mack et al., 1997), it is not included in the following paragraphs where we compute the polarization detection rates.

Out of the 36 polarized sources in the GRG catalog, 33 are FR II type sources, two are FR I (i.e., GRG 51 and GRG 57), and GRG 136 has a peculiar morphology (see Tab. 7.1). Only six of them have a quasar host, while all of the others are radio galaxies (Dabhade et al., 2020). In 75% of cases, the detection is coincident with the hotspots of FR II radio galaxies. This is consistent with the fact that compact emission regions probe smaller Faraday depth volumes and they are thus less depolarized. In 19% of cases, the polarized emission is detected from the more diffuse lobe regions. In these cases, the hotspots may have a lower intrinsic fractional polarization than the lobes. In one case (GRG 117), we detected polarization that is coincident with the core within our spatial resolution. Since the core of a radio galaxy is not expected to be significantly polarized, this may be a restarted radio galaxy (e.g., Mahatma et al., 2019) with polarized emission arising from the unresolved inner jets. The other detections are from the outer edge of FR I type galaxies and from the extended lobe of the peculiar GRG 136.

The histogram distributions of the total radio flux density, the total radio power,

and the projected linear size of the whole sample of 239 GRGs are shown in Fig. 7.2, together with the distribution of polarized ones. The GRGs detected in polarization have $S_{144MHz} \geq 56$ mJy in total intensity, suggesting a selection effect due to the sensitivity of the survey. Out of the 239 GRGs in the parent sample, 179 sources have $S_{144MHz} > 50$ mJy: Above this threshold, the detection rate is thus 20.1 %. With a lower flux density limit of 10 mJy (i.e., 223 GRGs), the detection rate is 16.1 %.

The preliminary LoTSS polarized point-source catalog compiled by Van Eck et al. (2018) obtained a $\ll 1\%$ polarization detection rate for all of the sources in the DR1 with total flux densities above 10 mJy (see also O'Sullivan et al., 2018a). Our results cannot be directly compared with this work because of the different resolution and the peculiar nature of GRGs. While the majority of the sources in our sample have a large physical and also angular extent, the detection rate computed by Van Eck et al. (2018) takes more compact sources into account. Furthermore, Van Eck et al. (2018) used preliminary LoTSS images with 4.3′ angular resolution. In-beam depolarization, caused by the mixing of different lines-of-sight into the same resolution element, can substantially affect the detection rate. Despite their large physical size, only 29 GRGs out of 239 are larger than 4.3′. All of the others are unresolved in the Van Eck et al. (2018) catalog, and thus suffer from the same in-beam depolarization as more compact radio sources. To better compare our work with Van Eck et al. (2018), we cross-matched the position of the 195 GRGs with an angular size lower than 4.3′ with the point source catalog compiled by Van Eck et al. (2018). The cross-match resulted in 11 sources, which were also detected in polarization in this work with 20″ resolution. The polarization detection rate of the unresolved GRGs in the Van Eck et al. (2018) catalog is thus 5.6 % (11/195). A parent population with a large physical size has a higher polarization detection rate than the overall population, even if it is not resolved. The high detection rate within the GRG sample suggests the presence of a small amount of depolarization (see also Sec. 7.2.4). Out of the 29 GRGs that are larger than 4.3′ and thus also resolved in the Van Eck et al. (2018) catalog, four are cataloged as point-sources while only for GRG 85 were both of its lobes detected in polarization. We refer the reader to Mahatma et al. (2020, submitted) for a more complete statistical study of the polarization properties and detection rate of radio galaxies within LoTSS DR1.

The central panel of Fig. 7.2 shows a clear selection effect for GRGs with high total radio power. The median radio power of GRGs detected in polarization is 4.07×10^{26} W/Hz, while it is 1.03×10^{26} W/Hz for undetected sources (1.8×10^{26} W/Hz considering only sources with a flux density above 50 mJy).

The fraction of GRGs detected in polarization increases with the linear size of the source (see Fig. 7.3), being 31% for the GRGs with physical sizes larger than 1.5 Mpc. This points to a possible decrease in the amount of Faraday depolarization

with larger distances from the local environment of the host galaxy. In fact, Faraday depolarization decreases far away from the host galaxy and possible groups or clusters of galaxies (Strom & Jaegers, 1988; Machalski & Jamrozy, 2006). However, this effect is conflated with the fact that the majority of sources with linear sizes that are larger than 1.5 Mpc have high radio power. Using the Kolmogorov-Smirnov (KS) test to compare the linear sizes, we found a marginal difference between the samples of detected and undetected GRGs with $S_{144MHz} > 50$ mJy (p-value of 0.08). Although beam depolarization may also play a role, the KS test between the angular sizes of detected and undetected sources with $S_{144MHz} > 50$ mJy suggests that they are drawn from a similar distribution (p-value of 0.29).

Dabhade et al. (2020) found 21/239 GRGs to be associated with the brightest cluster galaxies (BCGs) by cross-matching their catalog with the Wen, Han & Liu (2012) and Hao et al. (2010) cluster catalogs. None of them were detected in polarization apart from GRG 85, whose polarization properties have already been studied (O'Sullivan et al., 2019). We note that GRG 85 has a linear size of 3.4 Mpc and probably resides in a small group of galaxies. The localization of the sources in galaxy group or cluster environments seems to be an exclusion criterion for polarization detection at 144 MHz, and this is likely due to the effect of Faraday depolarization.

Polarization, Faraday rotation, and depolarization information for all sources are reported in Tab. 7.2, when both of the lobes were detected, and in Tab. 7.3, when only one source component was detected. The histograms of RM and fractional polarization of the detected components, considering both lobes and hotspots of single and double detections, are shown in Fig. 7.4.

Table 7.2: Results of the polarized intensity study of detected double-lobed sources. Column 1: as in Tab. 7.1 with a letter to distinguish the two lobes; Column 2 and 3: J2000 celestial coordinates of the highest signal-to-noise pixel; Column 4: polarized flux density of the detected source component; Column 5: polarization noise derived from the Faraday Q and U spectra; Column 6: fractional polarization at the position of the most significant pixel. The uncertainty was derived from the propagation of the root mean square noise in the polarized and total intensity images; Column 7: Faraday rotation derived from the main peak of the Faraday spectrum of the most significant pixel. The uncertainty was computed as the resolution of the Faraday spectrum divided by two times the signal-to-noise ratio of the detection. This does not include the systematic error from the ionospheric RM correction (on the order of $\sim$0.1 rad m^{-2}, Van Eck et al., 2018); Column 8: depolarization factor. The uncertainties were derived with standard propagation from the root mean square noise of the images. The values reported in Column 2 to 7 were derived from the 20″ images, while the depolarization factor in Column 8 was obtained using 45″ resolution images.

GRG	R.A. (deg)	Dec. (deg)	P (mJy)	σ_{QU} (mJy/beam)	p (%)	RM (rad/m^2)	$D_{1.4\ \mathrm{GHz}}^{144\ \mathrm{MHz}}$
0a	151.228	35.026	4.5	0.2	11.7 ± 0.5	3.23 ± 0.02	0.7 ± 0.2
0b	151.918	34.687	26.2	0.3	5.40 ± 0.06	9.071 ± 0.006	0.126 ± 0.007
1a	164.276	53.430	44.0	0.2	5.28 ± 0.02	12.855 ± 0.002	0.83 ± 0.02
1b	164.264	53.448	4.69	0.08	2.57 ± 0.05	12.20 ± 0.01	0.167 ± 0.008
2a	164.257	48.613	14.83	0.09	8.56 ± 0.05	16.940 ± 0.003	0.70 ± 0.02
2b	164.339	48.725	1.23	0.07	0.67 ± 0.04	19.01 ± 0.04	0.072 ± 0.007
19a	167.363	53.255	1.5	0.2	3.2 ± 0.3	11.18 ± 0.06	0.5 ± 0.1
19b	167.422	53.211	1.3	0.2	0.75 ± 0.09	11.39 ± 0.07	0.088 ± 0.007
22a	168.399	46.381	0.87	0.09	1.4 ± 0.2	4.04 ± 0.06	
22b	168.381	46.364	0.48	0.07	0.9 ± 0.1	4.57 ± 0.09	
51a	180.311	49.384	0.96	0.09	7.4 ± 0.7	22.03 ± 0.05	0.13 ± 0.04
51b	180.380	49.458	3.1	0.1	10.3 ± 0.3	22.70 ± 0.02	0.40 ± 0.09
64a	184.574	53.441	1.9	0.1	0.32 ± 0.02	15.30 ± 0.03	0.062 ± 0.007
64b	184.569	53.477	1.8	0.1	1.28 ± 0.07	14.57 ± 0.03	0.21 ± 0.07

65a	184.659	50.431	33.6	0.2	3.21 ± 0.02	27.784 ± 0.003	0.72 ± 0.02
65b	184.742	50.445	17.0	0.1	3.00 ± 0.02	26.682 ± 0.005	0.43 ± 0.01
77a	186.468	53.153	0.8	0.1	0.73 ± 0.09	13.10 ± 0.08	0.07 ± 0.02
77b	186.514	53.168	1.25	0.09	3.5 ± 0.3	11.90 ± 0.04	
85a	188.648	53.376	5.95	0.1	4.41 ± 0.09	7.51 ± 0.01	0.64 ± 0.07
85b	188.853	53.247	1.0	0.1	4.5 ± 0.4	10.08 ± 0.06	0.12 ± 0.01
87a	189.208	46.064	1.6	0.1	3.1 ± 0.2	21.44 ± 0.04	0.18 ± 0.03
87b	189.190	46.083	0.8	0.1	1.4 ± 0.2	16.92 ± 0.08	0.08 ± 0.02
91a	190.090	53.581	11.2	0.1	2.86 ± 0.03	17.952 ± 0.006	0.185 ± 0.006
91b	190.027	53.573	10.35	0.09	3.02 ± 0.03	19.353 ± 0.005	0.88 ± 0.09
103a	195.379	54.130	4.53	0.07	1.28 ± 0.02	13.676 ± 0.009	0.097 ± 0.002
103b	195.441	54.145	13.85	0.09	1.71 ± 0.01	14.017 ± 0.004	0.61 ± 0.03
120a	200.110	49.284	0.61	0.07	4.1 ± 0.4	10.85 ± 0.06	
120b	200.127	49.277	0.48	0.06	6.9 ± 0.9	10.90 ± 0.08	
144a	204.835	50.982	0.93	0.09	8.4 ± 0.8	9.05 ± 0.06	
144b	204.847	50.937	0.57	0.08	4.3 ± 0.6	8.22 ± 0.08	
145a	205.259	49.278	3.18	0.07	2.33 ± 0.05	10.52 ± 0.01	0.32 ± 0.02
145b	205.266	49.258	5.27	0.07	6.68 ± 0.09	10.002 ± 0.008	0.71 ± 0.06
165a	210.762	51.456	2.91	0.07	7.0 ± 0.2	19.41 ± 0.01	1.0 ± 0.3
165b	210.714	51.458	0.97	0.07	1.01 ± 0.07	17.62 ± 0.04	0.4 ± 0.1
166a	210.770	51.749	1.47	0.07	0.87 ± 0.04	11.38 ± 0.03	0.096 ± 0.007
166b	210.851	51.744	1.48	0.07	0.27 ± 0.01	12.87 ± 0.03	0.25 ± 0.03
168a	211.414	54.197	7.6	0.09	8.9 ± 0.1	14.998 ± 0.007	1.0 ± 0.3
168b	211.428	54.173	0.84	0.07	0.27 ± 0.02	13.34 ± 0.05	0.13 ± 0.03
177a	213.511	48.707	2.14	0.07	0.79 ± 0.02	19.94 ± 0.02	0.7 ± 0.2
177b	213.545	48.694	0.51	0.07	0.14 ± 0.02	19.18 ± 0.08	0.31 ± 0.07
222a	222.690	53.000	4.86	0.09	0.80 ± 0.02	16.91 ± 0.01	0.45 ± 0.07

222b	222.761	53.005	1.35	0.08	0.29 ± 0.02	15.19 ± 0.04	0.12 ± 0.02
233a	226.152	50.501	3.0	0.2	3.5 ± 0.2	6.16 ± 0.03	0.044 ± 0.003
233b	226.225	50.505	2.4	0.2	0.88 ± 0.06	5.71 ± 0.04	0.25 ± 0.04

Table 7.3: Results of the polarized intensity study for sources with a single polarized detection. Column headings are the same as in Tab. 7.2.

GRG	R.A. (deg)	Dec. (deg)	P (mJy)	σ_{QU} (mJy/beam)	p (%)	RM (rad/m^2)	$D_{1.4\ \mathrm{GHz}}^{144\ \mathrm{MHz}}$
7	164.634	51.687	0.81	0.07	2.5 ± 0.2	21.67 ± 0.05	0.19 ± 0.06
44	174.908	47.332	0.54	0.06	5.3 ± 0.6	22.20 ± 0.07	0.19 ± 0.05
47	177.991	49.837	0.59	0.07	0.16 ± 0.02	16.53 ± 0.07	0.052 ± 0.007
57	182.675	53.485	4.69	0.07	5.81 ± 0.09	12.214 ± 0.009	0.70 ± 0.09
80	187.512	53.531	0.57	0.06	1.0 ± 0.1	10.71 ± 0.07	0.13 ± 0.04
83	188.252	49.119	1.14	0.08	1.19 ± 0.08	13.56 ± 0.04	0.037 ± 0.004
112	197.578	52.222	0.86	0.09	1.8 ± 0.2	3.19 ± 0.06	
117	199.144	49.544	1.2	0.07	3.0 ± 0.2	13.00 ± 0.03	0.19 ± 0.02
122	200.906	47.511	0.61	0.079	3.4 ± 0.4	7.47 ± 0.07	0.21 ± 0.05
136	203.374	53.521	1.1	0.1	11.0 ± 1.0	10.91 ± 0.07	0.050 ± 0.009
137	203.561	55.013	0.76	0.08	0.073 ± 0.008	8.05 ± 0.06	
148	206.071	48.787	0.8	0.1	0.8 ± 0.1	12.50 ± 0.07	0.045 ± 0.004
149	206.178	50.395	1.1	0.08	7.1 ± 0.5	10.45 ± 0.04	0.4 ± 0.2
207	220.024	55.487	0.56	0.06	2.0 ± 0.2	11.64 ± 0.07	0.26 ± 0.07
234	226.541	51.591	0.93	0.09	2.1 ± 0.2	9.74 ± 0.06	0.27 ± 0.06

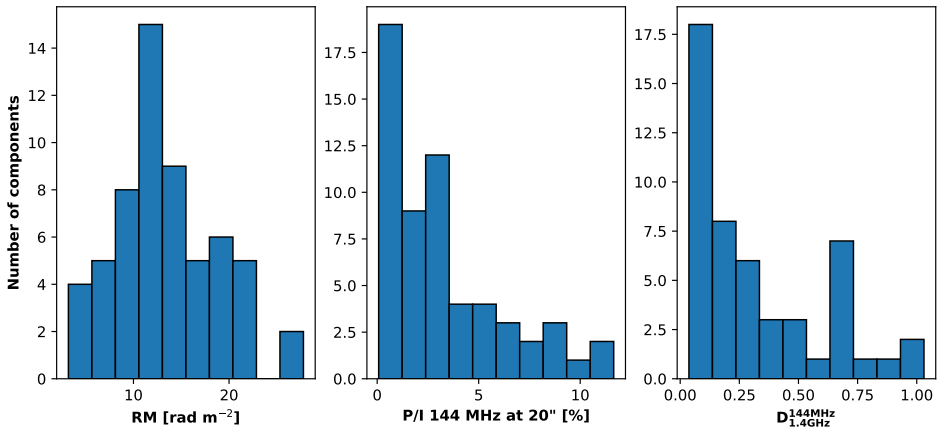

Figure 7.4: Distribution of Faraday rotation measure (left), fractional polarization (center), and depolarization factor between 1.4 GHz and 144 MHz (right) of the 59 components (lobes, hotspots, and core) detected in polarization.

7.3.1 RM difference between lobes

The observed RM was derived from the main peak of the Faraday spectrum at each pixel because all of the detected components show a simple Faraday spectrum (see Sec. 2.2).

The values of RM obtained are between 3 and 28 rad m^{-2} with a median value of 12.8 rad m^{-2} (see left panel of Fig. 7.4). The fact that they are all positive points out that in the sampled 424 deg^2 sky region, the magnetic field of our Galaxy is pointing toward us and it is the dominant source of the mean Faraday rotation. This implies a smooth Galactic magnetic field on scales of $\sim$10 deg (i.e., the median distance between the sources).

Among the 36 detected sources, both lobes were detected in polarization for 21 GRGs (at least one above the 8σ significance level). For these sources, plus GRG 0, we computed the RM difference between the two lobes (ΔRM). This quantity indicates a difference in the intervening magneto-ionic medium on large scales (on the order of 1 Mpc at the redshifts of the sources). We note that ΔRM can be caused by variations in the Galactic RM, in addition to a different line-of-sight path length between the two lobes in the local environment and/or differences in the IGM on large scales.

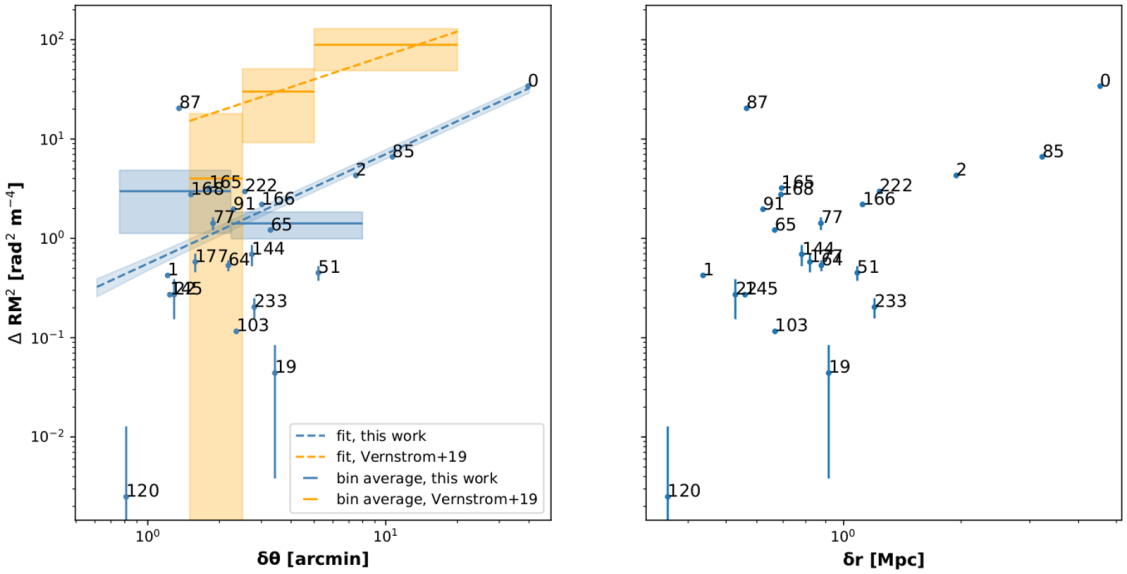

Figure 7.5: Squared RM difference versus angular (left) and physical (right) separation between the detected lobes. A number corresponds to each GRG and the numbers are listed in Tab. 7.2. The blue dashed line is the power-law fit to the data with 1σ uncertainty (see Sec. 7.3.1). Orange bars show the binned averages between $1.5'$ and $20'$ obtained by Vernstrom et al. (2019) for physical pairs observed at 1.4 GHz and the dashed orange line shows the derived structure function. Blue bars show the binned averages of the sources in this work with an angular separation lower than $10'$: Each bin contains ten sources, the uncertainty was computed as the standard deviation on the mean. Shadowed areas show the uncertainties.

The reconstruction of the Galactic RM by Oppermann et al. (2015) has a resolution of 1° (i.e., the typical spacing of extra-galactic sources in the Taylor, Stil & Sunstrum 2009 catalog) so that most of our double-lobed GRGs lie in the same resolution element of the reconstruction. All of the measured RMs are within the 3σ error of the estimated Galatic RM, with the exception of GRG 144 for which the difference is within the 4σ error. The average of the Galactic RM values at the position of the detected components (i.e., on scales of ∼10 deg) is 13±1 rad m^{-2}, which is consistent with the one found from our measurements. Due to its low angular resolution, this map cannot be used to probe RM variations on scales smaller than 1° for selected sources. However, RM structure function studies (i.e., $< \Delta RM^2 >$ versus angular separation) have probed the RM variance on scales below 1°, but with large uncertainties (Stil, Taylor & Sunstrum, 2011; Vernstrom et al., 2019). The Galactic RM variance was found to have a strong dependence on angular separation, in particular at low Galactic latitude. The 22 double GRGs have angular separations ($\delta\theta$) ranging between ∼1.8′ and ∼40′ and they all have a Galactic latitude above 50°, with GRG 0 being the largest in size and closest to the Galactic plane. The study of ΔRM^2 as a function of angular separation in our sample can

be used to understand if the RM difference is dominated by the turbulence in the Galactic interstellar medium.

We note that $\Delta\mathrm{RM}^2$ is plotted against the angular separation of the lobes in the left panel of Fig. 7.5. Despite the large scatter at low angular separation, a general increasing trend of $\Delta\mathrm{RM}^2$ with $\delta\theta$ is observed. We computed the average $\Delta\mathrm{RM}^2$ for the sources with $\delta\theta < 10'$ (thus excluding GRG 85 and GRG 0), which were divided into two bins with ten sources each; the uncertainties were computed as the standard deviation on the mean. The binned averages are over-plotted in Fig. 7.5. We fit the following power law:

$$\Delta\mathrm{RM}(\delta\theta)^2 = A\delta\theta^B \ , \tag{7.1}$$

and we obtained: $A = 0.56 \pm 0.06$ rad^2 m^{-4} and $B = 1.1 \pm 0.1$ with $\chi^2 = 515$ (the blue line in Fig. 7.5). The fit suggests an increasing influence of the Milky Way foreground with angular size. However, it is dominated by a few GRGs with the largest angular sizes and more sources at large $\delta\theta$ would be required to confirm this behavior. Conversely, the binned average for sources at low angular separation shows a large scatter and points to a flattening of the power-law slope for $\delta\theta < 2'$. This could be related to an increasing influence of the extra-galactic contribution over the Galactic one at small angular scales.

We can compare our result with the structure function studies of Stil, Taylor & Sunstrum (2011) and Vernstrom et al. (2019). While Stil, Taylor & Sunstrum (2011) considered all kinds of source pairs together (physical and nonphysical), Vernstrom et al. (2019) separated physical and nonphysical pairs. The latter is thus best suited for a direct comparison with our work where all pairs are physical. Vernstrom et al. (2019) made use of the Taylor, Stil & Sunstrum (2009) catalog of polarized sources observed at 1.4 GHz. For a sample of 317 physical pairs with angular separations between $1.5'$ and $20'$, they obtained $A = 11 \pm 15$ rad^2 m^{-4} and $B = 0.8 \pm 0.2$. The fit is shown as a comparison in the left hand panel of Fig. 7.5. The slopes are consistent within the 2σ uncertainty. The slightly steeper power-law compared to the one obtained by Vernstrom et al. (2019) can be attributed to the presence of GRG 0 in our sample. In both cases, the trend is dominated by pairs of sources at $\delta\theta > 10'$, indicating an increasing contribution from the Galactic RM.

Due to their large size, GRGs are expected to lie at large angles to the line of sight and to extend well beyond the group or cluster environment so that the differential Faraday rotation effect originating in the local environment should be minimal (Laing, 1988; Garrington et al., 1988). Furthermore, none of our sources show a prominent one-sided large-scale jet that would indicate motion toward the line of sight, not even the six sources with a quasar host (i.e., GRG 1, GRG 47, GRG 91, GRG 120, GRG 137, GRG 222). Thus, ΔRM is not expected to strongly

correlate with the source physical size. However, to investigate the local contribution, we plotted the RM difference squared against the physical separation between the two lobes (Fig. 7.5, right panel). The similarity between the right-hand and left-hand panel of Fig. 7.5 is notable. If the main contribution was due to the local environment, we would typically expect a larger RM difference between the lobes at smaller physical separations. Conversely, the similarity between the panels of Fig. 7.5 suggests that this trend is dominated by the angular separation trend, which is driven by Galactic structures. This points out that the local environment is subdominant in determining ΔRM.

Asymmetries in the foreground large-scale structures could also contribute to the RM difference between the two lobes. We expect much more large-scale asymmetries close to galaxy clusters (Böhringer, Chon & Kronberg, 2016). We note that, according to the environment analysis of Dabhade et al. (2020), none of the GRGs detected in polarization are associated with the BCG of a dense cluster of galaxies. However, foreground galaxy clusters are Faraday screens for all of the sources that are in the background. Therefore, we cross-matched the position of the 22 GRGs with the cluster catalog of Wen & Han (2015) in order to find the foreground galaxy cluster at the smallest projected distance from each GRG. This catalog is based on photometric redshifts from the SDSS III and lists clusters in the redshift range of $0.05 < z < 0.8$. In the redshift range of $0.05 < z < 0.42$, it is 95% complete for clusters with a mass of $M_{200} > 10^{14}$ $M_{\odot}$. Taking into account the uncertainty on the photometric redshift estimates, $\Delta z = 0.04(1 + z)$, we considered a cluster as being in the foreground of a particular GRG for all clusters with $z - \Delta z$ lower than the redshift of the GRG plus its uncertainty.

We computed the angular separation between each GRG lobe and the closest foreground galaxy cluster ($\delta\theta^{\rm min}_{\rm cluster}$ and $\delta\theta^{\rm max}_{\rm cluster}$, for the closest and farthest lobe, respectively). We note that $\Delta{\rm RM}^2$ is plotted against $\delta\theta^{\rm min}_{\rm cluster}$ divided by the angle subtended by R_{500} of the cluster ($\theta_{R_{500}}$, in arcminutes) in the top panel of Fig. 7.6. Most of the GRGs lie at projected distances larger than R_{500} and the trend does not show a clear dependence of ΔRM on the distance from the closest foreground cluster. Asymmetries in the foreground large-scale structures are thus probably subdominant compared to the ones caused by the Galactic RM. However, this is discussed further in Sec. 7.4.

7.3.2 Faraday depolarization

RM fluctuations within group and cluster environments can be caused by turbulent magnetic field fluctuations over a range of scales. While large scale fluctuations are mostly responsible for the RM difference between the lobes, fluctuations on the smallest scale may be at the origin of Faraday depolarization. Hence, the RM dispersion, $\sigma_{\rm RM}$ is responsible for the Faraday depolarization, which in the case of

an external screen is expressed by Eq. 2.14.

In the GRGs sample, the fractional polarization at 20″ resolution ranges between 0.07 and 11.7 % with a median value of 2.6 % (see central panel of Fig. 7.4). LOFAR has a unique capability to reliably detect very low fractional polarization values (i.e., < 0.5 %) when RM is outside of the range $-3 < \phi < 1$ rad m^{-2} because of the high resolution in Faraday space that allows for a clear separation from the leakage contribution.

Four components detected at 20″ are under the detection threshold at 45″. This is due to the lower sensitivity at 45″ resolution. Only in one case (GRG 112) is the nondetection likely caused by beam depolarization on scales between 20″ and 45″ (i.e., 140 and 315 kpc at the source redshift). Instead, five sources were not detected in the NVSS due to the lower sensitivity of this survey. Hence, there are 28 sources with depolarization measurements. The distribution of depolarization factors computed at 45″ is shown in the right panel of Fig. 7.4. All of the sources have $D_{1.4\ \mathrm{GHz}}^{144\ \mathrm{MHz}} > 0.03$ and the median value is 0.2.

Our measurements enable us to probe magnetic field fluctuations on scales below the 45″ restoring beam, which for the redshift range of our sample corresponds to physical scales of 80-480 kpc. Faraday depolarization can occur internally to the source or it can be due to the small-scale fluctuation of the magnetic field in the medium that is external to the source.

With LoTSS data, we were not able to observe internal depolarization, which would appear as a thick Faraday component through RM synthesis. This is because the largest observable Faraday scale is smaller than the resolution in Faraday space (see Sec. 7.2.2). Broad-band polarization studies at higher frequencies and/or detailed modeling of internal Faraday screens would be needed to distinguish between these two scenarios.

In the case of external depolarization, Eq. 2.14 implies that the effect of a $\sigma_{\mathrm{RM}} \leq 1$ rad m^{-2} is only observable at very large wavelengths. For this reason, by comparing measurements at 1.4 GHz and at 144 MHz, it is possible to study the depolarization caused by low σ_{RM}. On the other hand, $\sigma_{\mathrm{RM}} \geq 1$ rad m^{-2} can completely depolarize the emission and make it undetectable by LOFAR. Within galaxy clusters, where $B \sim 0.1 - 10$ μG, $n_e \sim 10^{-3}$ cm^{-3} and the magnetic field is tangled on a range of scales, the RM dispersion is clearly above this level (e.g., Murgia et al., 2004; Bonafede et al., 2010).

The distribution of distances from the closest foreground cluster is compared for detected and undetected GRGs in polarization in the top panel of Fig. 7.7, while the detection rate was computed as a function of the distance from the foreground cluster in the bottom panel (for GRGs with $S_{144\mathrm{MHz}} > 50$ mJy). We find that 8 % of the GRGs observed within $2R_{500}$ of the closest foreground cluster are detected in polarization, while the detection rate increases to 27 % outside $2R_{500}$. The

Kolmogorov-Smirnov test indicates a significant difference between the samples of detected and undetected GRGs with $S_{144\mathrm{MHz}} > 50$ mJy (p-value of $2{\times}10^{-3}$). Together with the nondetection of the GRGs at the center of clusters (Sec. 7.3), this shows that in general, to be detected by LoTSS, sources need to avoid locations both within and in the background of galaxy clusters where the RM dispersion is too high.

Only four GRGs are detected within R_{500}: GRG 2, GRG 91, GRG 120, and GRG 136. Among them, GRG 2 ($z = 0.27627 \pm 0.00005$) and GRG 136 ($z = 0.354 \pm 0.034$) have similar redshifts with respect to the clusters (at redshifts 0.27 ± 0.05 and 0.37 ± 0.05, respectively). They have been considered in the background due to the uncertainties on the photometric redshift estimates, but it is also possible that these GRGs are cluster members or instead lie in the foreground of the clusters. GRG 91 and GRG 120 are associated with compact foreground clusters with R_{500} equal to 570 kpc and 650 kpc, respectively.

Using $\mathrm{D}_{1.4\ \mathrm{GHz}}^{144\ \mathrm{MHz}}$ in Eq. 2.14, we can compute σ_{RM}. The distribution of observed σ_{RM} is shown in Fig. 7.8. The maximum value is 0.29 rad m^{-2}. Given the small amount of depolarization, it is important to consider that the residual error in the ionospheric RM correction within the 8 hours of the observation could account for $\sim 0.1 - 0.3$ rad m^{-2} (Van Eck et al., 2018). In principle, this could explain most or all of the depolarization observed, but the residual ionospheric correction error is subtracted out in the difference in depolarization between the two hotspots of the same radio galaxy, $|\Delta\ \mathrm{D}_{1.4\ \mathrm{GHz}}^{144\ \mathrm{MHz}}|$. We note that $|\Delta\ \mathrm{D}_{1.4\ \mathrm{GHz}}^{144\ \mathrm{MHz}}|$ represents a lower limit to the depolarization that leads to σ_{RM} values between 0.05 and 0.25 rad m^{-2} in the observer's frame. Supposing that the depolarization is caused by a turbulent Faraday screen local to each source, we can apply the redshift correction to recover the σ_{RM} in the source's frame. In this case the intrinsic σ_{RM} values are between 0.1 and 1 rad m^{-2}. These estimates are further discussed in Sec. 7.4.

We tested the possibility that the closest foreground cluster was the main origin of the measured depolarization by plotting $|\Delta\ \mathrm{D}_{1.4\ \mathrm{GHz}}^{144\ \mathrm{MHz}}|$ versus the distance from the cluster in the bottom panel of Fig. 7.6. However, we do not find a correlation between these quantities.

We note that $\mathrm{D}_{1.4\ \mathrm{GHz}}^{144\ \mathrm{MHz}}$is also not correlated with the distance from the host galaxy, probably because all of the sources are very extended and are already well beyond the host galaxy's halo (Strom & Jaegers, 1988). The Laing-Garrington effect (i.e., the differential Faraday depolarization that causes the counter-lobe to be more depolarized than the lobe closer to us Laing 1988; Garrington et al. 1988) is indeed not expected to have a strong effect in this case. We note that none of the GRGs show a prominent jet in the total intensity images (see Fig. 7.9), which is in line with the expectation that these sources are observed at large angles to the line of sight.

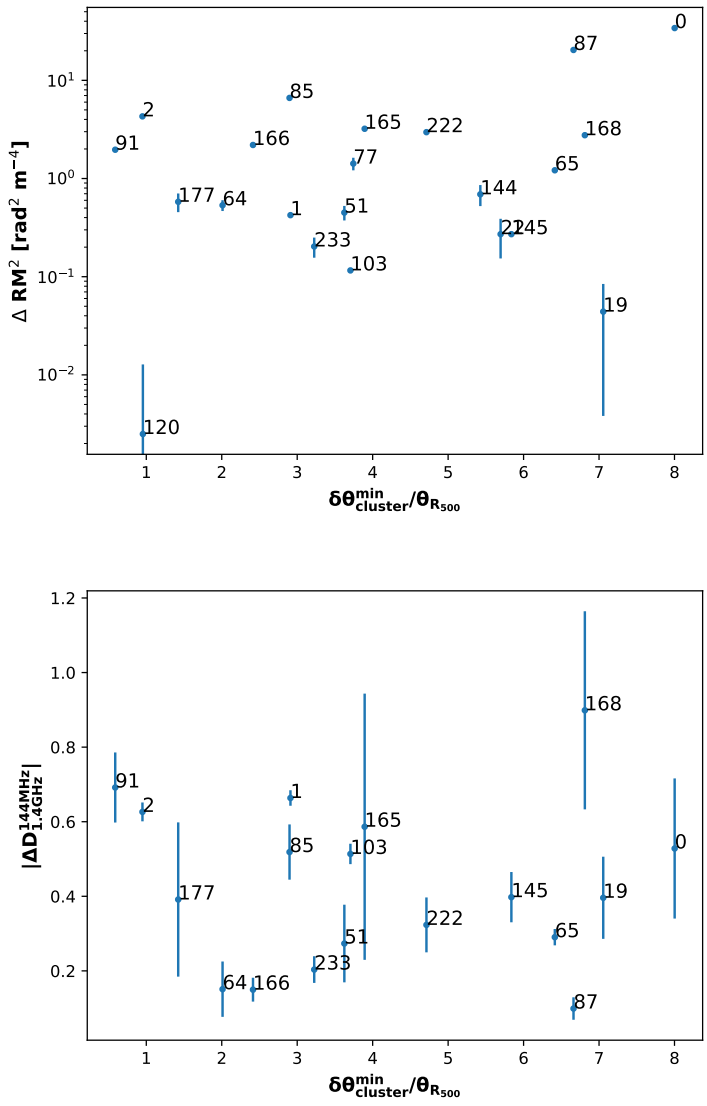

Figure 7.6: Squared RM difference (top panel) and depolarization factor difference between the two lobes (bottom panel) versus the minimum distance from the closest foreground galaxy cluster scaled by R_{500} of the cluster.

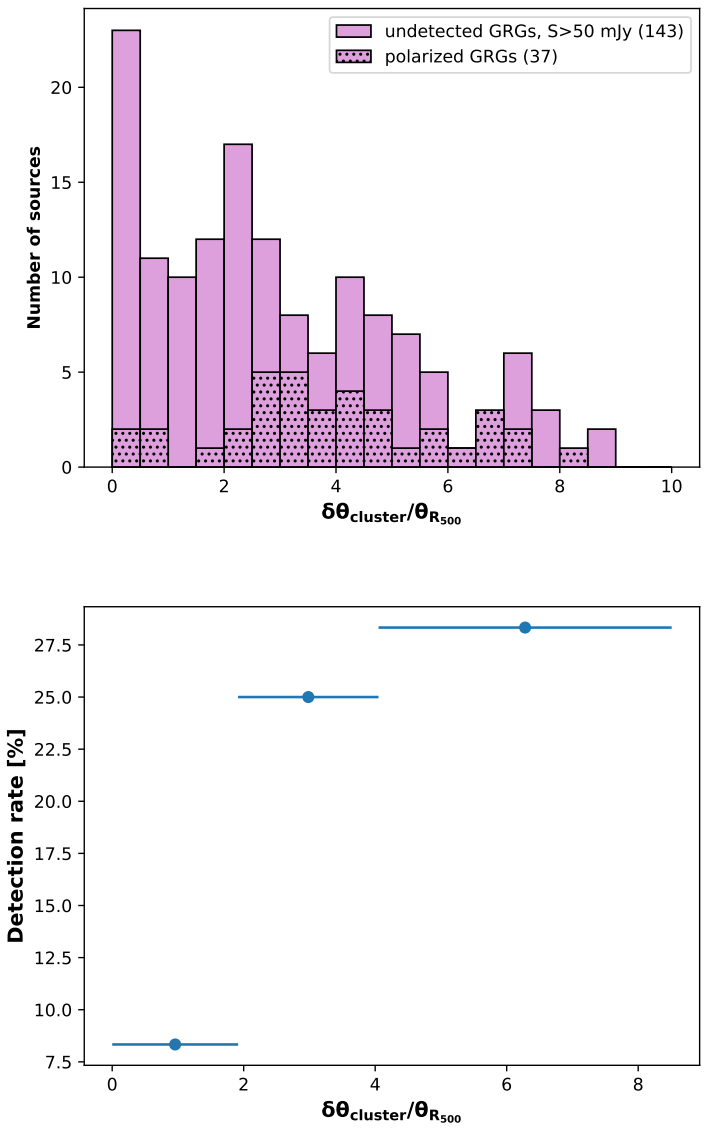

Figure 7.7: Distribution of minimum distance from the closest foreground cluster for detected and undetected sources in polarization (top panel), and detection rate as a function of the minimum distance from foreground clusters (bottom panel). The widths of the bins were computed to contain the same total number of sources (i.e., 60). Markers were positioned at the center of each bin and the error bars show the width of the bins.

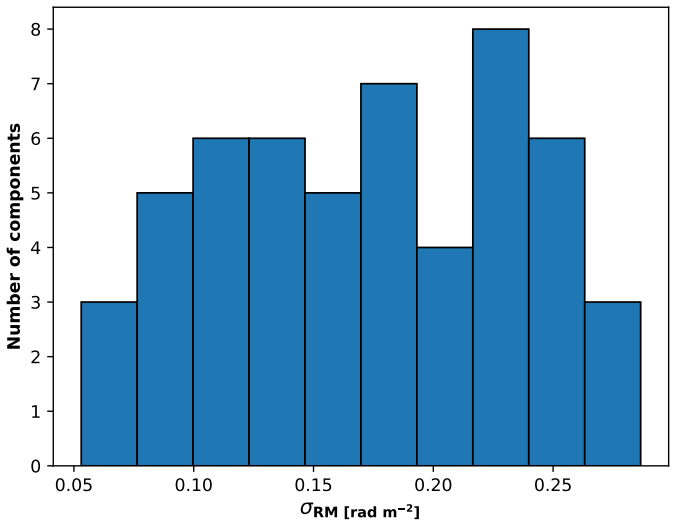

Figure 7.8: Distribution of RM dispersion values obtained using an external Faraday screen model.

7.4 Discussion

Since both RM and depolarization are integrated effects along the line of sight (Eq. 2.5 and 2.9), in order to disentangle the contribution of the different Faraday rotation and depolarization screens, one should have detailed information on the environment surrounding each radio galaxy, the foreground, and the geometry and physical properties of the lobes. This requires a detailed study of each single source. We instead investigated several possible origins of the RM difference and Faraday depolarization considering the correlation of ΔRM and $\mathrm{D}_{1.4\ \mathrm{GHz}}^{144\ \mathrm{MHz}}$ with different physical quantities.

7.4.1 Milky Way and local contributions

Several statistical analyses on the RMs of extra-galactic sources have been performed. Structure function studies verified the dependence of ΔRM on the angular separation that originated by the Galactic magnetic field (e.g., Simonetti, Cordes & Spangler, 1984; Sun & Han, 2004; Stil, Taylor & Sunstrum, 2011). The presence of a growing contribution to the RM with redshift was investigated by Pshirkov, Tinyakov & Urban (2015). The RM variance of background sources was modeled to separate an extra-galactic contribution of 6-7 rad m^{-2} from the Galactic one (e.g., Schnitzeler, 2010; Oppermann et al., 2015). Bringing these works together, Vernstrom et al. (2019) studied the average $\Delta\mathrm{RM}^2$ as a function of angular separation, redshift, spectral index, and fractional polarization using two large samples

of physical and nonphysical pairs in order to isolate the extra-galactic contribution. A difference of ~ 10 rad m^{-2} in the average ΔRM^2 between the two samples was attributed to the IGM to derive an upper limit on the extra-galactic magnetic field of 40 nG. A contribution from the local magnetic field, producing a larger variance for nonphysical pairs, cannot be excluded. All of these studies were performed at 1.4 GHz, thanks to the presence of the RM catalog produced with NVSS (Condon et al., 1998; Taylor, Stil & Sunstrum, 2009). With the advent of LOFAR, these kinds of studies are also possible at low frequencies. With respect to NVSS, LoTSS allows for a better resolution, sensitivity, and precision in the the determination of RMs.

In this work, the RM difference between the lobes was found to be marginally correlated with the angular distances of the lobes (Fig. 7.5). Although the correlation is not strong (with a Spearman correlation coefficient of 0.35), we found the relation between ΔRM^2 and $\delta\theta$ to be consistent with the Galactic structure function found by Vernstrom et al. (2019) for physical pairs. This strongly suggests a Galactic origin of the ΔRM between the lobes. The accuracy in the determination of the amplitude parameter is 250 times higher than the one obtained using NVSS measurements. The same trend observed with the angular separation also dominates the correlation between ΔRM and the physical distance. This suggests that the local gas densities and magnetic fields, which should have a stronger effect on the RM variation for normal size galaxies, are not dominant in this sample. This would also explain the fact that, although consistent within the errors, the amplitude of the power-law at 144 MHz is one order of magnitude lower than the one at 1.4 GHz (see Fig. 7.5). While in Vernstrom et al. (2019) the physical size of the sources is not taken into account, our GRG sample constitutes a population where the local contribution to ΔRM is negligible. A selection of a source population with low local RM variance is an important requirement for future RM grid experiments (Rudnick, 2019).

Recently, O'Sullivan et al. (2020) applied the same method of Vernstrom et al. (2019) to the RMs derived at 144 MHz from LoTSS (see Chapter 6). This study resulted in an extra-galactic contribution < 1.9 rad m^{-2}, which yielded to an upper limit on the comoving magnetic field of 4 nG. Since the magnetic field in the IGM is not expected to vary with frequency, the discrepancy between the results obtained at 1.4 GHz and 144 MHz was attributed to the Faraday depolarization effect. Since a high local RM variance can depolarize sources below the detection level at low frequencies, observations at 144 MHz selects sources with a low RM variance, which unveils the effect of weaker magnetic fields and lower thermal gas densities.

To measure and investigate the origin of the depolarization is thus complementary to the aforementioned studies. In this context, the depolarization is caused by RM variance on scales of the synthesized beam, which consequently affect the measurement of the RM variance on the scale of the angular separation between the

sources (or the sources lobes). The dependence of the RM variance and depolarization on the physical size of classical double radio sources was investigated by Strom & Jaegers (1988) and Johnson, Leahy & Garrington (1995) in order to study the local magnetic field. Machalski & Jamrozy (2006) extended this work by comparing normal size and giant radio galaxies, finding that the depolarization factor strongly correlates with the size of the sources. Within the GRG sample collected by Machalski & Jamrozy (2006), the median depolarization factor between 4.9 GHz and 1.4 GHz is 1.04±0.05, with the majority of sources showing undetectable levels of depolarization. The RMs, which were obtained with a fit between the two frequencies and thus subject to the $n\pi$ ambiguity, are also consistent with zero within the large uncertainties. The wavelength at which substantial depolarization occurs increases with the size of the sources. The depolarization caused by a $\sigma_{\rm RM} \sim 0.3$ rad m^{-2} would be undetected at gigahertz frequencies. Low-frequency observation are thus necessary to measure the small amount of depolarization experienced by the lobes of GRGs in order to constrain the magneto-ionic properties of their environment.

While RM differences between the lobes probe magnetic field fluctuations on large scales (i.e., ∼1 Mpc), the depolarization is sensitive to angular scales below the 45″ resolution. This implies scales of 80-480 kpc in the redshift range of the sources. In the most common model of external Faraday dispersion, the depolarization roughly scales as $1/\sqrt{N}$ where N is the number of Faraday cells within the beam (see Tribble, 1991b, and Sec. 2.1.3). A model of random magnetic field fluctuations in N ∼25 cells is able to explain the median $\mathrm{D}^{144\ \mathrm{MHz}}_{1.4\ \mathrm{GHz}}$=0.2 and it implies a magnetic field reversal scale of 3-25 kpc.

The depolarization observed thus most likely occurs in a very local environment. This is also supported by Fig. 7.3, which shows an increasing detection rate at larger distances from the host galaxy and thus from the local enhancement of gas density. A simple model of constant thermal electron density of $\sim 10^{-5}$ cm^{-3} and a magnetic field of ~ 0.1 μG tangled on scales of 3-25 kpc could explain the values of $\sigma_{\rm RM}$ observed using Eq. 2.9 with an integration length < 100 kpc. Sub-μG magnetic fields and thermal electron densities of a few times 10^{-5} cm^{-3} are consistent with the findings from detailed studies on single giant radio galaxies (e.g., Willis, Wilson & Strom, 1978b; Laing et al., 2006). From the study of five well known GRGs, Mack et al. (1998) also concluded that the density estimates in the environments of these sources are one order of magnitude lower than within clusters of galaxies. This is the typical environment that polarization observations with LOFAR allow us to study since larger $\sigma_{\rm RM}$ would completely depolarize the emission. This automatically excludes all of the sources lying within a dense cluster environment, as confirmed by the fact that all 21 GRGs known to reside in clusters are undetected in polarization. Sources residing in such an under-dense environment are thus the dominant population of physical pairs that are also in the work by O'Sullivan et al.

(2020).

We note that the $\sigma_{\rm RM}$ values shown in Fig. 7.8 were derived assuming external depolarization (Eq. 2.14). With measurements at only 144 MHz and 1.4 GHz, we cannot exclude other depolarization models (e.g., Sokoloff et al., 1998; Tribble, 1991a; O'Sullivan et al., 2018b). A detailed depolarization analysis with a larger wavelength-square coverage would be needed. For example, in the case in which the polarized emission at 144 MHz originates from an unresolved region within the 45″ beam across which the RM gradient is effectively zero and the rest of the polarized structure is completely depolarized by RM fluctuations, our $\sigma_{\rm RM}$ estimates are not applicable. This would imply that the true $\sigma_{\rm RM}$ of the local environment could be much higher, but that our measurements at 144 MHz cannot detect this emission.

7.4.2 The influence of foreground galaxy clusters

Having investigated the Galactic and local Faraday effects on ΔRM and $\mathrm{D}_{1.4\ \mathrm{GHz}}^{144\ \mathrm{MHz}}$ and their implication for present and future polarization studies with LOFAR, we shift our attention to the possible presence of Faraday screens in the foreground of our targets. Several statistical studies of the Faraday rotation of background sources have demonstrated the presence of a magnetic field in clusters of galaxies (e.g., Lawler & Dennison, 1982; Clarke, Kronberg & Böhringer, 2001; Böhringer, Chon & Kronberg, 2016). The scatter in the RMs was found to be enhanced by the cluster magnetic field up to 800 kpc from the cluster center (Johnston-Hollitt & Ekers, 2004). The majority of the double detected sources in our study lie outside R_{500} of foreground clusters (see Fig. 7.6). Therefore, it is not surprising that the correlation between $\Delta\mathrm{RM}^2$ and the distance from the closest foreground cluster is rather weak (Spearman correlation coefficient of 0.11). In any case, because of LOFAR's high sensitivity to small RMs, LOFAR allows us to explore regions that are far outside galaxy clusters, which are traced by the lobes of GRGs.

We can use a β-model (Cavaliere & Fusco-Femiano, 1976) to describe the gas density profile in clusters (Eq. 1.7) where we assume the central gas density, $n_0 \sim 10^{-3}$ cm^{-3}, the core radius, $r_c \sim 200$ kpc, and β=0.7. We assume that the magnetic field strength scales with the gas density: $B(r) = \langle B_0 \rangle (n(r)/n_0)^{0.7}$ and that $\langle B_0 \rangle \sim 3$ μG (Dolag et al., 2001; Bonafede et al., 2010; Govoni et al., 2017). The choice of these parameters is somewhat arbitrary, but they can reasonably describe galaxy cluster environments (see also Chapter 4). Less massive clusters have a lower electron column density along the line of sight for a given radius scaled by R_{500} and in our sample R_{500} ranges between 0.56 and 1.01 Mpc. Considering a median $R_{500} \sim 800$ kpc outside of the projected distance of four times R_{500}, the thermal electron density is $< 3 \times 10^{-6}$ cm^{-3} and the magnetic field strength is < 0.05 μG. Assuming a large magnetic field fluctuation scale of 500 kpc, the mean RM from Eq. 2.5 is < 0.06 rad m^{-2} (where we used $B_{\parallel} = B/\sqrt{3}$). For GRGs with $\delta\theta_{\rm cluster}^{\rm min} > 4\theta_{R_{500}}$, the foreground

clusters cannot be the dominant origin of the RM difference since their signature would be too weak even for LOFAR RM accuracy. Therefore, the effect of foreground clusters and large-scale asymmetries to the RM difference is disfavored, but it is still non-negligible for some of the GRGs in our sample.

Three double-detected GRGs lie within R_{500} of the closest foreground cluster, namely GRG 2, GRG 91, and GRG 120. For each of them, we computed $\delta\theta^{\rm min}_{\rm cluster}$ and $\delta\theta^{\rm max}_{\rm cluster}$, that is, the distances of the two lobes from the cluster. GRG 91 is associated with a compact foreground cluster with R_{500} of 570 kpc . While for GRG 2 the two lobes are at $\sim$2 and $\sim$0.95 R_{500}, respectively, the distance of both lobes of GRG 120 from the foreground cluster is $\sim$0.96 R_{500}. Using the simplified galaxy cluster model previously assumed, we would expect a ΔRM^2 of $\sim$20 rad m^{-2} for GRG 2 and $\sim$0.1 rad m^{-2} for GRG 120. Although this model overestimates the observed values, it is able to explain more thoroughly the two order of magnitude difference between the two sources. This suggests that both the source distance and the difference in distances of the two lobes from foreground clusters can, in principle, play a role in determining ΔRM. For other sources, that is, GRG 0 and GRG 87, which lie more than $4R_{500}$ away from the closest foreground cluster, the enhanced RM difference could also be influenced by the presence of large-scale structure filaments, as proposed for GRG 85 (O'Sullivan et al., 2019). A detailed study of the local environment and of the foreground of the GRGs is required in this cases. Such a study may be addressed in future work. A complementary approach that was used by Mahatma et al. (2020, submitted) is to invoke a universal pressure profile to predict the distributions of RM toward the population of radio galaxies with local and large-scale contributions.

The fractional polarization, and thus depolarization factor, is also known to scale with the distance from the cluster center. Bonafede et al. (2011) performed a study of the polarization fraction of sources in the background of galaxy clusters and found that the median fractional polarization at 1.4 GHz decreases toward the cluster center. The trend is observed up to $\sim$ 5 core radii (corresponding to $1.25R_{500}$ in the framework of the simple cluster model described above), while far outside, the median fractional polarization reaches a constant value of $\sim$ 5 %. Fig. 7.6 (bottom panel) and Fig. 7.7 show that, while the depolarization does not correlate with the distance from foreground clusters, the presence of the latter disfavors the detection of the sources in polarization. This is consistent with the value of $D^{144\ \rm MHz}_{1.4\ \rm GHz}$ depending mostly on the magneto-ionic properties of the local environment of each GRG. Within R_{500}, the higher RM variance due to the turbulence in the foreground ICM influences the fractional polarization at gigahertz frequencies and depolarizes the radio emission at 144 MHz below the LoTSS detection limit. It is plausible that only under particular condition some background sources can be detected, for example, when the foreground cluster is poor and/or the polarized emission

originates in a very compact region of the source. Thus, the detection rate at 144 MHz is strongly reduced up to 2-2.5 R_{500}. This highlights the presence of a magnetic field at larger distances from galaxy clusters than was shown by previous studies at higher frequencies (Clarke, 2004). This also has the important consequence that future RM grid studies using LoTSS will mainly sample the lines of sight in the extreme peripheries of galaxy clusters through filaments and voids.

7.5 Conclusions

In this work we used data from the LoTSS to perform a polarization analysis of a sample of giant radio galaxies selected by Dabhade et al. (2020). Our aims were to *(i)* study the typical magnetic field in the environment of this class of sources, which is unveiled by their polarization properties at low-frequencies, and *(ii)* understand how GRGs can be used in a RM grid to derive important information on foreground magnetic fields. We measured the linear polarization, Faraday rotation measure, and depolarization between 1.4 GHz and 144 MHz of the 37 sources detected in polarization. Compared to previous studies at gigahertz frequencies, this study allowed us to measure the small amount of Faraday rotation and depolarization experienced by these sources. The high precision in the RM determination (~ 0.05 rad m^{-2}) enables for the detection of a very small difference between the lobes of the GRGs (ΔRM) that we studied against the angular and physical separation and the distance from foreground galaxy clusters. Since the Faraday depolarization has a strong impact on the detection rate at 144 MHz, the latter was also used as a tool to investigate the presence of depolarizing screens. Our results are summarized as follows:

1. Among the 179 giant radio galaxies observed at 20″ resolution with a flux density above 50 mJy, the polarization detection rate is 20 % above an $8\sigma_{QU}$ detection threshold. A comparison with the polarized point-source catalog by Van Eck et al. (2018) indicates that sources with a large angular size have a much greater chance of being detected. Our study suggests that this class of sources preferentially reside in very rarefied environments experiencing low levels of depolarization. GRGs thus represent a good sample for targeted polarization studies of the magneto-ionized foreground medium.

2. The RM variation on scales below 40′ was investigated using the RM difference between the lobes of the same galaxy. Our study supports the idea that the main contribution to ΔRM on scales between 2′ and 40′ comes from the Milky Way foreground as obtained by Vernstrom et al. (2019). With respect to previous studies performed at gigahertz frequencies, our investigation provides two orders of magnitude higher precision in the determination of ΔRM. A larger sample of sources would be needed to confirm this trend. Local and foreground galaxy cluster

contributions to ΔRM are subdominant but non-negligible for some of the sources.

3. Using NVSS archival data, we studied the depolarization between 1.4 GHz and 144 MHz. We detected Faraday depolarization caused by a Faraday dispersion of up to $\sim$0.3 rad m^{-2}. Such small amounts of depolarization cannot be detected at higher frequencies. This may occur in the local environment of the lobe and hotspot due to small-scale (few tens of kiloparsecs) magnetic field fluctuations. In this case, the intrinsic $\sigma_{\rm RM}$ in the source's frame is lower than 1 rad m^{-2}. A factor of ten better in ionospheric RM correction would be needed to constrain the true astrophysical depolarization of each source.

4. From our analysis, we observed that the environment of the detected giant radio galaxies is extremely rarefied, with thermal electron densities $< 10^{-5}$ cm^{-3} and magnetic fields below $\sim$ 0.1 μG. This is likely the typical environment of the majority of sources that LOFAR can detect in polarization. Studies of the extra-galactic magnetic field performed with LoTSS (e.g., O'Sullivan et al., 2019) need to take a lower local contribution into account than studies performed at higher frequencies.

5. Furthermore, at LOFAR frequencies, the chance of detecting a giant radio galaxy for background RM studies of galaxy clusters is three times higher outside $2R_{500}$ than within it. This indicates that the magnetic field in the outskirts of galaxy clusters has an impact on the polarization of background sources at larger distances than previously observed (Bonafede et al., 2011).

This work shows the polarization and RM properties of the largest class of sources detected by LOFAR in polarization, and it highlights the potential of their use to study the magneto-ionic properties of large-scale structures. A denser RM grid is needed to constrain the extra-galactic contribution to the RM variance. Future studies, on the basis of thousands of RMs with known redshifts detected by the LoTSS, will enable us to probe the weak signature of the intergalactic magnetic field both in the peripheries of, and far outside, galaxy cluster environments.

7.6 Images

The images of all of the GRGs detected in polarization are shown in Fig. 7.9. We show the total intensity images at 20″ resolution and the fractional polarization images at 45″ compared with the NVSS fractional polarization images at 1.4 GHz. In some cases, the detected regions appear as a few scattered pixels that are not beam-shaped. This is a consequence of having peak polarized intensities that are very close to the detection threshold cutoff.

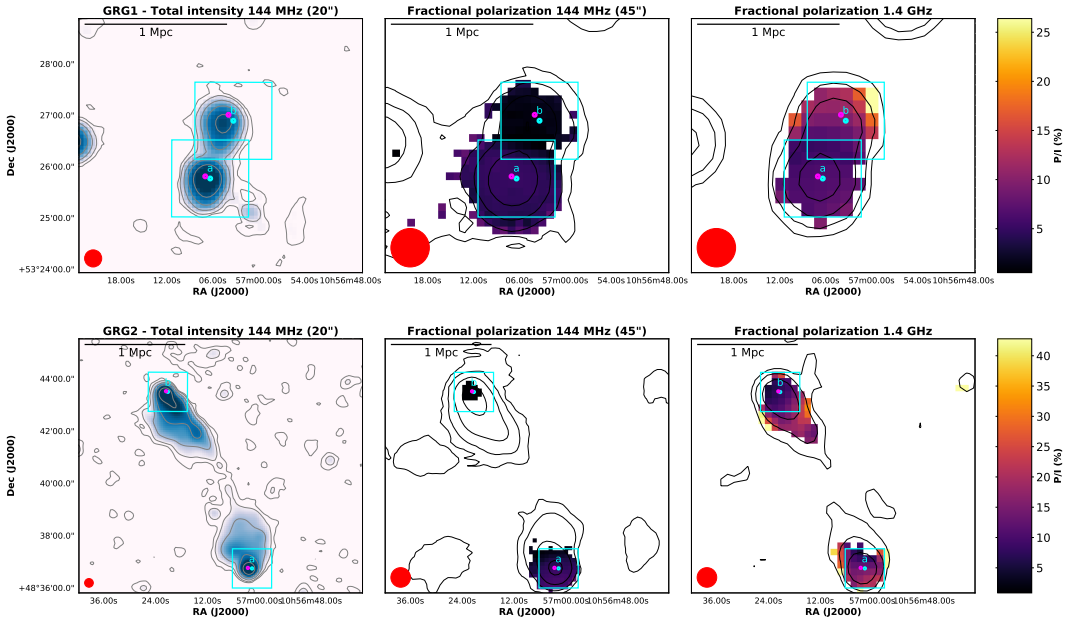

Figure 7.9: Images of the GRGs detected in polarization. Left: LoTSS total intensity image at 20″ resolution with contours overlaid. Contours start at 3σ noise level and are spaced by a factor of four (with σ ranging between 0.09 and 0.9 mJy/beam). Center: LoTSS fractional polarization at 45″ resolution with total intensity contours overlaid. Contours start at 3σ noise level and are spaced by a factor of four (with σ ranging between 0.1 and 8 mJy/beam). Only pixels above the $8\sigma_{QU}$ detection threshold in polarization are shown (except for GRG 78, for which the threshold is seven times σ_{QU}, and GRG 80 and GRG 87, for which it is $6\sigma_{QU}$). Right: NVSS fractional polarization with total intensity contours overlaid. Contours start at 3σ noise level and are spaced by a factor of four (with σ ranging between 0.2 and 0.7 mJy/beam). Only pixels with a signal-to-noise ratio higher than three in polarization are shown. The color scale and limits are the same in both P/I images for each source. The cyan squares mark the component detected at 20″, cyan points mark the peak of polarized intensity at 20″ (RM and fractional polarization values at this position are listed in Tab. 7.2 and Tab. 7.3), while magenta points mark the position where we computed the depolarization factors. Letters mark the two components listed in Tab. 7.2 for double-lobed detected sources.

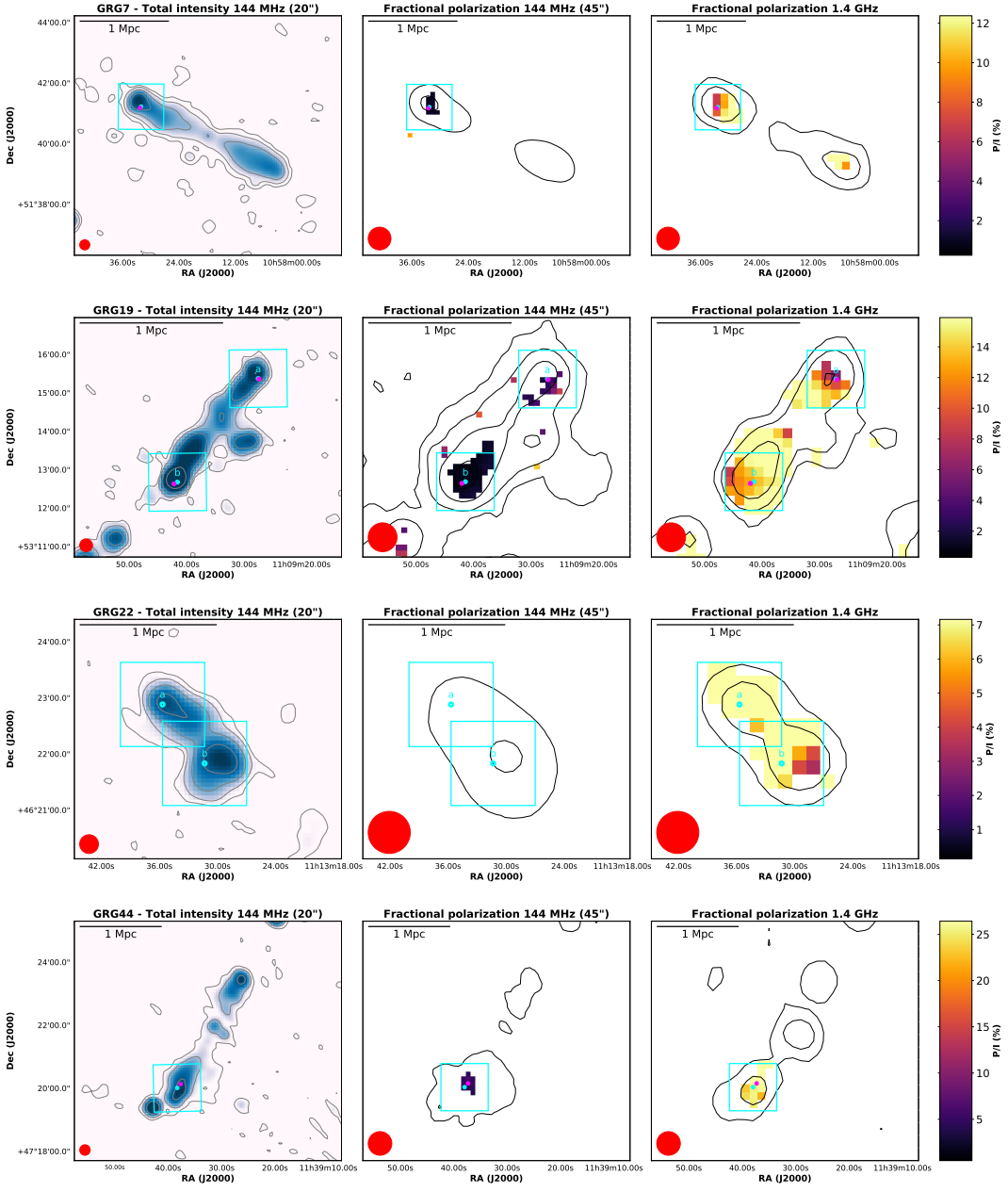

Figure 7.9 (continued)

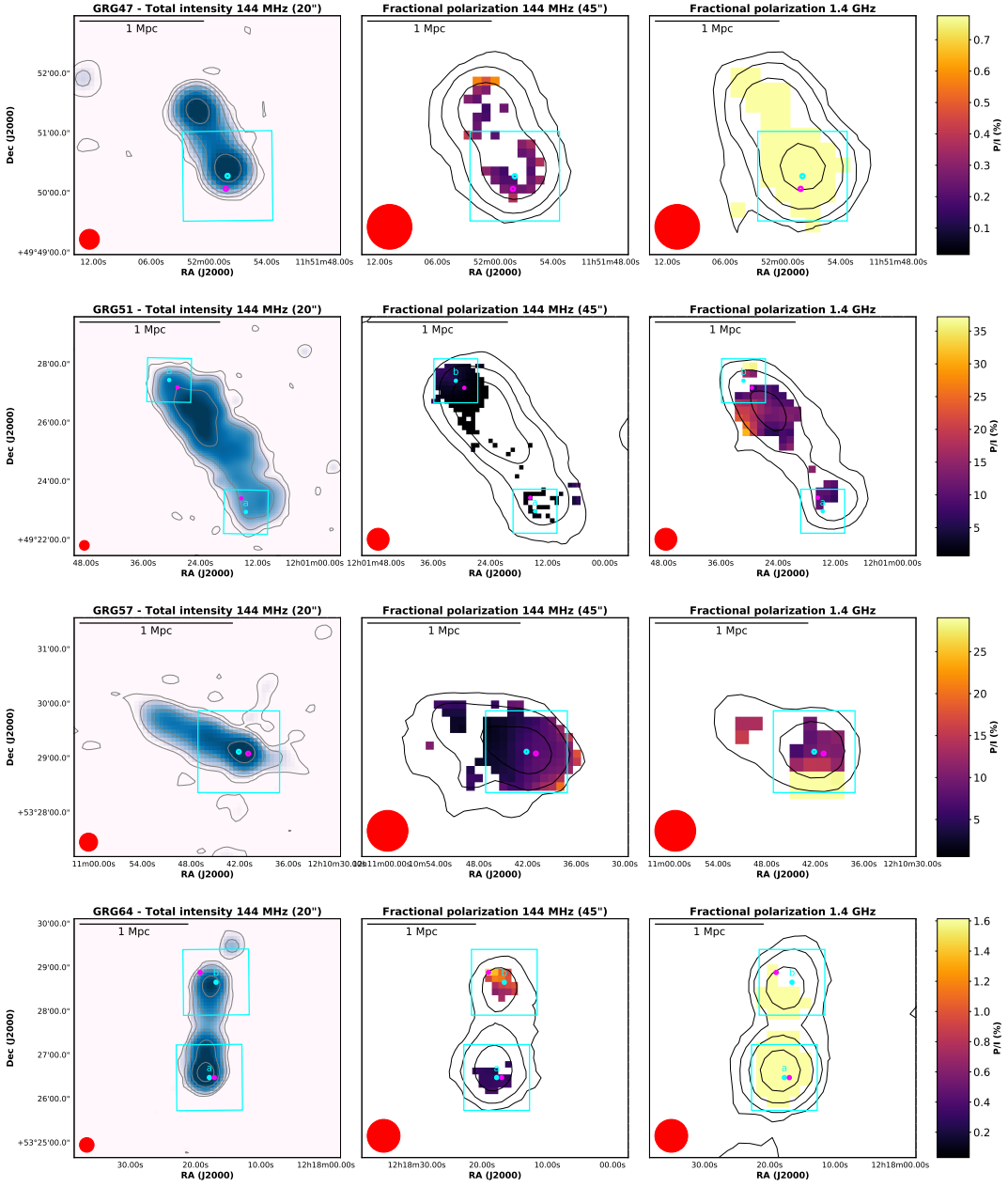

Figure 7.9 (continued)

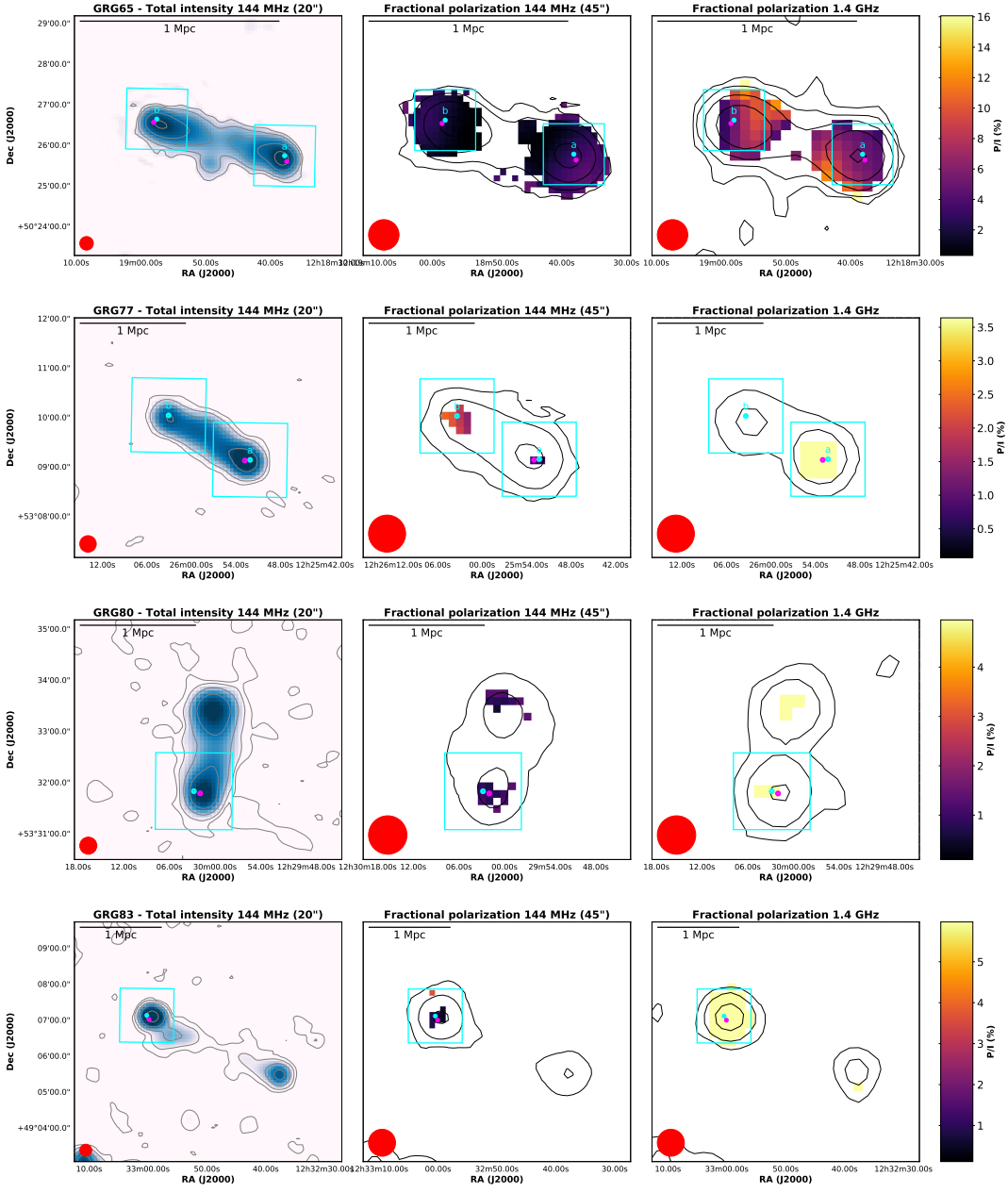

Figure 7.9 (continued)

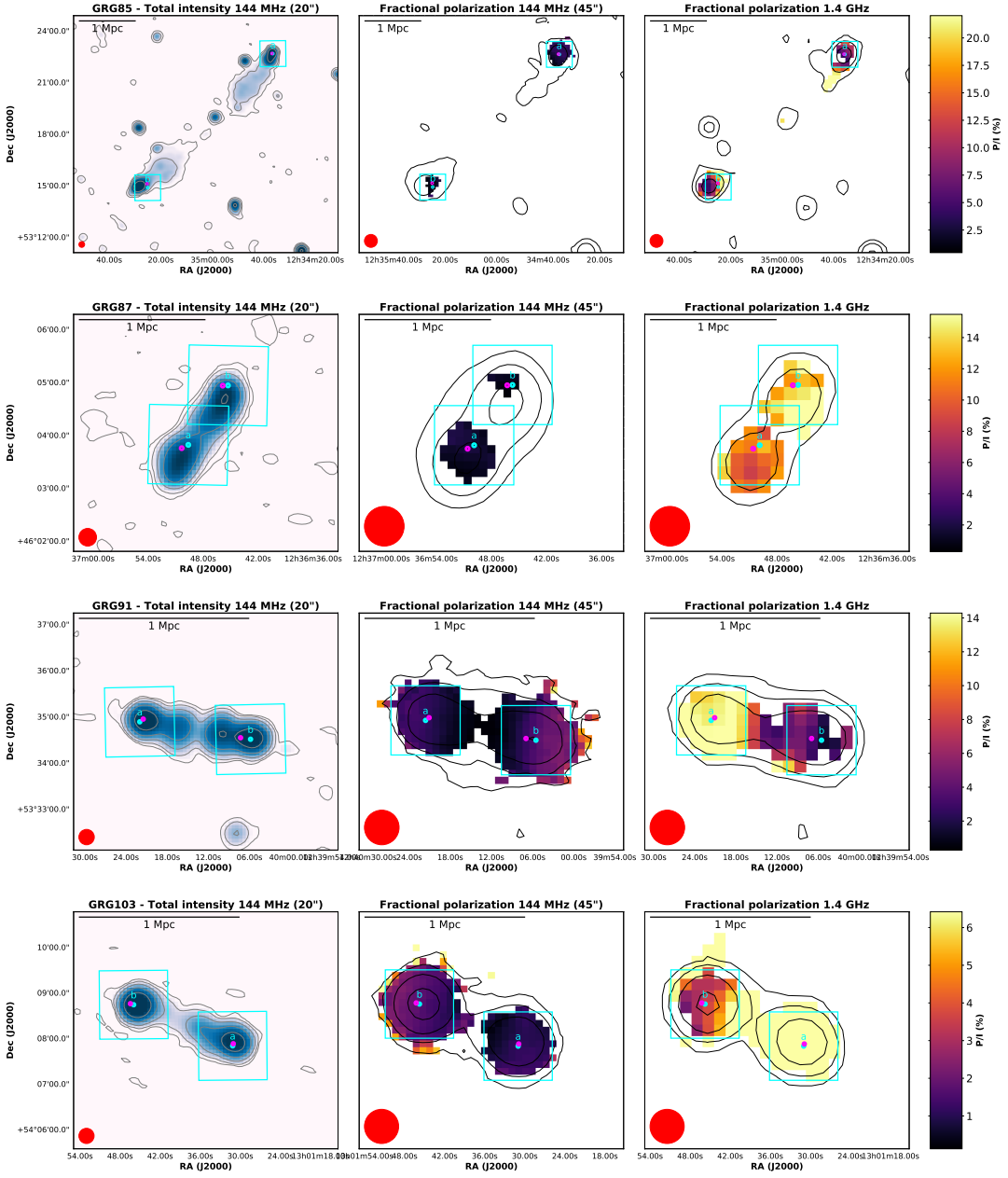

Figure 7.9 (continued)

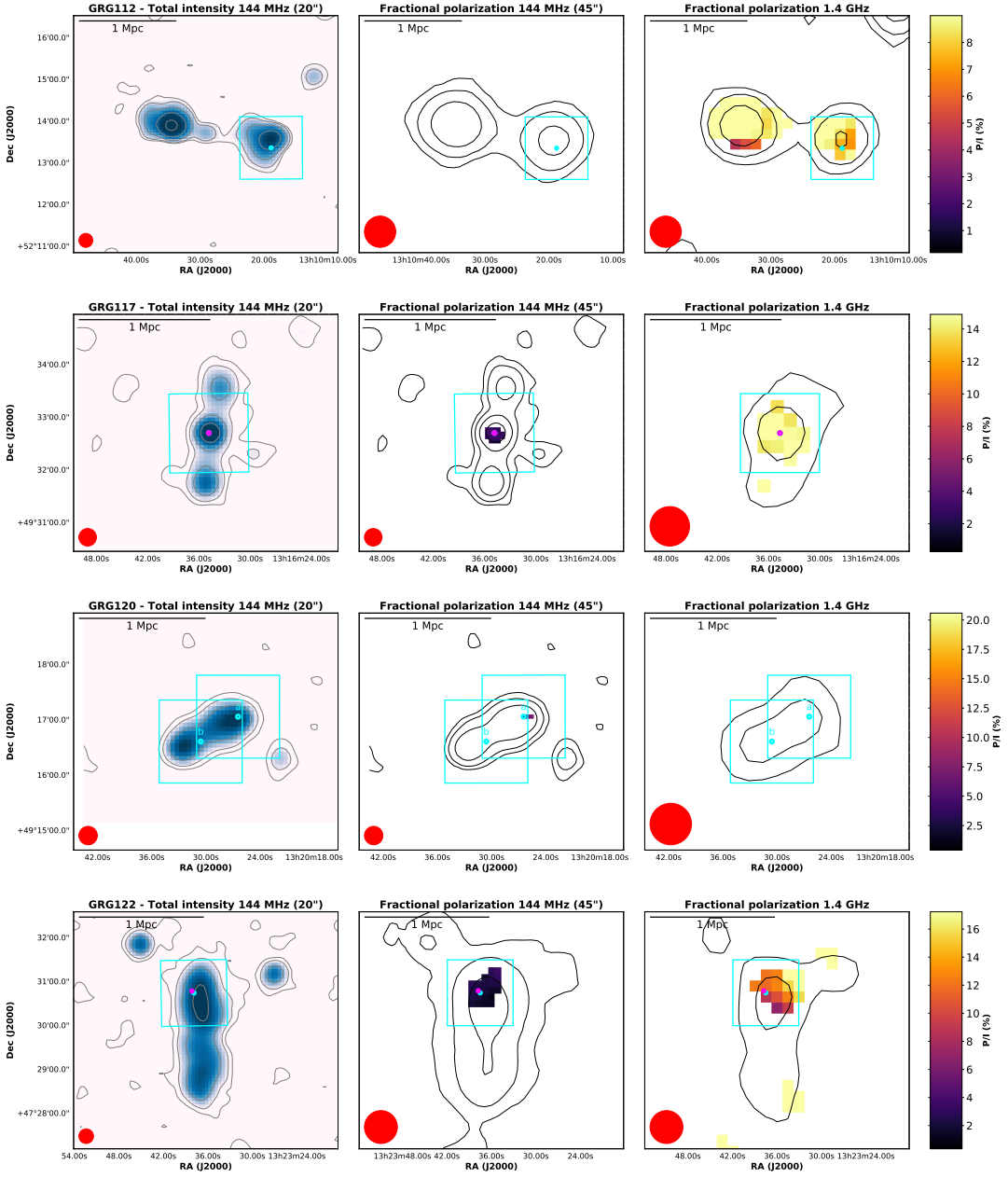

Figure 7.9 (continued)

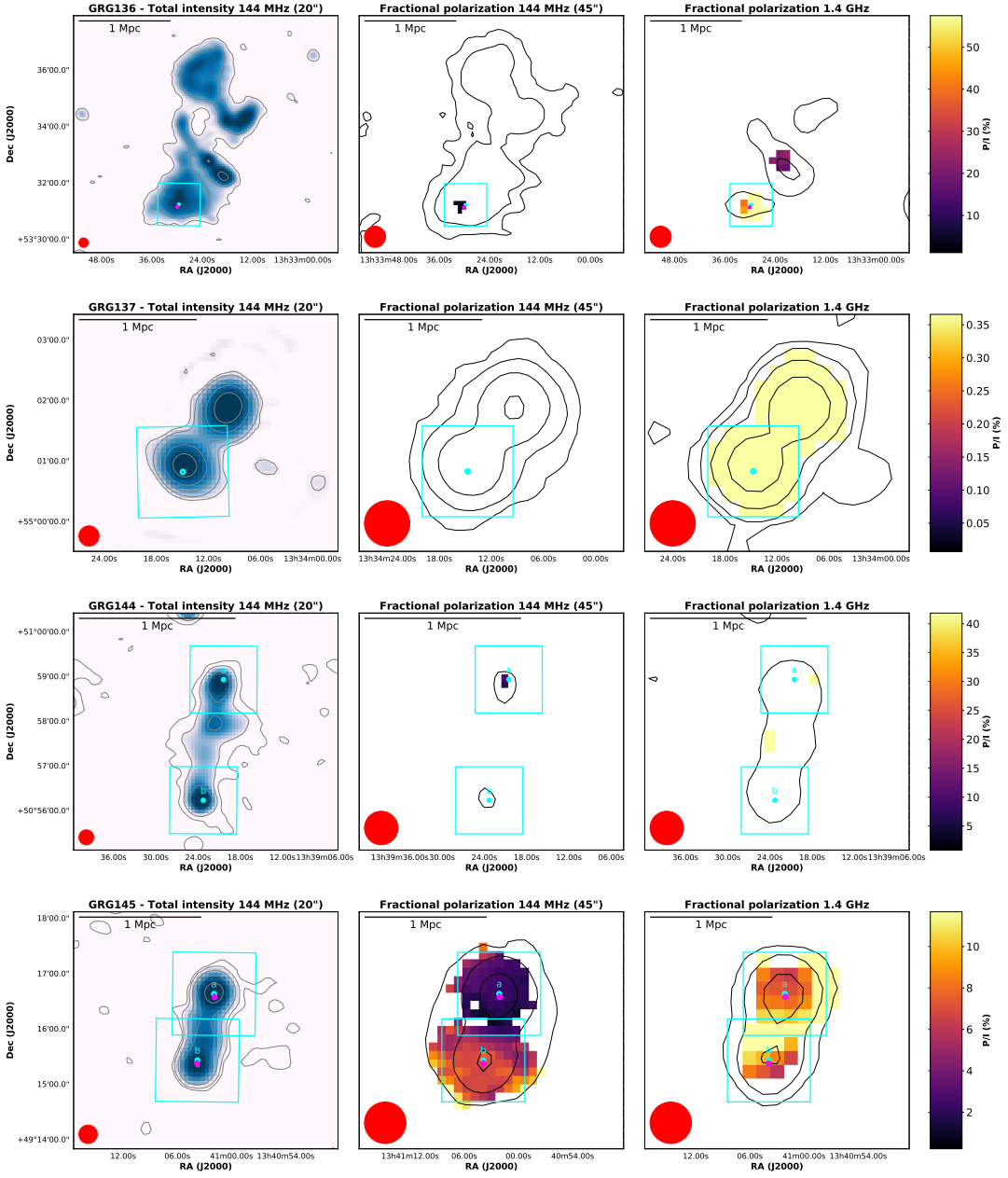

Figure 7.9 (continued)

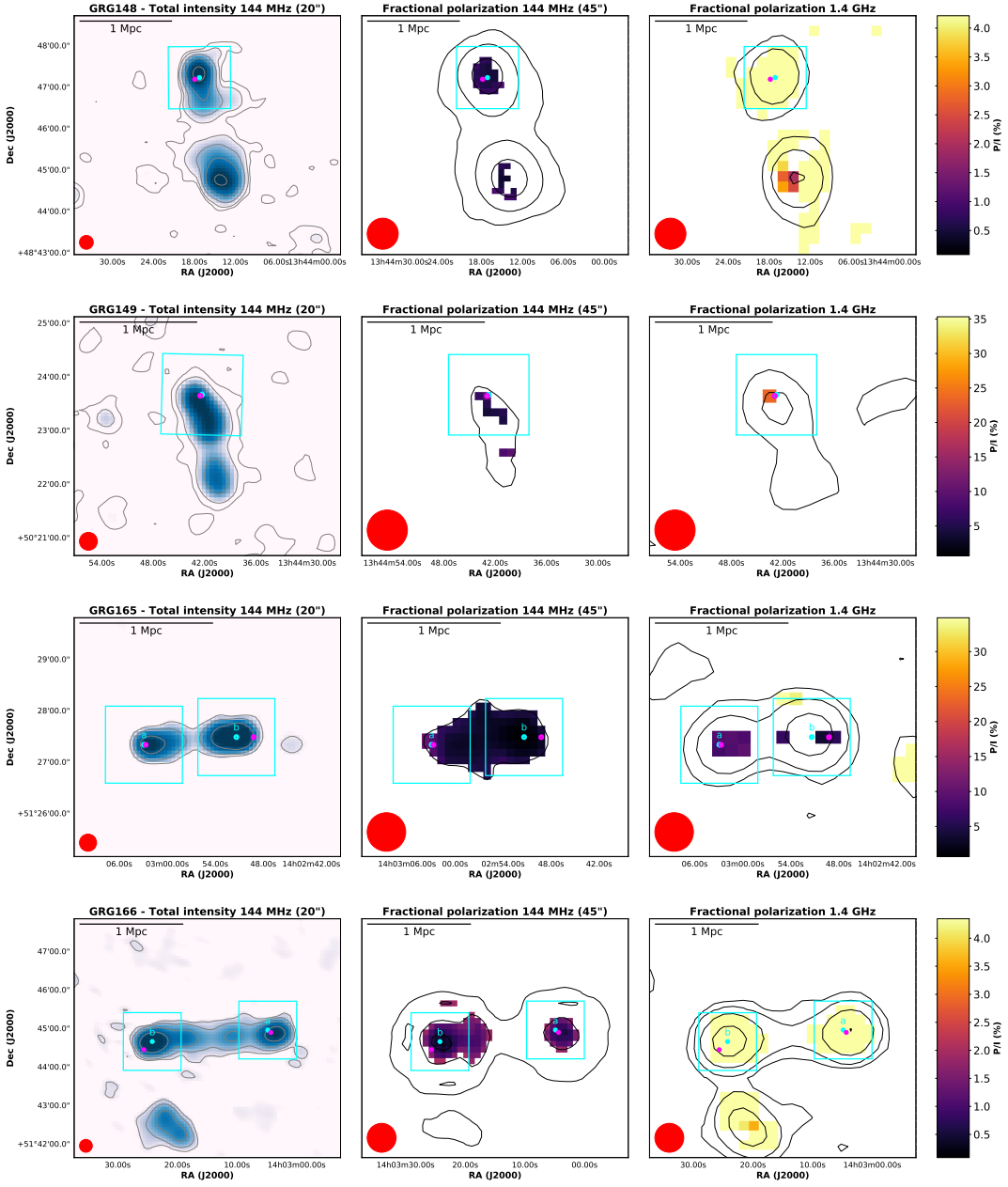

Figure 7.9 (continued)

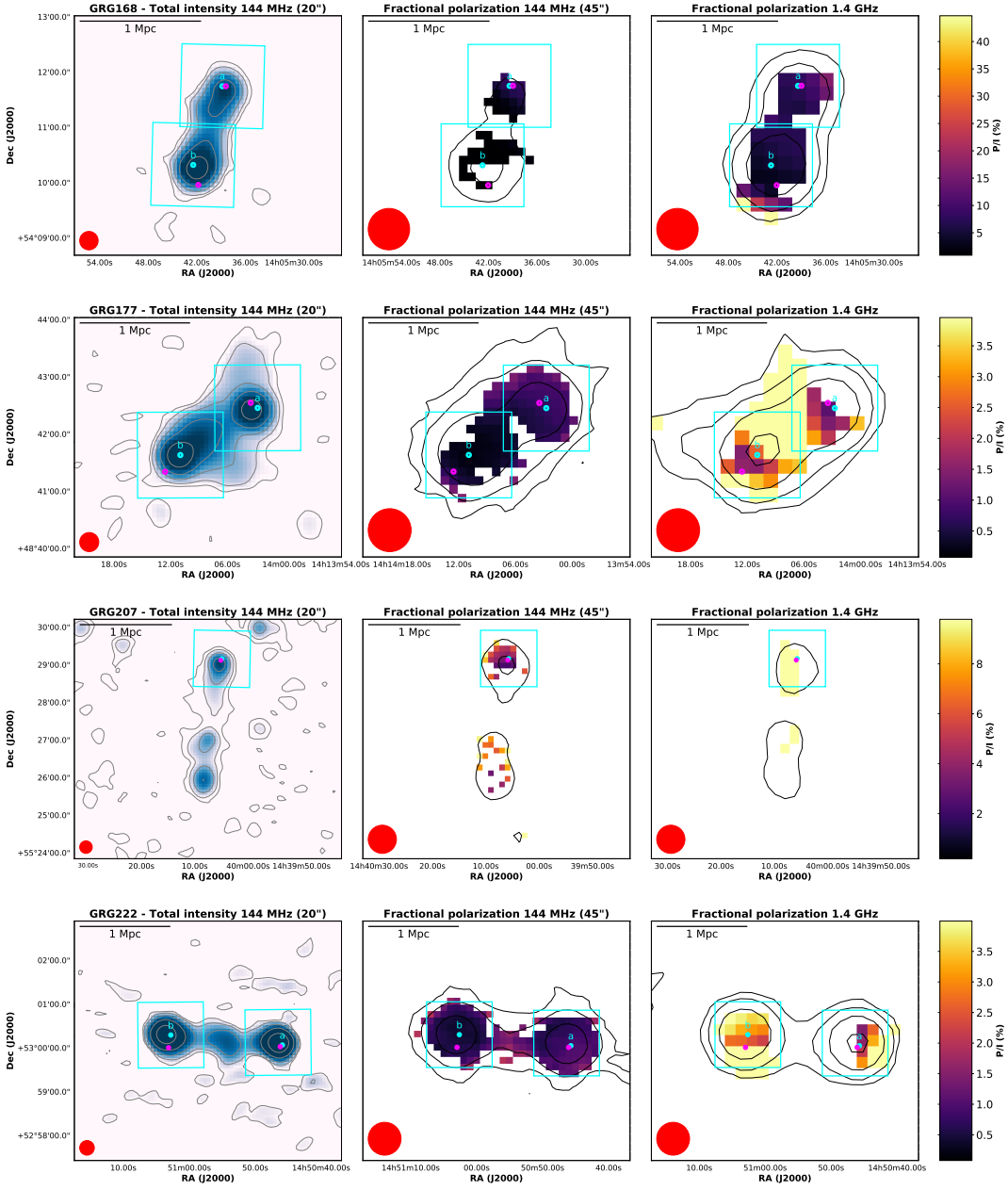

Figure 7.9 (continued)

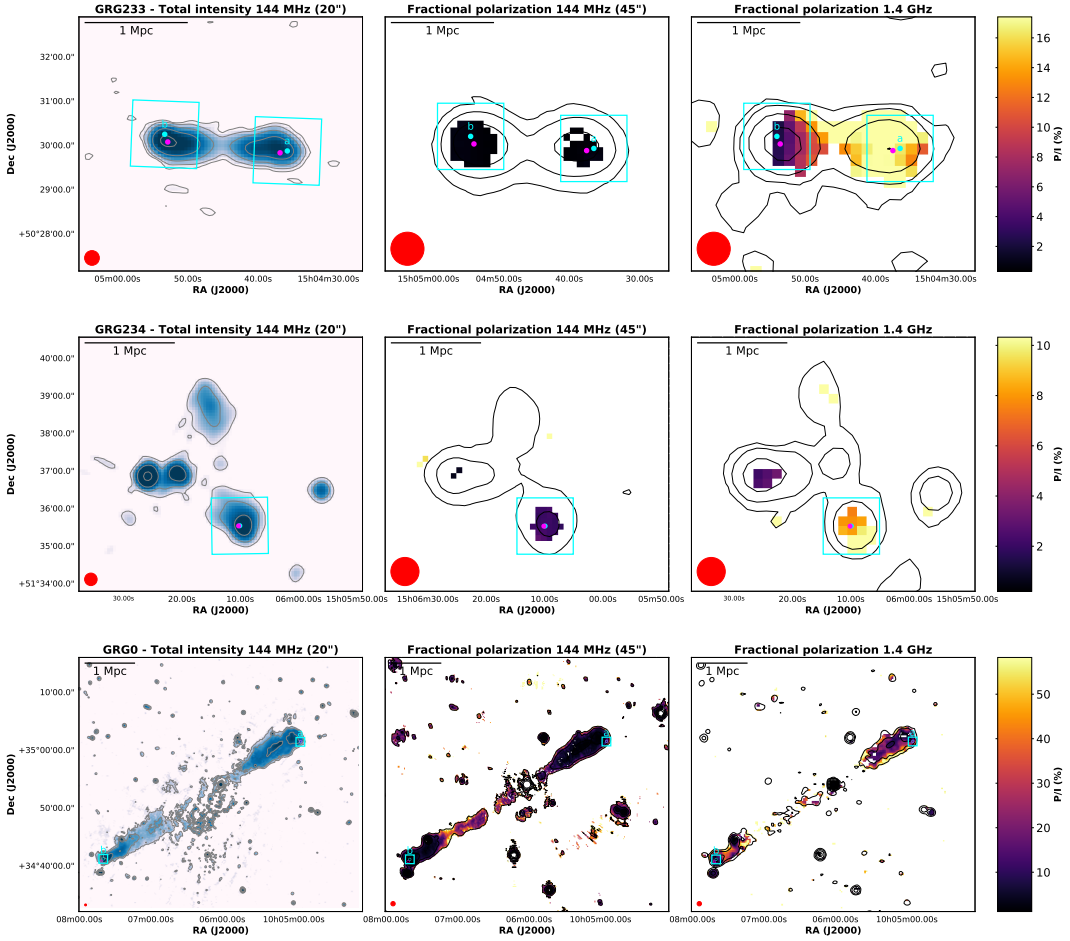

Figure 7.9 (continued)

Thesis conclusions

The last decades have brought great progresses in the knowledge of large-scale magnetic fields, both within galaxy clusters and beyond, and in the understanding of the origin of diffuse cluster radio emission. Many efforts have been made in the complementary fields of theoretical interpretation, numerical simulation and observation. From an observational point of view, the advent of new broad-band receivers on existing radio interferometers (such as the *Jansky Very Large Array*, JVLA) and the advances in computing science, boosted the polarimetric observation techniques into a new frontier, especially at low radio frequencies. Although much work remains to be done, we have now the possibility to automatically apply sophisticated techniques, such as the Rotation Measure (RM) synthesis, to polarization data and compare our results with increasingly more realistic simulations, in order to retrieve important information on magnetic fields.

During my PhD project, I exploited these cutting-edge capabilities to study large-scale magnetic fields, with a particular focus on the magnetic fields within radio relics and in the outskirts of galaxy clusters. This work was mainly motivated by recent observational results which have suggested the presence of magnetic field amplification within radio relics, therefore in regions crossed by low Mach number shock waves. Furthermore, the need for a deeper comprehension of magnetic fields within relics has been raised by theoretical work that stressed the importance of magnetic fields in the particle acceleration mechanisms which power radio relic emission. At the same time, the *Low Frequency Array* (LOFAR) opened up a new window for polarization studies at low-frequencies, which promises to be important for the study of very weak magnetic fields in the outskirts of galaxy clusters.

In the work presented in this Thesis, we have found no evidence of magnetic field amplification at clusters radio relics, although current limitations on the number of background sources detected in the pre-shock region do not allow us to draw general conclusions. This statement is mainly supported by the studies of the the two double relic clusters RXC J1314.4-2515 and Abell 2345 reported in Chapter 3 and in Chapter 4, respectively. In both galaxy clusters, we found that the average RM of the relics is broadly consistent with the Milky Way foreground, while the RM dispersion is more indicative of the intra-cluster magnetic field at the relic position.

In the case of Abell 2345, the RM dispersion of the studied relic was found to be consistent with the magnetic field profile derived for this galaxy cluster. At the position of the relic, the profile predicts an average magnetic field of ~ 0.3 μG. The magnetic field at the position of the studied relic in the RXC J1314.4-2515 galaxy cluster was found to be consistent with the one shown by cosmological simulations, i.e., of the order of 1 μG.

While low Mach number shocks seem to be inefficient in amplifying the intracluster magnetic field, they can affect its topology, stretching and aligning magnetic field lines along the direction perpendicular to the shock normal, as shown by polarization vectors observed at the relics.

The RM synthesis has proven to be a useful tool, both, to derive high precision RMs used to study the magnetic fields in clusters and outside them and to probe more complex Faraday structures. In particular, the analysis presented in Chapter 3 revealed that complex and likely filamentary magnetic field morphologies are mixed with a turbulent thermal plasma within the relic volume. This is confirmed by the detection of internal Faraday depolarization from a peculiar region of the relic.

Moreover, the comparison of observed quantities with cosmological magnetohydrodynamical (Chapter 3) and numerical (Chapter 4) simulations of galaxy clusters has greatly improved our ability to interpret polarization and RMs results. In the case of the RXC J1314.4-2515 galaxy cluster, we were able to apply the RM synthesis to a simulated radio relic and to derive synthesized fractional polarization and RMs. This study probed that, while the observed polarization and RM properties are overall recovered by the simulations, current acceleration models require significant re-acceleration of fossil electrons to match the observed radio power of the relic.

Finally, the study presented in Chapter 6 and in Chapter 7 showed that low-frequency observations are indeed an important tool to unveil weak magnetic fields outside galaxy clusters. In particular, the Faraday depolarization of giant radio galaxies observed at 140 MHz with LOFAR (Chapter 7) suggests that the magnetic field strength drops below 0.1 μG outside the virial radius of galaxy clusters. Intracluster magnetic fields are able to influence the polarization detection rate of such sources up to $2R_{500}$, while at GHz frequencies depolarization effects are only visible closer to the cluster center. Faraday depolarization effects are important also in the outskirt of galaxy clusters where relics are mainly observed, preventing their detection in polarization below 1 GHz (Chapter 6).

Future prospects

The study of diffuse cluster radio sources and large-scale magnetic fields are central topics in the key science programs of the next generation radio and X-ray facilities,

such as the *Square Kilometre Array* (SKA) and *Athena*. Up-coming radio polarimetric surveys, such as the LOFAR Two-Metre Sky Survey (LoTSS), the Polarisation Sky Survey of the Universe's Magnetism (POSSUM) and the Very Large Array Sky Survey (VLASS) promise to shed light on the magnetized Universe, providing unprecedented RMs statistics at both high and low radio frequencies.

The analyses presented in this Thesis will be extended to larger samples, opening new perspectives for the study of magnetic fields in radio relics and on the largest scales. However, the work done in this Thesis has highlighted the need for a further development of the techniques for wide field polarization, and the need for tools to interpret Faraday-complex structures. The analysis of the full double relic galaxy cluster sample presented in Chapter 5 will lead to a deeper knowledge of the role played by magnetic fields in radio relic emission, but more developments will be crucial to push forward our understanding of large-scale magnetic fields.

Bibliography

Abell G. O., 1958, ApJS, 3, 211

Ackermann M. et al., 2014, ApJ, 787, 18

Ackermann M. et al., 2016, ApJ, 819, 149

Akamatsu H., Inoue S., Sato T., Matsusita K., Ishisaki Y., Sarazin C. L., 2013, PASJ, 65, 89

Akamatsu H., Kawahara H., 2013, Publications of the Astronomical Society of Japan, 65, 16

Andernach H., Feretti L., Giovannini G., 1984, A&A, 133, 252

Anderson C. S., Gaensler B. M., Feain I. J., Franzen T. M. O., 2015, ApJ, 815, 49

Angelinelli M., Vazza F., Giocoli C., Ettori S., Jones T. W., Brunetti G., Brüggen M., Eckert D., 2020, MNRAS, 495, 864

Arieli Y., Rephaeli Y., Norman M. L., 2010, ApJ, 716, 918

Arshakian T. G., Beck R., 2011, MNRAS, 418, 2336

Bacchi M., Feretti L., Giovannini G., Govoni F., 2003, A&A, 400, 465

Bagchi J., Enßlin T. A., Miniati F., Stalin C. S., Singh M., Raychaudhury S., Humeshkar N. B., 2002, New Astron., 7, 249

Bagchi J., Sankhyayan S., Sarkar P., Raychaudhury S., Jacob J., Dabhade P., 2017, ApJ, 844, 25

Ballarati B., Feretti L., Ficarra A., Giovannini G., Nanni M., Olori M. C., Gavazzi G., 1981, A&A, 100, 323

Basu A., Fletcher A., Mao S. A., Burkhart B., Beck R., Schnitzeler D., 2019, Galaxies, 7, 89

Beck A. M., Hanasz M., Lesch H., Remus R. S., Stasyszyn F. A., 2013, MNRAS, 429, L60

Beck R., Krause M., 2005, Astronomische Nachrichten, 326, 414

Beck R., Wielebinski R., 2013, Magnetic Fields in Galaxies, Oswalt T. D., Gilmore G., eds., Vol. 5, p. 641

Becker R. H., White R. L., Helfand D. J., 1995, ApJ, 450, 559

Bell A. R., 2013, Astroparticle Physics, 43, 56

Bell M. R., Oppermann N., Crai A., Enßlin T. A., 2013, A&A, 551, L7

Bennett C. L., Larson D., Weiland J. L., Hinshaw G., 2014, ApJ, 794, 135

Benson B., Wittman D. M., Golovich N., Jee M. J., van Weeren R. J., Dawson W. A., 2017, ApJ, 841, 7

Bhatnagar S., Cornwell T. J., Golap K., Uson J. M., 2008, A&A, 487, 419

Bhatnagar S., Rau U., Golap K., 2013, ApJ, 770, 91

Blandford R., Eichler D., 1987, Phys. Rep., 154, 1

Blandford R. D., Rees M. J., 1974, MNRAS, 169, 395

Blasi P., Colafrancesco S., 1999, Astroparticle Physics, 12, 169

Blasi P., Gabici S., Brunetti G., 2007, International Journal of Modern Physics A, 22, 681

Blumenthal G. R., Gould R. J., 1970, Reviews of Modern Physics, 42, 237

Böhringer H., Chon G., Kronberg P. P., 2016, A&A, 596, A22

Bonafede A. et al., 2018, MNRAS, 478, 2927

Bonafede A. et al., 2012, MNRAS, 426, 40

Bonafede A. et al., 2020, arXiv e-prints, arXiv:2011.08856

Bonafede A. et al., 2009a, A&A, 503, 707

Bonafede A., Feretti L., Murgia M., Govoni F., Giovannini G., Dallacasa D., Dolag K., Taylor G. B., 2010, A&A, 513, A30

Bonafede A., Giovannini G., Feretti L., Govoni F., Murgia M., 2009b, A&A, 494, 429

Bonafede A., Govoni F., Feretti L., Murgia M., Giovannini G., Brüggen M., 2011, A&A, 530, A24

Bonafede A., Intema H. T., Brüggen M., Girardi M., Nonino M., Kantharia N., van Weeren R. J., Röttgering H. J. A., 2014, ApJ, 785, 1

Bonafede A., Vazza F., Brüggen M., Murgia M., Govoni F., Feretti L., Giovannini G., Ogrean G., 2013, MNRAS, 433, 3208

Boschin W., Barrena R., Girardi M., 2010, A&A, 521, A78

Boschin W., Girardi M., Barrena R., 2013, MNRAS, 434, 772

Botteon A., Brunetti G., Ryu D., Roh S., 2020a, A&A, 634, A64

Botteon A. et al., 2020b, ApJ, 897, 93

Botteon A., Gastaldello F., Brunetti G., 2018, MNRAS, 476, 5591

Botteon A., Gastaldello F., Brunetti G., Dallacasa D., 2016a, MNRAS, 460, L84

Botteon A., Gastaldello F., Brunetti G., Kale R., 2016b, MNRAS, 463, 1534

Botteon A. et al., 2020c, MNRAS, 499, L11

Brentjens M. A., 2018, Astrophysics and Space Science Library, Vol. 426, Polarization Imaging with LOFAR, p. 159

Brentjens M. A., de Bruyn A. G., 2005, A&A, 441, 1217

Bridle A. H., Davis M. M., Fomalont E. B., Willis A. G., Strom R. G., 1979, ApJ, 228, L9

Brienza M. et al., 2017, A&A, 606, A98

Brienza M. et al., 2020, A&A, 638, A29

Briggs D. S., 1995, in American Astronomical Society Meeting Abstracts, Vol. 187, p. 112.02

Brown S., Rudnick L., 2011, MNRAS, 412, 2

Brüggen M., Bykov A., Ryu D., Röttgering H., 2012, Space Sci. Rev., 166, 187

Brüggen M. et al., 2020, arXiv e-prints, arXiv:2012.08775

Brüggen M., Ruszkowski M., Simionescu A., Hoeft M., Dalla Vecchia C., 2005, ApJ, 631, L21

Brunetti G., Blasi P., Cassano R., Gabici S., 2004, MNRAS, 350, 1174

Brunetti G., Cassano R., Dolag K., Setti G., 2009, A&A, 507, 661

Brunetti G., Jones T. W., 2014, International Journal of Modern Physics D, 23, 1430007

Brunetti G., Jones T. W., 2015, Cosmic Rays in Galaxy Clusters and Their Interaction with Magnetic Fields, Lazarian A., de Gouveia Dal Pino E. M., Melioli C., eds., Vol. 407, p. 557

Brunetti G., Lazarian A., 2011, MNRAS, 410, 127

Brunetti G., Setti G., Comastri A., 1997, A&A, 325, 898

Brunetti G., Setti G., Feretti L., Giovannini G., 2001, MNRAS, 320, 365

Brunetti G., Vazza F., 2020, Phys. Rev. Lett., 124, 051101

Brunetti G., Zimmer S., Zandanel F., 2017, MNRAS, 472, 1506

Bryan G. L. et al., 2014, ApJS, 211, 19

Buote D. A., 2001, ApJ, 553, L15

Burn B. J., 1966, MNRAS, 133, 67

Button C., Marchegiani P., 2020, MNRAS, 499, 864

Bykov A. M., Vazza F., Kropotina J. A., Levenfish K. P., Paerels F. B. S., 2019, Space Sci. Rev., 215, 14

Cantwell T. M. et al., 2020, MNRAS, 495, 143

Caprioli D., Spitkovsky A., 2014, ApJ, 783, 91

Cassano R., Brunetti G., Röttgering H. J. A., Brüggen M., 2010a, A&A, 509, A68

Cassano R., Brunetti G., Setti G., Govoni F., Dolag K., 2007, MNRAS, 378, 1565

Cassano R. et al., 2013, ApJ, 777, 141

Cassano R., Ettori S., Giacintucci S., Brunetti G., Markevitch M., Venturi T., Gitti M., 2010b, ApJ, 721, L82

Cavaliere A., Fusco-Femiano R., 1976, A&A, 500, 95

Chen R., Peng B., Strom R. G., Wei J., 2011, MNRAS, 412, 2433

Chisari N. E. et al., 2019, The Open Journal of Astrophysics, 2, 4

Clarke T. E., 2004, Journal of Korean Astronomical Society, 37, 337

Clarke T. E., Kronberg P. P., Böhringer H., 2001, ApJ, 547, L111

Condon J. J., Cotton W. D., Greisen E. W., Yin Q. F., Perley R. A., Taylor G. B., Broderick J. J., 1998, AJ, 115, 1693

Cooray S., Takeuchi T. T., Akahori T., Miyashita Y., Ideguchi S., Takahashi K., Ichiki K., 2021, MNRAS, 500, 5129

Cornwell T. J., Golap K., Bhatnagar S., 2008, IEEE Journal of Selected Topics in Signal Processing, 2, 647

Croston J. H., Hardcastle M. J., Harris D. E., Belsole E., Birkinshaw M., Worrall D. M., 2005, ApJ, 626, 733

Cuciti V., Cassano R., Brunetti G., Dallacasa D., Kale R., Ettori S., Venturi T., 2015, A&A, 580, A97

Cypriano E. S., Sodré, Laerte J., Kneib J.-P., Campusano L. E., 2004, ApJ, 613, 95

Dabhade P., Gaikwad M., Bagchi J., Pand ey-Pommier M., Sankhyayan S., Raychaudhury S., 2017, MNRAS, 469, 2886

Dabhade P. et al., 2020, A&A, 635, A5

Dahle H., Kaiser N., Irgens R. J., Lilje P. B., Maddox S. J., 2002, ApJS, 139, 313

Dallacasa D. et al., 2009, ApJ, 699, 1288

Dasadia S. et al., 2016, ApJ, 820, L20

Davé R. et al., 2001, ApJ, 552, 473

Dawson W. A. et al., 2015, ApJ, 805, 143

de Gasperin F., Intema H. T., van Weeren R. J., Dawson W. A., Golovich N., Wittman D., Bonafede A., Brüggen M., 2015, MNRAS, 453, 3483

de Gasperin F., van Weeren R. J., Brüggen M., Vazza F., Bonafede A., Intema H. T., 2014, MNRAS, 444, 3130

Delhaize J. et al., 2020, MNRAS

Dennison B., 1980, ApJ, 239, L93

Di Gennaro G. et al., 2020, Nature Astronomy

Di Gennaro G. et al., 2018, ApJ, 865, 24

Diaferio A., Schindler S., Dolag K., 2008, Space Sci. Rev., 134, 7

Dolag K., Bartelmann M., Lesch H., 1999, A&A, 348, 351

Dolag K., Bykov A. M., Diaferio A., 2008, Space Sci. Rev., 134, 311

Dolag K., Kachelriess M., Ostapchenko S., Tomàs R., 2011, ApJ, 727, L4

Dolag K., Schindler S., Govoni F., Feretti L., 2001, A&A, 378, 777

Domínguez-Fernández P., Brüggen M., Vazza F., Banda-Barragán W. E., Rajpurohit K., Mignone A., Mukherjee D., Vaidya B., 2020, MNRAS

Domínguez-Fernández P., Vazza F., Brüggen M., Brunetti G., 2019, MNRAS, 486, 623

Donnert J., Vazza F., Brüggen M., ZuHone J., 2018, Space Sci. Rev., 214, 122

Donnert J. M. F., Stroe A., Brunetti G., Hoang D., Roettgering H., 2016, MNRAS, 462, 2014

Duncan K. J. et al., 2019, A&A, 622, A3

Ebeling H., Voges W., Bohringer H., Edge A. C., Huchra J. P., Briel U. G., 1996, MNRAS, 281, 799

Eckert D. et al., 2016a, A&A, 592, A12

Eckert D., Ettori S., Molendi S., Vazza F., Paltani S., 2013a, A&A, 551, A23

Eckert D., Ettori S., Pointecouteau E., Molendi S., Paltani S., Tchernin C., 2017, Astronomische Nachrichten, 338, 293

Eckert D. et al., 2019, A&A, 621, A40

Eckert D., Jauzac M., Vazza F., Owers M. S., Kneib J. P., Tchernin C., Intema H., Knowles K., 2016b, MNRAS, 461, 1302

Eckert D., Molendi S., Paltani S., 2011, A&A, 526, A79

Eckert D., Molendi S., Vazza F., Ettori S., Paltani S., 2013b, A&A, 551, A22

Eckert D., Produit N., Paltani S., Neronov A., Courvoisier T. J. L., 2008, A&A, 479, 27

Eckert D., Roncarelli M., Ettori S., Molendi S., Vazza F., Gastaldello F., Rossetti M., 2015, MNRAS, 447, 2198

Ehlert K., Weinberger R., Pfrommer C., Springel V., 2021, MNRAS, 503, 1327

Enßlin T., Pfrommer C., Miniati F., Subramanian K., 2011, A&A, 527, A99

Ensslin T. A., Biermann P. L., Klein U., Kohle S., 1998, A&A, 332, 395

Enßlin T. A., Brüggen M., 2002, MNRAS, 331, 1011

Enßlin T. A., Gopal-Krishna, 2001, A&A, 366, 26

Enßlin T. A., Röttgering H., 2002, A&A, 396, 83

Enßlin T. A., Vogt C., 2003, A&A, 401, 835

Ensslin T. A., Vogt C., Clarke T. E., Taylor G. B., 2003, ApJ, 597, 870

Ettori S. et al., 2019, A&A, 621, A39

Fanaroff B. L., Riley J. M., 1974, MNRAS, 167, 31P

Felten J. E., 1996, Astronomical Society of the Pacific Conference Series, Vol. 88, Mitigating the Baryon Crisis in Clusters: Can Magnetic Pressure be Important?, Trimble V., Reisenegger A., eds., p. 271

Felten J. E., Gould R. J., Stein W. A., Woolf N. J., 1966, ApJ, 146, 955

Feretti L., Brunetti G., Giovannini G., Kassim N., Orrú E., Setti G., 2004, Journal of Korean Astronomical Society, 37, 315

Feretti L., Giovannini G., 1996, in IAU Symposium, Vol. 175, Extragalactic Radio Sources, Ekers R. D., Fanti C., Padrielli L., eds., p. 333

Feretti L., Giovannini G., Govoni F., Murgia M., 2012, A&ARv, 20, 54

Feretti L., Schuecker P., Böhringer H., Govoni F., Giovannini G., 2005, A&A, 444, 157

Fermi E., 1949, Physical Review, 75, 1169

Ferrari C., Govoni F., Schindler S., Bykov A. M., Rephaeli Y., 2008, Space Sci. Rev., 134, 93

Finoguenov A., Sarazin C. L., Nakazawa K., Wik D. R., Clarke T. E., 2010, ApJ, 715, 1143

Frick P., Sokoloff D., Stepanov R., Beck R., 2010, MNRAS, 401, L24

Furlanetto S. R., Loeb A., 2001, ApJ, 556, 619

Gabici S., Blasi P., 2003, ApJ, 583, 695

Gabriel C. et al., 2004, in Astronomical Society of the Pacific Conference Series, Vol. 314, Astronomical Data Analysis Software and Systems (ADASS) XIII, Ochsenbein F., Allen M. G., Egret D., eds., p. 759

Gabuzda D. C., Cawthorne T. V., Roberts D. H., Wardle J. F. C., 1992, ApJ, 388, 40

Garrington S. T., Leahy J. P., Conway R. G., Laing R. A., 1988, Nature, 331, 147

Gaspari M., Churazov E., 2013, A&A, 559, A78

Gaspari M., Sądowski A., 2017, ApJ, 837, 149

George L. T. et al., 2017, MNRAS, 467, 936

George S. J., Stil J. M., Keller B. W., 2012, Publications of the Astronomical Society of Australia, 29, 214

Ghirardini V. et al., 2019a, A&A, 621, A41

Ghirardini V., Ettori S., Eckert D., Molendi S., 2019b, A&A, 627, A19

Giacintucci S., Markevitch M., Cassano R., Venturi T., Clarke T. E., Brunetti G., 2017, ApJ, 841, 71

Giovannini G., Bonafede A., Feretti L., Govoni F., Murgia M., 2010, A&A, 511, L5

Giovannini G., Feretti L., Stanghellini C., 1991, A&A, 252, 528

Giovannini G., Feretti L., Venturi T., Kim K. T., Kronberg P. P., 1993, ApJ, 406, 399

Giovannini G., Tordi M., Feretti L., 1999, New Astron., 4, 141

Girardi M. et al., 2016, MNRAS, 456, 2829

Gitti M., Brighenti F., McNamara B. R., 2012, Advances in Astronomy, 2012, 950641

Golovich N. et al., 2019a, The Astrophysical Journal Supplement Series, 240, 39

Golovich N. et al., 2019b, ApJ, 882, 69

Govoni F., Feretti L., 2004, International Journal of Modern Physics D, 13, 1549

Govoni F., Murgia M., Feretti L., Giovannini G., Dallacasa D., Taylor G. B., 2005, A&A, 430, L5

Govoni F., Murgia M., Feretti L., Giovannini G., Dolag K., Taylor G. B., 2006, A&A, 460, 425

Govoni F. et al., 2017, A&A, 603, A122

Govoni F. et al., 2019, Science, 364, 981

Govoni F., Taylor G. B., Dallacasa D., Feretti L., Giovannini G., 2001, A&A, 379, 807

Grasso D., Rubinstein H. R., 2001, Phys. Rep., 348, 163

Guidetti D., Laing R. A., Bridle A. H., Parma P., Gregorini L., 2011, MNRAS, 413, 2525

Guidetti D., Laing R. A., Croston J. H., Bridle A. H., Parma P., 2012, MNRAS, 423, 1335

Guidetti D., Laing R. A., Murgia M., Govoni F., Gregorini L., Parma P., 2010, A&A, 514, A50

Guidetti D., Murgia M., Govoni F., Parma P., Gregorini L., de Ruiter H. R., Cameron R. A., Fanti R., 2008, A&A, 483, 699

Guo X., Sironi L., Narayan R., 2014a, ApJ, 794, 153

Guo X., Sironi L., Narayan R., 2014b, ApJ, 797, 47

Gupta Y. et al., 2017, Current Science, 113, 707

Ha J.-H., Ryu D., Kang H., 2018, ApJ, 857, 26

Ha J.-H., Ryu D., Kang H., 2020, ApJ, 892, 86

Ha J.-H., Ryu D., Kang H., van Marle A. J., 2018, ApJ, 864, 105

Hackstein S., Vazza F., Brüggen M., Sigl G., Dundovic A., 2016, MNRAS, 462, 3660

Hales C. A., Gaensler B. M., Norris R. P., Middelberg E., 2012, MNRAS, 424, 2160

Hao J. et al., 2010, ApJS, 191, 254

Hardcastle M. J. et al., 2019, MNRAS, 488, 3416

Heald G., 2009, in IAU Symposium, Vol. 259, Cosmic Magnetic Fields: From Planets, to Stars and Galaxies, Strassmeier K. G., Kosovichev A. G., Beckman J. E., eds., pp. 591–602

Herrera Ruiz N. et al., 2020, arXiv e-prints, arXiv:2011.08292

Hill G. J., Goodrich R. W., Depoy D. L., 1996, ApJ, 462, 163

Hitomi Collaboration et al., 2016, Nature, 535, 117

Hitomi Collaboration et al., 2018, PASJ, 70, 9

Hlavacek-Larrondo J. et al., 2018, MNRAS, 475, 2743

Hoang D. N. et al., 2017, MNRAS, 471, 1107

Hoang D. N. et al., 2018, MNRAS, 478, 2218

Hoeft M., Brüggen M., 2007, MNRAS, 375, 77

Hoeft M., Nuza S. E., Gottlöber S., van Weeren R. J., Röttgering H. J. A., Brüggen M., 2011, Journal of Astrophysics and Astronomy, 32, 509

Hong S. E., Kang H., Ryu D., 2015, ApJ, 812, 49

Hu Y., Lazarian A., Li Y., Zhuravleva I., Gendron-Marsolais M.-L., 2020, ApJ, 901, 162

Hudson D. S., Mittal R., Reiprich T. H., Nulsen P. E. J., Andernach H., Sarazin C. L., 2010, A&A, 513, A37

Hutschenreuter S., Enßlin T. A., 2020, A&A, 633, A150

Iapichino L., Brüggen M., 2012, MNRAS, 423, 2781

Ideguchi S., Miyashita Y., Heald G., 2018, Galaxies, 6, 140

Inogamov N. A., Sunyaev R. A., 2003, Astronomy Letters, 29, 791

Ishwara-Chandra C. H., Saikia D. J., 1999, MNRAS, 309, 100

Itahana M., Takizawa M., Akamatsu H., Ohashi T., Ishisaki Y., Kawahara H., van Weeren R. J., 2015, PASJ, 67, 113

Jaffe W. J., 1977, ApJ, 212, 1

Jagannathan P., Bhatnagar S., Rau U., Taylor A. R., 2017, AJ, 154, 56

Ji S., Oh S. P., Ruszkowski M., Markevitch M., 2016, MNRAS, 463, 3989

Johnson A. R., Rudnick L., Jones T. W., Mendygral P. J., Dolag K., 2020, ApJ, 888, 101

Johnson R. A., Leahy J. P., Garrington S. T., 1995, MNRAS, 273, 877

Johnston S. et al., 2007, Publ. Astron. Soc. Australia, 24, 174

Johnston-Hollitt M., Dehghan S., Pratley L., 2015, in IAU Symposium, Vol. 313, Extragalactic Jets from Every Angle, Massaro F., Cheung C. C., Lopez E., Siemiginowska A., eds., pp. 321–326

Johnston-Hollitt M., Ekers R. D., 2004, arXiv e-prints, astro

Johnston-Hollitt M. et al., 2015, in Advancing Astrophysics with the Square Kilometre Array (AASKA14), p. 92

Jonas J., MeerKAT Team, 2016, in MeerKAT Science: On the Pathway to the SKA, p. 1

Jones F. C., Ellison D. C., 1991, Space Sci. Rev., 58, 259

Kaczmarek J. F., Purcell C. R., Gaensler B. M., Sun X., O'Sullivan S. P., McClure-Griffiths N. M., 2018, MNRAS, 476, 1596

Kaiser N., 1986, MNRAS, 222, 323

Kalberla P. M. W., Burton W. B., Hartmann D., Arnal E. M., Bajaja E., Morras R., Pöppel W. G. L., 2005, A&A, 440, 775

Kale R. et al., 2015, A&A, 579, A92

Kang H., Ryu D., 2011, ApJ, 734, 18

Kang H., Ryu D., 2013, ApJ, 764, 95

Kang H., Ryu D., 2015, ApJ, 809, 186

Kang H., Ryu D., 2016, ApJ, 823, 13

Kang H., Ryu D., Ha J.-H., 2019, ApJ, 876, 79

Kardashev N. S., 1962, Soviet Ast., 6, 317

Kierdorf M., Beck R., Hoeft M., Klein U., van Weeren R. J., Forman W. R., Jones C., 2017, A&A, 600, A18

Kim K. T., Tribble P. C., Kronberg P. P., 1991, ApJ, 379, 80

King I. R., 1972, ApJ, 174, L123

Kravtsov A. V., Borgani S., 2012, ARA&A, 50, 353

Krymskii G. F., 1977, Akademiia Nauk SSSR Doklady, 234, 1306

Kulsrud R. M., Zweibel E. G., 2008, Reports on Progress in Physics, 71, 046901

Kuźmicz A., Jamrozy M., Bronarska K., Janda-Boczar K., Saikia D. J., 2018, ApJS, 238, 9

Laing R. A., 1988, Nature, 331, 149

Laing R. A., Bridle A. H., Parma P., Murgia M., 2008, MNRAS, 391, 521

Laing R. A., Canvin J. R., Cotton W. D., Bridle A. H., 2006, MNRAS, 368, 48

Laing R. A., Riley J. M., Longair M. S., 1983, MNRAS, 204, 151

Large M. I., Mathewson D. S., Haslam C. G. T., 1959, Nature, 183, 1663

Lawler J. M., Dennison B., 1982, ApJ, 252, 81

Lazarian A., Beresnyak A., 2006, MNRAS, 373, 1195

Lazarian A., Yuen K. H., 2018, ApJ, 865, 59

Lazarian A., Yuen K. H., Ho K. W., Chen J., Lazarian V., Lu Z., Yang B., Hu Y., 2018, ApJ, 865, 46

Le Roux E., 1961, Annales d'Astrophysique, 24, 71

Leccardi A., Rossetti M., Molendi S., 2010, A&A, 510, A82

Li F., Brown S., Cornwell T. J., de Hoog F., 2011, A&A, 531, A126

Locatelli N. T. et al., 2020, MNRAS, 496, L48

Loi F. et al., 2019, MNRAS, 490, 4841

Loi F., Murgia M., Govoni F., Vacca V., Prandoni I., Li H., Feretti L., Giovannini G., 2018, Galaxies, 6, 133

Loi F. et al., 2020, MNRAS, 498, 1628

Lovisari L. et al., 2017, ApJ, 846, 51

Lovisari L., Reiprich T. H., Schellenberger G., 2015, A&A, 573, A118

Lovisari L. et al., 2020, ApJ, 892, 102

Lovisari L., Schindler S., Kapferer W., 2011, A&A, 528, A60

Lyskova N., Churazov E., Zhang C., Forman W., Jones C., Dolag K., Roediger E., Sheardown A., 2019, MNRAS, 485, 2922

Machalski J., Jamrozy M., 2006, A&A, 454, 95

Mack K. H., Klein U., O'Dea C. P., Willis A. G., 1997, A&AS, 123, 423

Mack K. H., Klein U., O'Dea C. P., Willis A. G., Saripalli L., 1998, A&A, 329, 431

Mahatma V. H. et al., 2019, A&A, 622, A13

Malarecki J. M., Jones D. H., Saripalli L., Staveley-Smith L., Subrahmanyan R., 2015, MNRAS, 449, 955

Malavasi N., Aghanim N., Tanimura H., Bonjean V., Douspis M., 2020, A&A, 634, A30

Mandal S. et al., 2020, A&A, 634, A4

Marinacci F., Vogelsberger M., Mocz P., Pakmor R., 2015, MNRAS, 453, 3999

Markevitch M., Gonzalez A. H., David L., Vikhlinin A., Murray S., Forman W., Jones C., Tucker W., 2002, ApJ, 567, L27

Markevitch M., Govoni F., Brunetti G., Jerius D., 2005, ApJ, 627, 733

Markevitch M., Vikhlinin A., 2007, Phys. Rep., 443, 1

Martin-Alvarez S., Planelles S., Quilis V., 2017, Ap&SS, 362, 91

Massaro F., Álvarez-Crespo N., Capetti A., Baldi R. D., Pillitteri I., Campana R., Paggi A., 2019, ApJS, 240, 20

Mazzotta P., Bourdin H., Giacintucci S., Markevitch M., Venturi T., 2011, Memorie della Societa Astronomica Italiana, 82, 495

McLean B. J., Greene G. R., Lattanzi M. G., Pirenne B., 2000, in Astronomical Society of the Pacific Conference Series, Vol. 216, Astronomical Data Analysis Software and Systems IX, Manset N., Veillet C., Crabtree D., eds., p. 145

McNamara B. R., Nulsen P. E. J., 2007, ARA&A, 45, 117

Mevius M., 2018, RMextract: Ionospheric Faraday Rotation calculator

Miley G., 1980, Annual Review of Astronomy & Astrophysics, 18, 165

Mingo B. et al., 2019, MNRAS, 488, 2701

Miniati F., Ryu D., Kang H., Jones T. W., 2001, ApJ, 559, 59

Mirakhor M. S., Walker S. A., 2020, MNRAS, 497, 3204

Missaglia V., Massaro F., Capetti A., Paolillo M., Kraft R. P., Baldi R. D., Paggi A., 2019, A&A, 626, A8

Miyashita Y., Ideguchi S., Takahashi K., 2016, Publications of the Astronomical Society of Japan, 68, 44

Molendi S., Pizzolato F., 2001, ApJ, 560, 194

Morandi A., Cui W., 2014, MNRAS, 437, 1909

Morganti R. et al., 2020, arXiv e-prints, arXiv:2011.08239

Mulcahy D. D. et al., 2014, A&A, 568, A74

Murgia M., Fanti C., Fanti R., Gregorini L., Klein U., Mack K. H., Vigotti M., 1999, A&A, 345, 769

Murgia M., Govoni F., Feretti L., Giovannini G., Dallacasa D., Fanti R., Taylor G. B., Dolag K., 2004, A&A, 424, 429

Neld A. et al., 2018, A&A, 617, A136

Neronov A., Vovk I., 2010, Science, 328, 73

Noordam J. E., 2004, in Society of Photo-Optical Instrumentation Engineers (SPIE) Conference Series, Vol. 5489, Ground-based Telescopes, Oschmann Jacobus M. J., ed., pp. 817–825

Offringa A. R., McKinley B., Hurley-Walker, et al., 2014, MNRAS, 444, 606

Offringa A. R., Smirnov O., 2017, MNRAS, 471, 301

Ogrean G. A., Brüggen M., 2013, MNRAS, 433, 1701

Ogrean G. A., Brüggen M., van Weeren R. J., Burgmeier A., Simionescu A., 2014, MNRAS, 443, 2463

Okabe N., Akamatsu H., Kakuwa J., Fujita Y., Zhang Y., Tanaka M., Umetsu K., 2015, PASJ, 67, 114

Okabe N., Takada M., Umetsu K., Futamase T., Smith G. P., 2010, PASJ, 62, 811

Oppermann N. et al., 2015, A&A, 575, A118

Oppermann N. et al., 2012, A&A, 542, A93

Orrù E. et al., 2015, A&A, 584, A112

O'Sullivan S. et al., 2018a, Galaxies, 6, 126

O'Sullivan S. P. et al., 2020, MNRAS, 495, 2607

O'Sullivan S. P., Lenc E., Anderson C. S., Gaensler B. M., Murphy T., 2018b, MNRAS, 475, 4263

O'Sullivan S. P. et al., 2019, A&A, 622, A16

Owen F. N., Rudnick L., Eilek J., Rau U., Bhatnagar S., Kogan L., 2014, ApJ, 794, 24

Ozawa T. et al., 2015, PASJ, 67, 110

Parma P., Murgia M., Morganti R., Capetti A., de Ruiter H. R., Fanti R., 1999, A&A, 344, 7

Pearce C. J. J. et al., 2017, ApJ, 845, 81

Peng B., Chen R. R., Strom R., 2015, in Advancing Astrophysics with the Square Kilometre Array (AASKA14), p. 109

Penzias A. A., Wilson R. W., 1965, ApJ, 142, 419

Perley R. A., Butler B. J., 2013, The Astrophysical Journal Supplement Series, 206, 16

Peterson J. R., Fabian A. C., 2006, Phys. Rep., 427, 1

Petrosian V., 2001, ApJ, 557, 560

Piffaretti R., Arnaud M., Pratt G. W., Pointecouteau E., Melin J. B., 2011, A&A, 534, A109

Pinzke A., Oh S. P., Pfrommer C., 2013, MNRAS, 435, 1061

Pizzo R. F., de Bruyn A. G., Bernardi G., Brentjens M. A., 2011, A&A, 525, A104

Planck Collaboration et al., 2016a, A&A, 594, A19

Planck Collaboration et al., 2016b, A&A, 594, A27

Proctor R. N., Mendes de Oliveira C., Azanha L., Dupke R., Overzier R., 2015, MNRAS, 449, 2345

Pshirkov M. S., Tinyakov P. G., Urban F. R., 2015, MNRAS, 452, 2851

Quici B. et al., 2021, Publ. Astron. Soc. Australia, 38, e008

Raja R. et al., 2020, MNRAS, 493, L28

Rajpurohit K. et al., 2018, ApJ, 852, 65

Rajpurohit K. et al., 2020a, A&A, 636, A30

Rajpurohit K. et al., 2020b, A&A, 642, L13

Rau U., Cornwell T. J., 2011, A&A, 532, A71

Ravi V. et al., 2016, Science, 354, 1249

Reiprich T. H., Basu K., Ettori S., Israel H., Lovisari L., Molendi S., Pointecouteau E., Roncarelli M., 2013, Space Sci. Rev., 177, 195

Rephaeli Y., 1979, ApJ, 227, 364

Roettiger K., Burns J. O., Stone J. M., 1999, ApJ, 518, 603

Roncarelli M., Ettori S., Borgani S., Dolag K., Fabjan D., Moscardini L., 2013, MNRAS, 432, 3030

Rosati P., Borgani S., Norman C., 2002, ARA&A, 40, 539

Rossetti M. et al., 2016, MNRAS, 457, 4515

Rossetti M., Molendi S., 2004, A&A, 414, L41

Rudnick L., 2019, arXiv e-prints, arXiv:1901.09074

Rudnick L., Lemmerman J. A., 2009, ApJ, 697, 1341

Rudnick L., Owen F. N., 2014, ApJ, 785, 45

Ruel J. et al., 2014, ApJ, 792, 45

Ruszkowski M., Oh S. P., 2010, ApJ, 713, 1332

Ryu D., Kang H., Cho J., Das S., 2008, Science, 320, 909

Ryu D., Kang H., Ha J.-H., 2019, ApJ, 883, 60

Ryu D., Kang H., Hallman E., Jones T. W., 2003, ApJ, 593, 599

Ryu D., Schleicher D. R. G., Treumann R. A., Tsagas C. G., Widrow L. M., 2012, Space Sci. Rev., 166, 1

Sakelliou I., Merrifield M. R., 2000, MNRAS, 311, 649

Sanderson A. J. R., O'Sullivan E., Ponman T. J., 2009, MNRAS, 395, 764

Sarazin C. L., 1986, Reviews of Modern Physics, 58, 1

Savini F. et al., 2019, A&A, 622, A24

Schindler S., Muller E., 1993, A&A, 272, 137

Schlickeiser R., Vainio R., Böttcher M., Lerche I., Pohl M., Schuster C., 2002, A&A, 393, 69

Schnitzeler D. H. F. M., 2010, MNRAS, 409, L99

Schnitzeler D. H. F. M., 2018, MNRAS, 474, 300

Schnitzeler D. H. F. M., Lee K. J., 2017, MNRAS, 466, 378

Schober J., Schleicher D. R. G., Federrath C., Bovino S., Klessen R. S., 2015, Phys. Rev. E, 92, 023010

Sereno M. et al., 2018, Nature Astronomy, 2, 744

Seymour N. et al., 2020, Publ. Astron. Soc. Australia, 37, e013

Shabala S. S., Godfrey L. E. H., 2013, ApJ, 769, 129

Shan Y., McDonald M., Courteau S., 2015, ApJ, 800, 122

Shimwell T. W. et al., 2017, A&A, 598, A104

Shimwell T. W. et al., 2019, A&A, 622, A1

Shulevski A. et al., 2019, A&A, 628, A69

Simionescu A., Werner N., Mantz A., Allen S. W., Urban O., 2017, MNRAS, 469,

1476

Simionescu A. et al., 2013, ApJ, 775, 4

Simionescu A. et al., 2012, ApJ, 757, 182

Simionescu A. et al., 2019, Space Sci. Rev., 215, 24

Simmons J. F. L., Stewart B. G., 1985, A&A, 142, 100

Simonetti J. H., Cordes J. M., Spangler S. R., 1984, ApJ, 284, 126

Simonetti J. M., 1992, ApJ, 386, 170

Skillman S. W., Xu H., Hallman E. J., O'Shea B. W., Burns J. O., Li H., Collins D. C., Norman M. L., 2013, ApJ, 765, 21

Snowden S. L., Mushotzky R. F., Kuntz K. D., Davis D. S., 2008, A&A, 478, 615

Sokoloff D. D., Bykov A. A., Shukurov A., Berkhuijsen E. M., Beck R., Poezd A. D., 1998, MNRAS, 299, 189

Sotomayor-Beltran C. et al., 2013, A&A, 552, A58

Springel V. et al., 2005, Nature, 435, 629

Stasyszyn F. A., de los Rios M., 2019, MNRAS, 487, 4768

Stil J. M., Taylor A. R., Sunstrum C., 2011, ApJ, 726, 4

Stokes G. G., 1851, Transactions of the Cambridge Philosophical Society, 9, 399

Strom R. G., Jaegers W. J., 1988, A&A, 194, 79

Stuardi C., Bonafede A., Lovisari L., Domínguez-Fernández P., Vazza F., Brüggen M., van Weeren R. J., de Gasperin F., 2021, MNRAS, 502, 2518

Stuardi C. et al., 2019, MNRAS, 489, 3905

Stuardi C. et al., 2020, A&A, 638, A48

Subrahmanyan R., Saripalli L., Safouris V., Hunstead R. W., 2008, ApJ, 677, 63

Subramanian K., 2016, Reports on Progress in Physics, 79, 076901

Subramanian K., Shukurov A., Haugen N. E. L., 2006, MNRAS, 366, 1437

Sun X. H., Han J. L., 2004, in The Magnetized Interstellar Medium, Uyaniker B., Reich W., Wielebinski R., eds., pp. 25–30

Sun X. H. et al., 2015, AJ, 149, 60

Sunyaev R. A., Zeldovich Y. B., 1972, A&A, 20, 189

Tang H., Scaife A. M. M., Wong O. I., Kapińska A. D., Rudnick L., Shabala S. S., Seymour N., Norris R. P., 2020, MNRAS, 499, 68

Tasse C., 2014, A&A, 566, A127

Tasse C. et al., 2018, A&A, 611, A87

Tasse C. et al., 2020, arXiv e-prints, arXiv:2011.08328

Tavecchio F., Ghisellini G., Bonnoli G., Foschini L., 2011, MNRAS, 414, 3566

Taylor A. R., Stil J. M., Sunstrum C., 2009, ApJ, 702, 1230

Terni de Gregory B., Feretti L., Giovannini G., Govoni F., Murgia M., Perley R. A., Vacca V., 2017, A&A, 608, A58

Tingay S. J. et al., 2013, Publ. Astron. Soc. Australia, 30, e007

Trasatti M., Akamatsu H., Lovisari L., Klein U., Bonafede A., Brüggen M., Dallacasa D., Clarke T., 2015, A&A, 575, A45

Tribble P. C., 1991a, MNRAS, 250, 726

Tribble P. C., 1991b, MNRAS, 253, 147

Tsien S. C., 1982, MNRAS, 200, 377

Urdampilleta I., Akamatsu H., Mernier F., Kaastra J. S., de Plaa J., Ohashi T., Ishisaki Y., Kawahara H., 2018, A&A, 618, A74

Urry C. M., Padovani P., 1995, PASP, 107, 803

Vacca V., Murgia M., Govoni F., Feretti L., Giovannini G., Orrù E., Bonafede A., 2010, A&A, 514, A71

Vacca V., Murgia M., Govoni F., Feretti L., Giovannini G., Perley R. A., Taylor G. B., 2012, A&A, 540, A38

Valtchanov I., Murphy T., Pierre M., Hunstead R., Lémonon L., 2002, A&A, 392, 795

Van Eck C., 2018, Galaxies, 6, 112

Van Eck C. L. et al., 2019, A&A, 623, A71

Van Eck C. L. et al., 2018, A&A, 613, A58

van Haarlem M. P. et al., 2013, A&A, 556, A2

van Weeren R. J. et al., 2017, Nature Astronomy, 1, 0005

van Weeren R. J., Bonafede A., Ebeling H., Edge A. C., Brüggen M., Giovannini G., Hoeft M., Röttgering H. J. A., 2012a, MNRAS, 425, L36

van Weeren R. J., Brüggen M., Röttgering H. J. A., Hoeft M., Nuza S. E., Intema H. T., 2011a, A&A, 533, A35

van Weeren R. J. et al., 2016a, ApJ, 818, 204

van Weeren R. J., de Gasperin F., Akamatsu H., Brüggen M., Feretti L., Kang H., Stroe A., Zandanel F., 2019, Space Sci. Rev., 215, 16

van Weeren R. J., Hoeft M., Röttgering H. J. A., Brüggen M., Intema H. T., van Velzen S., 2011b, A&A, 528, A38

van Weeren R. J. et al., 2009, A&A, 506, 1083

van Weeren R. J., Röttgering H. J. A., Brüggen M., Hoeft M., 2010, Science, 330, 347

van Weeren R. J., Röttgering H. J. A., Intema H. T., Rudnick L., Brüggen M., Hoeft

M., Oonk J. B. R., 2012b, A&A, 546, A124

van Weeren R. J. et al., 2020, arXiv e-prints, arXiv:2011.02387

van Weeren R. J. et al., 2016b, ApJS, 223, 2

Vazza F., Brüggen M., 2014, MNRAS, 437, 2291

Vazza F., Brüggen M., Gheller C., Hackstein S., Wittor D., Hinz P. M., 2017, Classical and Quantum Gravity, 34, 234001

Vazza F., Brüggen M., van Weeren R., Bonafede A., Dolag K., Brunetti G., 2012, MNRAS, 421, 1868

Vazza F., Brüggen M., Wittor D., Gheller C., Eckert D., Stubbe M., 2016, MNRAS, 459, 70

Vazza F., Brunetti G., Brüggen M., Bonafede A., 2018, MNRAS, 474, 1672

Vazza F., Brunetti G., Gheller C., 2009a, MNRAS, 395, 1333

Vazza F., Brunetti G., Gheller C., 2009b, MNRAS, 395, 1333

Vazza F., Brunetti G., Kritsuk A., Wagner R., Gheller C., Norman M., 2009, A&A, 504, 33

Vazza F., Eckert D., Brüggen M., Huber B., 2015, MNRAS, 451, 2198

Vazza F., Ettori S., Roncarelli M., Angelinelli M., Brüggen M., Gheller C., 2019, A&A, 627, A5

Vazza F., Roediger E., Brüggen M., 2012, A&A, 544, A103

Venturi T., Giacintucci S., Brunetti G., Cassano R., Bardelli S., Dallacasa D., Setti G., 2007, A&A, 463, 937

Venturi T., Giacintucci S., Dallacasa D., Cassano R., Brunetti G., Macario G., Athreya R., 2013, A&A, 551, A24

Vernstrom T., Gaensler B. M., Rudnick L., Andernach H., 2019, ApJ, 878, 92

Vogelsberger M. et al., 2014, MNRAS, 444, 1518

Walker S. et al., 2019, Space Sci. Rev., 215, 7

Walker S. A., Fabian A. C., Sanders J. S., Simionescu A., Tawara Y., 2013, MNRAS, 432, 554

Wang Q. H. S., Markevitch M., Giacintucci S., 2016, ApJ, 833, 99

Wen Z. L., Han J. L., 2015, ApJ, 807, 178

Wen Z. L., Han J. L., Liu F. S., 2012, ApJS, 199, 34

Werner N., Urban O., Simionescu A., Allen S. W., 2013, Nature, 502, 656

Wiita P. J., Rosen A., Gopal-Krishna, Saripalli L., 1989, Giant Radio Galaxies via Inverse Compton Weakened Jets, Meisenheimer K., Roeser H.-J., eds., Vol. 327, p. 173

Wik D. R. et al., 2014, ApJ, 792, 48

Wik D. R., Sarazin C. L., Finoguenov A., Matsushita K., Nakazawa K., Clarke T. E., 2009, ApJ, 696, 1700

Wilber A. et al., 2018, MNRAS, 473, 3536

Williams W. L. et al., 2019, A&A, 622, A2

Williams W. L. et al., 2016, MNRAS, 460, 2385

Willis A. G., Strom R. G., Wilson A. S., 1974, Nature, 250, 625

Willis A. G., Wilson A. S., Strom R. G., 1978a, A&A, 66, L1

Willis A. G., Wilson A. S., Strom R. G., 1978b, A&A, 66, L1

Willson M. A. G., 1970, MNRAS, 151, 1

Wittman D., Cornell B. H., Nguyen J., 2018, ApJ, 862, 160

Wittor D., Hoeft M., Vazza F., Brüggen M., Domínguez-Fernández P., 2019, MNRAS, 490, 3987

Wittor D., Vazza F., Brüggen M., 2017, MNRAS, 464, 4448

Wittor D., Vazza F., Ryu D., Kang H., 2020, MNRAS, 495, L112

Wright E. L., 2006, Publications of the Astronomical Society of the Pacific, 118, 1711

Xue Y.-J., Wu X.-P., 2000, MNRAS, 318, 715

Yan H., Lazarian A., 2011, ApJ, 731, 35

York D. G. et al., 2000, AJ, 120, 1579

Yuan Z. S., Han J. L., 2020, MNRAS, 497, 5485

Zhang X. et al., 2020, A&A, 642, L3

ZuHone J. A., Markevitch M., Johnson R. E., 2010, ApJ, 717, 908

Zweibel E. G., Heiles C., 1997, Nature, 385, 131

Zwicky F., 1937, ApJ, 86, 217